Fakultät für Mathematik und Naturwissenschaften | RWTH AACHEN UNIVERSITY

Synthetic anisotropic multiphasic hydrogels for *in vitro* tissue models

Von der Fakultät für Mathematik
und Naturwissenschaften der RWTH Aachen University
zur Erlangung des akademischen Grades einer Doktorin
der Naturwissenschaften genehmigte Dissertation

vorgelegt von

Ninon Dorothea Colette Lucienne Möhl, M.Sc.

aus Worms, Deutschland

Berichter: Universitätsprofessorin Dr. -Ing. Laura De Laporte
Universitätsprofessor Dr. rer. nat. Andrij Pich

Tag der mündlichen Prüfung: 01.12.2025

Pour tous ceux qui m'ont porté jusque-là.

When in doubt, go check out D. Weitz's papers
to read about your most recent idea. xD

Declaration of Authorship

I, Ninon Möhl, declare that this thesis and the work presented in it are my own and has been generated by me as the result of my own original research. I do solemnly swear that:

1. This work was done wholly or mainly while in candidature for the doctoral degree at this faculty and university;

2. Where any part of this thesis has previously been submitted for a degree or any other qualification at this university or any other institution, this has been clearly stated;

3. Where I have consulted the published work of others or myself, this is always clearly attributed;

4. Where I have quoted from the work of others or myself, the source is always given. This thesis is entirely my own work, with the exception of such quotations;

5. I have acknowledged all major sources of assistance;

6. Where the thesis is based on work done by myself jointly with others, I have made clear exactly what was done by others and what I have contributed myself;

7. Parts of this work have been published before as:

a. **N. Möhl** and L. De Laporte, "Multiphasic anisotropic systems," in Advanced Polymer Life Science,*World Scientific*, 2025, pp. 231–278.
b. EP 25223617.9, 15.12.2025, Title: Production of anisometric microparticles, Inventors: M. Mork, L. De Laporte, **N. Möhl**
c. **N. Möhl**, et al. "Exploring Compartmentalized Jet Polymerization for novel rod-shaped microgels and their potential in tissue engineering applications."

Biomaterials (2025): 123866.

d. **N. Möhl**, et al. "Development of a Synthetic 3D Platform for Compartmentalized Kidney In Vitro Disease Modeling." Advanced Healthcare Materials (2025): e03287.

e. M. Mork, **N. Möhl**, et al. "Upscaling the fabrication of rod-shaped microgels: a microfluidic method combining step-emulsification with consecutive droplet confinement in parallelized microchannels." Chemrxiv (2025).

08.01.2026, Ninon Möhl

List of publications

1. M. Mork*, **N. Möhl***, G. Romahn, and L. De Laporte, "Upscaling the fabrication of rod-shaped microgels: A microfluidic method combining step-emulsification with consecutive droplet confinement in parallelized microchannels.," 2025, Chemrxiv.

2. M. Mork, **N. Möhl**, and L. De Laporte, "Production of anisometric microparticles.," EP 25223617.9, 15.12.2025, patent filed.

3. **N. Möhl**, S. Babu, C. Bonhomme, et al., "Exploring compartmentalized jet polymerization for novel rod-shaped microgels and their potential in tissue engineering applications.," *Biomaterials*, 2025, 123866.

4. **N. Möhl***, D. Bouwens*, J. Abele, et al., "Development of a synthetic 3D platform for compartmentalized kidney in vitro disease modeling.," *Advanced Healthcare Materials*, 2025, e03287.

5. **N. Möhl** and L. De Laporte, "Multiphasic anisotropic systems.," in Advanced Polymer Life Science, *World Scientific*, 2025, pp. 231–278.

6. K. A.Waibel, R. Nickisch, **N. Möhl**, R. Seim, and M. A. R. Meier, "A more sustainable and highly practicable synthesis of aliphatic isocyanides.," *Green Chem.*, vol. 22, pp. 933–941, 3 2020. DOI:10.1039/C9GC04070F.

* Authors contributed equally.

Author's contributions

1. The published book chapter in Advances in Polymer Life Science called "Multiphasic anisotropic systems" is partially incorporated into **Chapter 1**. N.Möhl wrote the chapter and L. De Laporte corrected it.

2. The published article called "Development of a synthetic 3D platform for compartmentalized kidney in vitro disease modeling" in *Advanced Healthcare Materials* is incorporated in **Chapter 3**. The idea and results were obtained in collaboration with the research group of R. Kramann at the Uniklinik Aachen. The idea was drafted by L. De Laporte and R. Kramann. N. Möhl and D. Bouwens contributed equally to this work. R. Kramann and D. Bouwens provided the cell lines. Parts of this work have been previously submitted as a master thesis by J. Abele and a Bachelor thesis by A. Hans at RWTH Aachen University, which were supervised and planned by N. Möhl and examined by L. De Laporte and A. Pich. N.Möhl, A. Hans, J.Abele, T. Topic produced the microgels. N.Möhl, A. Hans, J.Abele, T. Topic and performed cell experiments, which was supported by D. Bouwens and Nina Schöling. All experiments were conceptualized and planned by N. Möhl and D. Bouwens. N.Möhl quantified all material related data presented in this work and analyzed the results, supported by J. Abele and A. Hans. N. Möhl performed and quantified metabolic essays. Immunohistochemistry was performed by N.Möhl and D. Bouwens, supported by T. Topic. N. Möhl imaged the samples via confocal microscopy and D. Bouwens analyzed the images quantitatively. D. Bouwens performed all qPCR experiments and analyzed the results. L. De Laporte and R. Kramann supervised the project. N.Möhl and D. Bouwens wrote the manuscript, which was corrected by L. De Laporte, R. Kramann and J. Jansen. All authors finalized the manuscript

3. **Chapter 4** first focuses on the upscaling of radical-free rod microgels via microfluidics. Parts of this work have been previously submitted as a Bachelor thesis by J. Török at RWTH Aachen University, which was supervised and planned by N. Möhl and examined by L. De Laporte and A. Pich. N. Möhl and M.Mork designed the

microfluidic chips and M.Mork farbicated them. J. Török performed the microfluidic experiments. A manuscript called "Upscaling the fabrication of rod-shaped microgels: A microfluidic method combining step-emulsification with consecutive droplet confinement in parallelized microchannels" available on Chemrxiv and submitted for peer review is incorporated partially in **Chapter 4**, regarding a microfluidic platform for producing rod-shaped microgels in parallel microchannels. Certain aspects of this platform have been additionally filed as a patent (EP 25223617.9, 15.12.2025). The content of this chapter is reduced to the parts and aspects of the manuscript/patent relevant to the context of this thesis. The initial idea of the method was conceptualized by M. Mork and L. De Laporte. M. Mork conceptualized, designed, and fabricated the initial microfluidic chip designs. M. Mork investigated the functionality of these microfluidic prototype designs with support of G. Romahn during microfluidic operation. Based on the findings, M. Mork and N. Möhl conceptualized an optimized chip design, which was designed and fabricated by M. Mork. M. Mork and N. Möhl developed the concept and designed the experiments of the manuscript in preparation with equal contribution. M. Mork conceptualized the microfluidic chip holder which was fabricated by A. Omidinia-Anarkoli. M. Mork and G. Romahn performed the microfluidic experiments regarding the PEGDA chemistry. M. Mork characterized the droplet sizes and flow behavior with support of G. Romahn during microfluidic operation which can be found in M. Mork dissertation. N. Möhl performed the microfluidic experiments regarding radical mediated thiol ene click chemistry. N. Möhl performed corresponding rheology measurements of bulk hydrogels for both polymer systems. M. Mork and N. Möhl characterized the corresponding microgels in nanoindentation measurements. S. Rütten and N. Assasa performed the sample preparation via critical point drying and the scanning electron microscopy of the microgels. Additional details regarding microfluidic chip design and droplet size with flow behavior are included in the corresponding patent/manuscript and dissertation of Ninon Möhl. The project was supervised by L. De Laporte.

4. A manuscript called "Exploring compartmentalized jet polymerization for novel rod-shaped microgels and their potential in tissue engineering applications" published in *Biomaterials* is incorporated into **Chapter 5**. S. Babu and N. Möhl designed the experiments, optimized the microfluidics setup for smaller channel dimensions and developed the concept of the article. S. Babu, N. Möhl, G. J. E. Yossa and C. Bonhomme performed the experiments. N. Möhl and M. Mork designed and M.Mork fabricated the microfluidic chips together with R. Nasehi. L. De Laporte supervised and developed the overall idea of the project. S. Babu submitted some results of these

experiments, partly shown in Figure 5.5 and Figure 5.9 of this thesis, as part of her PhD thesis about "Altering the mechanical anisotropy of the Anisogel to affect cell behaviour" that was conducted at DWI – Leibniz Institute for Interactive Materials and RWTH Aachen University. R. Nasehi conducted together with N.Möhl CFD simulations. N. Möhl performed the confocal experiments on the microfluidic set up, which was supported by R.Nasehi. R. Vinokur built the laser light set up. T. Haraszti performed quantitative analysis on some of the confocal images. Characterization of the material was conducted by N.Möhl and S. Babu. Optical characterization methods were performed in collaboration with the research group of J. Guck and conducted and analyzed by K. Kim. SAXS experiments were performed by B.Wu and G. Wittmann. The project was supervised by L. De Laporte. N. Möhl wrote the manuscript and S. Babu, M. Mork, R. Nasehi, R. Vinokur, T. Haraszti, K. Kim, B. Wu and G. Wittmann corrected it. All authors finalized the manuscript.

5. A manuscript in preparation is also partially incorporated in **Chapter 6**, which focuses on the development of an alternative hydrogel system for 3D cell culture. The work was conducted in a collaboration with H. Maynard's research group during a six months research stay at UCLA, CA, USA supported by a Fulbright scholarship. The initial idea was conceptualized by N. Möhl with support by L. De Laporte and H. Maynard. N. Möhl performed all experiments and results presented in this chapter.

6. Wording in individual sentences was sporadically refined using OpenAI's ChatGPT (Versions 4o and 5) to enhance clarity and readability. Herein, no contribution to the intellectual content was made.

7. For checking basic spelling, grammar, and punctuation errors the free version of Grammarly was used.

Acknowledgments

First, I would like to thank **Prof. Dr. -Ing. Laura De Laporte** for giving me the opportunity to pursue my PhD in her research group. During my time in the group, I especially valued the scientific knowledge I was able to gain from her, as well as the opportunity to work closely with her on my research projects. I am also grateful for her support with my fellowship applications and for enabling me to spend a few months of my PhD abroad. Beyond the scientific aspects, I truly appreciated her compassion and understanding during these four years, particularly in times when there was much happening in my private life as well.

Furthermore, I would like to thank my second supervisor **Prof. Andrij Pich** as well as **Prof. Rafael Kramann** for their guidance and scientific input, which enriched the quality of my research.

Furthermore, I would like to express my sincere appreciation to **Prof. Heather Maynard** at the University of California, Los Angeles (UCLA) for hosting me as a visiting graduate researcher for six months in her group. This stay has truly been life changing, as I was able to grow not only scientifically but also personally. My special thanks go to her group members, **Maggie, Ryan, Felix, Katie, Ben**, and **Pedro**, for helping me settle in and for introducing me to American culture — and to **Ricky**, who made sure I was always well supplied. **Maggie**, thank you for becoming such a close friend and for sharing your bread-making skills. I especially want to thank **Hilan** for helping me find an apartment and for inviting me to different events — my stay would not have been the same without you. I am also grateful to **Michèle, Guy**, and **Lizzie**, who took me in during the fires and made sure I felt at home. I also thank **Angela Pitenis, Juan Vargas, Lisa Månsson**, and **Dixon Atkins** for their collaboration during this time and for allowing me to perform cell experiments as well as further material characterization in their labs at UCSB.

My time at DWI was filled with ups and downs, and I never quite knew what was

coming next, but it was certainly never boring. I am grateful to have been part of this community. I would like to thank my former supervisor and now sister, **Susan Babu**, who first introduced me to the institute and the group. You are my rock, even after leaving our labs. I also thank everyone in the group who helped with my research or simply made me smile. I am grateful for all the scientific discussions and support — I believe this is what makes our group unique. In particular, I would like to express my gratitude to **Susan Babu, Dr. Yonca Kittel, Matthias Mork, Laura Klasen, Dr. Ramin Nasehi, Dr. Daniel Günther, Tom Schneider, Dr. Cédric Bergerbit, Céline Bastard, Nina Schöling, Tanja Tôpic**, and **Bernhard Häßel**. My greatest thanks go to **Laura Klasen** for always having my back and for being such a wonderful friend. Also for showing me how Fahrenheit differ from Celsius.

I would also like to thank all other group members, **Philip (Piet), Iris, Veronica, Alisa, José, Ekin, Omid, Qianyu, Jace, Elif, Till, Misael, Claudia, Anna, Julia, Greta, Catarina, Caro, Corinna, Oscar, Emilia, Xin**, and **Fred**. I am grateful to my collaboration partner **Daphne Bouwens** for bringing biology a little closer to me — I am proud of what we have achieved together. Special thanks go to **PD Dr. Tamàs Haraszti** for taking the time to teach me AFM and help analyze my data, and to **Rostislav Vinokur** for building my new jet setup, which made my life so much easier. I also thank the institute staff, **Ahmed, Petra, Meike, Ewgeni, and Angela**, for all their help. It has also been a pleasure to supervise and teach great students who contributed to this thesis: **Aline, Johanna, Jonas, Simon, Camille, Leila**, and **LiJing**. Furthermore, I would like to thank **Dr. Kyoohyun Kim, Dr. Baohu Wu**, and **Dr. Gilles Wittmann** for performing Brillouin and SAXS measurements.

I am grateful for the KFO project as part of the **DFG (Deutsche Forschungsgemeinschaft)** for the funding I received during my PhD research, as well as the **Joachim Herz foundation** and **Fulbright**.

Finally, I would like to express my deepest gratitude to my friends. I want to thank the petrol gang — **LaufLa, Nitin, Max**, and **SL**, and everyone who joined (especially the **KVB boys**) — for taking my mind off the PhD every year during our vacation trips. I also thank **Saskia, Sandra, Nils**, and **Anton** for making my time in Aachen so much better and for growing so close as friends in the past years. **Anton**, you made my lunch breaks a culinary escape. **Chiara** - even from far you supported me and we know *'ein Ö kommt selten allein'*. I would not have been able to complete my PhD without the support of my family, especially my **Maman** and my two sisters, **Jülipnich**

and **Jalipnich**, who always reminded me that I could do anything. The same goes for my sisters-in-law, **Natascha** and **Esther**, who showed me what girlhood means.

Lastly, I would like to thank my favorite person in my life, **Max**. He has been with me from the very first day of my PhD, and I am so lucky to have met him during this time. I wouldn't miss it for the world. Today, we are parents to our two cats, **Suki** and **Raikou**, which makes this a full circle moment.

Contents

List of Figures

List of Tables

Abstract

The regeneration of complex, hierarchically organized native tissue and organs requires approaches that can provide directional guidance for cells. While most injectable hydrogels enable minimally invasive delivery and adaptable properties such as stiffness and degradation cues, they remain mostly isotropic and do not present cellular guidance cues. To overcome this limitation, multiphasic anisotropic hydrogels have been developed, employing external triggers (electrical, light, sound, or magnetic stimuli) or mechanical deposition. An emerging approach involves the use of rod-shaped microgels as tissue engineering building blocks. Rod microgels can be used as structural templates or as structural guidance, and both approaches were developed using microfluidics and are discussed in this thesis. First, a fully synthetic 3D kidney disease model designed to overcome current limitations in *in vitro* systems was developed, using anisometric PEG microgels that enable structural organization of a triple co-culture of key renal cell types, including epithelial cells ($CD10^+$), endothelial cells ($CD31^+$), and pericytes ($PDGFR\beta^+$). Furthermore, a robust and scalable method has been established to produce degradable rod microgels in a microfluidic high-throughput manner. The potential and feasibility of the microfluidic design are highlighted by using two photo-initiated PEG-based polymerization chemistries and comparing them side by side. Additionally, advances using compartmentalized jet polymerization are reported, enabling the continuous production of rod microgels with adjustable stiffness, aspect ratios, and sizes as small as 3 µm. This method is also used to produce ultra-soft and porous variants with pore sizes in the range of 2–5 µm. Finally, in this thesis an alternative cross-linking approach is introduced using dynamic covalent bonds. Different polymer architectures are compared and their influence on the hydrogel properties was assessed. The reaction kinetics were improved through the addition of a biocompatible catalyst.

1 Motivation and thesis overview

1.1 Introduction

The extracellular matrix (ECM) is present in all tissues and organs, including muscles, blood vessels, nerves, and the heart and is maintained, remodeled, and structured by the surrounding cells.[1] Besides controlling different cellular processes, *e.g.* proliferation, differentiation, or adhesion, the ECM also provides the native tissue's function.[2,3] The ECM forms a three-dimensional (3D) network that primarily consists of proteins, proteoglycans and glycoproteins forming a natural hydrogel. Its structural and spatial organization and composition are distinctive to each tissue's function (Figure 1.1).[4] For example, the ability to regulate blood pressure in our body is given by the orientation of the smooth muscle cells, that arrange in a circumferential manner forming multiple layers in arterioles and arteries.[5] Furthermore, force is generated through the skeletal muscle that is built of oriented fibers, that exhibit viscoelastic and anisotropic behavior.[6–10] Other tissues provide a more complex ECM architecture, *e.g.* the heart, where differently oriented myocardial cells create an anisotropic structure that ensures contraction and pumping action, which is crucial for a healthy pump function.[11] Continuing the increase in structural complexity, the ECM organization in cartilage consists of three different zones with distinct orientation of collagen fibers, which have proven to be a key factor for correct tissue function.[12]

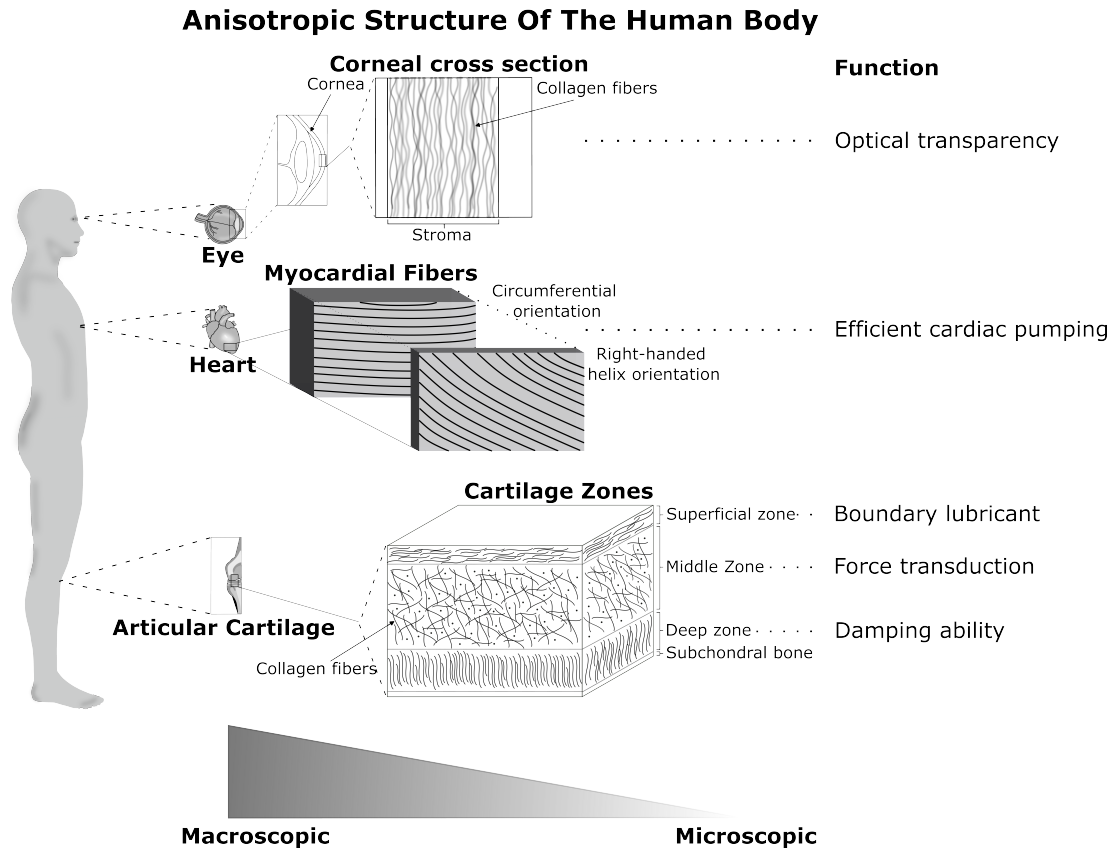

Fig. 1.1: Anisotropic structure of the human body. Reproduced from[4] with permission.

Traditionally, synthetic polymers such as poly (glycolic acid) (PGA), poly (lactic acid) (PLA), or poly (lactic-co-glycolic) acid (PLGA)[13,14] were used to provide scaffolds that are well known and Food and Drug Administration (FDA) approved. However, scaffolds made of these polymers are not capable of mimicking the mechanical, (bio)chemical and structural complexity of the ECM and require high invasive surgery for transplantation, potentially associated with trauma, and a prolonged healing process.[15] Therefore, advanced materials better mimicking the ECM characteristics and allowing for low invasive delivery by injection are of high interest for tissue engineering applications.[16] A class of material called hydrogels has been widely studied as potential injectable materials, as they are liquid at first, and can cross-link after injection and swell in water.[17] In addition, their mechanical and chemical structure resembles that of the natural ECM and features biocompatibility.[18] However, most hydrogels are intrinsically isotropic and lack the structural complexity found in the native ECM. More recently, hydrogels can either be rendered anisotropic through inherent anisotropic characteristics of the material or, anisotropy can be introduced by the application of external forces. Another strategy

consists of the incorporation of anisotropic (nano and micro) particles, leading to so-called multiphasic anisotropic hydrogels.[4] These advanced hydrogel systems offer control over material properties at different length scales, presenting a valuable tool for mimicking the structural, and functional complexity of native tissues.

1.2 Multiphasic anisotropic hydrogels

The regeneration of native tissue demands minimally invasive biomaterials that provide 3D microenvironments closely mimicking its mechanical properties. Hydrogels meet these demands as they are injectable and allow for cross-linking of their precursor *in situ*.[19] The resulting water-swollen networks can be modified with cell signaling and binding domains, or growth factors required for cellular attachment and proliferation.[20,21] For proper cell migration and proliferation, macropores in the range of tens to hundreds of microns, as well as pore interconnectivity, are essential. However, most hydrogels exhibit pore sizes in the range of 100 nm, impairing these processes.[22–24] Approaches to circumvent the lack of porosity include rendering the hydrogel susceptible to hydrolytic degradation or enzymatic degradation through the addition of peptide sequences sensitive to matrix metalloproteinases (MMP). Yet, these processes depend on cell-mediated remodeling or are inherently time-dependent.[25] More advanced approaches to ensure 3D macropores right after hydrogel formation have been studied based on leachable porogen, phase separation, or interlinking of microgels - either spherical or rod-shaped.[26–28] While leachable porogens can generate pores after gelation, pore interconnectivity, as well as pore size and their distribution is less guaranteed and relies on the presence of a leachable agent. Similarly, phase separation techniques might result in heterogeneous structures. In contrast, annealing of soft microgels, specifically rod microgels, allow for modular assembly into macroporous constructs with pore sizes depending on the dimensions and aspect ratio of the microgels.[28–30]

Beyond porosity, hydrogels are mostly isotropic and cannot direct cellular orientation, a key feature to regenerate anisotropic tissues like muscle or nerves.[4,19,31] To overcome this limitation, several strategies were used. For instance, a combination of microporosity and alignment within a hydrogel system was achieved by pressing pre-formed bulk hydrogels through a grid of adjustable mesh sizes. This creates high

aspect ratio microstrands that are connected by a secondary cross-linking step.[32] This method has been proven to be cell-instructive *in vitro*, triggering oriented muscle tissue maturation. Another method has been proven effective in supramolecular assembly of oriented nanofibers.[33] A water-based solution of charged peptide amphiphiles (PA) undergoes a modulated temperature change to generate aligned fiber bundles with a diameter of approximately 40 nm. *In vitro* cell experiments showed that human mesenchymal stem cells (hMSCs) and cardiomyocytes recognized the directionality of the fibers and aligned alongside them. These self-assembled PA can be employed to form anisotropic injectable scaffolds, although the orientation of the fibers is connected to the direction of the injection and cannot be adjusted independently.

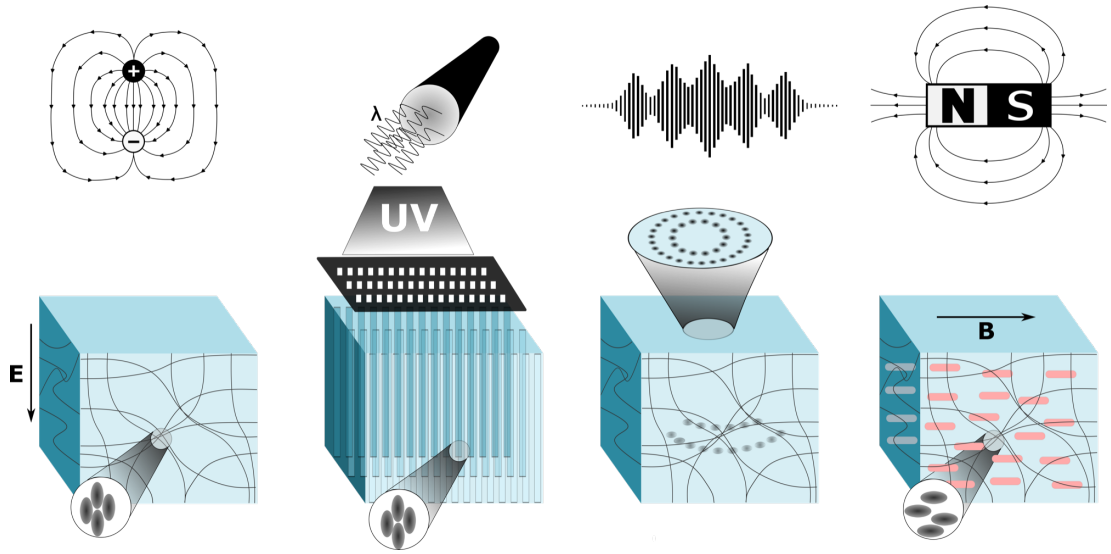

Fig. 1.2: Different external stimuli to induce anisotropy. From left to right: eletrically, light, sound, and magnetically induced. Adopted from[4] and reproduced with permission.

More control over physical and mechanical properties, as well as spatial properties, can be obtained by using external triggers, such as electrical fields, light or sound waves, or magnetic fields (Figure 1.2).[4,34–37] The effect of electrical stimulation (ES) on cell behavior in the human body has been well established. The excitation of cells at a single-cell level has been found to be linked to ion fluxes through voltage-activated Ca^{2+} channels.[38] Furthermore, fibroblasts that connect healthy tissue and regenerate injured tissue are eminent for their sensitivy towards mechanial, chemical, but also eletrical signals.[39–42] Conductivity in porous hydrogels can be induced through the addition of nanoparticles, such as graphene flakes or carbon nanotubes,[43] or through conductive polymers (CPs).[43,44] In order to provide

conductivity but also biocompatibility, researches have developed hybrid conductive hydrogels based on polyisocyanides (PICs) to form soft 3D matrices for cell culture and poly (aniline-co-*N*-(4-sulfophenyl) aniline (PASA) to render the constructs conductive.[45–49]

Looking at light as an external trigger to induce anisotropy in 3D hydrogels, researchers have recently developed a technique called filamented light (FLight) biofabrication to produce macroscopic hydrogels with unidirectional microfilaments with relevant sizes (1 to 100 µm) within seconds.[36,50,51] The method is based on optical modulation instability (OMI) describing the division of a coherent light beam into distinct light filaments, when propagating through an optical nonlinear media, such as photoreactive polymers.[52–55] FLight has been shown to induce anisotropy in normal human dermal fibroblasts (NHDFs) as well as to promote directed migration, a feature absent in conventional bulk hydrogels.

Acoustic methods also allow control over 3D cellular organization. One method called sound-induced morphogenesis (SIM) is the combination of acoustic patterning and cellular self-assembly to create complex and perfusable vascular networks.[37] Additionally, standing waves have been exploited to create spatially organized arrays of chondrocytes mimicking the architecture of the deep zone present in articular cartilage.[56]

Magnetic alignment was initially achieved employing the diamagnetic properties of ECM proteins like collagen or fibrin fibrils to regenerate peripheral nerves.[57,58] Later on, superparamagnetic iron oxide nanoparticles (SPIONs) were used to create aligned strings parallel to the magnetic field lines inside a collagen matrix and applied to align neurons.[59] However, most of these approaches required high amounts of nanoparticles with possible cytotoxic effects or with limited injectability and control over the microenvironment.[60,61] Compared to other methods, the addition of magneto-responsive short fibers or rod microgels creates a system where the properties such as stiffness, porosity, dimensions, *etc.* can be decoupled and controlled independently, while providing injectability, spatial organization, and alignment. Specifically, magneto-responsive rod microgels serve to introduce anisotropy into 3D hydrogel systems. Microgels, similar to hydrogels, are injectable water-swollen networks with diameters between 10 nm and 100 µm, whose (bio)chemical and mechanical properties are tunable.[62,63]

In this work, two distinct types of rod microgels are developed and produced using different fabrication techniques and applied in multiphasic hydrogels: one is designed to build a kidney tubule model via sacrificial templating, while the other is engineered to provide directional cues or support 3D cellular self-assembly by introducing unique mechanical properties. Furthermore, the degradable rods used for sacrificial templating are upscaled for the first time as part of a separate effort to increase the production rate and reduce valuable time and costs. To further enhance the physiological relevance of these multiphasic anisotropic hydrogels, a dynamically covalently cross-linked hydrogel is also investigated as an alternative to the covalently cross-linked matrix used in earlier stages.

1.3 Rod microgels in tissue engineering applications

A new class of materials, called microgels, has emerged as a promising material in tissue engineering applications, available in different sizes and shapes.[62] Spherical microgels have been widely applied in different applications, such as drug delivery, cell encapsulation, or as building blocks for granular hydrogels and bioinks.[64] The use of anisometric microgels has several advantages as compared to spherical ones, as they can be used to build 3D constructs with anisotropic properties. For example, our group has previously shown that magneto-responsive rod microgels can be used to introduce anisotropy inside bulk hydrogels.[35,65–67] In this technology, which has been published and patented as the Anisogel, the microgels are mixed and aligned with a low external magnetic field (<100 mT) and fixed in their position upon cross-linking of the surrounding matrix. The group also used this system to introduce multi-directionality into the Anisogel through the implementation of ellipsoidal maghemite nanoparticles, enabling control over the alignment in different directions.[68] Beyond the incorporation of rod-shaped microgels inside a hydrogel matrix, our group showed that rod microgels can be chemically interlinked to form macroporous structures called microporous annealed particles (MAPs), providing larger pores than their spherical counterpart.[28–30] This is particularly interesting for cell infiltration and nutrient supply. An increase in porosity was also observed when using anisometric microgels to form granular hydrogels.[69] These promising structural and functional features of rod microgels suggest their potential beyond the abovementionend findings - particularly as templates for more complex architectures.

1.3.1 Rod microgels as structural templates

The formation of tubular structures in tissue engineering is often desired, as they are present in many tissues such as vasculature, the intestines, or the kidney, and many others, and enable nutrient and oxygen transport. Therefore, researchers have focused on the development of models of tubular systems to study diseases or to accelerate drug development.[70–73] In order to obtain the desired tissue function, the composition and spatial organization of distinct cell types are crucial. Tubular architectures require epithelial or endothelial cells in combination with supporting cells. Epithelial cells form protective and functional barriers to control the movement of substances and protect against physical damage or pathogens.[74–77] Endothelial cells create the inner surface of blood vessels, and provide a barrier between the blood and surrounding tissue to control *e.g.* the blood flow, the permeability or inflammation.[78–81] Depending on the application, the cell lines vary. Furthermore, a continuous epithelial or endothelial lining is needed to mimic tubular scaffold. Most commonly, the cells are seeded on a two-dimensional (2D) surface, unable to reconstitute the 3D architecture of the native tissue. Researches have addressed this discrepancy by employing flat membranes that are coated with cells and subsequently rolled into tubes.[82–84] Another approach is to seed the cells onto surrounding walls during rotational or pressurized activation.[85–87] These methods aim to mimic the curvature and hollow geometry of native tubules, although they are often limited in uniformity or scalability. Another important criterion is to provide nutrients to all present cells. *In vitro* tissue models depend on perfusion to mimic nutrient and oxygen transport across the entire tissue mimetic.[88]

The kidney's hierarchically organized architecture makes it difficult to develop suitable *in vitro* models. Most established methods are based on 2D cultures of renal epithelial cells, organoids derived from induced pluripotent stem cells (iPSCs), or microfluidic platforms.[?,89–91] While kidney organoids mimic nephrogenesis, they exhibit limited maturation and comprise off-target cell types due to uncontrollable iPSCs differentiation.[92,93] Microfluidic-based approaches offer perfusable channels, though such devices are often expensive for one-time use and are not adaptable.[91,94,95] 3D bioprinting models can mimic the tubule-interstitium or the proximal tubule (PT) on perfusable chips using a gelatin-fibrin ECM.[96–98] This system was further improved through the addition of a second channel enabling vascularization and employing kidney organoids to better recapitulate the native tissue microenvironment.[99] Yet, no fully polymer-based synthetic 3D platform for *in vitro* kidney disease modeling has

been developed, offering control over the microenvironment and the possibility for transfer to automated high-throughput pipetting systems.

Different techniques have been established to produce tubular architectures, including casting, electrospinning, rolling, and 3D bioprinting or decellularization. However, each method presents several challenges. Casting is compatible with multiple material types and easy to implement, while electrospinning offers high control over the scaffold properties. However, both techniques often involve secondary cell seeding and generate toxic byproducts.[100–103] With the rolling technique 3D tubes can easily be obtained from seeding the cells in 2D. The difficulty here is to seal the tube properly.[100] A more sophisticated technique such as 3D printing anticipates a high degree of customization and control over the scaffold formation. However, this typically requires costly equipment and the printing resolution is often not high enough, especially with viscous materials.[100–102] Decellularization provides high biocompatibility as well as intrinsic biochemical factors that can support tissue engineering, but suffers from high variability and little control over the scaffold properties.[100–102] In another attempt to build tubular structures, our group has used cellulose nanofibrils (CNF) to create 3D scaffolds using extrusion sacrificial templating.[104] The tubule CNF constructs were coated with fibroblasts and subsequently dissolved enzymatically through cellulase with control over degradation time. This resulted in the formation of a 3D free-standing tube composed only of fibroblasts with a large lumen (0.8 mm diameter). These techniques cannot be easily upscaled or transferred to automated pipetting systems and also lack the appropriate physiologically relevant size, *e.g.* native kidney tubules have a diameter < 100 µm.

Researchers have also used spherical microgels as sacrificial templates, for example to create pores in 3D constructs. Gelatin methacryoyl (GelMA) microgels have been blended with sacrificial gelatin microgels to obtain a composite bioink with control over the void fraction to enhance cell migration.[105] This improved cell viability and function. Furthermore, alginate-based microbeads and 3D-printed filaments were simultaneously added to a gelatin-based hydrogel to obtain a porous scaffold and perfusable channels for vascularization.[106] The channels were in a size range of 300-400 µm enabling cell infiltration and blood flow *in vitro*. Additionally, spherical microgels have been used as a support matrix to print sacrificial materials that can be removed subsequently to form perfusable channels or other complex structures.[107] Compared to spherical microgels, rod shaped microgels have proven to enhance porosity in 3D microgel-based scaffolds, but also exhibit the ability to guide cells

and to provide spatial and structural organization in 3D hydrogels.[28,29,63,65,66] Rod microgels have, up to now, not been used as sacrificial templates in tissue engineering applications. Furthermore, the abovementioned studies using spherical microgels as sacrificial material, rely on natural polymers rather than synthetic polymers. Natural polymers such as gelatin or alginate do not provide control over the material's properties and often vary from batch to batch. For that reason, synthetic polymers such as poly (ethylene) glycol (PEG) are well established, as they can be chemically and biochemically tuned according to needs and ensure reproducibility. PEG is a biocompatible polymer, that is medically approved and used in a wide range of hydrogel and microgel applications.[108–110] The network of PEG-based microgels can be adjusted using multiple PEG polymers comprising different architectures and molecular weights.[111] The degradation rate can be tuned employing different cross-linkers, making it a versatile polymer backbone.[112–114]

Rod microgels are an interesting tool, as they provide anisotropy in size ranges closer to the native tissue (< 100 µm) and can be chemically, biochemically and mechanically adapted to mimic the suitable microenvironment. Depending on the desired dimensions, shape and mechanical and chemical properties, as well as production rate, rod microgels can be produced employing various techniques.[62,63] The fabrication methods will be further discussed in Chapter 2. This thesis focuses on the development of PEG-based rod microgels produced continuously *via* microfluidics. Microfluidics is defined as the manipulation of fluids within micron-scale channels, allowing for accurate production parameters.[115]

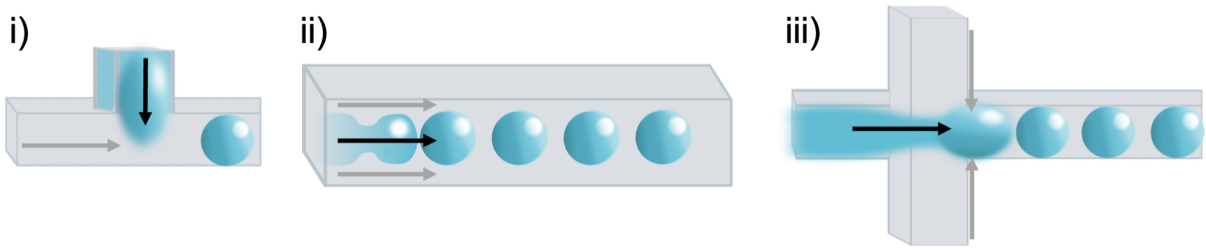

Fig. 1.3: Microfluidic flow regimes to obtain droplets. i) T-junction ii) Co-flow iii) flow-focused (FF).

Different regimes to produce droplets can be operated (see Figure 1.3), among which flow-focusing in the squeezing regime is most commonly used to produce rod microgels. In this thesis, the rod microgels were produced by flow-focusing squeezing microfluidics with on-chip gelation using PEG as a polymer backbone. The reaction mechanism followed a base-catalyzed Michael-type addition. The

microfluidic chip design is based on previous work,[116] and was further optimized in this thesis, through the addition of a flush at the outlet (Figure 1.4) to diminish pressure fluctuations. To address the limitations of current kidney disease platforms, such as poor spatial organization and scalability, we focused on the development of a platform that uses PEG-based rod microgels with a crosssectional diameter of 80 µm as structural templates to mimic the PT in Chapter 3. In order to obtain a functional kidney model, key renal cell types were provided by the group of Rafael Kramann at the Uniklinik Aachen (epithelial cells $CD10^+$, endothelial cells $CD31^+$ and pericytes $PDGFR\beta^+$ as supporting cells) to mimic the multicellular composition of the native tissue.

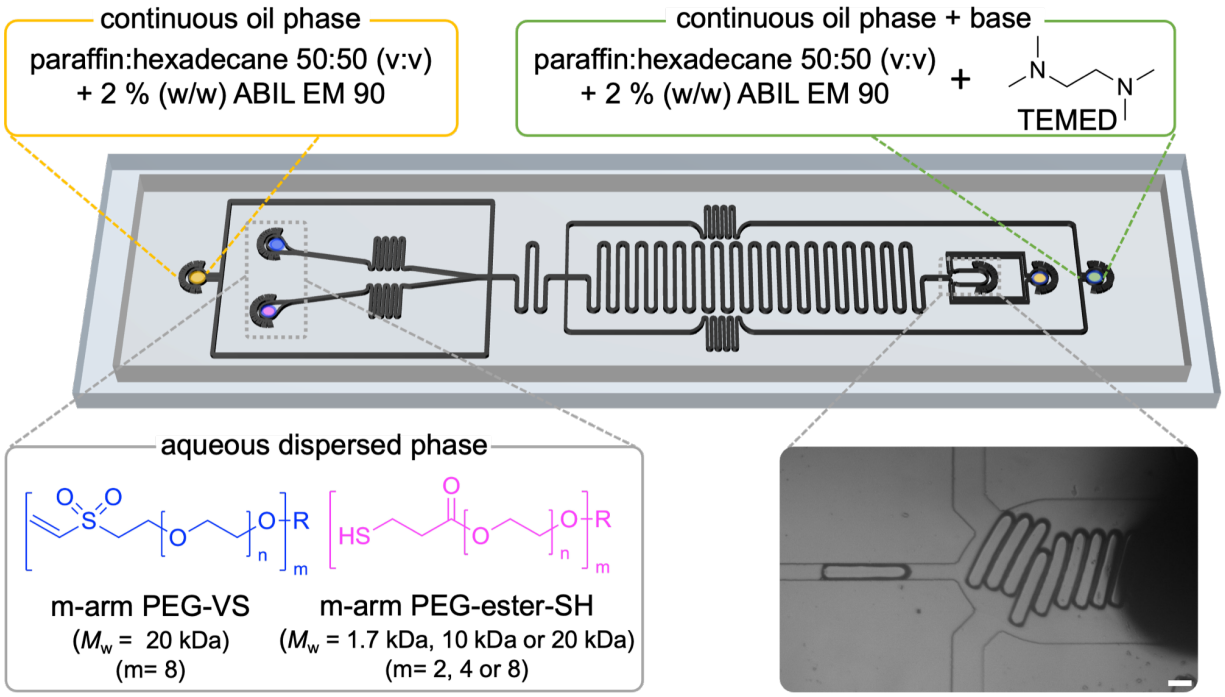

Fig. 1.4: Microfluidic chip design to produce degradable rod microgels based on a previous publication[116] with focusing oil at the outlet. The precursors are highlighted with different colors: poly (ethylene glycol) vinylsulfone (PEG-VS) in blue and PEG-ester-SH in pink. The continuous phase consists of paraffin and hexadecane (50:50) with the addition of ABIL EM 90 (yellow). To initiate the reaction the continuous phase is supplemented with a base *N,N,N′,N′*-Tetramethylethane-*1,2*-diamine (TEMED) (green).

The microgels were rendered degradable and are the basis to Chapter 3, to develop a 3D synthetic compartmentalized kidney disease model. The degradability was ensured through the addition of an ester moiety that can be dissolved on demand by the addition of lipase. Lipase is known to specifically degrade esters through hydrolysis.[117] Therefore, the rod microgels can be used as synthetic sacrificial

templates to model kidney tubule. Before performing cell experiments, the bulk properties of three different star poly (ethylene glycol) (sPEG)-ester-SH were probed with different numbers of arms (m=2,4,8) and different molecular weights (1.7 kDa, 10 kDa and 20 kDa respectively) to cross-link with 8 arm PEG-VS 20 kDa resulting in 5 % (w/v) hydrogels. Their gelation time and storage modulus (G') were assessed using rotational rheology. The gelation time was then correlated to their ability to form rod microgels on-chip using the microfluidic device, as insufficiently cross-linked microgels would snap back to spheres. Using linear PEG-ester-SH during microfluidic production, a minimum of 15 % (w/v) of total PEG content was needed, whereas for the 4 and 8 arm precursors, 5 % (w/v) was sufficient to produce stable rods on-chip. The mechanical properties of the rod microgels were then assessed through nanoindentation to obtain the Young's modulus and their degradation rates were varied with the addition of different lipase concentrations. In doing so, degradation rates ranging from minutes to days could be achieved. After having characterized the rod microgels' properties, their cell compatibility had to be analyzed. First, the impact of the enzyme on the different cell types was determined through a metabolic assay probing different lipase concentration (0.00125 % - 0.5 % (w/v)) in a 2D culture. No significant difference could be observed in the samples with enzyme or controls. In order to form a confluent epithelial layer on the rod microgels, the cell attachment efficiency was assessed through live imaging, where the sPEG-ester-SH led to the best results. For all following experiments, the 8 arm sPEG-based microgels were used. To mimic the ECM, the PEGKQ hydrogel, developed in our group,[65] was used in combination with the remaining two cell types, CD31+ and PDGFRβ and a cell-adhesive peptide (GRGDSPC, 600 µM). The PEGKQ hydrogel contains 8-arm PEG-VS (sPEG-VS, 20 kDa) functionalized with two different peptides, Ac-FKGGGPQGIWGQERCG-NH_2 (K-peptide) or NQEQVSPLERCG-NH_2 (Q-peptide), *via* Michael-type addition with the free thiol on the cysteine (C). The Q-peptide is a substrate for activated Factor XIII (FXIIIa), which is a transglutaminase that couples the amine of the lysine (K) to glutamine (Q). This reaction then results in a covalently cross-linked hydrogel network. We optimized the cell ratios and concentrations, as well as the polymer concentration used to form the hydrogel. This resulted in a $CD31^+$:PDGFRβ^+ ratio of 1:1 with 1000 cells/µL in total and a PEGKQ concentration of 1.5 % (w/v), as this presented cell spreading and network formation. The need for a compartmentalization of the $CD10^+$ cells and the remaining two cell types became apparent when culturing all three cell types in a triple-co-culture inside the hydrogel matrix presenting poor cell spreading and network formation. To first culture the rod microgels with the $CD10^+$ cells until confluency and then transfer

them into the 3D hydrogel matrix together with the CD31$^+$ and PDGFRβ^+ resulted in a 3D compartmentalized *in vitro* kidney model as depicted in Figure 1.5. The tubule structure was then obtained through the addition of lipase to the cell culture media, which degraded the rod microgels and resulted in an epithelial layer inside a 3D hydrogel.

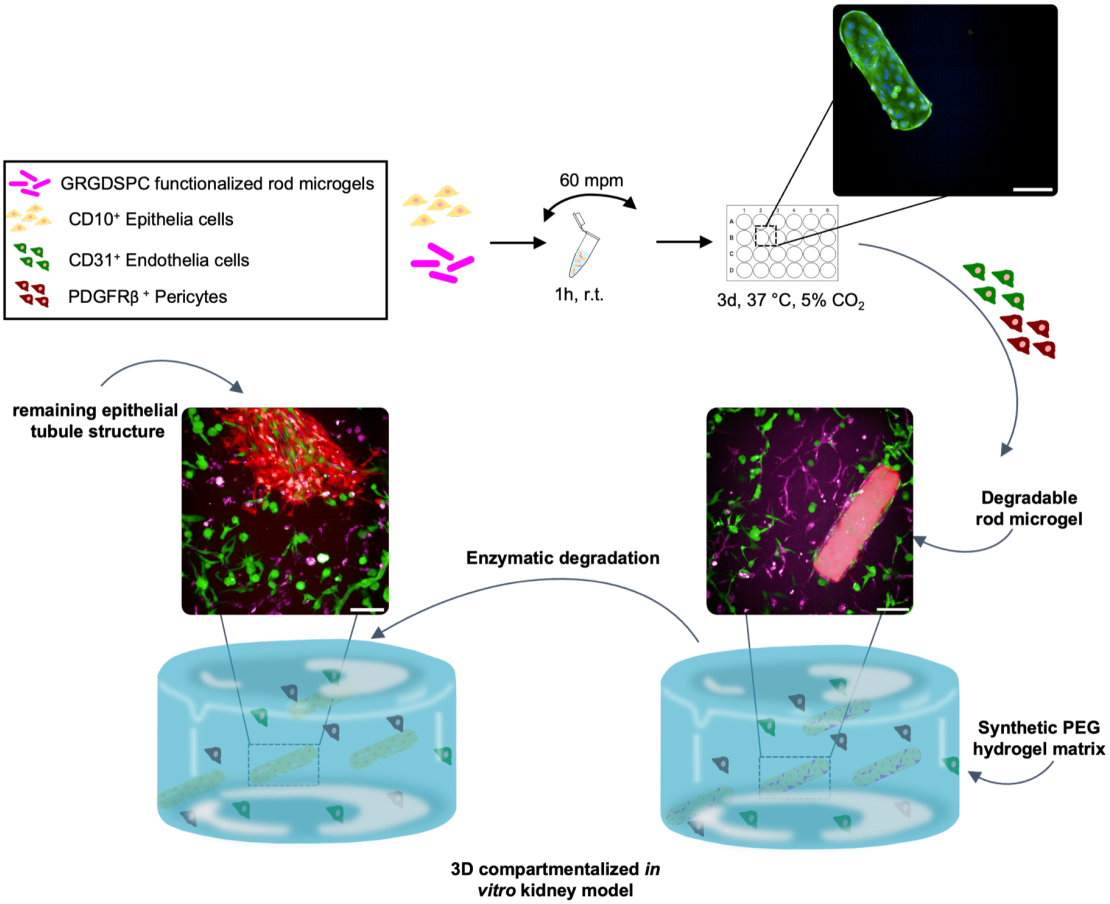

Fig. 1.5: Preparation of an *in vitro* synthetic 3D compartmentalized kidney disease model. After incubating the rod microgels with CD10$^+$ epithelial cells to obtain a confluent layer, they are transferred into the hydrogel matrix together with the endothelial cells (CD31$^+$, green) and the pericytes (PDGFRβ^+, magenta). The microgels degradation occurs upon addition of lipase, resulting in a epithelial tubule like structure.

The goal of Chapter 3 is to prove the concept of our model and to show functionality through the addition of an injury stimulus called TGFβ. TGFβ is a key driver of fibrosis, as well as of fibroblast-to-myofibroblast transition of the PDGFRβ^+ cells *in vitro*.[91,118] We hypothesized a higher expression in Collagen 1 in injured samples with degraded rod microgels, as other reports have shown that the pathological conditions of fibrosis are based on the injured PT and the spatial communication, during which

the PT directs signals to the interstitial space.[119,120] We could observe an increase in Collagen 1 expression in our 3D model compared to a conventional 2D model using inserts.

1.4 Upscaling of rod microgel production

While flow-focusing microfluidics in the squeezing regime offer control over structure, the scalability remains limited, especially for high-throughput screening platforms. Typically, such microfluidics are operated in a single channel, making it difficult to transfer to automated pipetting systems. The majority of microfluidic systems producing rod-shaped microgels with relevant properties and sizes for tissue engineering applications are considered low in throughput, as they are running at pre-polymer flow rates < 0.2 mL/h.[28,116,121,122] One challenge is the droplet geometry, as it demands a minimum residence time on-chip to preserve the elongated rod shape, which is prompted during cross-linking. Furthermore, the pressure within the microfluidic device has to be maintained at a constant level to avoid fluctuations or leaking. The upscaling of spherical microgels has been achieved with different production techniques and materials to obtain production rates in the range of a few ml/h up to L/h.[123–127] However, up to now, no microfluidic design has been established to produce degradable rod microgels in a high-throughput manner. Upscaling in microfluidic systems usually includes the parallelization of FF channels, though another approach is to implement parallelized step-emulsification (SE) to produce spherical droplets and particles in a high-throughput manner.[125,126,128–131]

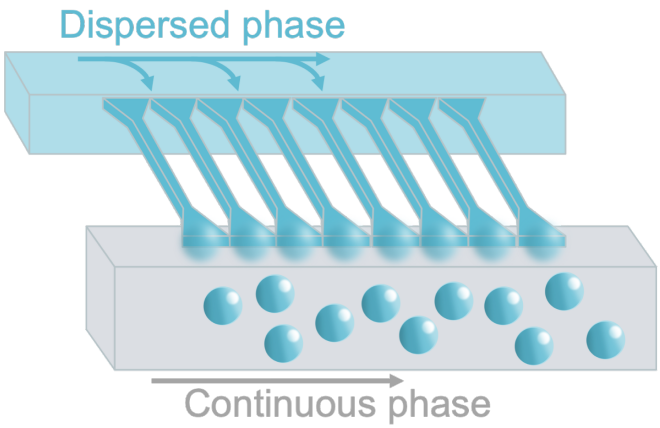

Fig. 1.6: Step-emulsification microfluidic configuration.

SE is based on a sudden pressure drop that arises between an array of individual shallow nozzle channels attached to a deep reservoir channel (Figure 1.6). The dispersed phase is typically introduced through the individual nozzles, consisting of, *e.g.* the pre-polymer solution, and the continuous phase, *e.g.* the oil phase, enters through the deep reservoir channel. In doing so, spherical droplets or particles are formed that are less affected by flow parameters than FF configurations. Although SE can only be used to generate spheres, it offers the possibility to a scalable production platform that can subsequently be integrated into a droplet squeezing-regime technique. In Chapter 4, we first focused on the development of a high-throughput microfluidic device using base-catalyzed Michael-type addition with the same precursors as in Chapter 3 to obtain degradable rod microgels in a high-throughput manner. However, the base-catalyzed rod formation could not be significantly upscaled, though prototypes and suggestions will be discussed in Chapter 4.

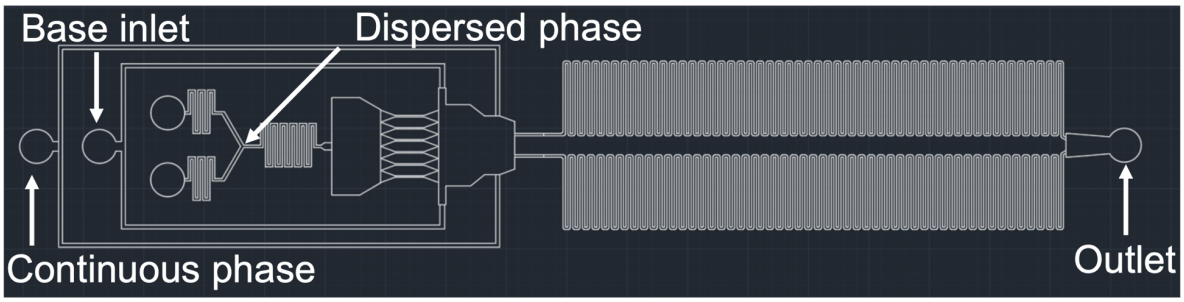

Fig. 1.7: High-throughput microfluidic device design to produce base-catalyzed Michael-type addition degradable rod microgels. The design is equipped with a SE section to first generate spheres with a subsequent addition of the base to initiate the reaction and parallelized FF channels to squeeze the spheres into rod microgels.

The idea was to first generate spheres through SE and to combine it with a second step on-chip where the spheres are squeezed into rod-shaped droplets and subsequently cross-linked by adding the base (Figure 1.7). However, the design complexity was too high to achieve stable production at significantly higher flow rates.

The throughput of a microfluidic device depends on the configuration but also on the chemistry used. For this reason, in Chapter 4, we then explored an alternative chemistry that is now based on light-mediated click-chemistry. This enabled a reduction in complexity in the microfluidic device design, as the cross-linking could now be induced through ultra violett (UV) light, while maintaining the degradability of the rod microgels. Together with my colleague Mattias Mork, we assessed the

differences in free radical polymerization (FRP) and radical mediated thiol-ene click chemistry. In collaboration, we optimized the polymer and continuous phase as well as the production parameters and assessed the materials' properties side-by-side.

1.4.1 Cross-linking strategies for microgel formation during microfluidics

The molecular structure of a microgel precursor influences the reaction pathway, and thus the properties of the final gel network.[132] Chemical characteristics, including polarity and molecular affinity, shape the precursors' interactions and govern reaction kinetics and efficiency. In this work, the rod microgel formation is performed on-chip, thus requiring a cross-linking time that is sufficiently short to occur during the residence time on-chip. There is a variety of cross-linking strategies for rapid gelation, such as ionic cross-linking, where charged polymers like alginate form a gel with the addition of cross-linking ions (*e.g.*, calcium).[133,134] Covalent cross-linking techniques are well established, such as photo-polymerization employing UV or visible light to initiate the gelation of photo-polymers like GelMA or PEG derivatives, thiol-ene "click" reactions or inverse electron demand Diels-Alder (iEDDA) click reactions that enable rapid and efficient gelation.[28,122,133,135–137] Beyond photo-polymerization, our group also employed base-catalyzed Michael-type addition to produce the rod microgels presented in Chapter 3 based on a previous study.[116] However, although this cross-linking technique has been proven to be suitable for *in situ* cell encapsulation,[116] and to develop a kidney disease model in Chapter 3, the technique is ultimately constrained by the slow cross-linking kinetics to achieve large scale production. We, therefore, opted for light-mediated thiol-ene "click" chemistry to allow for faster cross-linking kinetics and compared it side-by-side with FRP using a newly developed microfluidic design. These two cross-linking mechanisms exhibit different characteristics that influence the microfluidic production parameters and microgel properties. FRP engages the random addition of monomers or pre-polymers *via* free radicals, often leading to broad molecular weight distributions and potential side reactions, such as uncontrolled termination, oxygen inhibition, or backbiting, among others. This gives little control over the gel architecture and uniformity. In contrast, thiol-ene "click" chemistry is part of free-radical-mediated reactions during which thiols add to carbon-carbon double bonds (enes) in a very efficient and selective manner in the presence of a radical initiator and an appropriate external

stimulus, such as light or heat.[138–140] Thiol-ene reactions are deemed "click" reactions, as they offer high yield, comprise minimal byproducts, and form more defined gel networks.[138] In terms of network formation, the FRP follows a chain growth mechanism,[141] whereas the thiol-ene "click" reaction is based on a step-growth mechanism (Figure 1.8).[140]

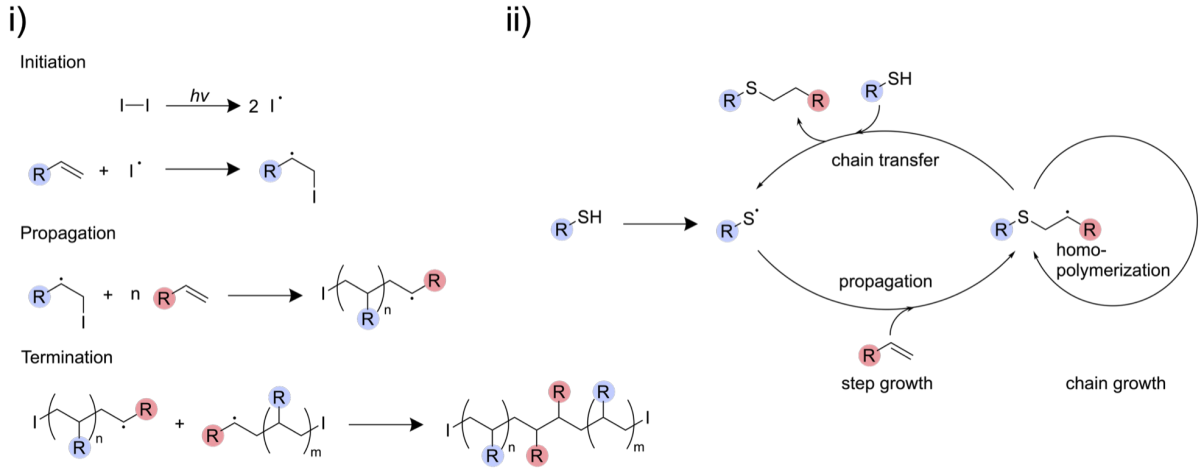

Fig. 1.8: Chain-growth (i) vs step-growth (ii) mechanism. Chain-growth polymerization takes place through sequential/random addition of the monomer/polymer to the reactive site (radical). The process involves initiation, propagation and termination reactions. Step-growth polymerization includes monomers/polymers reacting in a stepwise fashion.

Chain-growth reactions achieve high molecular weights already at the beginning of the reaction, while step-growth reactions exhibit high molecular weight increases only near the end (Figure 1.9).[142]

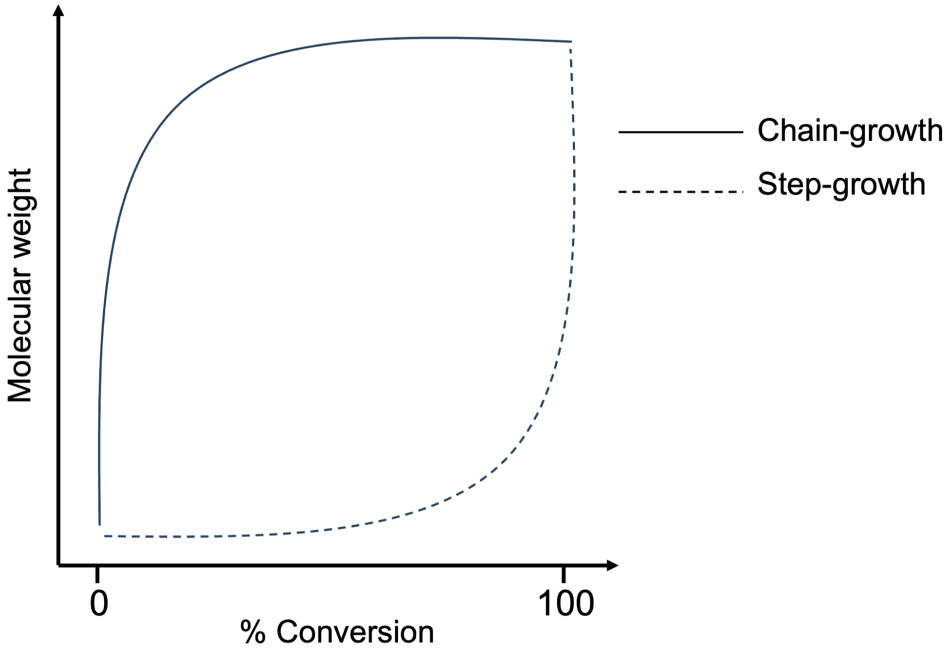

Fig. 1.9: Chain-growth vs step-growth growth kinetics adopted from.[142,143]

Furthermore, since oxygen acts as a radical scavenger in FRP to form peroxy radicals comprising less reactivity, thus diminishing chain growth, step-growth polymerizations are less affected by that. The high oxygen insensitivity originates from the facile abstractibility of the thiol hydrogen, making this reaction a good candidate for photo-polymerization in the presence of atmospheric oxygen.[138,144] As shown in Figure 1.8, the step-growth mechanism can be expanded with a subsequent chain growth through homopolymerization, enabling polymer networks that are not achievable using thiol-ene Michael-type addition. The ratio between those two mechanisms can be tuned with the used precursors and their concentrations, modifying the network structure and mechanical properties.[138] Light-mediated thiol-ene reactions occur quicker with electron-rich olefins, such as norbornenes and vinyl ethers, and slower with maleimides and conjugated dienes.[138,145] The fast reaction kinetics of norbornenes are attributed to the ring strain of the structure.[146] Therefore, thiol-ene reactions with norbornenes and vinyl ethers are considered ideal reactions, as no homopolymerization is exhibited owing to the equal kinetics of the chain transfer and propagation.[138,146]

Based on the rational above, we opted for light-mediated thiol-ene click chemistry using PEG-based polymers with thiols and norbornenes as functional groups, using 8 arm PEG-norbornene 20 kDa and 8 arm PEG-ester-SH 20 kDa as used in Chapter 3. This enabled a reduction in complexity in the microfluidic device design, as

the cross-linking could now be induced through UV light, while maintaining the degradability of the rod microgels when providing an ester moiety. Together with Mattias Mork, we evaluated the differences in FRP and radical mediated thiol-ene click chemistry using our newly designed microfluidic device. The design is based on SE to obtain large amounts of spherical droplets, which are then squeezed into rod-shaped droplets in multiple parallelized channels. In order to cross-link, a UV diode is placed on top of the channels, where the rods are formed and irradiated in a continuous manner. With the new optimized microfluidic device, we were able to reach polymer precursor rates of 3 ml/h, which has up to now, not been achieved for rod microgel production on chip. Furthermore, we observed a decreased required polymer concentration when using the light-mediated thiol-ene click chemistry (5 % (w/v)) compared to the FRP using poly (ethylene glycol) diacrylate (PEGDA) (30 % (w/w)). This is most likely because of the different architecure of sPEG polymers versus PEGDA.[121,147]

1.5 Rod microgels as structural guidance in tissue engineering

Beyond scalable production, this thesis also focused on how rod microgels produced by microfluidics can be used as structural guidance in 3D tissue engineering applications. From previous studies, we know that magneto-responsive PEG-based rod microgels can be combined with a fibrin or synthetic hydrogel to induce anisotropy and structural guidance for cell orientation and unidirectional outgrowth.[35,65,66] This dual hydrogel system, called the Anisogel (Figure 1.10), is injectable and provides directional cues that are key for tissue regeneration in contexts such as the myocardium, spinal cord, and cartilage.[11,12,148] Regarding primary neurons cultured inside an Anisogel, we observed the longest neurite extension using thin microgels (width = 2.5 µm), with unidirectional nerve growth along the long axis of the aligned microgels. Thicker microgels (*e.g.* 5 µm), on the other hand, can impede neurite extension.[67]

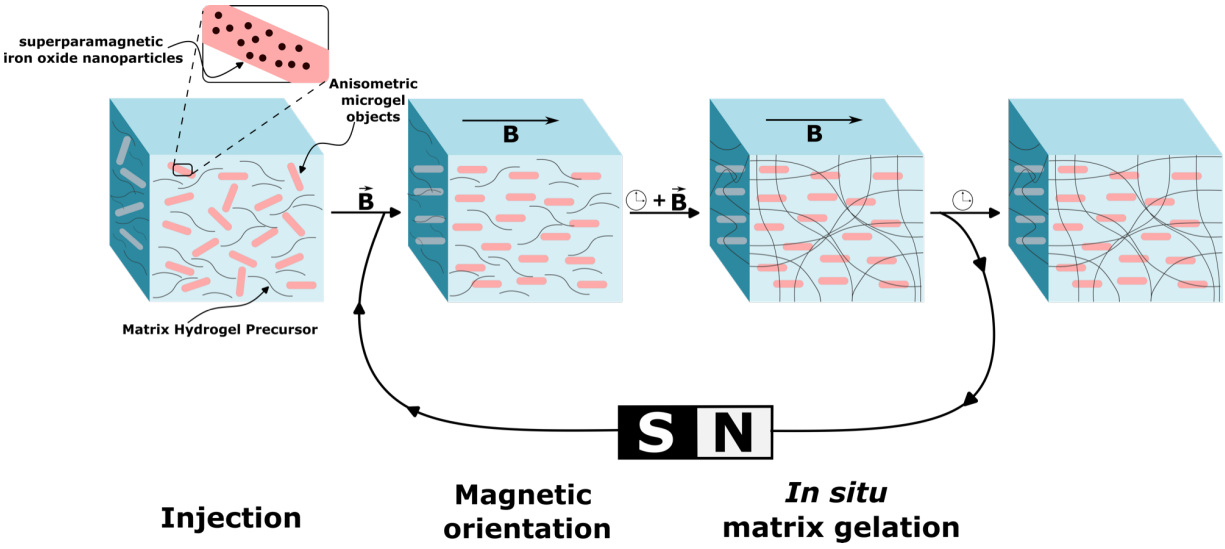

Fig. 1.10: Anisogel formation adopted from.[35,65,66] Magneto-responsive fibers or microgels are mixed with a hydrogel pre-cursor. The anisometric particles align inside an external magnetic field and are fixed in their position during *in situ* matrix gelation.

For all of these studies, the particle replication in non-wetting templates (PRINT) technique[149] was employed, where the range of microgel stiffness is limited to an E-modulus of 35–950 kPa, depending on PEGDA concentrations ranging from 10 to 80 % (w/v). Across all tested polymer concentrations and thus stiffnesses, neurite alignment still occurred, likely due to the microgels being approximately 90-fold stiffer than the surrounding hydrogel matrix in which the cells grow. However, this hypothesis can currently not be addressed, as either microgels produced by microfluidics are not reaching relevant size scales of PRINT microgels for neurite alignment, or PRINT microgels cannot be produced with lower stiffness. To overcome this size and functionality gap, a microfluidic technique developed by our group compartmentalized jet polymerization (CJP) enables the generation of rod microgels that are ten times thinner than the channel width.[122] The rod microgels are formed through spatially controlling photo-polymerization using a modulated laser on a thin PEGDA polymer jet. This method is now based on jetting-regime (Figure 1.11) in contrast to droplet formation, which is based on the dripping-regime in microfluidic devices.

Fig. 1.11: Dripping (i) vs jetting (ii) and stable jetting regime (iii) in microfluidics, adopted from.[150]

The microgel dimensions can be controlled through the process parameters (laser modulation (on-time), the laser spot size and the flow rate). Previously, this method has been used to produce high-aspect-ratio microgels with a minimum diameter of 8 µm using a channel width of 80 µm. Despite the initial success of this microfluidic setup, a few challenges remained. The dimensions of the microgel were restricted by the channel size and the material diversity with only PEGDA as a precursor, limiting the tunability of the mechanical and biochemical properties of the microgels. The generation of thinner microgels was particularly challenging because of the combination of the required smaller channel dimensions and the high viscosity of the precursors, leading to increased flow resistance. Furthermore, the reproducibility was affected by the polydimethylsiloxane (PDMS)-based microfluidic device that is known to be highly permeable to oxygen, leading to localized inhibition of FRP. Oxygen inhibition is assumed to be a key factor regarding the difficulty to reliably produce rod microgels < 10 µm in microfluidic systems.[151–153]

1.5.1 The role of oxygen inhibition during free radical polymerization microfluidic systems

FRP can be terminated through molecular oxygen that either reacts with an initiator or a growing polymer radical.[154–157] This effect is already present in bulk material, where researchers observed an inhibition of the FRP close to the molding interface. This resulted in a thin layer that exhibited less cross-linking than other parts of the hydrogel.[158] In 3D bioprinting, oxygen inhibition has been attributed with poor shape fidelity of printed hydrogel constructs, especially at the hydrogel air interface.[159] Some methods actually exploit this effect, such as in liquid interface production to allow for continuous stereolithography or stop-flow lithography where a "dead-zone" is created at the interface of the polymer solution and a thin PDMS layer to avoid clogging.[160–162] This effect becomes predominant in microfluidic systems, where the volume-to-surface ratio is small. When using PDMS microfluidic devices that have high oxygen permeability, the atmospheric oxygen diffuses through the channel walls and inhibits the FRP close to the channel walls.[151,152] Oakey *et al.* created a reaction-diffusion model, illustrating that the critical size threshold of PEGDA-based microgels is primarily governed by oxygen transport and saturation in the continuous oil phase.[152] As a solution, they proposed a nitrogen jacket around the microfluidic channel to reduce oxygen within the polymer phase and to facilitate the continuous

production of PEGDA microspheres. Another approach to reduce oxygen inhibition during microfluidics is to use cross-linking mechanisms that are less prone, such as is described in Chapter 4. In Chapter 4, we used light-mediated thiol-ene click chemistry, using norbornene and thiols, which is less affected by oxygen. However, as Chapter 4 and 5 were investigated in parallel, Chapter 5 only employs PEGDA and sPEG acrylates as precursors. Using CJP with thiol-ene click chemistry was done towards the end of my thesis.

In Chapter 5, we adapted the microfluidic design for CJP with respect to the oxygen inhibition effect. We observed that, with channel dimensions of 25 µm in width and 25 µm in height (in order to produce $1/10^{th}$ of the channel diameter in microgel width), no microgel production was possible. This was independent of the initiator concentration or the polymer concentration of PEGDA. Therefore, we further adapted the design to rectangular channel geometries (25x50 µm and 50x80 µm, width x height). We hypothesized that most of the oxygen would come from the channel walls and that a critical jet diameter was needed to produced rod microgels reliably with CJP. We then also analyzed the 3D shape of the formed jet during CJP using confocal microscopy as well as computational fluid dynamics (CFD) to get a better understanding of the system. To prove an effect of oxygen inhibition during CJP, we also designed a microfluidic design comprising a nitrogen jacket, based on a previous publication.[152] Here, we could prove that, using a 25 µm channel in width and height equipped with a nitrogen jacket the production of PEGDA based rod microgels was possible. However, the microgel diameter was limited to approx. 10 µm after purification, while we were aiming to produce even thinner microgels below 3 µm. Afterwards, we used the 50x80 µm design to produce 40 % (w/w) PEGDA-based ultra-thin rod microgels with a diameter of approx. 3 µm for magnetic alignment (Figure 1.12). This was done without a nitrogen jacket and was possible by increasing the distance between the oxygen rich layer and the polymer jet. Analyzing the rod microgels using atomic force microscopy (AFM) revealed a Young's modulus of approximately 4 kPa, which is now a factor 10 lower than the previously used PRINT microgels. Chapter 5 also provides insights into different attempts to render the rod microgels magnetic, providing a novel protocol to post-functionalize them with magnetic nanoparticles. Post-functionalization has the advantage of requiring less magnetic nanoparticles, as mostly the microgel surface will be functionalized. It has been shown that surface-magnetized solid rods are able to align in weak magnetic fields (1-10 mT), which has been supported by a mathematical model presenting the need of 69% weaker magnetic field with particles

that are functionalized on the surface, rather than throughout their entire volume.[163] To enable post-functionalization, poly (ethylene glycol) methacrylate (PEGMA) coated SPIONs were used, as these can covalently bind to the microgel network. After having magnetized the rod microgels, we analyzed the effect of their aspect ratio (AR) on the magnetic alignment. We observed that rod microgels with a higher AR show alignment at lower SPIONs concentrations, compared to smaller AR. This was in contrast with previous findings, were shorter magneto-responsive microgels rotated quicker, which may be due to the more open polymer network reducing the counteracting viscous torque.[164] The magneto-responsive CJP microgels were then used as proof-of-concept to analyze whether their stiffness remained high enough to guide and align cells in a 3D hydrogel matrix.

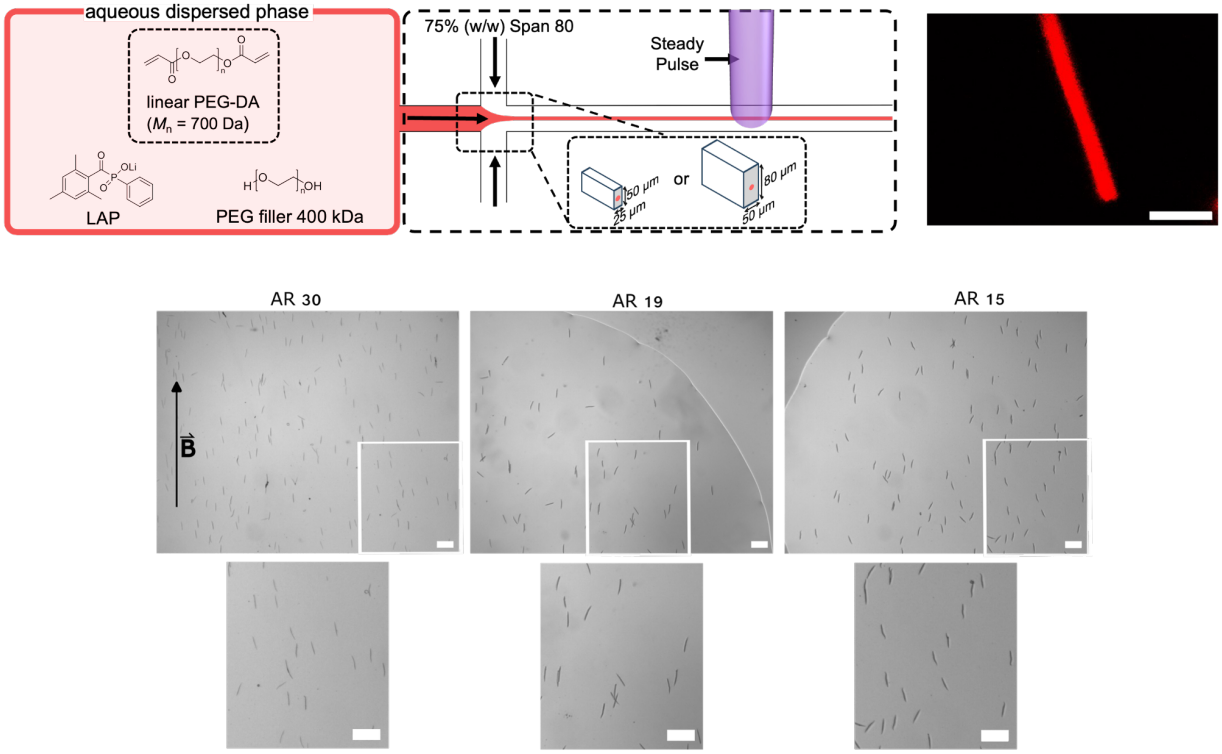

Fig. 1.12: Refined CJP microfluidic design with a rectangular geometry in different sizes to reliably produce ultra-thin PEGDA rod microgels. Scale bar is 10 µm (top). The rods were magnetized post-production and their alignment properties were analyzed with respect to their AR keeping the SPIONs concentration constant. Scale bars are 200 µm (bottom).

Besides ultra-thin rod microgels, we also investigated the limitations of the polymer concentration to still obtain stable rod microgels using multi-arm star PEG acrylates. We made use of the short irradiation times in CJP and the oxygen-inhibited FRP to form ultra-soft and ultra-porous rod microgels and were able to decrease the

polymer concentration to 3 % (w/v), leading to microgels with pore sizes in the range of 3-5 µm. These microgels were then used to functionalize with cell-adhesive peptides and applied in cell-induced microgel assembly into 3D cellular constructs. Such microgels hold great potential in tissue engineering applications to support diffusion of nutrients and oxygen via the microgel network.[28] In Chapter 5, various characterization techniques are used to demonstrate how different precursor molecules alter the microgels' structural and mechanical properties to create a larger variety of building blocks for tissue engineering applications.

1.5.2 Effect of molecular building blocks on microgel properties

Beyond the structural properties of the rod microgels, the mechanical properties further determine the microgel's functionality, as it influences the physical support provided to cells and the biological outcomes of engineered tissues. Microgels can be altered regarding their stiffness, porosity, and cross-linking density. Rod microgels produced through droplet microfluidics as used in Chapter 3 and 4 show Young's moduli from 4.5 to 20 kPa for PEG concentrations ranging from 5 to 15 % (w/v) when using Michael-type addition or thiol-ene click chemistry. Now employing CJP and using PEGDA as a precursor, the stiffness was at approx. 2 kPa.

Our co-worker Kittel *et al.* analysed how different molecular building blocks affect the internal structure of PEG-based rod microgels prepared through droplet microfluidics versus bulk hydrogels using FRP.[121] By systematically varying the architecture, mass and concentration of sPEG and PEGDA, it is possible to control the mesh size and cross-linking density, which in return affect the mechanical stiffness and the ability for molecules to diffuse through the microgel network. Throughout this study, 8 arm sPEG-acrylates were used varying the molecular weight (10 kDa and 20 kDa), in combination with PEGDA 700 Da using UV FRP in a plug flow microfluidic device to produce rod microgels. Analyzing the properties of bulk hydrogels prepared with 8 arm sPEGacrylates suggested an effect of the lower coil density of 20 kDa sPEG acrylate versus 10 kDa sPEG acrylate. The 20 kDa may offer a higher accessibility of the reactive groups for cross-linking, leading to the highest storage modulus observed. The lower diffusion rate in bulk hydrogels made with 10 kDA sPEG acrylates may be caused by the higher coil density of the precursor molecules during cross-linking. Furthermore, the addition of PEGDA to the hydrogels decreased their stiffness for both molecular weights of the sPEG acrylates,

as the amount of sPEG was decreased that would contribute to a greater network formation.

These findings follow the theory for brushes introduced by Daoud and Cotton (DC), which further developed findings by Alexander and de Gennes about neutral star-shaped polymers in good solvents.[165–167] Daoud and Cotton found that in contrast to linear polymers comprising a homogeneous density profile, star polymers exhibit an inhomogeneous structure, where the highest density can be found at the core and decreases with distance from the center. Furthermore, stars with a low molecular weight or a low number of arms comprise independently behaving neighboring chains and display more a mushroom-like conformation, while for high molecular weight or more arms, the chains begin to interact and stretch away from the center because of crowding.[168] This can then be illustrated as a brush-like conformation with greater spatial extension.[168,169] These theories supported the highest storage modulus obtained with the 8 arm sPEG acrylate with 20 kDa.

Following these results, we expected a better network formation employing sPEG acrylates rather than PEGDA, especially in the presence of atmospheric oxygen. We also hypothesized a decrease in minimum polymer concentration required to produce stable rod microgels using CJP with sPEG. To compare different architectures and to understand how the number of arms and chain length affect the microgel structure and stiffness, we did not only focus on 8 arm sPEG, but also included 4 arm sPEG acrylates with molecular weights of 10 and 20 kDa. We first analyzed the bulk properties through rotational rheology prior to conducting microfluidics. In line with previous findings, the softest hydrogel was achieved with PEGDA, while the stiffest using 8 arm sPEG acrylate 20 kDa.[121] Interestingly, 20 kDa 4 arm sPEG acrylate resulted in a lower storage modulus than its 10 kDa equivalent, which is in contradiction with the theories described above, where 20 kDa polymers would lead to better cross-linking, compared to 10 kDa, as the chains are able to reach each other better and experience less steric hindrance from neighboring chains. Here, molecular diffusion might have a greater impact for 4 arm sPEG acrylates, where smaller polymers diffuse faster, increasing cross-linking. Furthermore, depending on the molecular weight the star shaped 4 arm polymers might exhibit different conformations. As the number of arms is lower, the 'brush' effect described above may be less prominent.

With the aim to reduce the amount of synthetic material used, we tested whether we

can yield stable microgel production at polymer concentration below 20 % (w/w) using sPEG acrylates, as this was not possible with PEGDA (Figure 1.13). For all sPEG acrylate variants (as well as PEGDA for comparision), a PEG filler (400 kDa) and 1 % (w/w) photoinitiator were added to the polymer phase, as was done in an 80 x 100 µm microfluidic chip. Smaller geometries were not possible with this precursor composition, due to the high viscosity. The lowest polymer concentration using CJP was achieved with 8 arm sPEG acrylate 20 kDa, as low as 3 % (w/w), in agreement with the previous rheological data, where 20 kDa 8 arm sPEG acrylate showed the highest storage modulus. Furthermore, 5 % (w/w) for 10 kDa 8 arm, 8 % (w/w) for 4 arm (10 or 20 kDa) were required to result in stable microgels after purification. The mechanical properties were characterized through AFM, where the 4 arm sPEG acrylates presented the lowest Young's moduli of 1.1 $\pm$ 1.6 kPa and 0.3 $\pm$ 0.1 kPa for the 10 and 20 kDa molecular weights, respectively. To our knowledge, this is the first time such soft rod microgels were produced using microfluidics. For comparison, rod microgels prepared with 20 % (w/w) linear PEGDA showed a Young's modulus of 2.5 $\pm$ 1.2 kPa. Additionally, we investigated the pore size of the soft microgels using confocal microscopy and image analysis. The microgels with the lowest Young's modulus, made with 8 % (w/w) of 4 arm 20 kDa sPEG acrylate, featured the largest pores, ranging from 1 to 5 µm in diameter, representing 94 % of the area occupied by pores. The stiffest microgels produced with 8 arm sPEG acrylate 20 kDa presented pores with sizes from 1-3 µm. All of the rod microgels produced with sPEG had diameters greater than 50 µm, due to a minimal required jet diameter of 30 µm. The ultra-thin microgels could only be produced with PEGDA. Beyond AFM and confocal microscopy, the rod microgels were also assessed through Brillouin microscopy, optical diffraction tomography (ODT) and small angle x-ray scattering (SAXS). To get a better understanding of the influence of the precursor molecules on the mechanical and structural properties, we set the polymer concentrations for all sPEG variants to 10 % (w/w) and kept PEGDA at 20 % (w/w), as below no microgel production was possible. SAXS measurements demonstrated local domains of ordered structures for microgels made with 20 kDa 4 arm sPEG acrylates, indicating accumulation and stacking of unreacted polymer arms, which correlated to the low Young's modulus for these samples. Furthermore, were observed more heterogeneous mechanical properties using Brillouin microscopy that are probably caused by the highly porous network. Such soft and porous rod microgels are suitable for tissue engineering applications and we later used the rod microgels to attach a cell adhesive peptide and to determine whether fibroblasts can assemble them into 3D microporous annealed particle (MAP) scaffolds through cell-assembly, as described in a previous

publication from our group using spherical microgels.[170]

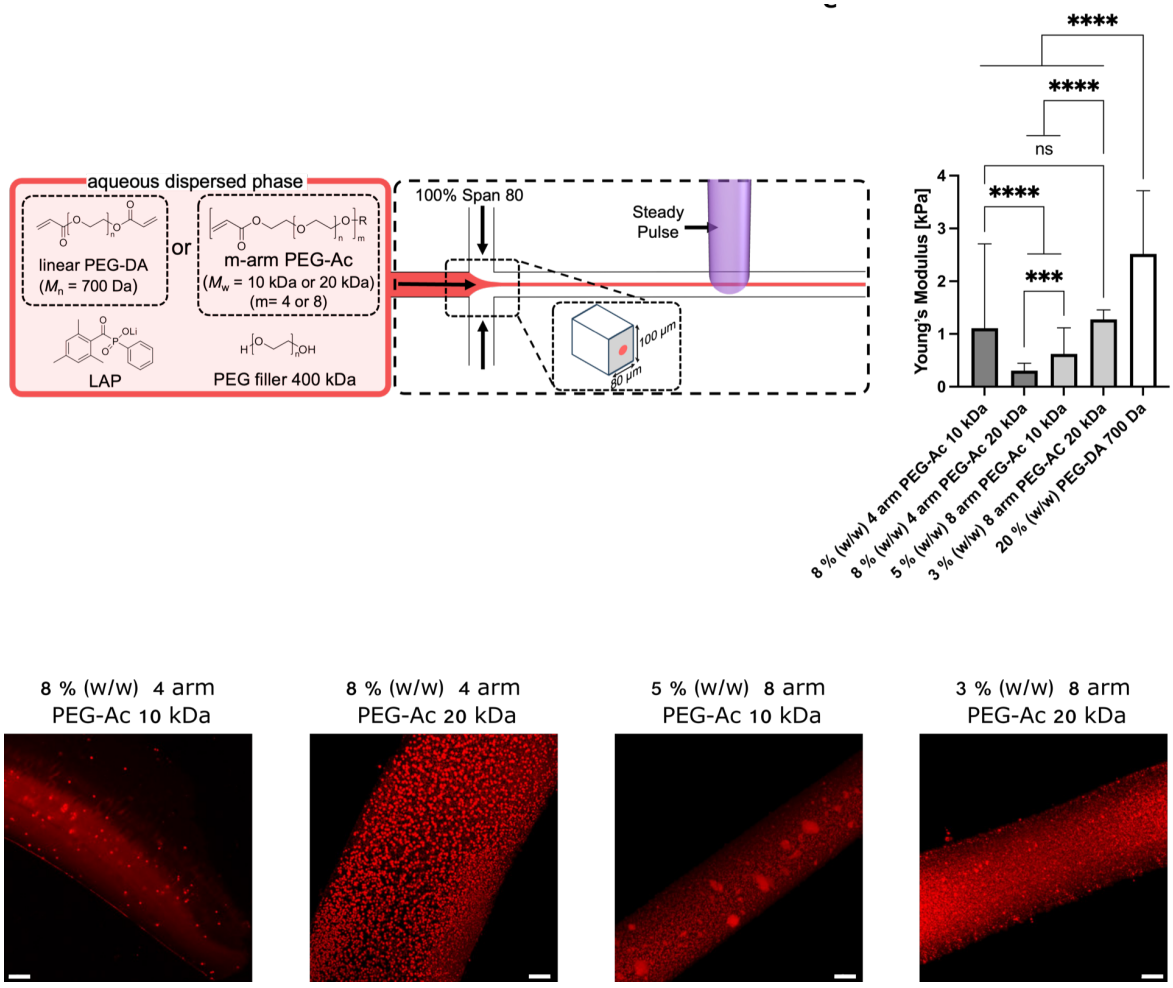

Fig. 1.13: Effect of molecular building blocks on microgel properties using CJP. Microgels are produced in a channel with 80 µm in width using sPEG acrylates and PEGDA for comparison. Young's moduli were determined through AFM and were as low as 0.3 kPa. Pore sizes in a range of 1-5 µm were achieved depending on the sPEG variant and polymer concentration. The porosity was analyzed using confocal microscopy. Scale bars are 15 µm.

1.6 Moving towards dynamic covalent chemistries for alternative hydrogel systems

Having established control over structure and alignment of the microgels, the next challenge lies in tuning the dynamic behavior of the surrounding matrix, a feature largely absent in traditional covalently cross-linked hydrogels.

The PEG system currently used in the Anisogel as surrounding matrix to fixate the aligned microgels is called the PEGKQ hydrogel.[35,66] However, this results in a very elastic hydrogel, while it is well known that the ECM is of an adaptable and responsive nature and cannot be closely resembled by covalent and static hydrogel networks. Furthermore, the PEGKQ hydrogel can be injected and formed *in situ*, however first unpublished *in vivo* studies show the difficulty in forming the hydrogel at the injury site due to body fluids. No high concentrations of aligned microgels were observed *in vivo*. Another challenge is the storage of the enzyme FXIIIa, which needs to be stored at -80 $°C$, and the rapid loss of activity of the enzyme at room temperature. These difficulties support the need of an alternative to the currently used surrounding hydrogel for the Anisogel system.

Recently, dynamic covalent chemistries (DCC) are increasingly applied to design 3D hydrogels[171] as they can reversibly form and break bonds, allowing for tunable mechanics, self-healing, and cell-responsive remodeling (Figure 1.14).

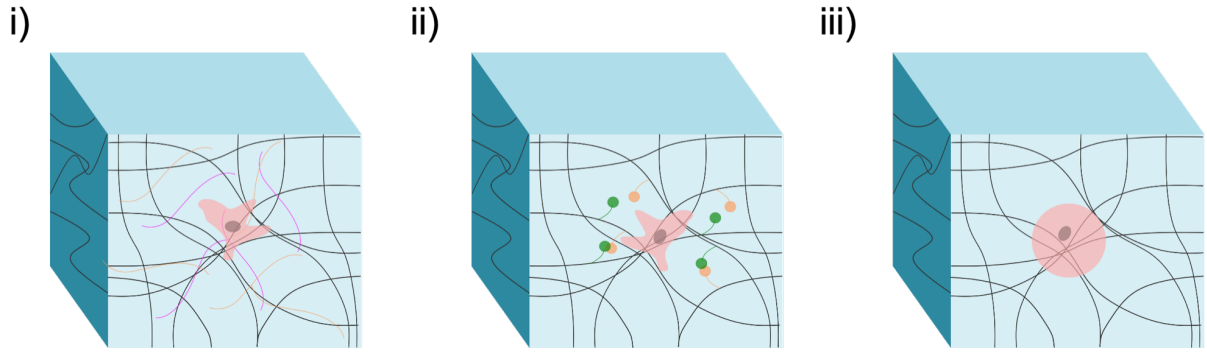

Fig. 1.14: DCC enable tunable viscoelasticity. Similar to the ECM (i), in DCC-based hydrogels (ii) cells can spread and remodel, while covalent chemistries (iii) restrict such cell behavior. Adopted from.[172]

One key feature of dynamic covalent bonds is that they offer tissue-like stress relaxation that influences cell spreading, migration, and differentiation.[171,173,174] Furthermore, they can recover after deformation making them suitable candidates for bioprinting and delivery by injection.[175–178] There are different types of dynamic covalent chemistries, such as boronic ester, Schiff base bonds, disuldife and thiosulfinate bonds, among others (Table 1.1).

Tab. 1.1: Dynamic Covalent Hydrogels: Stimuli, Storage Modulus, Applications, and References (Ref.).

DCC Type	Chemical Basis	Key Features for Tissue Engineering	Example	Ref.
Hydrazone	Hydrazine + Aldehyde/Ketone	reversible, tunable gelation time, dynamic remodeling, biocompatible	3D cell culture + organoids	[171,179]
Schiff Base (Imine)	Amine + Aldehyde/Ketone	reversible, mild conditions, self-healing, adjustable stiffness	injectable hydrogels	[171,180]
Boronate Ester	Diol + Boronic Acid	pH-responsive, reversible	cell delivery	[176]
Disulfide	Thiol + Thiol (Oxidation)	redox-responsive, reversible	injectable hydrogels	[181]
Diels-Alder	Diene + Dienophile	Thermoreversible	3D cell culture	[182]
Enzyme mediated	Enzyme-catalyzed reactions	biocompatible, rapid gelation	Bone/cartilage tissue engineering	[183]

Depending on the type of bonds, their relaxation time will have different length scales and can therefore be used to mimic different native tissues. Boronic acid derivatives, for example, exhibit control over orders of magnitude and are thus used to mimic various tissue types.[184] Schiff base bonds, such as imine, hydrazone, and oxime bonds, can comprise relaxation times from seconds to months, which would resemble *e.g.* the brain or cartilage.[173,185,186,186] These bonds have been extensively studied using natural polymers such as hyaluronic acid (HA), but also PEG-based polymers. The advantage of using Schiff Base PEG-based hydrogels is their strong self-healing capacity, making them ideal for injectable hydrogels or 3D bioprinting, as well as their mechanical properties that can be superior to other dynamic hydrogels.[187] Their

hydrogel degradability can be slow and controlled making them good candidates for long-term scaffolds to support tissue regeneration.[188] Other DCC exhibit faster degradation rates, due to high pH sensitivity or the presence of glucose.[189]

When looking for alternative hydrogels to our current PEGKQ hydrogel, Schiff base hydrogels are good candidates due to their relaxation time, injectability, mechanical stability, and tunability. In Chapter 6, I focused on the development of a Schiff base PEG-based hydrogel system, combining hydrazone and imine chemistries, to find a new suitable replacement for the Anisogel surrounding hydrogel matrix. This work was based on the following publication and was conducted during my six month Fulbright research stay in the group of Professor Heather Maynard at the University of California, Los Angeles (UCLA) in the United States.[180] In the first publication, Boehnke *et al.* employed 8 arm sPEG with three different functional groups: hydrazide, aldehyde, and aminooxy, to build hydrazone and oxime cross-links. The combination of both cross-linking types allowed for a greater control over the degradation properties. Hydrazone cross-links are known to be more reversible than aminooxy cross-links. They showed the biocompatibility of the obtained hydrogels through the addition of a cell adhesive peptide and successfully cultured mesenchymal stem cells (MSCs) inside them. Yet, they did not characterize the hydrogels beyond their storage moduli, nor did they perform any other cell experiments.

We first synthesized the precursors and optimized the protocol to be suitable for 8 arm sPEG 20 kDa as well as 4 arm sPEG 10 kDa. That way we could tune the network architecture keeping the chain length constant. After purifying and confirming the structure using ^{1}H nuclear magnetic resonance (NMR), we performed initial rheological tests to analyze the stiffness and gelation time of the hydrogels. Furthermore, we looked at their self-healing properties and their injectability. The cross-linking kinetics are best at a pH = 5.5, which was also reflected by rheological analysis. An acid pH might not be the right environment for certain cell types, even though the addition of MSCs showed sufficient cell viability. Performing this reaction at physiological pH at 7.4 drastically increased the gelation time from minutes to multiple hours. Considering using this hydrogel with the Anisogel system, such long gelation times are not feasible, as for example *in vitro*, all rod microgels present in the matrix would sediment to the bottom of the hydrogel. To solve this issue, there are several measures that can be taken. One would be to adapt the functional groups, such as analyzing the difference of aliphatic or aromatic derivatives with

respect to the reaction rate.[190] However, as this would mean to synthesize new compounds, we decided to look for ways to catalyze the reaction. Based on literature, a biocompatible benzimidazole-based catalyst has been shown to catalyze HA-based hydrazone chemistries, and to increase the reaction rate by 30-fold.[191] Additionally, using a catalyst can offer the possibility to temporally tune the dynamic exchange of the bonds, which in return affects the mechanical properties of the hydrogel.[191] Furthermore, we looked for amino acids that resemble the structure of aniline, a well known catalyst for this type of reaction, though aniline cannot be used in this context due to its cytotoxicity.[192] We opted for 3-aminotyrosine, an unnatural amino acid, that could comprise biocompatibility. we then performed a small molecule screening using both catalysts employing the analytical High Performance Liquid Chromatography (HPLC) at different pH (5.5 and 7.4). As a standard, we used aniline in the same concentration to compare the reaction rate. A significant increase in reaction rate (50-fold) could be observed using both proposed catalysts at physiological pH. Afterwards, we tested the catalysts to make hydrogels at different polymer concentrations and in different combinations of the functional groups.

1.7 Summary and motivation

The goal of my thesis is to develop synthetic multiphasic anisotropic hydrogels with control over spatial organization and the microenvironment in 3D for tissue engineering applications. In **Chapter 1**, the thesis is motivated, and ways are explored to induce compartmentalization, anisotropy, and macroporosity in 3D hydrogel networks. **Chapter 2** gives an overview over different microgel production techniques, as well as characterization techniques on different length scales.

In **Chapter 3**, a synthetic compartmentalized *in vitro* kidney disease model was developed, highlighting the potential and challenges. Here, base-catalyzed Michael-type cross-linked and degradable rod microgels, produced through plug flow microfluidics, were employed as sacrificial templates to mimic kidney PT. These building blocks were characterized and then used in 3D cell culture. We show proof-of-concept of the kidney disease model through the addition of TGFβ and analyze the Collagen 1 expression using qPCR and protein expression.

In **Chapter 4**, a new microfluidic design is introduced to produce degradable rod

microgels in a high-throughput manner. We tested an alternative chemistry using light-mediated thiol-ene click chemistry to reduce the design complexity and compare it to FRP. Establishing the combination of the microfluidic design and used chemistry enables the reduction of synthetic material used and increases the production rate significantly.

In **Chapter 5**, a technique called CJP was further refined to produce ultra-thin rod microgels that can be rendered magnetic through post-functionalization with SPIONs. Such thin microgels cannot be produced through conventional droplet based microfluidics and is based on the jetting regime. We further explored this technique by analyzing the effect of molecular building blocks on the microgel properties using sPEG-acrylates in a comparative study with PEGDA

In **Chapter 6**, the focus was then switched from microscopic building blocks to the surrounding hydrogel matrix. Here, the need for alternative cross-linking chemistries was addressed that closer resemble the native ECM. Currently, the hydrogel matrix used in this thesis is based on covalent cross-links, lacking the ability to be remodeled by the cells.

2 State of the art

2.1 Introduction

Hydrogel-based materials are key for tissue engineering applications as they mimic the central properties of the ECM providing high tunability.[17] Yet, conventional isotropic bulk hydrogels or spherical microgels lack the spatial control and dynamic properties to direct complex cell behaviors.[63] This chapter highlights different research advances that enable materials with programmable mechanical and spatial properties. The first focus is on rod microgels, how they can be produced and characterized. Furthermore, 3D tissue-mimetics as well as advances using rod microgels will be addressed, emphasizing key challenges in tissue engineering. Finally, non-covalent hydrogels for 3D cell culture are discussed, offering superior characteristics to covalent cross-links, as they closer resemble the dynamic nature of the native ECM.

2.2 Rod microgels

Spherical microgels, that are isotropic in shape, have been extensively used because of their uniformity and their various fabrication techniques.[62] Compared to that, anisometric microgels have shown direction-dependent features that can enhance their functionality for various tissue engineering applications.[4,63]

2.2.1 Production techniques for rod microgel formation

Rod microgels can be fabricated using various techniques, each offering different control over particle size, production rate, and mechanical attributes.[63,122] A batch process based on soft lithography called PRINT can be used to produce monodisperse rod microgels with precise control over particle size, composition, and functionality.[149] In this method, a mold containing predefined cavities is filled with a precursor solution. The mold can be made of perfluoropolyether (PFPE) or PDMS, and the precursor can be cross-linked through FRP or step-growth polymerization, resulting in microgels that replicate the cavity's dimensions and shape.[193] PRINT also allows for the creation of multi-compartments structures by sequentially polymerizing distinct precursor layers.[194] Yet, the multi-compartmentalization poses challenges such as incomplete polymerization or solvent evaporation, which can be mitigated using non-volatile and non-reactive polymer fillers.[35,195] While this technique is highly applicable for rod microgel production with diameters as small as 1 µm, it remains limited in terms of mechanical properties and scalability. Continuous production can instead be achieved using microfluidic techniques.[193,196] These approaches generally employ PDMS-based devices fabricated by soft lithography that are fixed onto a glass slide. Within these devices, droplets are formed in flow-focusing or T-junction channel geometries, and can be operated either in the dripping or jetting regime as the dispersed and continuous phase meet on chip. To ensure rapid gelation on-chip, cross-linking can either be induced through step-growth polymerization or FRP. Both polymerization techniques are basis to this thesis. Guerzoni *et al.* developed a microfluidic technique to produce rod microgels using sPEG-precursors that are cross-linked via Michael-type addition.[116] Degradation moieties were introduced through an enzymatically degradable cross-linker. Biocompatible soft rod microgels were generated and used to encapsulate cardiomyocytes from human iPSCs and primary dermal fibroblasts. Furthermore, this technique enabled different AR that could be adjusted through manipulation of the flow rates during the production process. This microfluidic design and polymeric material is the basis to Chapter 3 in this thesis. With plug-flow microfluidics the microgel diameter is typically limited by the channel diameter.[122] For this reason a more advanced method has been developed by our group known as CJP. Here, the microfluidic device is operated in the jetting regime enabling the production of rod microgels with diameter with $1/10$ of the channel cross-section. A polymeric jet is cross-linked through FRP using a modulated laser, that initiates the reaction during the laser ON-time. When the

laser is turned off, uncross-linked polymer material is washed away. This technique offers control over the microgel diameter, length and mechanical characteristics, by tuning the flow velocity and laser ON-time. CJP is the basis to Chapter 5 where the technique was further refined to produce ultra-thin rod microgels and employed different sPEG acrylate variants to increase functionality. Another technique to produce rod microgels is stop-flow lithography (SFL) that combines microfluidics with photolithography making it a continuous high-throughput production of microgels comprising different sizes and complex shapes.[161,162] A solution containing photo-cross-linkable precursors is introduced into a microfluidic channel, where it is exposed to patterned UV light through a mask. To create microgels, the fluid flow is paused, while a designated section of the channel is illuminated. After cross-linking has occured, the flow is restarted to transport the newly formed microgels out of the illuminated region. Coordinating the timing of flow interruption, UV exposure time and intensity, and channel clearing enables the efficient fabrication of 2D microgels in customizable shapes.

Although microfluidic systems offer a continuous production platform, most setups designed to generate rod microgels with features and dimensions suitable for tissue engineering or biomedical applications present low throughput, typically operating at polymer precursor flow rates below 0.2 mL/h.[28,116,121,122] This limitation is due in part to the nature of droplet formation, where maintaining an elongated shape requires a minimum residence time on the chip during crosslinking. Additionally, pressure within the microfluidic channels must be carefully controlled to avoid large fluctuations or leakage.

In contrast, the upscaling of spherical microparticle production has been widely studied, achieving significantly higher throughput, from several milliliters per hour to even liters per hour, depending on the fabrication method and materials used.[123–127] Microfluidic scaling strategies commonly involve parallelizing multiple channels. Beyond parallelized FF designs, SE has emerged as a highly effective microfluidic technique for producing large quantities of spherical droplets and particles.[125,126,128–131]

SE relies on a distinct device design consisting of multiple shallow nozzle channels feeding into a deeper reservoir channel. As the dispersed phase transitions from the narrow to the deep region, the abrupt increase in channel height drives droplet formation. Unlike FF systems, SE is less sensitive to flow rate variations, offering a

more robust performance. SE has primarily been used to produce spherical droplets and particles, but can also generate complex structures, such as double emulsions, through droplet reinjection into secondary SE devices.[130] While SE is inherently restricted to forming spherical droplets, it serves as a scalable, adjustable platform that could potentially be coupled with post-processing methods to alter droplet shapes, which is the basis to Chapter 4 of this thesis.

Despite advancements in microfluidic parallelization, progress in scaling up the production of non-spherical, anisometric microgels—like rods—remains limited. A recent study demonstrated a parallelized approach to producing rod-shaped microgels using a silicon-based microfluidic device with multiple flow-focusing droplet generators.[197] Although this method confirmed the feasibility of forming rod-shaped microgels via UV-induced polymerization of PEGDA in parallel channels, the maximum total stable flow rate remained below 800 µL/h. Moreover, silicon-based devices are generally more costly and require specialized fabrication equipment compared to commonly used PDMS systems. Depending on the production method and the used material, microgels will exhibit different mechanical and chemical traits that influence their functionality in tissue engineering applications.

2.2.2 Characterization of microgels

There are multiple characterization techniques probing different length scales and readouts. Commonly, the physical dimensions in terms of length, width and AR of rod microgels are first assessed.[28] This can be analyzed through optical microscopy and involves sizes ranging from 1 µm to several hundred micrometers. It is particularly valuable for microgels produced through microfluidics, offering high-throughput analysis and real-time monitoring. However, its resolution is limited and can only be used in 2D. For characterization in 3D confocal scanning laser microscopy (CSLM) is suitable as it provides high resolution by using a pinhole, and can scan through z-stacks in fluorescently labeled microgels reconstructing the full 3D morphology. This method is particularly interesting when visualizing internal structure, and was used for the analysis of the pore sizes in Chapter 5. It can resolve sizes from 0.5 µm to about 100 µm and provides high resolution data in 3D. For more quantitative, label-free 3D mapping, ODT has become a powerful tool. ODT can recreate the 3D refractive index distribution of transparent samples by recording how light waves are diffracted as they pass through the sample. The refractive index correlates with

material density and composition, allowing ODT to give insights into mechanical and chemical properties. When determining mechanical properties at a subcellular or microscale level, Brillouin microscopy presents a novel, contact-free method. It assesses the Brillouin frequency shift that is linked to the longitudinal modulus and provides the viscoelastic properties in hydrated microgels at submicron resolution. Brillouin microscopy can be complementary to rheological or AFM techniques. Beyond optical methods, the rod microgels can also be characterized using AFM. AFM is based on a mapping surfaces using a sharp tip attached to a cantilever, that deflects *e.g.* upon surface changes. AFM can provide high resolution topography (1-10 nm horizontally, subnanometer vertically) and mechanical measurements such as the Young's modulus using force-indentation curves. In Chapter 5 AFM was used to determine the Young's modulus of the rod microgels, as well as colloidal probe nanoindentation, which is the most established technique to analyze the mechanical properties of microgels, following the same theory as AFM. Looking at the topology scanning electron microscopy (SEM) can also be a useful tool to display structures from 10 nm to up to several 100 µm, which was used in Chapter 4. When using SEM on water-swollen and soft networks, such as microgels, the sample preparation is crucial, as the structure needs to be preserved after freeze-drying. To go to even smaller length scales, SAXS is often used to determine size, shape and the internal structure of features in the range of 1-100 nm. This gives insights into the particle shape, the form factor, or core-shell structures. In this thesis I used this method, to analyze the polymer structure within a cross-linked microgel in Chapter 5. To determine diffusion properties NMR is often used.

2.3 Advances in 3D anisotropic tissue mimetics using rod microgels

Advances in 3D anisotropic tissue mimetics using rod microgels have enabled the creation of biomaterials that better resemble the structural and functional complexity of the native tissues. They can be used to guide cells[35,65,66] in 3D or pre-programmed for MAP assembly, enhancing cell infiltration and promoting vascular networks or in granular hydrogels.[28,69] MAP scaffolds using rod microgels produced through droplet-based microfluidics were reported by Qazi *et al.* using norbornene-modified HA.[69] Here, the material exhibited shear-thinning and self-healing properties

enabling injectability followed by scaffold formation.[69] Rod microgels can be employed to encapsulate cells promoting tissue-specific organization.[116,198] Cardiomyocytes from human induced pluripotent stem cells (hiPSCs) as well as fibroblasts were encapsulated and presented first results on mini heart tissues for cardiac tissue regeneration methods.[198] Recently, magnetically-assisted 3D bioprinting has been further developed implementing magnetically-responsive microfibers.[199] This method offers control over the distribution of the added magnetic materials that would otherwise impede printing fidelity. Low viscosity bioinks are used in a way that they are uncross-linked temporally after printing giving sufficient time to facilitate alignment of magneto-responsive fibers without impacting printing resolution. Similarly to the Anisogel, the microfibers allow for low inorganic contents and weak external magnetic fields. This approach presents the fabrication of anisotropic 3D bioprinting exhibiting high resolution and remote control over external stimuli.

Another method addressing cellular organization is called FLight that can either be used to generate anisotropic microgels or to induce anisotropic structures in 3D hydrogels.[36,200] FLight is based on OMI where a coherent light beam is directed through a nonlinear medium separating it into microfilaments. Applicable to a wide range of photoresins, FLight produces centimeter-scale hydrogel constructs with high cell viability in a few seconds (<10 s per construct). Furthermore, different directionalities can be achieved, enabling complex tissue engineering constructs.

In addition to magnetic and optical alignment, shear-induced alignment during extrusion-based bioprinting can orient rod microgels along the printing direction, providing directionally reinforced constructs without needing external fields. For example, aligning collagen fibrils in corneal stroma analogs has demonstrated enhanced structural and cellular organization.[201]

2.4 Advances in non-covalent hydrogel crosslinking strategies

In tissue engineering, the choice of hydrogel cross-linking mechanism alters the material's (bio)chemical and mechanical properties, thus the cellular interactions. While covalent cross-linking typically exhibits stable and robust networks, they

are generally static and irreversible, restricting the dynamic exchange a key feature for mimicking the native ECM. In contrast, non-covalent and dynamic covalent crosslinking strategies present reversible, adaptable, and stimuli-responsive interactions, enabling network remodeling, self-healing, and stress relaxation.[179,202] These features offer cellular remodeling closer to the native tissue supporting proliferation migration, and differentiation. Thus, non-covalent chemistries have gained increasing importance for engineering hydrogels that better resemble the complexity and dynamic nature of the native ECM. Dynamic crosslinking can occur through chemical (*e.g.* imine (Schiff base), hydrazone, oxime) or physical crosslinking that include ionic bonding, host-guest interactions, and hydrogen bonding. Depending on the cross-linking strategy the bond stability can be adjusted, ranging from most labile but highly reversible to more durable but less adaptive. This in return will impact the tissue engineering application. Physical interactions, *e.g.* hydrogen bonding or host-guest interactions offer the least stable bonds, while being highly reversible.[203] These bonds can form and break easily, exhibiting self-healing injectability, and shear-thinning, *e.g.* for bioprinting. Host-guest interactions are often based on cyclodextrins and adamantane or PEG resulting in networks comprising cytocompatibility and adaptibility. In tissue engineering such hydrogels have been used for fast-dissociating cross-links that support rapid cell growth and mechanosensing.[174] In a different study supramolecular hydrogels have been developed to spatiotemporally engineer the mechanics in 3D.[204] Here, the hydrogel is based on a squaramide monomer co-assembled with a 1,2-dithiolane (DT)-based monomer that can form disulfide bonds without the addition of an initiator. The light-instructed hydrogels exhibit storage moduli ranging from 200 Pa to 10 kPa, enabling an *in vitro* mimetic of disease progression. Furthermore, stimulus-responsive, gelatin-based supramolecular nanofibers have been developed that can be employed to modulate the microenvironment for cells.[205] The fibers' Young's moduli can be tuned reversibly under physiological conditions using soluble guest molecules in the surrounding media. Furthermore, injectable hydrogels have been developed using ureido-pyrimidinone (UPy) supramolecular interactions, composed of a PEG backbone equipped with two UPy units that are able to establish transient supramolecular networks through four fold hydrogen-bonding. Different chemical and mechanical characteristics can be obtained through alteration of the PEG architecture.[206–209] Another class of physically cross-linked hydrogels employs β-sheet forming self-assembling peptide hydrogels (SAPHs).[210,211] Here, the hydrogel matrix presents beneficial characteristics of natural and synthetic materials. Because of their adaptability and control over composition, degradaion, as well

as ECM-like configuration these hydrogel matrices have been widely applied in tissue engineering applications.[212–214] Maturing hiPSCs-derived kidney organoids in such hydrogels have been proven to result in complex structures as can also be found in animal derived Matrigel, making this approach a suitable alternative.[212–215] Often, their mechanical strength of supramolecular hydrogels is weak and may need reinforcement or a combination with more stable cross-links. Dual or double network strategies introduce a static covalent network with a physical network, rendering the hydrogel more stable while maintaining adaptibility.[216] Cross-links offering higher permanence are dynamic covalent bonds, that comprise breaking and forming of bonds under physiological conditions. DCC can be categorized in four different groups with respect to the chemical mechanism, reversible exchange reactions, reversible addition/ condensation reaction, coordinate interactions and enzymatic/mechanical covalent reactions.[172] The advantage of using DCC networks for hydrogel strategies, is, that while keeping the mechanical stability, the microscopic dynamics are accelerated creating a more "liquid-like" material.[172] The native tissue exhibits both solid and liquid properties and is typically not composed of elastic materials, but show viscoelastic behavior.[2,217,218] This time-dependent mechanical response is crucial for the native tissue's function, such as skin shear needs rapid regeneration after deformation or bone having the ability to dissipate energy when impacted through an injury.[219,220] To offer the appropriate microenvironment, for different tissue, different tissue relaxations need to be considered when designing DCC based hydrogels. This can be controlled through external stimuli, crosslinking density or dual network design.[172] With an increasing kinetic constant the bonds become more dynamic, thus the fluidity becomes more pronounced and the network relaxation is enhanced. Employing external stimuli can offer control over the relaxation time. The addition of an organic catalyst to a viscoelastic hydrogel has been reported to modulate the crosslinking density and exchange kinetics independently.[221]

Different dynamic covalent bonds can be exploited to control hydrogel mechanics and responsiveness in distinct ways, including boronate esters, hydrazones, oximes, and disulfides.[222] Each exhibit distinctive stabilities, exchange kinetics, and stimuli-responsiveness. These chemistries not only determine the rate of stress relaxation and self-healing but also influence how cells interact with and remodel the hydrogel matrix. For example, boronate ester bonds provide rapid and reversible crosslinks that are pH- and glucose-sensitive, enabling their use in glucose-responsive systems and injectable hydrogels. However, this feature also makes boronate ester

based hydrogels unsuitable in a cell culture environment, as they lack stability. Researchers have tackled this challenge through the introduction of a secondary network that is based on strain promoted azide-alkyne cycloaddition (SPAAC). Using these hydrogels, at different ratios of boronate ester and SPAAC enabled the encapsulation of human MSCs and showed a remodling of the microenvironment.[223] In contrast, hydrazone and oxime linkages have shown higher stability under physiological conditions while maintaining reversibility, making them attractive for long-term cell encapsulation and *in situ* generated biomaterials. Alginate and HA are well established polymers for hydrazide and aldehyde functionalization and application in 3D cell culture.[224,225] Hydrazone-based hydrogels have been used to modulate the stress relaxation, which is impacting the cellular remodeling of the microenvironment.[226] With different amount of alkyl-hydrazone *vs* benzyl-hydrazone inside the hydrogel network the stress relaxation time could be varied over multiple days and the cells could be cultured up to four weeks.[185] Imine-cross-linked hydrogels are attractive for 3D cell culture but typically degrade quickly. Their stability can be improved using benzaldehyde groups or secondary cross-links (*e.g.*, disulfide, acrylate, hydrazone), enabling longer culture times and better support for cell growth and migration. Many of these hydrogels are also adaptable by cell-secreted enzymes in the presence of MMP-cleavable cross-linkers or inherently, allowing dynamic interactions with encapsulated cells.[227–229] Importantly, their viscoelastic properties regulate key cell functions. A faster stress relaxation in imine-cross-linked collagen hydrogels, for instance, activates mechanosensitive pathways (*e.g.* TRPV4 ion channels), promoting osteogenic differentiation.[230] Oxime-based hydrogels are, unlike imine-based hydrogels, highly stable and suitable for long-term 3D cell culture. However, this stability comes with a limited viscoelasticity, as oxime bonds present slow stress relaxation times, unless catalysts support bond exchange.[231] Small molecules, such as, aniline, excess alkoxyamines, aldehydes, or acids can enhance bond exchange, rendering the gels more dynamic and adaptable.[232,233] Disulfide-cross-linked hydrogels exhibit fast reaction rates through thiol-disulfide exchange. Although this makes them appropriate candidates for cell encapsulation, they are also part of several side reactions with proteins, are labile towards reducing environments, and are sensitive towards air oxidation, making this crosslinking strategy challenging.[234–236] Nonetheless, many applications in 3D cell culture are reported, such as the spatiotemporal control of chemical and viscoelastic properties when using photo-mediated thiol-disulfide exchange. This feature resembles the dynamic nature of the ECM.[237–239] By tailoring the chemistry of DCC, hydrogels can thus be adapted for diverse tissue engineering applications, ranging from soft tissue

regeneration to disease-mimetic platforms.

3 Development of a high-throughput platform for kidney disease modeling

3.1 Introduction

3D *in vitro* disease models are becoming an important tool in tissue engineering and biomedical research as they provide a more accurate representation of the native tissue than conventional 2D monolayer cell cultures. These advanced *in vitro* models could allow for therapeutic screenings in healthy and diseased conditions on a large scale. Recent developments have expanded the potential of 3D *in vitro* models for multiple diseases, such as cancer, cystic fibrosis, cardiovascular and kidney diseases.[98,240] Kidney disease modeling in particular has made various advances modeling polycystic kidney disease (PKD), acute kidney injury (AKI), and fibrosis, using organoids from iPSCs, as well as from adult stem cells.[89,90,241] iPSCs-derived kidney organoids overcome multiple drawbacks from the conventional monolayer cell-culture, as the iPSCs self-differentiate into over 15 cell types of the kidney, and demonstrate complex cell-cell and cell-matrix interactions in 3D.[242,243] However, iPSCs-derived organoids only embody human fetal kidney development, lack immune cells and contain off-target cell types because of uncontrollable iPSCs differentiation.[90,92,93] Additionally, the potential of microfluidic-based kidney models to stimulate maturation has been studied.[94] The advantage here is having the perfusable microfluidic channels, however they often rely on commercially available expensive chips with one-time use and are not readily tunable.[91,94,95] Other models use bioprinters and a gelatin-fibrin based ECM to establish a 3D environment for tubule-interstitium or PT on perfusable chips.[96–98] Kroll *et al.* recently further developed this system by adding a second channel for vascularization and using kidney organoids to better mimic the native tissue microenvironment.[99] Up to now, no fully polymer-based synthetic 3D platform for *k*idney disease modeling

has been established, providing precise control over the microenvironment and the ability to be transferred to automated pipette systems. Therefore, to meet the demand of larger, reproducible tissue constructs with precise and complex structures, novel biomaterials are needed that can assemble into 3D constructs for tissue formation. Here, 3D hydrogels exhibit high potential as they can easily be tuned (bio)chemically and resemble the extracellular matrix due to their water swollen network.[244] ECM-mimicking materials can either be naturally derived or synthetic, where the latter offers a more reliable and reproducible hydrogel formation, with control over gelation, mechanical, physical, and biochemical properties as well as its degradation mechanism and rate. PEG is one of the most common synthetic polymers for 3D cell culture inside hydrogels, as it is bioinert and biocompatible, and can functionalized with defined bioactive molecules. Conventional hydrogels are intrinsically isotropic and do not offer any hierarchically structured organization, though, as we believe function follows form, structural compartmentalization is needed to generate 3D functional physiological or pathological tissue models. For example, other reports have demonstrated that fibrosis is mechanistically depended on injured PT and spatial communication, during which the PT sends signals to the interstitial space, leading to the pathological conditions of fibrosis.[119,120] Previously, our group has used CNF to create 3D scaffolds via extrusion sacrificial templating.[104] Tubule CNF structures were coated with fibroblasts and degraded enzymatically using cellulase in a controlled manner at specific time points. Doing so, a 3D free-standing cellular tube with large lumen (0.8 mm diameter) could be formed, composed of fibroblasts. In this work, we developed an entirely synthetic compartmentalized 3D *in vitro* disease model and employed the kidney as our model system. To create a multiphasic anisotropic hydrogel system, we employed plug flow microfluidics to produce sacrificial PEG-based rod microgels that can be embedded inside a surrounding PEG-based hydrogel matrix. This combination allows for a compartmentalized triple co-culture, implementing three key renal cell types of tubule-epithelial- ($CD10^+$) and endothelial ($CD31^+$) cells, and fibroblasts ($PDGFR\beta^+$) to achieve the required cell-cell interaction and tissue-mimicking structures. The tubular epithelial compartments, mimicking kidney proximal tubuli, are provided by on-demand enzymatic degradation of the rod microgels. We studied the material-cell interaction to create the 3D compartmentalized kidney models and demonstrated proof of concept to use the model as disease model by inducing fibrosis through TGFβ.

3.2 Results and Discussion

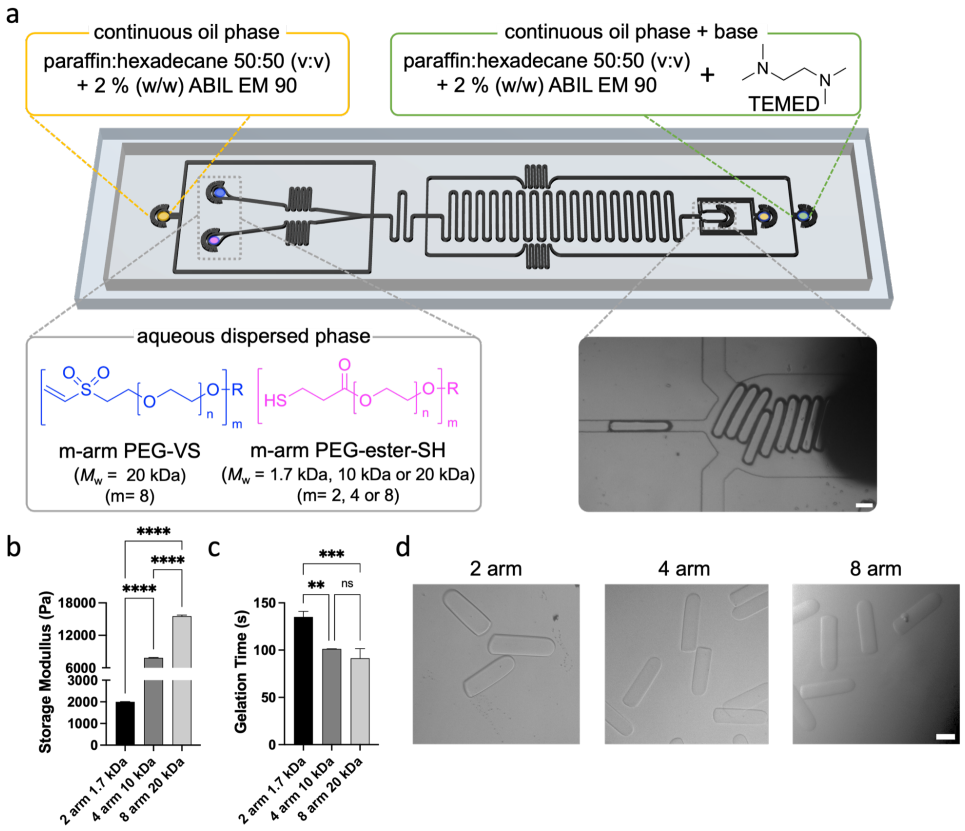

Fig. 3.1: Microfluidic production of enzymatically degradable rod microgels. (a) Plug-flow microfluidic chip design[198] , using Michael-type addition. Different degradable pre-polymers, such as linear and star-PEG-ester-thiols (4 or 8-arm), are combined with 8-arm 20 kDa PEG-VS to tune the microgel properties. First, the storage modulus (b) and gelation time (c) of bulk hydrogels (5 % (w/v) PEG) were produced at pH = 8 for the different precursor combinations. Brightfield images of produced rod microgels with different m-arm sPEG-ester-SH, scale bar = 100 µm, (d).

The development of the synthetic 3D compartmentalized kidney model required different building blocks, that needed to be optimized individually, to enable the formation of tubule-like epithelial structures, as well as the network formation of endothelial and supporting cells inside a 3D hydrogel. To emulate native kidney tubule structures, anisometric rod microgels were employed as structural templates. These were obtained through plug flow microfluidics based on previous work from our group.[116] The microfluidic design was refined by adding a focusing oil at the outlet of the channel to reduce pressure fluctuations upon gelation that influence the microgels' properties (Figure 3.1a). The crosslinking mechanism of the rod microgels is based on a Michael-type thiol-ene addition utilizing 8-arm PEG-VS and m-arm

star PEG-ester-thiol (m= 2, 4 or 8) (PEG-ester-SH), initiated through a basic pH using TEMED. The introduction of an ester moiety to the network enabled hydrolytic degradation, as well as enzymatic degradation on demand using lipase.[117] For all experiments, 8-arm PEG-VS (20 kDa) was used as a Michael-acceptor, whereas the donor was altered with a different number of arms and molecular weight (Figure 3.1a). Prior to conducting microfluidic production, the bulk hydrogel properties of the precursors (5 % (w/v) PEG) were evaluated through rheology. The storage modulus (G') increased proportionally with the number of arms, with the highest storage modulus (G') observed for 8-arm PEG-ester-SH and the lowest for the linear PEG-ester-SH (Figure 3.1b). At the same time, the gelation time decreased (Figure 3.1c) with increasing functionality per molecule. These compositions were then applied to produce rod microgels, where the concentration of the linear PEG-ester-SH was now adapted to 15 % (w/v), as below this concentration, no microgel production was possible. This is due to the long gelation time, which was observed for the bulk hydrogels. The microfluidic compositions, as well as the production parameters, can be found in Table 3.1 and Table 3.2. Brightfield images of the produced rods dispersed in water are shown in Figure 3.1d.

Tab. 3.1: Microfluidic pre-polymer solutions compositions with respect to the used m-arm PEG-ester-SH. For all microfluidic conditions 8 arm PEG-VS 20 kDa was used.

	Polymer concentration %(w/v)	**Base concentration in O_2 %(v/v)**
2 arm 1.7 kDa	15	4.5
4 arm 10 kDa	5	1
8 arm 20 kDa	5	1

Tab. 3.2: Microfluidic production settings. VS/ SH represent the flow rate for the pre-polymer solutions individually. O_1 is the oil phase and O_2 is the oil phase containing the base initiator.

	Flow rate VS/SH (µL/h)	**Flow rate O_1 (µL/h)**	**Flow rate O_2 (µL/h)**	**Flow rate flush (µL/h)**
2 arm 1.7 kDa				
4 arm 10 kDa	30	55-80	60	500
8 arm 20 kDa				

The size range of the rod microgels was 80-120 µm in width and 300 µm in length (Figure 3.2a). This size range could show a higher physiological size relevance, as previously reported tubule-like structures were > 150 µm. With microfluidics,

diameters < 100 µm can be achieved. The mechanical properties of the rod microgels were subsequently analyzed through nanoindentation (Figure 3.2b), where the composition with the linear precursor comprising the highest polymer concentration showed the highest Young's modulus, and the microgels made with 4 or 8-arm PEG-SH crosslinker did not exhibit any significant difference. The latter is likely because the arm length of the employed stars remained the same (2.5 kDa). Interestingly, the swelling ratio did not correlate completely with the Young's modulus. Here, the linear samples swell the most, despite having the highest Young's modulus and the 8 arm samples swell the least (Figure 3.2a). This might be due to the arm length, as the linear samples exhibit shorter PEG chains and are thus more hydrophilic, enabling a higher incorporation of water.

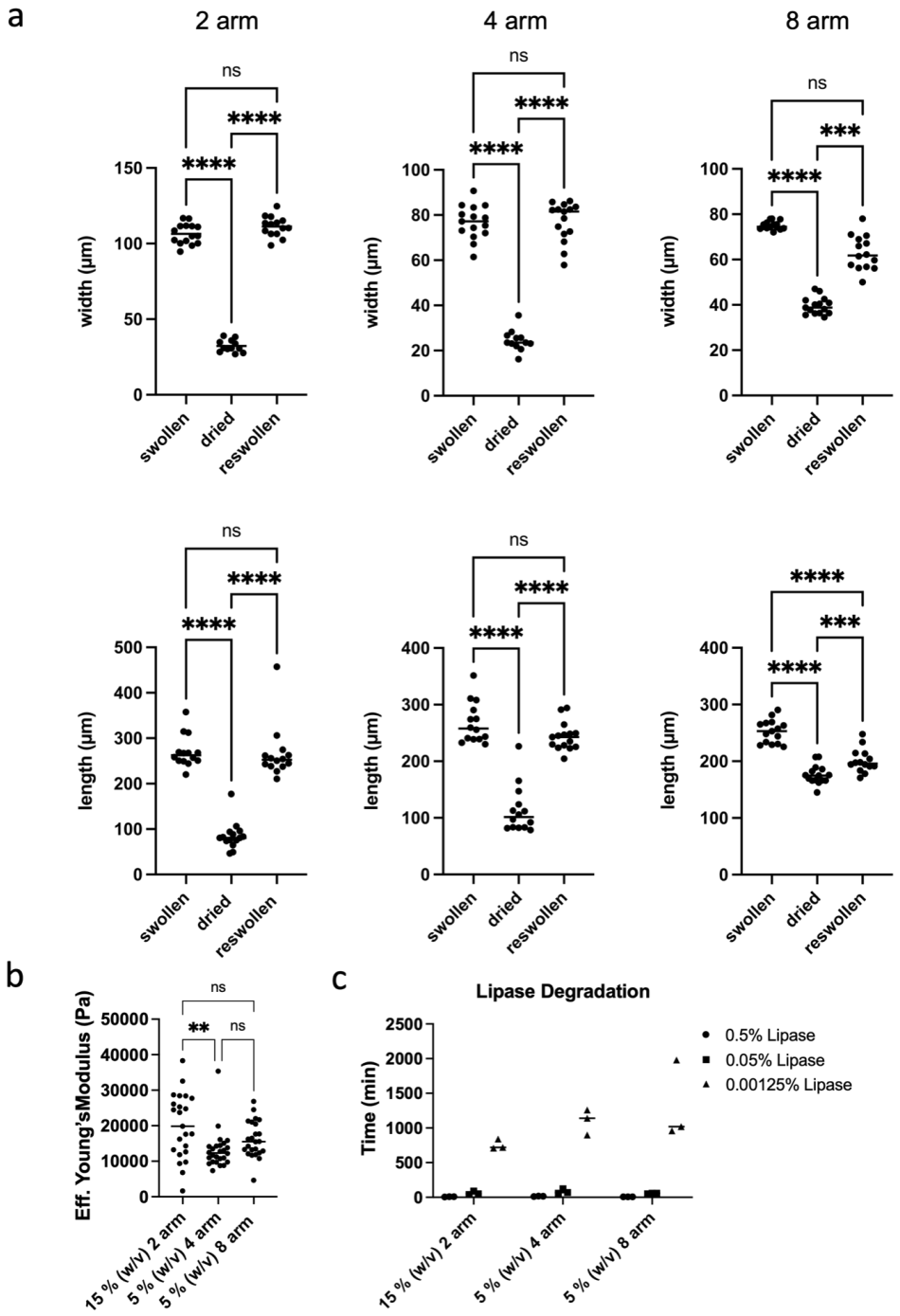

Fig. 3.2: Mechanical properties of obtained rod microgels. (a) Swelling behavior of obtained rod microgels with different m-arm sPEG-ester-SH. Data are means ± standard errors. Statistical significance was determined by one-way ANOVA with Tukey's multiple comparison test (*p < 0.05; **p < 0.01; ***p < 0.001; ****p < 0.0001) (b) Young's moduli determined through nanoindentation. (c) Enzymatic degradation time of rod microgels using different lipase concentrations at 37 °C and 5 % CO_2 in EGM-2 media.

As the rod microgels were employed to mimic kidney tubules and function as a

template for kidney epithelial, their on-demand degradability was assessed through the addition of an enzyme. Lipase was chosen as an enzyme, as it is known to selectively degrade esters through hydrolysis.[117] The microgels were dispersed in cell media to which the enzyme was added at different concentrations (0.00125 – 0.5 % (w/v)) and monitored through microscopy at 37 °C and 5 % CO_2. A higher enzyme concentration led to a faster degradation for all samples (Figure 3.2c). That way, the degradation time can be tuned from about 10 min with a concentration of 0.5 % (w/v), to 1 h and 18 h with 0.05 % and 0.00125 % (w/v) Lipase, respectively. The microgel composition did not show an influence on the degradation rate. The linear samples do not degrade more slowly than the star samples, despite the higher polymer concentration, which is probably linked to the network structure and high swelling degree. We then assessed whether the $CD10^+$ epithelial cells are compatible with the used enzyme by performing a metabolic assay over six days, where the enzyme was added at different concentrations at day one for two days. After two days, the media was refreshed without enzyme and the metabolic activity was tested until day six. The enzyme did not affect the metabolic activity, as all samples continued growing (Figure 3.3).

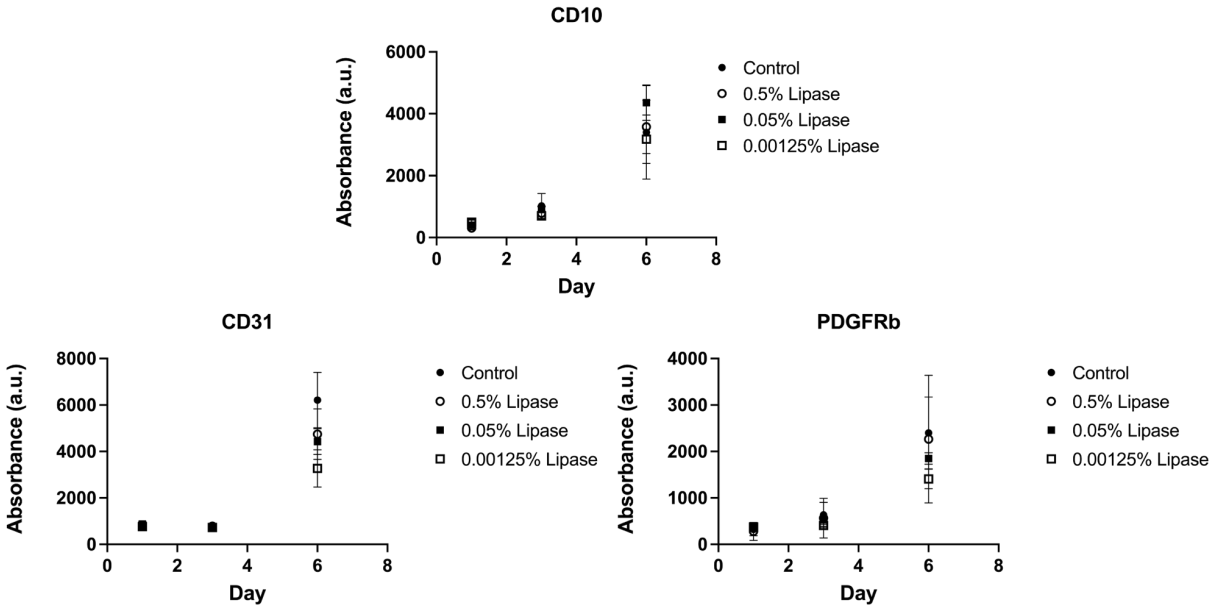

Fig. 3.3: Cell and enzyme comptability. Kidney cells and lipase compatibility was assessed through a metabolic assay. Lipase was added from days 1-3.

To guarantee efficient cell attachment, the different microgel compositions were assessed in the presence of cells through live imaging at 37 °C and 5 % CO_2. Therefore, the rod microgels were post-functionalized with a cell adhesive peptide

GRGDSPC and pipetted into a well plate together with $CD10^+$ cells (250 000/mL). Images were recorded for a period of two hours (Figure 3.4). Quantification of the cell attachment efficiency indicated a higher efficiency for microgels made with 4 or 8-arm PEG-SH compared to the linear PEG cross-linker. Based on all the results, we chose the microgel produced with 8-arm PEG-SH for all subsequent cell experiments as they remained the thinnest, more closely mimicking the kidney tubule.

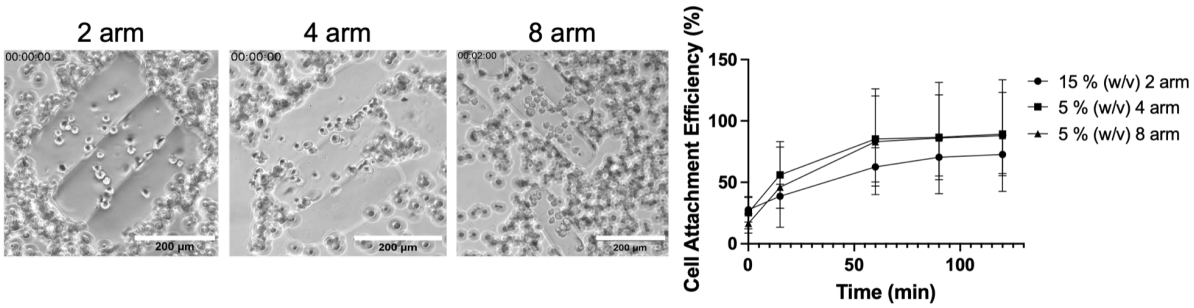

Fig. 3.4: Cell microgel interaction. Cell attachment efficiency of $CD10^+$ epithelial cells on GRGDSPC-functionalized rod microgels with different compositions at 37 °C and 5 % CO_2 after 2 h, scale bar = 200 µm. Data are means ± standard errors.

After optimizing the microgel composition, the 3D surrounding hydrogel matrix to culture kidney specific cells needed to be analyzed. Epithelial injury is a shared trait between all kidney diseases whether its downstream of glomerular injury with subsequent proteinuria or due to direct injury to the tubule. Its interplay with endothelial cells and fibroblasts is considered a driver of fibrosis and kidney functional decline.[119,120] We, therefore, used immortalized and genetically tagged cell lines derived from human nephrectomies for our 3D co-cultures. We previously demonstrated the origin and characteristics of each cell line, confirming the epithelial nature of the $CD10^+$ cells, the endothelial nature of $CD31^+$ cells and $PDGFR\beta^+$ cells as precursors of myofibroblasts.[97] The surrounding matrix consists of an enzymatically crosslinked PEG-based hydrogel. It consists of 8-arm PEG-VS 20 kDa functionalized with two peptides, AC-FKGGGPQGIWGQERCG-NH_2 = K-peptide or NQEQVSPLERCG-NH_2 = Q-peptide, that can covalently bind through activated FXIIIa.[65] For the co-culture of both cell types ($PDGFR\beta^+$ and $CD31^+$), different cell ratios were probed (1:1, 1:3, 1:2, 2:1 and, 3:1; $CD31^+$: $PDGFR\beta^+$) inside a 1.5 % (w/v) PEGKQ hydrogel for seven days (Figure 3.5a). A ratio of 1:1 proved to offer the best network formation (Figure 3.5a) with 1000 cells/µL in total. When culturing $CD10^+$ cells as a monoculture in the hydrogel for seven days, no growth was observed. Similarly, the addition of $CD31^+$ and $PDGFR\beta^+$ cells as a triple-co-culture did not

result in network formation or cell growth, possibly due to signaling of the CD10$^+$ (Figure 3.5b).

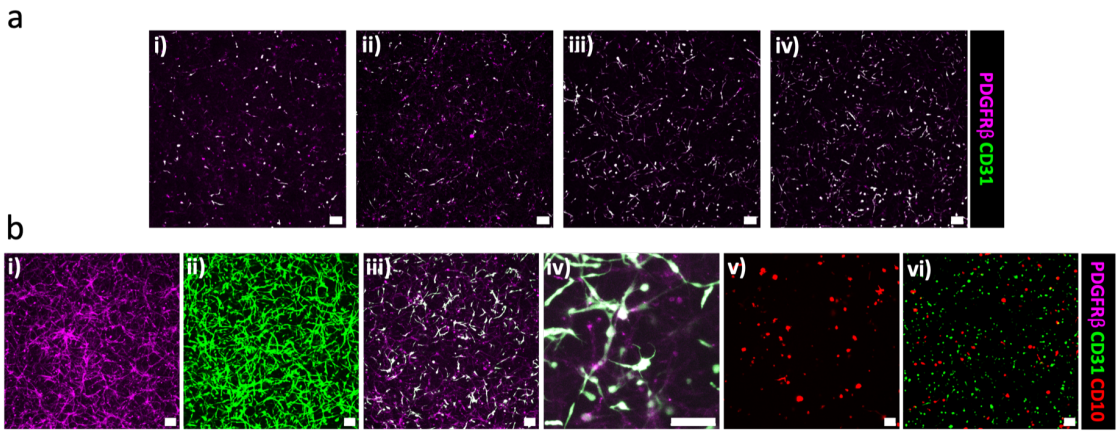

Fig. 3.5: Optimization of CD31$^+$ to PDGFRβ$^+$ ratio and triple-co-culture inside a 1.5 % (w/v) PEGKQ hydrogel matrix. (a) Optimization of CD31$^+$ to PDGFRβ$^+$ ratio inside a 1.5 % (w/v) PEGKQ hydrogel matrix: i) 1:3, ii) 1:2, iii) 2:1, iv) 3:1 (CD31$^+$:PDGFRβ$^+$). The hydrogel contained 600 µM GRGDSPC peptide and a total of 1000 cells/µL. The samples were incubated for seven days and fixed subsequently. Scale bars = 100 µm. (b) Monocultures and co-cultures of CD31$^+$, PDGFRβ$^+$ and CD10$^+$ cells in a 1.5 % (w/v) PEGKQ hydrogel with 600 µM GRGDSPC and cultured for seven days. i) mono-culture of PDGFRβ$^+$ or ii) CD31$^+$ with 1000 cell/µL, iii) co-culture (CD31$^+$ + PDGFRβ$^+$) in a 1:1 ratio with 1000 cells/µL in total, iv) higher magnification of the cellular network formation, v) mono-cultures of CD10$^+$ with 1000 cell/µL in 3D without proliferation, vi) triple-co-culture (CD31$^+$ + PDGFRβ$^+$ + CD10$^+$) (1:1:1, 500 cells/µL per cell type) inside the PEGKQ hydrogel not exhibiting network formation. PDGFRβ$^+$ signal was too weak to be displayed. Scale bars = 100 µm.

As epithelial cells naturally form thin layers of tissue to line hollow structures inside the body, *e.g.* tubules, we aimed to better mimic this by create a compartmentalized 3D hydrogel system. The CD10$^+$ cells were introduced into the system via rod microgels as their 2.5D substrate and were subsequently embedding them inside the 3D hydrogel, after which the rod microgels could be degraded on demand. As the endothelial cells and fibroblasts would also be in contact with the lipase once the microgels are degraded, a metabolic assay was performed with each cell type individually. We followed the same protocol as with the CD10$^+$ cells and could not observe a significant difference in cell activity with different enzyme concentrations (Figure 3.3). After analyzing the boundary conditions, we coated the GRGDSPC-functionalized microgels with CD10$^+$ cells so they could grow to confluence. To achieve a monolayer of epithelial on the microgel surface, we optimized the cell to microgel ratio to be 100 cells per microgel and put the microgel and cell mixture on an orbital shaker at 60 mpm for one hour prior to incubation

(Figure 3.6a). A ZO1 staining confirmed the presence of tight junctions that are responsible for sealing and preventing leakage of solutes and water (Figure 3.6b).

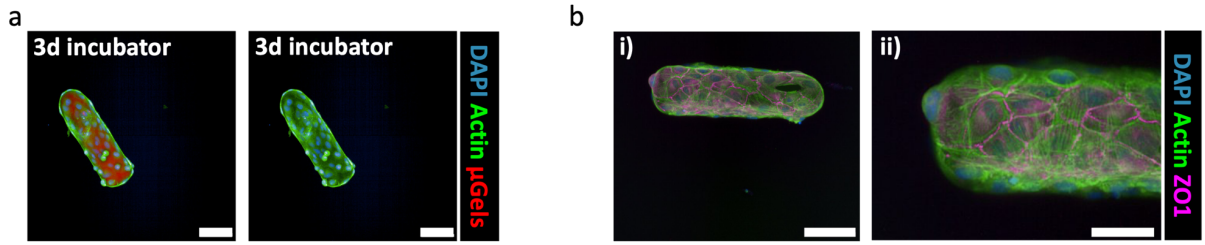

Fig. 3.6: Epithelial coating of degradable biofunctionalized microgels. (a) Coating of $CD10^+$ cells on GRGDSPC-functionalized microgels after three days. Scale bars = 100 µm. (b) ZO1 staining of $CD10^+$ coated microgels to show epithelial junction formation after three days. Scale bars = 100 µm.

Next, to deepen biological validation and demonstrate the epithelial monolayer on the microgels, we transferred the CD10+ coated microgels into a 1.5 % (w/v) PEGKQ hydrogel matrix and assessed the presence of epithelial tight junctions and SLC34A2, a Na^+/Pi co-transporter (NaPi-IIb), before and after degradation of the rod microgels (Figure 3.7). Similarly to microgels in suspension, we observed a confluent monolayer of $CD10^+$ cells with tight junctions, and the presence of SLC34A2 indicates the active proximal tubule nature of the cells with their ability to take up phosphates with the cotransporter.

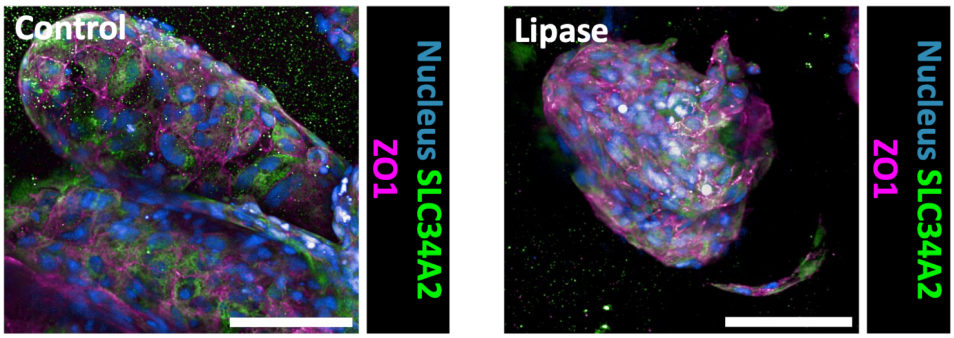

Fig. 3.7: ZO1 and SLC34A2 of $CD10^+$ coated rod microgels inside PEGKQ hydrogel matrix. $CD10^+$ coated microgels were transferred into a 1.5 % (w/v) PEGKQ matrix and cultured for seven days. Lipase (0.000625 % (w/v)) was added on day two and removed on day five to degrade the rod microgels. Microgels are not labeled. ZO1 and SLC34A2 staining show presence of epithelial tight junctions and NaPi-IIb co-transporter in the control and after degradation. Scale bars = 100 µm.

To note, we lowered the lipase concentration from 0.00125 % (w/v) to 0.000625 %, as too rapid microgel degradation within 24 h (observed via the loss of the rhodaminB

tag inside the microgel network) did not give the $CD10^+$ cells enough time to attach to the surrounding hydrogel matrix and maintain their hollow tubular shape (Figure 3.8).

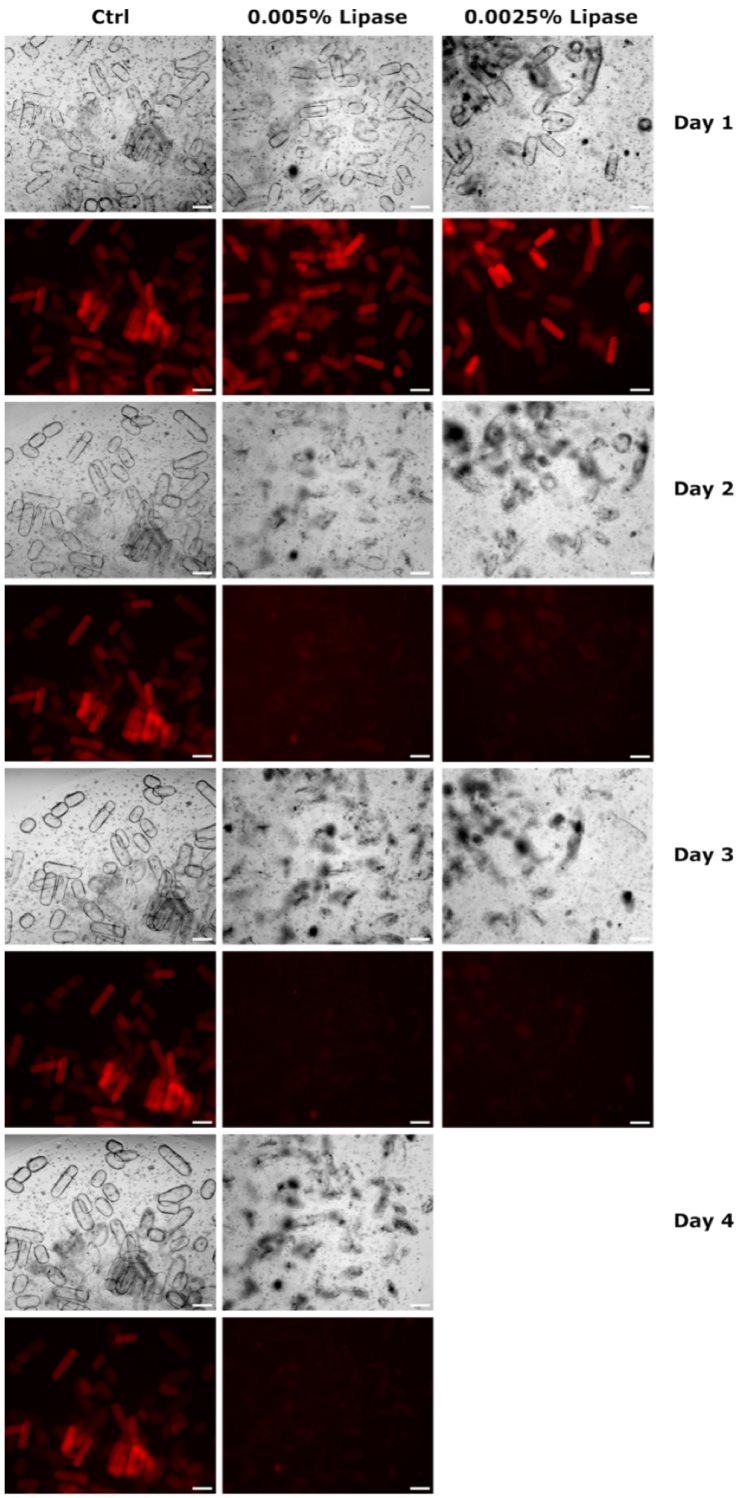

Fig. 3.8: Degradation study inside 1.5 % (w/v) PEGKQ hydrogel matrix with different lipase concentrations. Brightfield (top) and fluorescent (bottom) of Rhodamine B tagged microgels (red) to follow degradation on consecutive days inside a hydrogel matrix. The microgels are coated with $CD10^+$ epithelial cells. The hydrogel contains $CD31^+$ and $PDGFRb^+$ cells in a 1:1 ratio with in total 1000 cells/µL, as well as 600 µM GRGDSPC peptide. Scale bars = 200 µm.

In conclusion, the cell-coated microgels were introduced into the hydrogel matrix system containing the $CD31^+$ and $PDGFR\beta^+$ cells in a 1:1 ratio and cultured for 14 days. The microgels were enzymatically degraded at a chosen time during the culture using lipase to form the hollow structures (Figure 3.9a). We observed no effect of different lipase concentrations on the $CD31^+$ and $PDGFR\beta^+$ cells using a metabolic assay (Figure 3.3). To determine the influence of the surrounding hydrogel stiffness, we cultured our triple coculture in PEGKQ polymer concentrations of 1.5, 2.5 or 5 % (w/v). This resulted in hydrogels with Eff. Young's moduli determined through nanoindentation of 9.29 $\pm$ 6.22 kPa, 36.92 $\pm$ 6.71 kPa, and 42.67 $\pm$ 16.23 kPa, respectively (Figure 3.9b). The addition of microgels did not have a significant effect on the Eff. Young's modulus, also not after degradation. After forming the hydrogel with the $CD10^+$-coated microgels inside (day zero), lipase was added on day two (0.000625 % (w/v)). We observed no cell growth or network formation of the $CD31^+$ and $PDGFR\beta^+$ cells in the highest polymer concentration (Figure 3.9c).

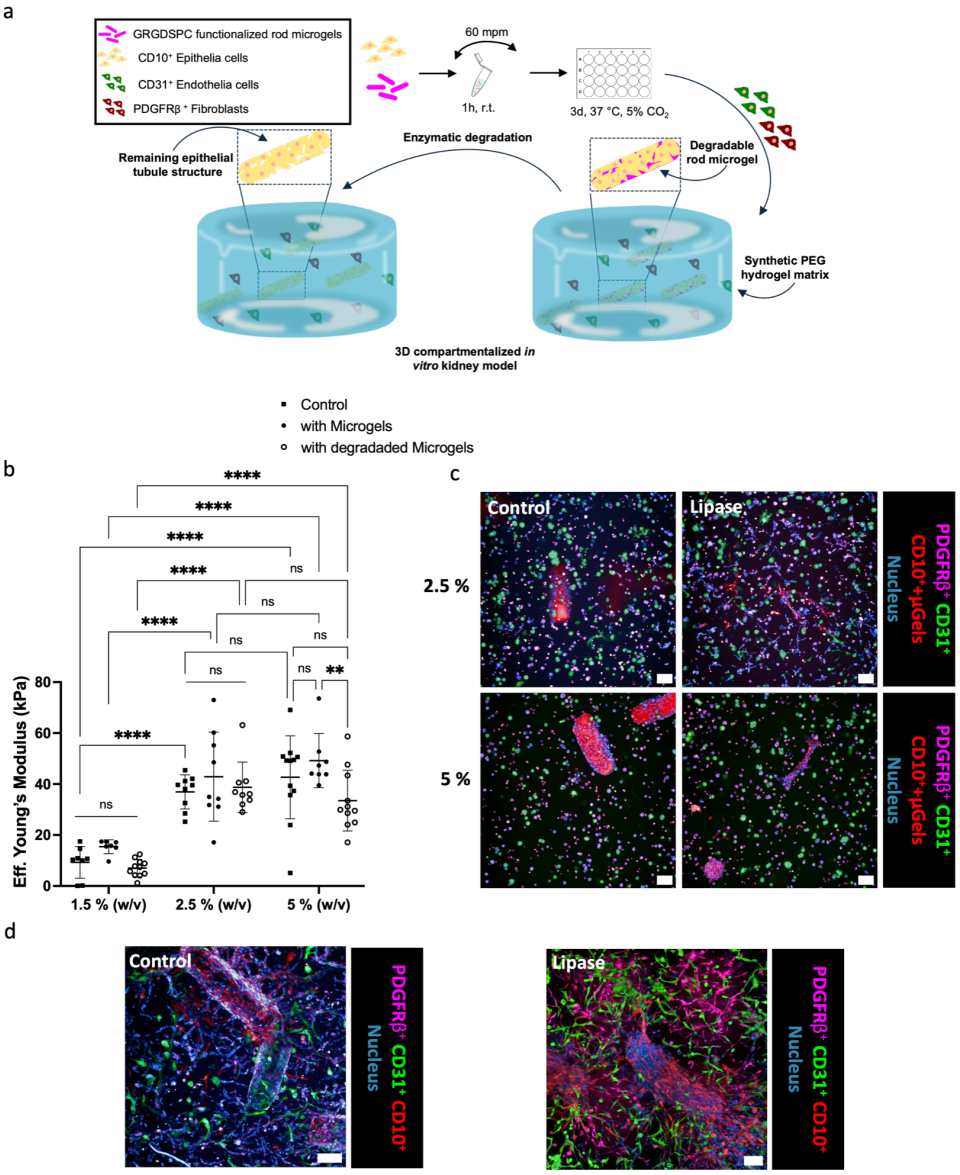

Fig. 3.9: 3D compartmentalized triple-co-culture hydrogel system. (a) Procedure to produce 3D compartmentalized triple-co-culture hydrogel system. (b) Effective Young's modulus of PEGKQ hydrogels with different polymer concentrations and microgels before and after degradation through lipase. A control is provided without microgels. Data are means ± standard errors. Statistical significance was determined by two-way ANOVA with Tukey's multiple comparison test (*p < 0.05; **p < 0.01; ***p < 0.001; ****p < 0.0001). (c) Triple-co-culture with different PEGKQ concentrations after 14 days. Confocal images in the degraded samples show shrinkage of the $CD10^+$ layer and do not keep the tubular shape. Furthermore, there is no sufficient network formation. Microgels are labeled. Scale bars= 100 µm (d) Confocal images of 3D compartmentalized triple-co-culture system with PEGKQ polymer concentrations of 1.5 % (w/v) after 14 days of culture. Lipase (0.000625 % (w/v)) was added on day two and removed on day five to degrade the rod microgels. Microgels are not labeled. Scale bars = 100 µm.

Likewise, the $CD10^+$ cells do not grow at higher PEGKQ concentration than 1.5 % (w/v) (Figure 3.9c+d). After microgel degradation, the $CD10^+$ cell layers

shrink and stretch over the void space, instead of keeping the rod shape of the microgel, resulting in a loss of the lumen. This result is in line with another study about kidney organoid lumen morphology inside an alginate-based soft and dynamic hydrogel matrix, that showed stiffer hydrogel matrices (20 kPa) caused a loss of lumen structures, whereas softer matrices (0.5 kPa) supported the maturity of lumen structures and reduced mesenchymal cells.[245]

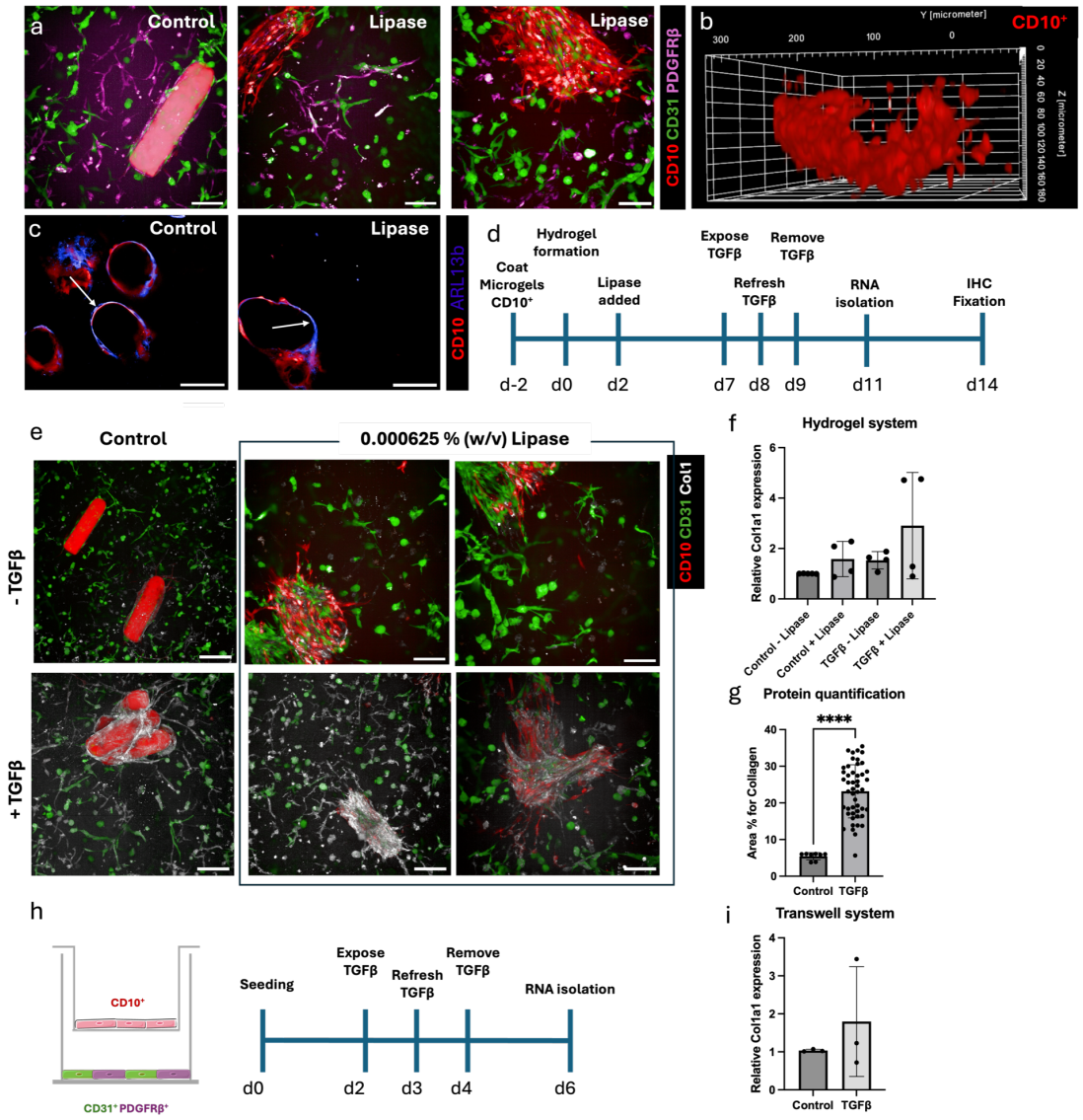

Fig. 3.10: Injury stimuli 2D vs 3D. (a) Anisotropic tubule-like formation of CD10$^+$ cells before degrading rod microgels (both CD10$^+$ and microgel labeled red) (left). Degraded microgel inside compartmentalized triple-co-culture inside a 1.5 % (w/v) PEGKQ hydrogel (middle, right). Scale bar = 100 µm (b) 3D view of the CD10$^+$ remaining tubule like construct after degradation. (c) Representative microscopy image of primary cilia (blue) before (control, unlabeled microgels) and after degradation (lipase) of the CD10$^+$ (red) covered microgels. Arrows indicate orientation of cilia. (d) Timeline of hydrogel formation and exposure to TGFβ. (e) TGFβ treated and untreated 3D triple-co-cultures. Control with undegraded microgels (labeled) (left panels), CD10$^+$ cells are depicted in red, CD31$^+$ cells in green, Collagen1 in white, PDGFRβ not shown. Scale bars = 200 µm. (f) Relative mRNA expression of Collagen1a1 in control and TGFβ exposed samples. Data are given as a mean and SD from 4 independent experiments each performed with four replicates. (g) Collagen1 protein expression quantification in treated and untreated triple co-cultures after degradation of the microgels. Data depicted as percentage of area positive for Collagen1, **** = $p < 0.0001$. (h) Schematic overview of triple co-culture in the transwell system and the experimental timeline. (i) Relative mRNA expression of Collagen1a1 in control and TGFβ exposed samples in the transwell system. Data are given as a mean and SD from three independent experiments each performed with three replicates.

Culturing the compartmentalized triple-co-culture (Figure 3.10a) inside a 1.5 % (w/v) PEGKQ hydrogel showed that the $CD10^+$ cells form a tubule-like structure upon degradation (Figure 3.10a-b). The 3D view reveals lumen formation with a size of approximately 100 µm; however, it should be noted that the structure is not fully enclosed and remains porous at this stage. Next, we demonstrated the polarity of epithelial cells before and after degradation of the microgel. We found that prior to degradation, the basement membrane of the $CD10^+$ cells is located towards the microgel surface, with the cilia pointing towards the surrounding hydrogel (Figure 3.10c). After degradation with lipase, the polarity is less clear. We propose that after degradation, the orientation of the cells is transitioning towards having the cilia on the apical side pointing towards the hollow lumen, in a manner consistent with physiological function. To assess the potential of our synthetic 3D in vitro system to model kidney disease, we stimulated the hydrogel network with TGFβ (Figure 3.10d). TGFβ is a known driver of fibrosis and has shown to initiate fibroblast-to-myofibroblast transition of the PDGFRβ+ cells *in vitro*.[97,118] After 48 h of TGFβ exposure, the hydrogel systems demonstrated an upregulation of the fibrosis readout collagen1 both on a protein- and gene expression level (Figure 3.10e-g). These results also reveal that in control conditions, lipase did not affect collagen mRNA production (Figure 3.10f). Quantification of Collagen1 relative mRNA expression revealed a 3-fold increase in injured kidney models compared to the control (Figure 3.10f) after the microgels are degraded through lipase and TGFβ is added. Only a weak increase is observed by the addition of TGFβ when the microgels are not degraded. This is particularly interesting since it demonstrates the importance of lumen formation, which may create a more physiologically relevant interaction of tubule epithelial cells and fibroblasts in the initiation of fibrosis. Despite the mRNA levels being only slightly upregulated, Col1 protein quantification revealed a significant 3-fold increase in the injured kidney model with lipase compared to the control (Figure 3.10g). To compare this engineered compartmentalized 3D microgel-in-hydrogel system to more conventional 2D co-culture systems, we used a 3D 6-well transwell system with a triple-culture in a similar manner to our hydrogel; using a 1:1 ratio of $CD31^+$:$PDGFR\beta^+$ cells on the bottom, and $CD10^+$ on the transwell (Figure 3.10h). After exposure of 48 h of TGFβ, we observed a 2-fold increase in relative Col1a1 mRNA expression in the transwell system (Figure 3.10i), compared to a 3-fold increase using our hydrogel model, indicating that the injury response may be enhanced in this model. Taken together, these results suggest its potential for drug development and future high-throughput screening when using automated pipetting systems.

3.2.1 Discussion

In this study, we developed a fully synthetic compartmentalized PEG-based hydrogel system including kidney tubular epithelial structures surrounding degradable microgels, leading to representative hollow tubular structures. Our multiphasic hydrogel system is the first to provide precise control over spatially organizing key renal cell types and both the microgels and surrounding hydrogel support the specific cell growth. After degradation of the microgels to mimic the tubule interstitium, we demonstrated its utility in modeling kidney fibrosis and showed an increased response in Collagen1 production in comparison to other 2Dculture methods. Therefore, the model allows for a strong cellular response to injury, suggesting that our system is valid and suitable for drug testing.

Previous studies have shown that (visco)-elasticity and the 3D microenvironment matter for cell growth, which became apparent when probing softer versus stiffer hydrogel matrices.[246–248] The softer hydrogel matrix promoted cell growth and network formation, as well as lumen formation, which is in line with previous findings when culturing kidney organoids inside alginate-based hydrogels.[245,249] The stiffer substrates on the other hand, did not exhibit cell spreading for the endothelial and pericyte cells. Furthermore, the epithelial layer portrayed shrinking after microgel degradation inside the stiffer microgels, which was not the case for the softer hydrogels. Interestingly, even though we observed that the epithelial cells grow on the entire microgel surface before incorporation inside the surrounding hydrogel, upon degradation of the microgels, the epithelial cells do not result in a perfect lumen. This could be due to insufficient attachment of the epithelial cells to the surrounding hydrogel matrix once they lose the microgel support. As we already know that the hydrogel stiffness influences the lumen formation, other drivers such as matrix viscoelasticity might play an important role, which will be studied in further studies. Currently, the hydrogel is completely elastic, lacking the viscoelasticity present in the native tissue. In literature stress-relaxing hydrogels have shown to influence cilia frequency and length, as well as epithelial-mesenchymal transition of kidney organoids.[245]

Kidney injury and fibrosis is characterized by a progressive accumulation of ECM proteins, leading to tubulointerstitial scarring and loss of renal function. The activation of fibroblasts leading to an increased expression of the extracellular matrix component Collagen1 in our model shows that it provides a physiologically

relevant 3D microenvironment that is responsive to fibrotic cues. The upregulation of Collagen1 observed in our system indicates active matrix remodeling and mimics early fibrotic events, making it a valuable platform for studying the progression of fibrosis and responsiveness to drugs. Moreover, the tunability of the hydrogel stiffness and potential to introduce viscoelastic components enables future work to probe how mechanical cues contribute to fibrogenesis, which has been identified as a major driver in chronic kidney disease.

While our hydrogel model provides a tunable and reproducible platform, it does not fully capture the complexity of *in vivo* kidney disease, particularly the influence of the immune cell populations or fluid flow. Incorporating immune cells into the culture media would more fully recapitulate the fibrotic niche. Furthermore, the addition of growth factors can support vascularization in 3D hydrogel systems and further improve the functionality of our platform.[250] In addition, to better represent the size of tubules *in vivo*, the diameter of the microgels could potentially be reduced. Our system currently consists of 100 µm microgels covered in epithelial cells, while 25-40 µm is standard in human kidney architecture. Bioprinting such small open channels still remains a challenge and to achieve smaller microgels, different microfluidic techniques would need to be employed, such as compartmentalized jet polymerization[122] or in mold polymerization.[122] However, so far, these methods have not used the chemistry employed in this report to enable the on demand enzymatic degradation to create lumens.

In the future, our platform could potentially be used to model different types of kidney injury, including hypoxia for AKI or IL1β for inflammatory kidney injury. Lastly, as our model is fully synthetic, it is suitable for trials with iPSCs to directly have spatial organization, surrounding on-demand degradable microgels for more efficient differentiation and less off-target cell populations. Moreover, this compartmentalized hydrogel system with tunable properties allows for broadly applicable platform for drug testing in a reproducible and high-throughput manner.

3.3 Conclusion

This chapter describes the development and characterization of a fully synthetic compartmentalized PEG-based hydrogel system implementing degradable rod

microgels to create representative hollow tubular structures. This multiphasic hydrogel system is the first to provide control over material properties on multiple length scales. After degradation of the microgels to mimic the tubule interstitium, we were able to show its utility in modeling kidney fibrosis and assessed an increased response in collagen 1 production in comparison to other 2D culture methods. These findings suggest that our system is valid and suitable for drug testing.

3.4 Materials and Methods

3.4.1 Chemicals and Cell Culture Material

ABIL EM 90 (Evonik Nutrition, Essen, Germany), 8-arm poly (ethylene glycol) PEG-OH 20 kDa (Creative PEGWorks, Chapel Hill, NC, USA, $\geq$ 95%), 4-arm PEG-OH 10 kDa (Creative PEGWorks, $\geq$ 95%), PEG-OH 1.7 kDa (Sigma-Aldrich, St. Louis, MO, USA, $\geq$ 95%), 8-arm PEG-VS 20 kDa (Creative PEGWorks, $\geq$ 95%), Sylgard® 184 silicone elastomer kit (The Dow Chemical Company), Dulbecco's modified Eagle medium (DMEM, Gibco, Grand Island, NY, USA, EGM-2 medium (Lonza, EBM-2 cc-3154, EGM-2 singleQuots Supplements cc-4176), TGFβ (100-21-10UG, Peprotech), ethanol (VWR-chemicals, Radnor, PA, USA,$\geq$ 98%), Novec 7500 (Sigma-Aldrich), paraffin (VWR-chemicals), paraformaldehyde (PFA) (Sigma-Aldrich), phosphate buffer saline (PBS, pH = 7.4, c = 1x,TGFβ (100-21-10UG, Peprotech), Thermo Fisher Scientific, Waltham, MA, USA), SYLGARD 185 silicone elastomer kit (Dow, Midland, MI, USA), methacryloxyethyl thiocarbamoyl rhodamine-B (Polysciences, Warrington, PA, USA), N,N,N',N'-Tetramethylethylenediamine (TEMED, Sigma-Aldrich, $\geq$ 99%), n-hexane (Sigma-Aldrich, $\geq$ 98%), iso-propanol (Sigma-Aldrich, $\geq$ 98%), 3-mercaptopropionic acid (Sigma-Aldrich, $\geq$ 99%), p-toluenesulfonyl acid monohydrate (p-TsOH) (Sigma-Aldrich, 98.5%), cyclohexane (Sigma-Aldrich, $\geq$ 98%), sodium bicarbonate (Sigma-Aldrich), GRGDS-PC H-Gly-Arg-Gly-Asp-Ser-Pro-Cys-OH (trifluoroacetate salt) (CPC Scientific, Sunnyvale, CA, USA, $\geq$ 98%), Corning® Costar® Ultra-Low Attachment Multiple Well Plate (Sigma-Aldrich), Protein LoBind® Tubes (Eppendorf, Hamburg, Germany), Tridecafluoro-1,1,2,2-tetrahydrooctyltrichlorosilane (Sigma-Aldrich, 97%), acetone (Sigma-Aldrich, $\geq$ 98%), dichloromethane, ether (Sigma-Aldrich), dimethly sulfoxide (DMSO) (Sigma-Aldrich, $\geq$ 98%), PTFE tubing (Instech)

3.4.2 Synthesis of m-arm poly (ethylene glycol) ester thiol

m-arm PEG-ester-SH (m=2, 4 or 8) were prepared by Fischer esterification of the respective PEG-$(OH)_m$ according to the literature.[251] Briefly, in a 250 mL two-neck round bottom equipped with a Dean-Stark PEG-(OH)m (1500 linear difunctional PEG-OH = 2 arm or 10000 Da sPEG-OH 4 arm or 20000 Da sPEG-OH 8 arm) (1 eq., 1.00 g) was dissolved together with 3-mercaptopropionic acid (40 eq.) and p-toluenesulfonic acid (p-TsOH) (0.1 eq.) in 70 mL cyclohexane. The reaction was refluxed at 130 °C for 24 h, and at least two volumes of Dean-Stark were removed. Afterwards, the reaction mixture was cooled down to r.t. and the cyclohexane was separated from the product via decantation. The remaining white wax was dissolved in DCM (50 mL) and washed with saturated NaHCO3 (2 x 15 mL), brine (1 x 15 mL) and dried over MgSO4. The solid is removed by filtration and the solution is concentrated until a viscous oil is obtained. The resulting oil is dissolved again in minimal amount of DCM (2-3 mL) and precipitated by dropwise addition in excess cold (-20 °C) diethyl ether (40x vol DCM) and the final product is isolated as a white powder (isolated yield 70%). ^{1}H NMR (CDCl3, 400 MHz): δ (ppm)= 4.26 (4H, m, –CH2CH2OC(O)–), 3.64 (133H, br),(CH2CH2O)n), 2.77 (4H, m, –CH2CH2SH), 2.68 (4H, m,CH2CH2SH), 1.68 (2H, t, SH).

3.4.3 Rheological measurements of bulk hydrgels

Rheological measurements of bulk hydrogels were performed using an HR-3 rheometer PHR3 (TA Instruments, New Castle, DE, USA) at room temperature using a 20 mm conical 2°geometry probe. 8-arm PEG-VS 20 kDa and m-arm PEG-ester-SH were mixed in phosphate buffer (100 mM, pH = 8) and pipetted onto the device. Time sweeps were conducted at 1 Hz and 1% strain until a plateau was reached. Subsequently, frequency sweeps at 1% and strain sweeps at 1 Hz were performed.

3.4.4 Microfludic device preparation

As described elsewhere,[116] microfluidic masters are produced via soft lithography. The PDMS mold was prepared using the Sylgard 184 silicone elastomer kitin a 10:1 ratio with the curing agent. The components were mixed and degassed using a PDMS

mixer (Thinky PDMS Mixer, Thinky USA Inc., Laguna Hills, CA, USA) (mixing: 2000 rpm for 2 min; defoaming: 2200 rpm for 2 min). The mixture was subsequently poured onto the microfluidic silicon master and degassed by placing it in a desiccator under vacuum (10^{-3} bar). The PDMS was cured at 60 °C for 12 h. After curing, the PDMS was cut out, and holes for inlets and outlets of the channels were punched (biopsy puncher, inner diameter 0.75 mm, Sigma-Aldrich). The PDMS chip was washed three times with isopropanol and water. A glass slide (75 x 50 x 0.16 mm, Carl Roth, Karlsruhe, Germany) was washed three times with isopropanol and acetone. The PDMS mold and glass slide were treated with oxygen plasma to covalently bind both parts inside an oxygen plasma oven (PVA TePla 100E, PVA TePla, Wettenberg, Germany) at an oxygen flow of 28 mL/min for 40 s at 100 W and 0.2 mBar. The completion of the bonding was done in an oven at 60 °C for 3 h. After finalization of the bonding, the microfluidic channels were rendered hydrophobic by chemically depositing 50 µL of tridecafluoro-1,1,2,2-tetrahydrooctyltrichlorosilane inside a desiccator at 10^{-3} bar overnight. The remaining residues of the silane were removed using paraffin.

3.4.5 Preparation of microfluidic solutions

The oil phase consisted of 50:50 (v/v) hexadecane/paraffine and 2 % (w/v) ABIL EN 90. To initiate the reaction, a catalyst oil phase was prepared, mixing TEMED and the oil phase at 1 % (v/v) – 5 % (v/v). Eight-arm PEG-VS 20 kDa and m-arm PEG-ester-SH were dissolved separately in water in the desired concentration (total PEG, % (w/v)). Furthermore, the PEG-ester-SH contained 0.05 % (w/v) of a methacryloxyethyl thiocarbamoyl rhodamine-B solution (10 mg in 100 µL DMSO).

3.4.6 Microfluidic production of rod microgels

Rod microgels were prepared via on-chip gelation in a flow-focusing microfluidic device comprising a channel diameter of 80 µm employed in the plug-flow regime based on.[116] An additional flow-focusing oil channel has been added to the channel design to ensure a homogenous flow, reducing pressure differences due to viscosity rises. To precisely control the flow rates, the microfluidic tubing (polytetrafluoroethylene (PTFE)) was attached to Hamilton® syringes (Gastight 1000 series, Hamilton, Reno, NV, USA) and fixed on syringe pumps (Elite 11, Harvard

Apparatus, Holliston, MA, USA). The pre-polymer solutions were filled in individual syringes, as well as the oil phase, the catalyst oil phase and focusing oil (five syringes in total). The rod microgels were collected in the oil phase and purified subsequently by washing three times with n-hexane, iso-propanol, and water, respectively. The rod microgels were stored in water at 4 °C until further use.

3.4.7 Degradation Experiments of Rod Microgels

Rod microgels were incubated in cell media ((Dulbeccos Modified Eagle Medium (DMEM), Gibco) with and without enzyme at the desired concentrations inside a 96 well plate. The well plate was placed on a microscope (Leica, DFC 7000 GT) comprising CO2 control at 5 % CO_2 and temperature control at 37 °C. A time lapse was recorded to assess the degradation time of the microgels.

3.4.8 Nanoindentation

Before nanoindentation, the rod microgels were immobilized on a cell culture well plate using a poly-L-lysine solution (0.01 % (w / v), Sigma-Aldrich). The well surface was covered with a thin film of the solution and left overnight to evaporate. The microgels were subsequently pipetted on the surface of the well plate and left for sedimentation. Once the microgels were fixed to the well bottom the measurements were started. The mechanical properties of the rod microgels were assessed using a Pavone Nanoindenter (Optics11Life, Amsterdam, Netherlands). The Nanoindenter was equipped with a cantilever probe comprising a spherical tip radius of 9 µm and a cantilever stiffness of 0.242 N/m. For each sample at least three microgels were indented. The piezo speed was set to 15 µm/s and the indentation depth to 1 µm. All measurements were conducted at r.t. and in water. The effective Young's modulus E_{eff} (Pa) was determined from the obtained load-indentation curves employing the Hertz contact model. The data analysis was carried out using the Software Dataviewer V2.5 (Optics11Life).

3.4.9 Swelling behavior microgels

For the swelling behavior, the microgels were measured in their swollen state. Then dried at room temperature and measured in their dried state. Afterwards, they were resuspended in water and their reswollen state was measured after one week.

3.4.10 Biofunctionalization of Rod Microgels and Sterilization

The rod microgels were post-functionalized with GRGDSPC inside a phosphate buffer (100 mM, 94.7 mM Na_2HPO_4, 5.3 mM NaH_2PO_4, pH = 8) overnight. For 1500 microgels (80 µm width, 300 µm length) 1.5 aliquots of peptide were used (25 mg/mL , 10 µL/ aliquot) in 300 µL buffer. Afterward, the microgels were washed five times with water. To sterilize, the microgels were incubated in ethanol (70 % (v/v)) for one hour and UV sterilized. They were again washed three times with sterile water in a sterile flow hood. Prior to cell experiments, the rod microgels were transferred into cell media by washing them three times.

3.4.11 Cell attachment efficiency through live imaging

For live imaging, sterile microgels were dispersed in methylcellulose to prevent microgel drift during imaging. 6 g of methylcellulose were sterilized and dissolved in 500 mL cell media and centrifuged at 2500x g prior to use. The final concentration was set to 20 % (v/v) of methylcellulose. The microgels and methylcellulose mixture was pipetted onto a well plate and sedimentation of the microgels was allowed for one hour. Subsequently, the $CD10^+$ cells were seeded on top at a concentration of 250 000/ml. Every 30 s an image of the sample was taken via differential interference contrast (DIC) microscopy on a ZEISS Axio Observer Z1 inverted microscope at 37 °C and 5 % CO_2 at humid environment over a period of 120 minutes.

3.4.12 Coating of rod microgels with $CD10^+$ epithelial cells

Post-functionalized and sterile rod microgels were dispersed in the required cell media. The $CD10^+$ epithelial cells and microgels were mixed inside a LoBind

Eppendorf tube at a ratio of 100 cells per microgel with a size of 80 µm in width and 300 µm in length. The total amount was calculated with respect to the number of triplicates. One triplicate contained 3000 microgels and per well 400 µL of microgel cell dispersion was needed. The tube was then placed on an orbital shaker at 60 mpm for one hour. The microgel cell dispersion was then pipetted onto an ultra-low attachment 24 well plate (Corning) and incubated for three days. Other well plates and coatings did not sufficiently inhibit the attachment of the cells. Low attachment of the $CD10^+$ cells to the well bottom is important, as the transfer into a hydrogel and complete cell coverage of the microgels is easier.

3.4.13 Staining of $CD10^+$ coated rod microgels

Microgel samples were washed twice for 5 min with phosphate-buffered saline (phosphate buffered saline (PBS), pH = 7.4, c= 1x, Thermo Fisher Scientific) and fixed with 4 % paraformaldehyde (PFA) for 30 min at room temperature. After washing again for 15 min with PBS, 0.1 % (v/v) TritonX-100 (Sigma-Aldrich) for 3 min was added, and washed afterwards with PBS. The samples were then incubated in 4 % bovine serum albumin (BSA) for 2 h. F-actin filaments of the cells are stained using phalloidin647 (1:1000 Abcam) (1:1000) in 1 % BSA in PBS for 1 h, followed by washing with PBS. Cell nuclei are stained using 4',6-diamidino-2-phenylindole (DAPI) (1:200) in PBS for 20 min, followed by washing twice with PBS. ZO-1 was stained using Invitrogen, # 40-2200 at 1:200 overnight at 4°C and subsequently with AF647 goat anti-rabbit (1:1000 Abcam) in PBS.

3.4.14 Transfer into 3D PEGKQ hydrogel matrix

The $CD10^+$ coated microgels were harvest from the well plate and centrifuged at 100 rcf for 5 min. Excess cell media was removed. Approximately 6000 cell-coated microgels were diluted with 1000 µL of cell media and then used to prepare the hydrogels. The PEG hydrogel was prepared as previously described [29, 42].[65,252] Briefly, two separate batches of eight-arm star PEG-VS (20 kDa; JenKem Technology) were conjugated with peptide solutions in triethanolamine, pH 8 (Sigma-Aldrich). The peptide sequences were H-NQEQVSPLERCG-NH_2 (Q-peptide; 1358.6 Da, GenScript, NL) and Ac-FKGGGPQGIWGQERCG-NH_2 (K-peptide; 1717.6 Da, GenScript).

Conjugation to cysteine residues involved Michael-type addition by incubating the solutions for 2 h at 37 °C. The solutions were then dialyzed for four days against water at 4 °C to remove any unreacted peptides. The solutions were lyophilized, dissolved in water, UV sterilized, and stored at -20 °C until further use. For gel preparation, equimolar amounts of the two PEG conjugates were mixed at a total concentration of 1.5 % (w/v) in cell culture medium, along with a 10× calcium buffer (0.1 M $CaCl_2$, 0.5 M Tris, 1.1 M NaCl (Sigma-Aldrich)), and 600 µM of the cell adhesion peptide GRGDSPC (CPC Scientific, Milpitas, CA, USA) and $CD10^+$ cell coated microgels. Gelation was initiated by adding 1250 U FXIIIa (CSL Behring, King of Prussia, PA, USA), which was activated by diluting 200 U/mL thrombin (Sigma–Aldrich) to 20 U/mL in a buffer (25 mM $CaCl_2$, 10 mM Tris, 150 mM NaCl) and incubating with the FXIII pro-enzyme for 30 min at 37 °C, shaking gently every 5 min. The FXIIIa was then aliquoted and stored at -80 °C until further use. The hydrogel mix was pipetted in 15-µL droplets into 8-well ibidi plates and flipped to ensure the distribution of the microgels in three dimensions. The hydrogels were flipped back after 5 min and incubated at 37 °C in a 5 % CO_2 atmosphere to complete the gelation. EGM-2 medium (Lonza, # EBM-2 cc-3154, EGM-2 singleQuots Supplements cc-4176) with added 1 % Pen/Strep was added to the hydrogels and incubated for seven days at 37 °C in a 5 % CO_2 atmosphere. Lipase was added with a concentration of 0.000625 % (w/v) at day two and removed at day five.

3.4.15 Metabolic activity assessment of cells

$CD10^+$, $CD31^+$ and $PDGFR\beta^+$ were seeded in a 24-well plate at a concentration of 2000 cells/cm^2 and incubated for 24h . After 24h, a solution of 10 % (v/v) of almarBlueTM in DMEM comprising 10 % fetal bovine serum (FBS) and 1 % amphotericin B (AMB) was prepared and added to the samples. The samples were incubated for 1 h at 37 °C and 5 % CO_2. Afterwards, triplicates (50 µL) of each sample were distributed on a 96 well plate and a photometric determination (excitation 530 nm, emission 590 nm) was performed using a Tecan plate reader. Between assays, the samples were incubated in the respective cell medium.

3.4.16 Nanoindentation analysis of microgel containing hydrogel

Flat disk-shaped hydrogels with a volume of 35 µl are formed in printed pluronic rings that have a radius of 3.5 mm and a height of 1.2 mm. After crosslinking of the hydrogels, the pluronic is removed by washing with cold PBS. The mechanical properties of the hydrogels were assessed using a Pavone Nanoindenter (Optics11Life, Amsterdam, Netherlands). The Nanoindenter was equipped with a cantilever probe comprising a spherical tip radius of 9 µm and a cantilever stiffness of 0.020 N/m. For each sample at least three hydrogels were indented. The piezo speed was set to 30 µm/s and the indentation depth to 1500 µm. All measurements were conducted at r.t. and in water. The effective Young's modulus E_{eff} (Pa) was determined from the obtained load-indentation curves employing the Hertz contact model. The data analysis was carried out using the Software Dataviewer V2.5 (Optics11Life).

3.4.17 Injury stimulation of cells

The hydrogel samples were incubated with 10ng/mL TGFβ (100-21-10UG, Peprotech) in culture media for a total of 48 hours with a refreshing of the TGFβ after 24 hours.

3.4.18 Fixation and staining (Orientation + ColI + ZO1 + SLC34A2)

Hydrogel samples were washed twice for 30 min with phosphate-buffered saline (PBS, pH = 7.4, c= 1x, Thermo Fisher Scientific) and fixed with 4 % PFA for 1 h at room temperature. After washing again for 30 min with PBS, 0.1 % (v/v) TritonX-100 (Sigma-Aldrich) for 20 min was added, and washed afterwards with PBS. The samples were then incubated in 4 % BSA for four h. After removal of the fixative, samples were washed with PBS and incubated with primary antibody at a 1:200 dilution in PBS + 1 % BSA overnight at 4 °C. After removal of the primary antibody, samples were again washed three times 30 min with PBS before adding the secondary antibody 1:200 for Col1, and 1:500 of ZO1 and SLC34A2 dilution in PBS overnight at 4 °C. To image, secondary antibody was washed away three times 30 min with PBS, and samples were covered with PBS. The following antibodies were used: Col1a1(Biozol, 1310-01, 1:200), ARL13b (Proteintech, 17711-1-AP, 1:200), AF405 donkey anti-goat (Dianova, 705-475-147, 1:200), AF647 donkey anti-rabbit (Dianova, 711-605-152,

1:200), ZO1 (ThermoFisher Scientific, #33-9100, 1:1200), SLC34A2 (Abcam, ab122431, 1:100).

3.4.19 Imaging

Imaging is performed using an Opera Phenix Plus High-Content Screening System (Perkin Elmer, Waltham, MA, USA) with a 10x or 20x water objective and the 405, 488, 568, 647 nm laser. Z-stacks of 100 µm thickness were recorded for each sample.

3.4.20 2D trans-well cell experiments

Cells were seeded with a density of a total 3.0×10^5 cells in a 1:1 ratio of PDGFRβ^+:CD31$^+$ on the bottom compartment of a Corning transwell system (Corning® Transwell® 6 well plates, CLS3450-24EA). 1.5×10^5 CD10$^+$ cells were seeded on the transwell. After one day, 75 % confluency was reached, and cells were exposed to 10 ng/mL TGFβ (100-21-10UG, Peprotech) in their respective culture media for a total of 48 hours, with a refreshing of the TGFβ after 24 hours. Cells were harvested for RNA isolation after an additional 48 h of incubation after TGFβ exposure.

3.4.21 Quantitative real time polymerase chain reaction (qPCR)

Samples were washed with PBS, followed by RNA extraction according to manufacturer's instructions using the InvitrogenTM PureLink TM RNA Mini-Kit (Invitrogen 12183025, 13355364). The hydrogels were disintegrated gently by pipetting using a 1000 µL pipette tip in 300 µL lysis buffer + 1:100 β-mercaptoethanol. RNA was stored at -80°C until further processing. RNA was reverse transcribed using the iScript cDNA Synthesis Kit (BioRad, 1708891BUN) using 200 ng total RNA as input. qRT-PCR was carried out with SYBR Green Mastermix in the Bio-Rad CFX96 Real Time System with C1000 Touch Thermal Cycler. The run started with 95 °C for 3 min, then 40 cycles of 95 °C for 15 s and 60 °C for 1 min, followed by 1 cycle of 95 °C for 10 s. Samples were kept on 4 °C until further processing. GADPH was used as

housekeeping gene, and data was analyzed using the ΔΔCT method. Primers used:

Tab. 3.3: Primer Sequences

Primer	**FW**	**RV**
GAPDH	AAGTGTGTGATGGGCTTCCC	GGCAAATTCAACGGCACAGT
Collagen type 1 alpha 1 chain	TGACTGGAAGAGCGGAGAGT	GTTCGGGCTGATGTA

3.4.22 Cultivation of cell lines

Cell lines were generated from the healthy part of human nephrectomies, immortalized and genetically tagged as described in Bouwens et al. (2024). $CD31^+$ cells were maintained in in EGM-2 medium (Lonza, # EBM-2 cc-3154, EGM-2 singleQuots Supplements cc-4176) with added 1 % Pen/Strep. $CD10^+$ cells were cultured in DMEM/F12 (1:1) + Glutamax (Gibco, # 31331) enriched with 10 % FBS and 1 % Pen/Strep. PDGFRβ^+ were cultured in low-glucose DMEM media (Thermo Fisher # 31885) enriched with 5 % FBS and 1 % Pen/Strep.

3.4.23 Protein quantification

For the hydrogel tripe co-cultures, images were taken in 10x and 20x using Opera Phenix Plus High-Content Screening System (Perkin Elmer, Waltham, MA, USA). Z-stacks of 100 µm thickness were recorded for each sample. Using the Qupath Pixel classifier[253] , we determined a threshold in our control samples above which a pixel is positive, and below which a pixel is negative for the marker. Equal areas between conditions were classified based on this threshold, and values were expressed as Positive Area in % of Collagen.

3.4.24 Statistical analysis

Data points are means ± standard errors. Statistical significance was determined by one-way ANOVA with Tukey's multiple comparison test (*p < 0.5; **p < 0.01; ***p <

0.001; ****p < 0.0001) using GraphPad Prism v10 (GraphPad Software, Boston, MA, USA).

4 Development of high-throughput production of degradable rod microgels

4.1 Introduction

Tissue engineering requires biomaterial systems that replicate the structural and functional complexity of native tissues. Hydrogels, widely studied for this purpose, offer ECM-like environments but typically suffer from isotropic nanometer-scale networks that limit cell migration and proliferation.[17,254,255] Granular hydrogels, assembled from micrometer-sized building blocks such as microgels, overcome this limitation by introducing microporosity and injectability, which enhance nutrient diffusion and cell-cell interactions.[30,256] Among granular hydrogel designs, rod-shaped microgels have emerged as particularly promising. Compared to their spherical counterparts, rod-shaped microgels create larger and more interconnected pores, allow scaffold anisotropy, and can even form stable injectable constructs through physical jamming without chemical cross-linking.[28,29,35,66,69,257,258] These features make them attractive candidates for engineering of structured tissues such as muscle, cardiac tissue, or the spinal cord.[68,259,260] Yet, their broader application is constrained by the challenge of producing rod-shaped microgels at a larger scale. Current fabrication strategies often rely on microfluidic or template-based techniques, which are limited in throughput and unsuitable for generating the quantities needed for clinically relevant constructs. To fully realize the potential of rod-shaped microgels in tissue engineering, it is therefore essential to develop time efficient, reproducible, and scalable manufacturing approaches.

Biocompatible anisometric microgels can be generated through batch-based or

continuous fabrication methods, as described in Chapter 2. While these approaches allow for the production of particles with well-defined geometries across broad size ranges, they typically suffer from low throughput and discontinuous processing, limiting their suitability for applications that demand large material quantities. Compared to that, continuous production methods such as droplet-based microfluidics present more advantages. Conventionally, rod-shaped microgels are fabricated inside microfluidic devices through droplet elongation under confinement in combination with rapid and controlled cross-linking triggered by stimuli such as light, temperature, or pH shifts.[28,69,121,198,261,262] In such systems, the microgel length can be adjusted by the flow rate ratio of the dispersed (Q_{disp}) and continuous (Q_{cont}) phases, whereas the droplet width is dictated by the dimensions of the microchannel. One method that enables the production of rod microgels with a diameter smaller than the channel dimensions is called CJP.[122]

The difficulties that arise when upscaling the production of rod microgels are introduced in Chapter 1.4.

Despite advances in the parallelization of microfluidic platforms, only limited efforts have been directed toward adaptation of these strategies for the fabrication of anisometric microgels. A recent study presented the first attempt to parallelize FF droplet generators for the creation of rod-shaped microgels, employing a silicon-based microfluidic device.[197] The work demonstrated that rod-shaped microgels could indeed be produced in parallel channels through UV polymerization of a PEGDA pre-polymer solution; however, the maximum total flow rate at which stable rod-shaped gels were obtained remained below 800 µL/h. Moreover, silicon-based microfluidic devices are costlier than their PDMS counterparts, and their fabrication requires specialized equipment, further limiting accessibility.

To address the low production rates in fabricating rod-shaped microgels, we first discuss the upscaling of base-catalyzed rod-shaped microgels. The idea here is to increase the production rate through the parallelization of FF channels. However, the base-catalyzed rod formation could not be significantly upscaled, though prototypes and suggestions will be discussed in this chapter. We then developed a combinative microfluidic approach to parallelize the fabrication of anisometric microgels, based on a step-emulsification droplet generation. This is the first SE based method capable of realizing the production of aspherical rod-shaped particles, including the parallelized generation of spherical droplets using SE, subsequently distributing the

droplets and confining them into parallelized narrowing microchannels, that can be cross-linked through UV-light on-chip. Together with my colleague Matthias Mork, we then compared two different UV-triggered cross-linking mechanisms: FRP and step-growth polymerization. Using two-photon polymerization (2PP) direct laser writing, a combinative master structure was fabricated, enabling the production of PDMS microfluidic devices, featuring distinct height profiles and angled height transitions. The parallelization of individual microchannels distributes the overall flow velocity over multiple channels, extending the residence time on-chip, while simultaneously distributing the pressure. Hence, higher production rates can be achieved for fabricating biocompatible rod-shaped microgels in a relevant size range for tissue engineering applications.[28,122,198] Rod-shaped microgels were generated at polymer precursor flow rates up to 3 mL/h, employing various polymer compositions and photo-polymerization strategies. In particular, by applying FRP with PEGDA 700 as well as light-mediated thiol-ene click chemistry, using a mixture of star PEG-norbornene (sPEG-Nb) and star-PEG-ester-thiol (sPEG-ester-SH), we examined how the chosen cross-linking mechanism affected the microgel production settings and the resulting mechanical properties. Together, this chapter addresses the need to advance methodologies to increase the production of anisometric microgels for applications involving studies with greater material demand, as previously discussed.[69]

4.2 Results and Discussion

4.2.1 High-throughput microfluidics to produce base-catalyzed Michael-type addition rod microgels

The rod microgels introduced in Chapter 3 are produced through plug-flow microfluidics employing a single channel in the FF squeezing regime. Here, two pre-polymer solutions consisting of star PEG-ester-SH and PEG-VS are mixed on-chip and cross-linked through the addition of a base - TEMED - catalyzing the reaction by Michael-type addition.[198] However, because of the cross-linking mechanism the flow rates are low, 30 µL/h for the pre-polymer phases individually, reducing the throughput. As a first attempt to upscale the rod production we opted for a combination of two microfluidic chip designs. The first device would

generate spherical droplets, that are not yet cross-linked (based on[198]) feeding into a microfluidic device, featuring a base inlet to catalyze the reaction and parallelized FF channels to increase the throughput of the production. The parallelized channels were equipped with serpentines to increase the residence time on-chip. The design can be found in Figure 4.1, comprising four FF channels with dimensions of 50 x 50 cm^2. However, the spherical droplets merged upon reaching the outlet of the first microfluidic device, making a transfer into the second chip design difficult. No stable flow could be established. The merging of the spheres is most likely due to the continuous oil phase consisting of hexadecane:paraffin oil (1:1) and 2 % (w/v) ABIL EN 90, which was also used in Chapter 3.

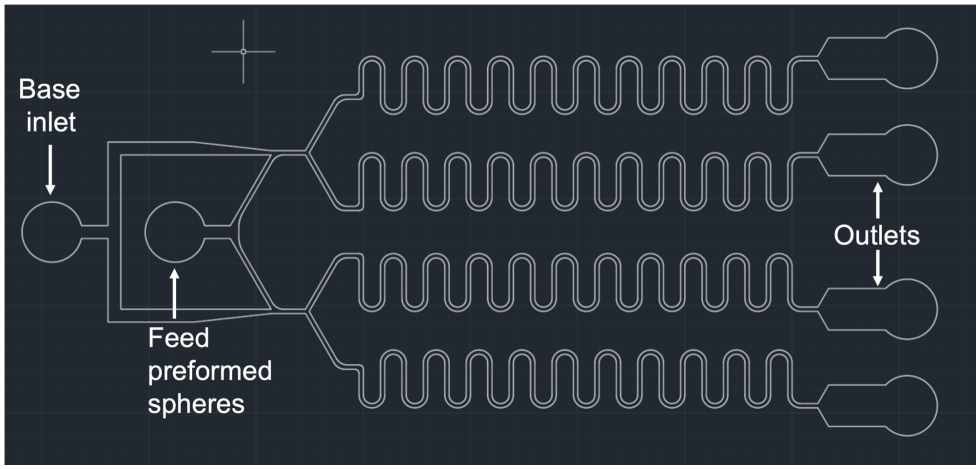

Fig. 4.1: High-throughput chip design to produce base-catalyzed rod microgels. The spheres were first prepared in another chip design[198] and then fed into microfluidic design shown here. The solution consisted of 15 % (w/v) of PEG in total, using 2-arm PEG-ester SH 1.7 kDa and 8-arm PEG-VS 20 kDa. To catalyze the reaction the base inlet comprised the oil phase with hexadecane:paraffin oil (1:1) and 2 % (w/v) ABIL EN 90 together with 4.5 % (v/v) TEMED.

In obtain stable spherical droplets at the outlet of the first microfluidic device, Novec 7500 with 1.5 % (v/v) KrytoxTM 157 FSH was now used as a continuous phase, as it exhibits a lower viscosity and thus increases the surface tension of the oil in combination with the surfactant, increasing the droplet stability.[263,264] The use of Novec 7500 with Krytox has also been shown in previous work to produce stable PEG-based microgels.[265,266] We were able to generate stable spherical droplets that could be transferred into the second chip design. The flow rate of the pre-polymer phase (spherical droplets) and the oil phase were set to 50 µL/h, and the base to 30 µL/h. Even though the flow rates were low, the droplets did not reside enough on-chip to cross-link sufficiently. Figure 4.2 shows the outlet, where the droplets remained spherical.

To reduce the cross-linking time, thus reducing the required residence time on-chip to maintain a rod shape, we used 8-arm PEG-ester-SH 20 kDa, instead of the linear counterpart. We set the total PEG concentration to 5 %, based on our findings in Chapter 3 and also reduced the base concentration to 1 % (v/v). The continuous phase remained the same as described above. We transferred the generated spherical droplets into the high-throughput chip, where we could observe a quick reaction at low flow rates (30 µL/h for the pre-polymer droplets, and 50 µL/h for the oil phase). Such low flow rates resulted in clogging of the channel, which was no longer observed at higher flow rates (continuous: 180-200 µL/h, base: 140-150 µL/h). We were able to produce rod microgel, not yet in a stable manner and still at a very low throughput (Figure 4.3).

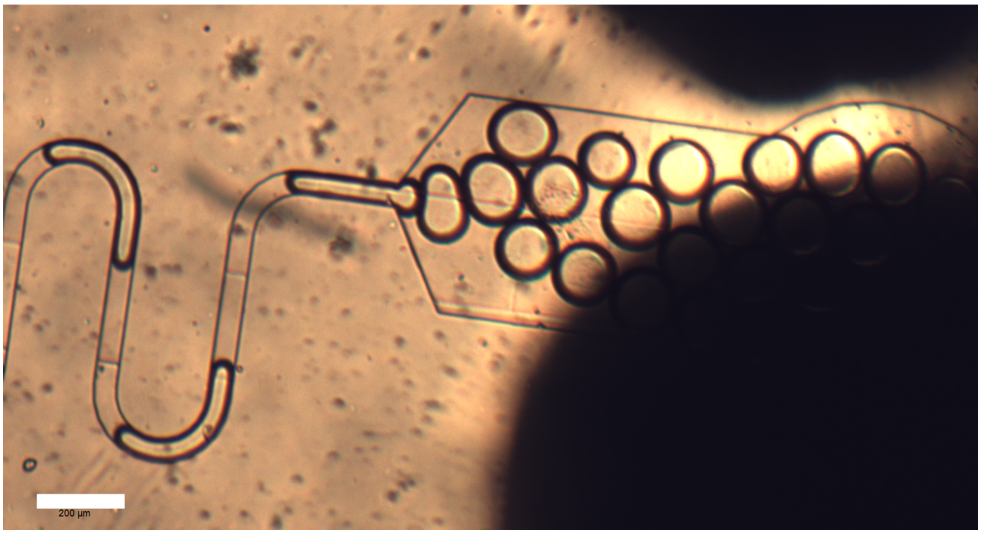

Fig. 4.2: Outlet of first high-throughput microfluidic design for base-catalyzed rods with 2-arm PEG-ester-SH. Here, Novec 7500 with 1.5 % (v/v) KrytoxTM 157 FSH as a continuous phase and 15 % PEG concentration in total with 2-arm PEG-ester-SH 1.7 kDa and 8-armPEG-VS 20 kDa and 4.5 % (v/v) TEMED as base. The outlet shows spherical droplets meaning that the residence time on-chip was too short to initiate enough cross-linking to keep the rod shape. Scale bar = 200 µm.

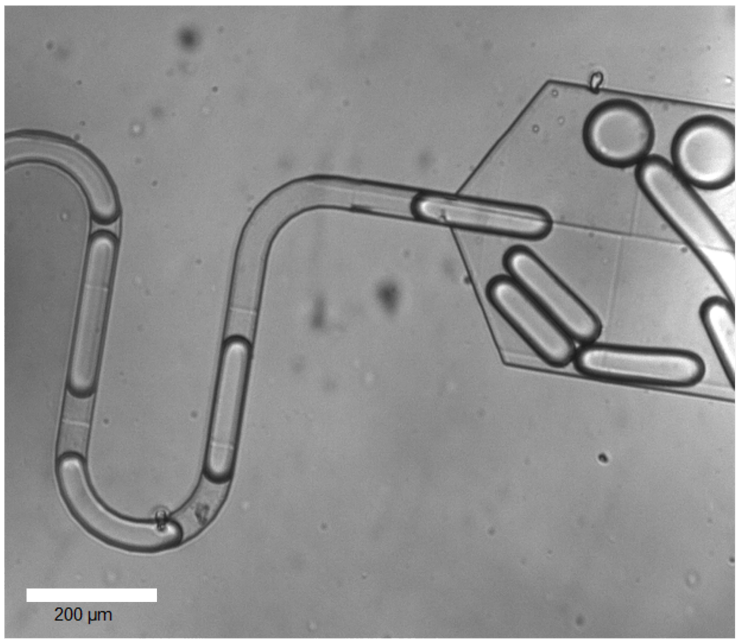

Fig. 4.3: Outlet of first high-throughput microfluidic design for base-catalyzed rods with 8-arm PEG-ester-SH. Here, Novec 7500 with 1.5 % (v/v) KrytoxTM 157 FSH as a continuous phase and 5 % PEG concentration in total with 8-arm PEG-ester-SH 20 kDa and 8-armPEG-VS 20 kDa and 1 % (v/v) TEMED as base. Scale bar = 200 µm.

Based on the findings described above, we designed a new microfluidic device that combines SE with FF on-chip, while introducing a base inlet and serpentines for prolonged reaction time (Figure 4.4).

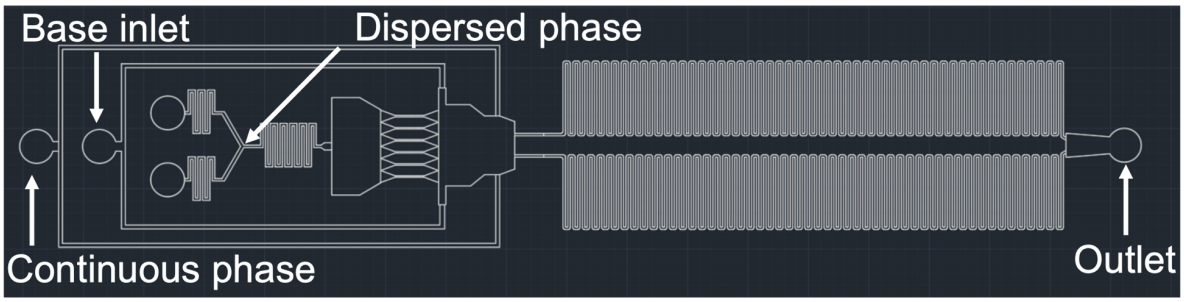

Fig. 4.4: High-throughput microfluidic device design to produce base-catalyzed Michael-type addition degradable rod microgels. The design is equipped with a SE section to first generate spheres with a subsequent addition of the base to initiate the reaction and parallelized FF channels to squeeze the spheres into rod microgels.

The idea was to first generate spheres through SE based on previous research and to combine it with a second step on-chip where the spheres are squeezed into rod-shaped droplets and subsequently cross-linked by adding the base (Figure 4.4).[131]

The channel design comprises first six nozzles for the SE part and is subsequently equipped with two FF channels with dimensions of 50 x 50 cm^2. We tested the same pre-polymer compositions as described above keeping the total PEG concentration at 5 % (w/v) and used the same oil and base phase. One requirement is good mixing of the two pre-polymer phases. Therefore, we introduced a mixer right after the dispersed phases meet (Figure 4.4). However, the design complexity was too high to achieve stable production at significantly higher flow rates.

4.2.2 High-throughput microfluidics to produce light-mediated rod microgels

The throughput of a microfluidic device depends on the configuration but also on the chemistry used. Therefore, in Chapter 4, we investigated an alternative approach based on light-mediated click-chemistry. This strategy simplified the microfluidic device design, since the cross-linking could triggered by UV irradiation, while still preserving the degradability of the rod microgels. Together with my colleague Mattias Mork, we evaluated the differences in FRP and radical mediated thiol-ene click chemistry. In collaboration, we optimized the polymer and continuous phase as well as the production parameters and assessed the materials' properties in parallel.

Development of microfluidic chip design

To generate rod microgels within an array of parallel microchannels, we produced microfluidic masters using 2PP direct laser writing. Compared to photolithographic methods, 3D microfabrication of master structures enables the seamless integration of complex height variations. Within the context of this work, such height features are essential not only for the droplet production via SE, but also for the droplet confinement. Accordingly, the main objective in the development of the microfluidic master was to establish an appropriate structural design, to produce droplets via SE and subsequently elongate them in an array of parallelized microchannels. In this regard, we fabricated an optimized microfluidic design displayed in Figure 4.5.

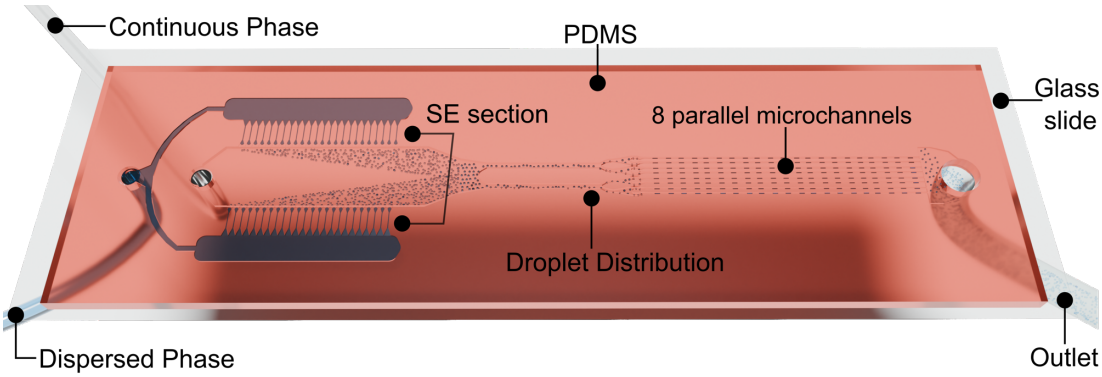

Fig. 4.5: Optimized high-throughput microfluidic chip design to generate rod microgels. Schematic of the microfluidic PDMS device, highlighting the different sections. For light-mediated cross-linking a UV diode (365 nm) is place on top of the parallelized channels close to the outlet.

In the refined microfluidic channel design, the dispersed phase is delivered into the oil reservoir from opposite directions via the nozzle channels, as displayed in Figure 4.5. This channel layout, adapted from earlier reported SE designs, enables an increase in the number of nozzle channels without requiring substantial broadening of the main channel, which could otherwise interfere with the droplet formation and distribution.[267] In total, the SE section featured 48 nozzle channels. The main channel was progressively divided three times, to distribute the spherical droplets into eight parallel microchannels with a cross-section area of 50 x 50 µm². More details about the design development, as well as droplet sizes and flow behavior can be found in Matthias Mork dissertation or in our joined publication.

Production of non-degradable rod microgels

To produce rod microgels, the microfluidic device was operated with a pre-polymer solution containing a photo-initiator, allowing precursor droplets to be cross-linked while still in their shape. Based on the FRP approach (Figure 4.6a), we fabricated microgel-rods with 30 % (w/w) PEGDA 700 Da at different total flow rates. After purification, the microgels featured comparable widths of approximately 50 ± 1.6 µm, while the lengths varied depending on the total flow rates (from 278.07 ± 31.25 µm or 427.54 ± 50.39 µm with a total flow rate of 3 or 6 ml/h, respectively) with Figure 4.6b showing a length of 278.07 ± 31.25 µm at a total flow rate of 3 ml/h. We further characterized the microgels by analyzing their swelling behavior (Figure 4.6c) and the mechanical properties of the microgels via nanoindentation (Figure 4.6d). As can

be seen, the microgels collapse to about half of their swollen diameter. We tested different combinations of the total applied flow rate (Q_{total}) and the set UV intensity, to characterize the stiffness tunability. The lowest obtained stiffness was 7.72 ± 2.40 kPa at an intensity of 260 mW/cm^2 at Q_{total} = 5 mL/h, representing the lowest analyzed UV dose. Consequently, the highest stiffness with 17.10 ± 6.92 kPa was obtained at Q_{total} = 3 mL/h and 442 mW/cm^2, representing the highest investigated UV dose. Overall, the mechanical data demonstrated with clear tendencies that the stiffness of the microgels can be tuned to a certain degree by either changing the UV intensity or the total flow rates. In turn, these results support that comparable mechanical properties can be achieved by adjusting the system to similar UV doses, independent of the applied flow rates. We also looked at the surface morphology of the obtained rod microgels after purification through scanning electron microscopy (Figure 4.6e). The images show a smooth surface, and upon closer examination (Figure 4.6e iii)) there is no roughness or open structure visible. This is likely due to the high polymer concentration.

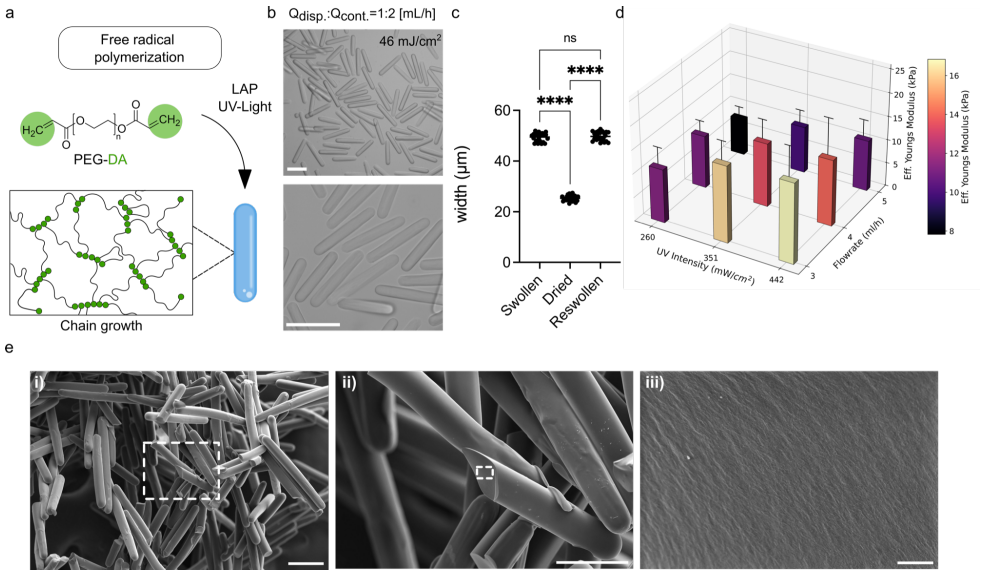

Fig. 4.6: Photo-cross-linking elongated PEGDA droplets into rod-shaped microgels in our parallelized microfluidic device. a) Chemical structure of PEGDA undergoing a free radical polymerization during photo-cross-linking, initiated by Lithium-Phenyl-2,4,6-trimethylbenzoyl phosphinate (LAP) photo-initiator, resulting in a chain growth polymer network. b) Representative brightfield images of produced PEGDA rod microgels after purification. Scale bars = 200 µm. c) Swelling behavior of rod microgels produced at a total flow rate of 3 ml/h and 351 mW/cm^2. d) Mechanical properties of rod-shaped microgels, obtained via nanoindentation at different total flow rates and UV doses. e) SEM images of rod microgels produced at 351 mW/cm^2 and a total flow rate of 3 ml/h. The square displays the magnified area on the images from left to right. Scale bar = 100 µm (i), 50 µm (ii), 1 µm (i).

Production of degradable rod microgels

To further increase the total flow rate, thereby enhancing the overall production rate and the flexibility of the microfluidic device, we also opted for an alternative cross-linking chemistry. FRP is known to be sensitive to oxygen inhibition, making it challenging to increase the production rate without increasing the polymer or initiator concentration. Oxygen acts as a radical scavenger in FRP to form peroxy radicals exhibiting a lower reactivity that results in less chain growth. However, in tissue engineering applications, reducing the polymeric material or the amount of free radicals is favorable. Light-mediated thiol-ene click chemistry using norbornene thiol is well known in the literature due to its reactivity and tunability.[138] This type of cross-linking follows a step-growth mechanism that is less affected by oxygen inhibition. The reason for that is the easy abstractability of the thiol hydrogen.[138,144] Furthermore, step-growth mechanisms offer greater control over the network formation and typically present more homogeneous networks compared to FRP. Microgels have been produced in single-channel devices using polymers including HA and PEG.[268,269] As reactants, we used 8 arm star PEG-ester-thiol (sPEG-SH) 20 kDa and 8 arm sPEG-norbornene (sPEG-Nb) 20 kDa, keeping the amount of initiator the same at 1 % (w/w) (Figure 4.7a). Introducing an ester moiety to the network enables the degradation of the rod microgels hydrolytically, further increasing the functionality.[270] Additionally, norbornenes are electron-rich olefins providing fast reaction kinetics, furthermore supported by the ring strain of the structure.[138,145,146] We first screened the reactivity of our material, analyzing bulk hydrogels using rotational rheology (Figure 4.7b). The total PEG concentration was set to 3 and 5 % (w/v), where we cannot observe a significant difference in gelation time (60 s). We compared the thiol-ene bulk hydrogels to PEGDA hydrogels consisting of 5, 15, 30 and 40 % (w/w) (Figure 4.7b). During microfluidics, concentrations below 30 % (w/w) PEGDA did not result in stable rod production for all probed UV intensity and flow rate combinations, and concentrations below 5 % (w/w) did not form any microgels using the high-throughput setup. This is supported by the rheological data, where the gelation time remains constant (60 s) for all samples except for 5 % (w/w), where an increase to 73 s can be observed. Furthermore, the thiol-ene samples show storage moduli (G') for 3 and 5 % (w/v) of 4.00 $\pm$ 0.038 kPa and 12.90 $\pm$ 0.40 kPa, respectively. These values are in a similar range as 15 and 30 % (w/w) of PEGDA samples of 7.20 $\pm$ 0.40 kPa and 18.30 $\pm$ 1.90 kPa, although the thiol-ene samples comprise much lower polymer concentrations. This is most likely

due to the effect of chain length and polymer architecture on cross-linking kinetics and density, which will in turn also affect microfluidic rod production.[121,147]

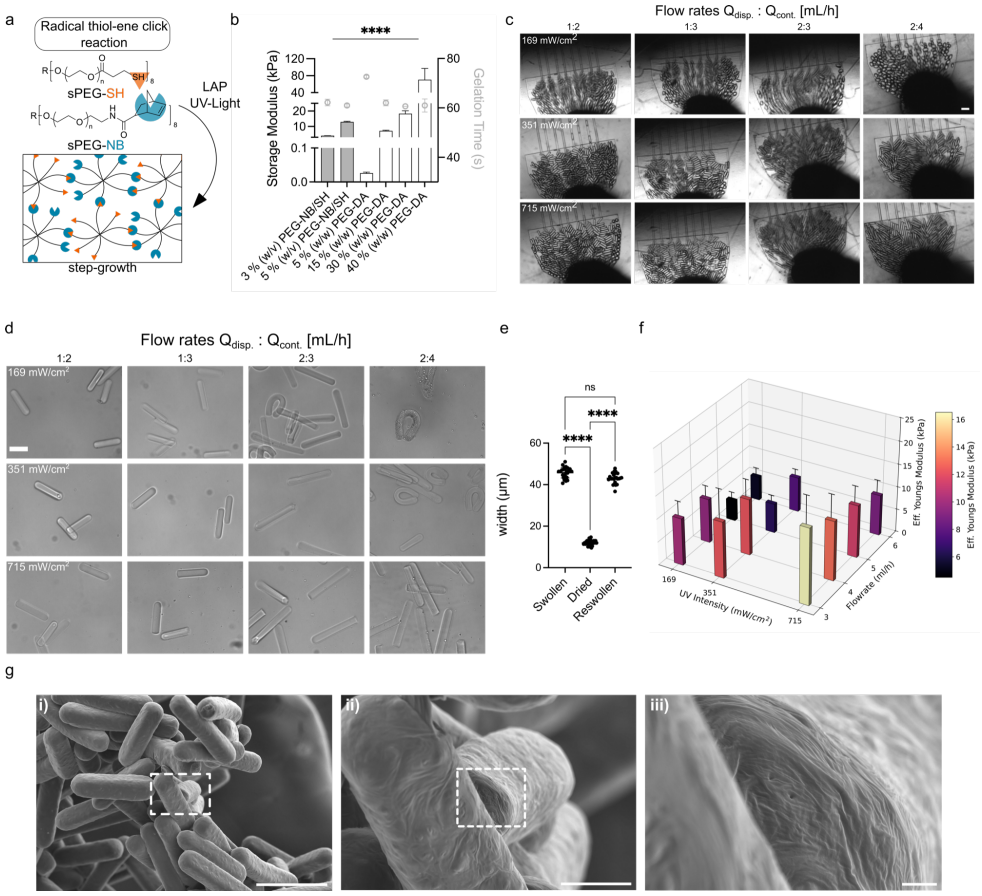

Fig. 4.7: Photo-cross-linking elongated PEG-Nb and PEG-ester-SH droplets into rod-shaped microgels in our parallelized microfluidic device. a) Chemical structure of PEG-Nb and PEG-ester-SH undergoing light-mediated thiol-ene click cross-linking, initiated by LAP photo-initiator, resulting in a step growth polymer network. b) Characterization of bulk hydrogels using rotational rheology to assess the storage modulus (G') (left y-axis) and gelation time (right y-axis) of different total PEG concentrations comparing sPEG-Nb/SH vs PEGDA. Statistical significance was determined by one-way ANOVA with Tukey's multiple comparison test (*p < 0.5; **p < 0.01; ***p < 0.001; ****p < 0.0001) c) Microscope images showing the droplet morphology upon subjecting them to the respective UV dose. The dispersed phase consisted of 5 % (w/v) of total PEG (stoichiometric addition of functional groups). The scale bar = 200 µm and is representative for all images in this series. d) Microscope images of the purified rods dispersed in water with their respective production parameters. Scale bar = 100 µm. e) Swelling behavior of rod microgels produced at a total flow rate of 3 ml/h and 351 mW/cm^2. f) Mechanical properties of rod-shaped microgels, obtained via nanoindentation at different total flow rates and UV doses. g) SEM images of rod microgels produced at 351 mW/cm^2 and a total flow rate of 3 ml/h. The square displays the magnified area on the images from left to right. Scale bar = 50 µm (i), 10 µm (ii), 1 µm (i).

We then set the polymer concentration to 5 % (w/v) to produce microgel rods using PEG-norbornene and PEG-ester-SH in the same microfluidic design as described

above. We opted for 5 % (w/v) instead of 3 % (w/v) to not performing microfluidics at the lower cross-linking limit. The oil phase was now adapted to 0.5 % (w/v) Fluorosurf C in Novec, and we probed four different flow rates alongside four different UV intensities (Figure 4.7c) to produce rod microgels (Figure 4.7d). Similar to the microgels obtained using PEGDA, the microgels collapse to about half of their initial swollen width (Figure 4.7e). Furthermore, the stiffness increases with increasing UV intensity. The lowest Eff. Young's modulus with 4.50 $\pm$ 1.60 kPa was obtained at an intensity and flow rate of 169 mW/cm^2 and 5 ml/h, while the highest modulus of 16.50 $\pm$ 6.30 kPa was observed at 715 mW/cm^2 and 3 ml/h. Tuning the flow rate resulted in a decrease in Young's modulus for higher flow rates at constant UV dose (Figure 4.7f). Compared to PEGDA, the lowest UV intensity to obtain stable rod microgels was at 169 mW/cm^2 when using a flow rate of 3 ml/h. This minimum intensity shifted with higher flow rates, as is shown in the brightfield images of the produced rod microgels (Figure 4.7d). At higher flow rates, such as 5 and 6 ml/h, some rods have a bend shape, due to the lower UV dose at these high flow rates. This is in line with the low recorded Young's moduli. To obtain straight rods, 351 mW/cm^2 at 5 ml/h and 715 mW/cm^2 at 6 ml/h would be required to obtain straight rods. We then, similar to the PEGDA rods, looked at the surface morphology of the sPEG-Nb rods using SEM (Figure 4.7g). Interestingly, the sPEG-Nb rods exhibit a very different surface roughness than the PEGDA rods. Looking at higher magnifications even exposes small open network structures (Figure 4.7g iii)). This difference is most likely due to the much lower polymer concentration and the different reaction mechanism. These findings support our chip design to enable to production of versatile rod microgels with different functionalities and properties in a high-throughput manner, making it highly interesting for tissue engineering applications.

4.3 Conclusion

This chapter focused on the upscaling of degradable rod microgels. Different chemistries were employed, analyzing the feasibility to produce rod microgels at significantly higher flow rates than single-channel plug flow microfluidics. We first considered base-catalyzed rod microgels and probed different microfluidics setups and designs to increase the production rate. However, because of the required prolonged residence time on-chip we were only able to design prototypes. Here, the maximum flow rates remained below 1 ml/h for the pre-polymer phase. In the

future, other microfluidic devices, such as 3D microfluidic designs might enable the upscaling of base-catalyzed rod microgels.[271] That way the base containing phase could be introduced from the top, which would make it easier to parallelize the channels. Furthermore, this chapter introduces, a SE-based microfluidic approach to parallelize the fabrication of rod-shaped microgels. We highlighted the potential and flexibility of this device by using two different cross-linking chemistries, enhancing the functionality of the obtained rod microgels and the production rate. In this approach, we were able to increase the production rate up to 3 ml/h of the pre-polymer phase using light mediated chemistries. Furthermore, we postulate that our presented microfluidic device provides a scalable platform that allows for further increasing the microgel rod production rate by altering the microfluidic chip design and parallelizing a larger number of microchannels than presented in this work. This especially highlights the relevance of this technique for studies with larger material demands, including the use in automated liquid handling systems or 3D bio printing, making rod-shaped microgels more accessible for tissue engineering applications.

4.4 Materials and Methods

4.4.1 Chemicals

Quinoline yellow (Sigma Aldrich, 95 %), oil red o (Sigma Aldrich), toluene (Alfa Aesar, 99.7 %), lithium phenyl-2,4,6-trimethylbenzoylphosphinate (LAP, Sigma Aldrich, #95 %), poly(ethylene glycol) diacrylate average Mn 700 (PEG-DA, Sigma Aldrich), Sylgard® 184 silicone elastomer kit (The Dow Chemical Company), 3M Novec™ HFE 7500 (Ionic liquids Technologies, > 99 %), Krytox™ 157 FSH (DuPont), n-hexane (Fisher Scientific, ≥99 %), Span 80 (Sigma Aldrich), propan-2-ol (IPA, Fisher Chemical, ≥99.8 %), trichloro-(1H,1H,2H,2H-perfluorooctyl)-silane (Sigma Aldrich, 97 %), L-ascorbic acid (Sigma Aldrich, 99 %), propylene glycol monomethyl ether acetate (PGMEA, Sigma Aldrich, ≥ 99.5%), 8 arm poly (ethylene glycol) norbornene Mn 20 kDa (>95%, CreativePegworks) were used as received. MilliQ water was used for the preparation and purification of the microgels.

4.4.2 Microfluidic master mold fabrication

The same procedure was applied for the fabrication of all different microfluidic master structures presented in this work. In short, a negative 3D structure of the microfluidic channel geometry was designed in AutoCAD 2024, processed in DeScribe 2.7, and was fabricated using two-photon direct laser writing (Nanoscribe GmbH, Photonic Professional GT). As previously described,[272] an acryl-silanized glass coverslip (LABSOLUTE® Th. Geyer 76 x 50 x 1 mm) was covered with a photoresist (Nanoscribe, IP-S) and mounted in the 3D printer. A 25x objective was mounted in the printer and the structure was fabricated with a blocksize of X: 200, Y: 200, Z: 160 µm at 15° shear. After printing completion, the master structure was submerged in propylene glycol methyl ether acetate (PGMEA) for 10 min to remove uncured polymer resin, followed by washing with isopropanol solution for 3 min. The substrate was dried under nitrogen flow and post-cured for 4 h using UV light (200 mW, λ=365 nm). The cured structure was fluoro-silanized with trichloro-(1H,1H,2H,2H-perfluorooctyl)-silane (50 µL per glass coverslip) in a desiccator under high vacuum overnight.

4.4.3 Microfluidic chip fabrication

The microfluidic chips were fabricated as previously described,[28] with minor variations. In short, PDMS base and curing agent (10:1 w/w) were mixed with a dye solution (100:1 w/w). The dye solution was prepared by mixing oil red O (60 mg, 3.00% w/w) and quinoline yellow (3 mg, 0.15% w/w) followed by dissolving in toluene (2 g). The PDMS mixture was cast on the master structure, degassed, and cured at 60 °C for 12 h. The PDMS replica was cut from the master mold and inlet and outlet holes were punched (inlet: 0.75 mm, outlet: 1.2 mm biopsy puncher, Electron Microscopy Science). The PDMS slab and a glass slide (Marienfeld 75 x 50 x 0.13 mm) were washed sequentially with isopropanol and deionized water, followed by drying under nitrogen flow. Plasma treatment was performed in a PVA TePla 100 Plasma System (28 mL/min O2, 100 W, 40 s). The microfluidic chip was stored at 60 °C for 12 h to complete the bonding. The device was rendered hydrophobic by chemical vapor deposition (CVD) with trichloro-(1H,1H,2H,2H-perfluorooctyl)-silane (50 µL per chip) in a vacuum desiccator overnight. Afterwards, the outside of the chip was rinsed with Novec™ 7500 and wiped using lint-free tissues.

4.4.4 Synthesis of m-arm poly (ethylene glycol) ester thiol

8-arm PEG-ester-SH was prepared by Fischer esterification of the respective PEG-(OH)m according to the literature.[251]Briefly, in a 250 mL two-neck round bottom equipped with a Dean-Stark -PEG-(OH)m (20000 Da sPEG-OH 8 arm) (1 eq., 1.00 g) was dissolved together with 3-mercaptopropionic acid (40 eq.) and p-toluenesulfonic acid (p-TsOH) (0.1 eq.) in 70 mL cyclohexane. The reaction was refluxed at 130 °C for 24 h, and at least two volumes of Dean-Stark were removed. Afterwards, the reaction mixture was cooled down to r.t. and the cyclohexane was separated from the product via decantation. The remaining white wax was dissolved in dichloromethane (DCM) (50 mL) and washed with saturated $NaHCO_3$ (2 x 15 mL), brine (1 x 15 mL) and dried over $MgSO_4$. The solid is removed by filtration and the solution is concentrated until a viscous oil is obtained. The resulting oil is dissolved again in minimal amount of DCM (2-3 mL) and precipitated by dropwise addition in excess cold (-20 ◦C) diethyl ether (40x vol DCM) and the final product is isolated as a white powder (isolated yield 70%). 1H NMR (CDCl3, 400 MHz): δ (ppm)= 4.26 (4H, m, –CH2CH2OC(O)–), 3.64 (133H, br), (CH2CH2O)n), 2.77 (4H, m, –CH2CH2SH), 2.68 (4H, m, –CH2CH2SH),

1.68 (2H, t, SH).

4.4.5 Microgel production

Rod-shaped microgels were prepared from aqueous solutions composed of PEGDA (15 or 30% w/w) or PEG-norbornene/vinylsulfone/-ester-SH (5% w/v). LAP (1% w/w) was used as photoinitiator. In the case of base-catalyzed production, the used oil was supplemented with the TEMED in a range of 1-5% (v/v). The solutions were stored in brown glass vials until use, to protect from undesired light exposure. The continuous oil phase was composed of Novec™ HFE 7500 with Krytox™ 157 FSH surfactant (4.5 % v/v) or 0.5 % (w/v) FluoSurf™C. The pre-polymer and oil solutions were transferred into a syringe (Hamilton Gastight® Series 1000, 5 mL) and the syringe containing the dispersed phase was wrapped in aluminum foil. In the case of PEG-Norbornene and PEG-ester-SH, both precursors were combined in one syringe. A 25G cannula was inserted into tubing (PTFE, OD 0.9 mm, ID 0.4 mm, TECHLAB GmbH) and attached to the syringes. Residual air was removed and the syringes were fixed in a syringe pump (Harvard Apparatus Pump 11 Elite). The other ends of the tubes, as well as an outlet tube (PE, OD 0.048 in ,ID 0.03 in, Instech Laboratories) were inserted into the dedicated holes on the microfluidic device. The microfluidic chip was positioned on a custom made microfluidic chip holder with the glass side facing upwards. Microfluidic production was initiated by starting the flow of the continuous phase to prefill the collection reservoir. Afterwards, the dispersed phase was started until droplet formation was visible. The flow rates were adjusted as indicated. The microfluidic channel was covered with a UV resistant photomask, creating a rectangular irradiation field. The UV diode was positioned on top of the irradiation field and operated at different UV intensities, as indicated. To prevent unwanted radicals during the collection of the rod microgels, L-ascorbic acid was added in excess to ethanol as a collection media. Purification of the microgels was achieved by multiple subsequent washing steps, as previously reported.[273] In short, the excess continuous phase was pipetted off and the microgels were sequentially washed with Novec™ HFE 7500, n-hexane + span 80 (1 % v/v), n-hexane, isopropanol, and water. Each solvent was applied five times before proceeding to the next solvent.

4.4.6 Rheological measurements of bulk hydrogels

Rheological characterization was carried out using a Discovery HR-3 hybrid rheometer (TA Instruments, New Castle, DE, USA) with 20-mm parallel plate geometry. We transferred 381 µL of the pre-polymer solution to the rheometer at 25 °C followed by the time-dependent measurement of polymerization under 10 mW/cm^2 UV light with a frequency of 1 Hz and an oscillation strain of 1 %. We also took frequency-dependent measurements at a set oscillation strain of 1 % and strain-dependent measurements at a set frequency of 1 Hz. Each material was measured as triplicate samples.

4.4.7 Swelling behavior

The purified microgels were analysed in their swollen state first and then in their collapsed state through the addition of isopropanol by measuring the their width. We subsequently added water to reswell and measured again. In total, 25 microgels were measured.

4.4.8 Nanoindentation

Before nanoindentation, the rod microgels were immobalized on a cell culture well plate using a poly-L-lysine solution (0. 01 % (w/v), Sigma-Aldrich). The well surface was covered with a thin film of the solution and left overnight to evaporate. The microgels were subsequently pipetted on the surface of the well plate and left for sedimentation. The mechanical properties of the rod microgels were assessed using a Pavone Nanoindenter (Optics11Life, Amsterdam, Netherlands). The Nanoindenter was equipped with a cantilever probe comprising a spherical tip radius of 3 µm and a cantilever stiffness of 0.510 N/m. For each sample at least three microgels were indented. The piezo speed was set to 30 µm/s and the indentation depth to 300 nm. All measurements were conducted at r.t. and in water. The effective Young's modulus E_{eff} (Pa) was determined from the obtained load-indentation curves employing the Hertz contact model. The data analysis was carried out using the Software Dataviewer V2.5 (Optics11Life).

4.4.9 Scanning electron miscroscopy

Samples were fixed in 3 % glutaraldehyde (Agar Scientific, Wetzlar, Germany) for at least 1 h at room temperature and stored at +4 °C. They were then washed for 15 min with 0.1 M Sørensen's phosphate buffer (0.2 M, pH 7.39; Merck, Darmstadt, Germany). Dehydration was carried out in a graded ethanol series: 10 min each in 30 %, 50 %, 70 %, and 90 % ethanol, followed by three 10 min steps in 100 % ethanol. The samples were subsequently subjected to critical point drying using liquid CO_2 in a Critical Point Dryer (Polaron, Quorum Technologies Ltd, Ashford, Kent, UK). Dried specimens were sputter-coated with a 10 nm layer of gold–palladium using a Sputter Coater EM SCD500 (Leica, Wetzlar, Germany) and examined in a scanning electron microscope (Quattro S Environmental SEM, Thermo Fisher Scientific, Eindhoven, The Netherlands; funded by the German Research Foundation, DFG project no. 495328185) at 10 kV under high vacuum. The measurements were conducted at the Uniklinik electron microscopy departments (Aachen,DE) in collaboration with the DWI-Leibniz Institute for Interactive Materials by Stephan Rütten and Naeem Assasa.

4.4.10 Statistical analysis

Data points are means ± standard errors. Statistical significance was determined by one-way ANOVA with Tukey's multiple comparison test (*$p < 0.5$; **$p < 0.01$; ***$p < 0.001$; ****$p < 0.0001$) using GraphPad Prism v10 (GraphPad Software, Boston, MA, USA),

5 Exploring CJP to produce versatile rod shaped microgels for tissue engineering applications

5.1 Introduction

Injectable biomaterials are sought after as they provide a complex structural architecture in tissue engineering applications comprising a 3D microenvironment. Similar to the native ECM biomaterial constructs are capable of supporting cellular processes including proliferation, adhesion and differentiation, while giving physical and mechanical support to promote tissue growth in hierarchically organized structures.[2,3] Furthermore, injectability makes minimally invasive delivery *in vivo*, the transfer to automated pipetting systems, and bioprinting possible.

Typically, injectable materials are composed of macromolecular liquid precursors undergoing isotropic 3D hydrogel formation. Hydrogels are water-swollen networks that can be adapted with cell signaling or binding sites to support cell growth and proliferation.[20] Due to the isotropic nature, hydrogels do not supply directional cell guidance cues.[31] However, anisotropy has proven to be a key factor for proper tissue function of native tissues, *e.g.* the myocardium, spinal cord, and cartilage.[11,12,274] Structured tissue-regenerative scaffolds can for instance be obtained through the incorporation of magneto-responsive rod microgels. Doing so will make otherwise isotropic 3D hydrogel systems structured scaffolds, as has been shown with the Anisogel system.[35,65] The effect of the dimensions, mechanical and biochemical properties of the rod microgels has been extensively studied.[66,67] The longest aligned neurite extension for primary neurons is observed when using microgel rods with a width = 2.5 µm, while thicker microgels (*e.g.*, 5 µm) impede neurite extension.[67]

Additionally, when probing a range of stiffness of the microgels (E-modulus: 35-950 kPa when varying the PEGDA concentration from 10 to 80 % (w/v)), the neurons were aligned in all conditions.
For all Anisogel studies, the rod microgels were obtained through an in-mold polymerization batch process called PRINT.[66,68,275] Another option is to use stop-flow lithography to generate complex PEGDA microgels comprising maghemites to induce actuation in a rotating magnetic field.[161]

Besides the missing anisotropy for most synthetic 3D hydrogels, the mesh size is in a range of 100 nm, making cell-cell interactions, cell migration and proliferation difficult, unless the hydrogel provides degradable moieties. Though, the latter reduces initial cell-cell interactions upon encapsulation of the cells within the gel.[22,23] Here, MAP scaffolds have gained a lot of importance, as they can result in pores with diameters of up to ∼225 µm when using rod microgels. Such pore sizes are ∼4.5-fold larger than those possible with MAP scaffolds made of spherical counterparts.[28] Larger pores can facilitate cellular processes within 3D scaffolds and support diffusion of oxygen or other important nutrients and factors into the system.

Rod microgels are mostly produced through PRINT or plug-flow microfluidics, as introduced in Chapter 2. However, both production techniques offer a tradeoff between possible microgel dimensions (1 µm diameter in PRINT and 80 µm in the case of plug-flow microfluidics) and the production manner (batch *vs* continuous process).[35,122] To overcome this, our group developed CJP to produce rod microgels that are ten times smaller than the channel diameter in a continuous manner.[122] CJP is based on two immiscible phases intersecting at a four-way junction on a microfluidic device to flow in a jetting regime. The jet contains a pre-polymer solution, in which free radical photo-polymerization is initiated by irradiation with a focused laser beam. When using a modulated laser, parts of the jet will be cross-linked when the light is on, while others will remain liquid and dissolve after collection. Depending on the laser modulation (on-time), the spot size and the flow rate, microgels with different lengths can be obtained in a controlled manner. Thus far, this method has generated high-aspect-ratio microgels with a minimum diameter of 8 µm using a channel width of 80 µm.[122] Producing narrower rod microgels has not been possible due to the microfluidic channel size and the viscosity of the continuous phase. Furthermore, the reproducibility is affected by the inhibitory effects of atmospheric oxygen present in the oxygen permeable PDMS based microfluidic chip. Oxygen inhibition is a key factor in producing stable microgels with diameter < 10 µm.[151–153]

This paper explored CJP further to generate ultra-thin rod microgels with a diameter of ~3 µm for magnetic alignment, or ultra-soft and ultra-porous rod microgels for cell-induced assembly into 3D constructs to enable cell-cell interaction and diffusion of enough diffusion through the microgel network.

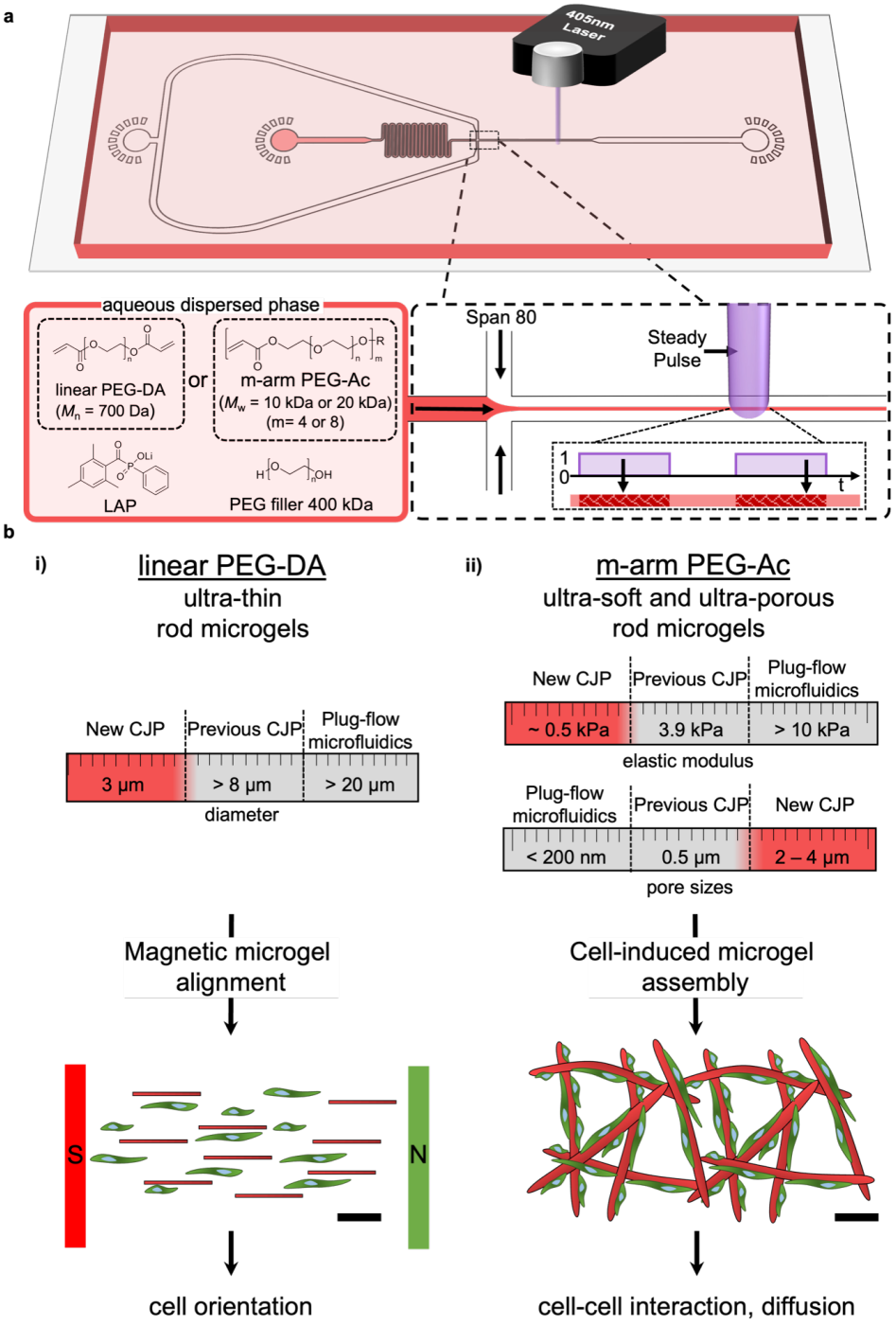

Fig. 5.1: Overview of the CJP method and the types of microgels produced. (a) CJP chip design adapted from another publication.[122] A time-modulated laser system (wavelength 405 nm) is used to irradiate the polymer jet. Span80 is used as the outer phase and different PEG-based polymers are used as the dispersed phase: (i) PEGDA (700 Da) to produce ultra-thin rod microgels and (ii) four-arm or eight-arm PEG-Ac to produce ultra-soft and ultra-porous rod microgels. The photo-initiator LAP is added to each pre-polymer composition along with a water-soluble PEG filler (PEG-OH, 400 kDa). (b) Two different types of rod microgels (ultra-thin or ultra-soft and ultra-porous) are used for two different tissue engineering applications. The ultra-thin microgels (3–10 µm diameter) are post-functionalized with magnetic particles for cellular alignment, whereas the larger ultra-soft and ultra-porous rod microgels (50–120 µm diameter) are used as building blocks for cell-induced assembly, resulting in large macroscopic pores between the microgels to enhance cell–cell interactions while the microgels enable diffusion.

5.2 Results and Discussion

5.2.1 Adjusting the microfluidic design to enable sufficient photopolymerization in the presence of atmospheric oxygen

Molecular oxygen terminates free radical polymerization by reacting with an initiator or growing polymer radicals.[154–157] In bulk solutions, the dissolved oxygen is rapidly depleted, enabling the polymerization reaction to propagate. However, oxygen inhibition becomes predominant when the solution is exposed to an oxygen source. This effect is magnified on the microscale due to the high surface-to-volume ratio.[152] In microfluidics, the chips are usually made from a PDMS elastomer with high oxygen permeability.[162,276] In CJP specifically, oxygen inhibition plays an important role due to the extremely thin jets (surface-to-volume ratio correlates with 1/r, where r is the radius). The oxygen used during free-radical polymerization is continuously replenished by oxygen diffusing through the microfluidic chip and reaching the continuous oil and aqueous polymer phases flowing inside the microchannels. The effect of oxygen inhibition became apparent when scaling the microfluidic channel down from 80 µm × 100 µm to 25 µm × 25 µm, intending to form an ultra-thin jet for the production of rod microgels with a diameter down to 2.5 µm (one-tenth of the microchannel size). This narrow microgel was shown to be optimal for extensive, oriented neurite outgrowth in a 3D Anisogel system, but so far can only be produced using the PRINT method.[67] Here, we intend to continuously produce microgels with the same dimensions by CJP. Due to the brief irradiation, much softer microgels can be obtained compared to the PRINT method that results in anisometric microgels with a Young's modulus of 35 kPa for a minimum required PEGDA (700 Da) concentration of 10 % (w/v). In CJP, we previously used 20 % (w/w) PEGDA (700 Da) as the reactive pre-polymer, mixed with 2.4 % (w/w) of a water-soluble non-reactive PEG filler (400 kDa) and 1 % (w/w) of the photo-initator LAP to form a jet within an 80 µm × 100 µm channel.[122]

While reducing the channel size to 25 µm in width and 25 µm in height, it became obvious that surface effects become predominant along with physical effects, such as pressure rise. Therefore, the viscosity of the continuous phase is reduced by diluting the oil phase (surfactant, Span80) with hexadecane, without significantly increasing the interfacial tension, which could hamper the formation of a jet. As a rise in interfacial tension between the two phases can destabilize the jet, the minimum

Span80/n-hexadecane ratio was determined through the Capillary (Ca) and Weber (We) numbers to ensure a stable jet (Table 5.1). The sum of the two numbers needs to be greater than one to achieve a stable jet.[150] For that reason, the ratio Span80/n-hexadecane is set to 3:1 when using smaller channel dimensions (25 µm width).

$$We = \frac{\rho_{jet} \cdot \ v_{jet}^2 \cdot \ d_{jet}}{\gamma} \tag{5.1}$$

$$We = \frac{\mu_{Span80} \cdot \ v_{out}}{\gamma} = \frac{\mu_{Span80} \cdot \ Q_{out}}{\gamma \ \cdot \ c^2} \tag{5.2}$$

$$c = \sqrt{h \ \cdot \ w} \tag{5.3}$$

ρ_{jet}=1070 kg/m^3 is the density of the jetting fluid composed 20 % (w/w) PEGDA (700 Da) and 2.4 % (w/w) water soluble PEG filler (PEG-OH, 400,000 Da), v_{jet} the velocity calculated based on

$$Q_{jet} = \frac{V}{t} = \frac{A \ \cdot \ d}{t} = A \ \cdot \ v_{jet} \tag{5.4}$$

with $A = w \ \cdot \ h = 25 \ \mu m \ \cdot \ 25 \ \mu m$, being w the channel width and h the channel height. The flow rate Q_{jet} was set to 125 µL/h, being the sum of Q_{in}=5 µL/h and Q_{out}=120 µL/h. d_{jet} = 2.5 µm is the jet diameter determined through microscopy images, and γ the interfacial tension between the polymer and outer phase, obtained through spinning drop measurements. μ_{Span80} is the viscosity of the outer phase experimentally determined through rheology, Q is the flow rate set to 120 µL/h. The velocity of the outer phase, v_{out}, is based on the flow rate Q_{out} while considering the channel geometry.

Tab. 5.1: Ca and We number in a 25 µm wide microfluidic channel with different Span80/n-hexadecane ratios at room temperature.

Span80 (% (v/v))	μ (Pa·s)	ρ (g/mL)	γ (N/m)	Ca	We	Sum
100	0.432	0.986	3.30×10^{-3}	6.98	0.00250	6.98
75	0.117	1.02	1.96×10^{-3}	3.18	0.00421	3.19
50	0.0256	0.92	5.89×10^{-3}	0.232	0.00140	0.233
25	0.00757	0.88	7.46×10^{-3}	0.0540	0.00111	0.0552
1	0.0052	0.86	8.25×10^{-3}	0.0336	0.00100	0.0346

Although a stable jet was formed, we could not produce ultra-thin rod microgels by CJP within a 25 µm × 25 µm channel, even when testing different polymer concentrations (20–100 % (w/w) PEGDA) or adding more photo-initiator (1–2 % (w/w))

among other measures to increase the reactivity of the jet precursor solution (data not shown). Reliable photopolymerization during microfluidics has been achieved by limiting the presence of oxygen, for example by degassing, nitrogen purging, adding oxygen scavengers, or confining the reaction to an inert environment.[277–280] However, these methods are laborious, cannot guarantee reproducible results, and are not always easy to handle in a microfluidic system. We therefore explored an additional measure to counter the oxygen inhibition effect and hypothesized that a larger height-to-width ratio in the microfluidic channel would increase the thickness of the jet so that the "dead zone" would not consume the entire jet.[158] Accordingly, we changed the dimensions of the microfluidic channel from 25 µm × 25 µm to 25 µm × 50 µm or 50 µm × 80 µm (Figure 5.2a). Both dimensions were evaluated for their ability to generate ultra-thin microgels with diameters < 5 µm using 40 % (w/w) PEGDA (700 Da) as a pre-polymer phase and 3:1 Span80 and n-hexadecane. Concentrations of PEGDA < 40 % (w/w) did not produce stable microgels using either of the redesigned channels.

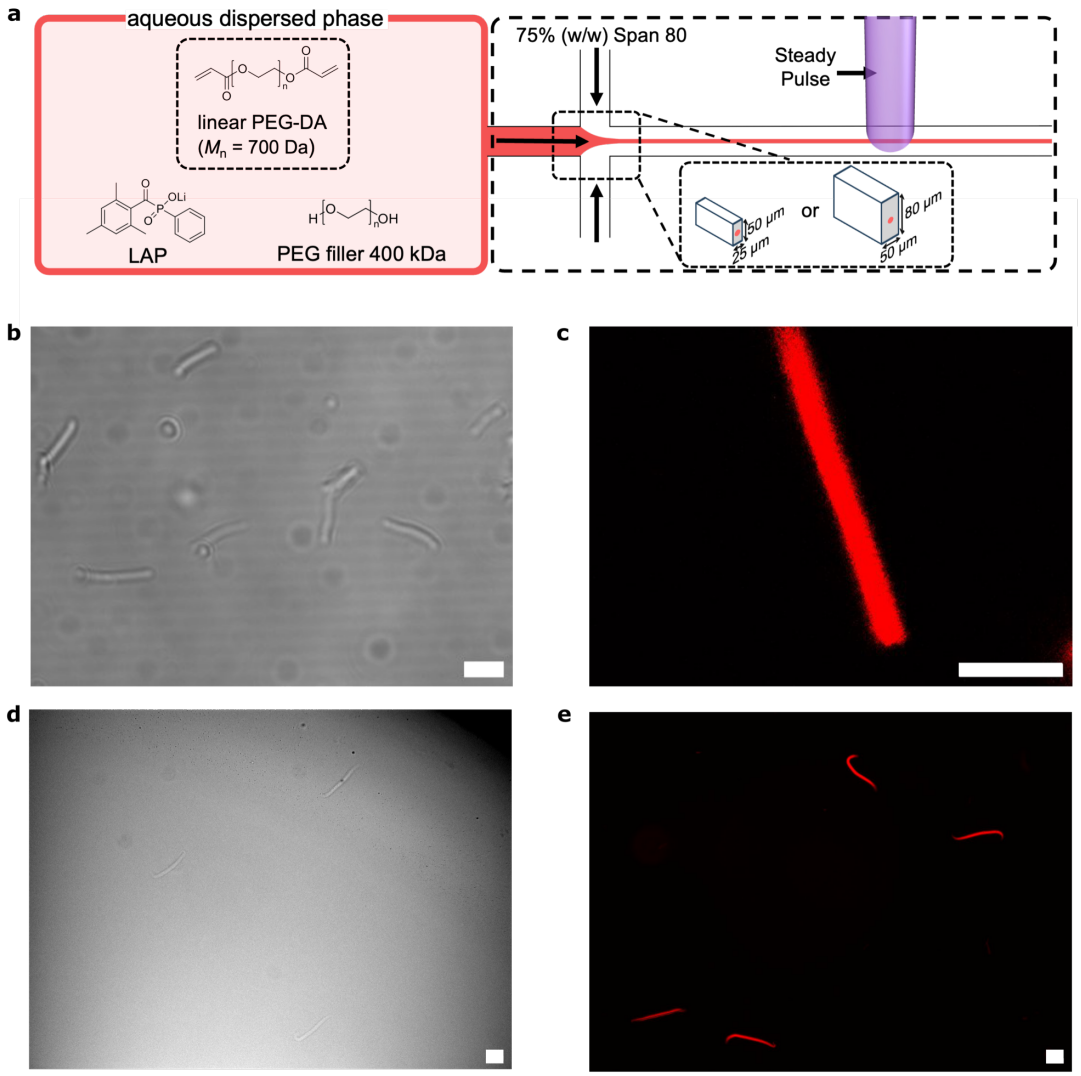

Fig. 5.2: Representative bright-field and confocal images of microgels produced within rectangular microfluidic channels (50 × 80 µm). (a) Microfluidic channel dimensions to produce ultra-thin rod microgels and pre-polymer used. (b) Microgels 3 ± 0.8 µm in width and 28 ± 5 µm in length, the smallest possible microgel obtained at 5 µL/h pre-polymer and 300 µL/h oil flow rates. Scale bar = 20 µm. (c) Confocal images of the same microgels as in (b) labeled with Rhodamine B in red. Scale bar = 10 µm. (d) Bright-field and (e) confocal images of microgels 6 ± 1 µm in width and 122 ± 9 µm in length, labeled with Rhodamine B in red, obtained at 10 µL/h pre-polymer and 300 µL/h oil flow rates. Scale bars = 50 µm. Flow rates and irradiation times are summarized in Table 5.2.

The flow rates were varied from 5 to 20 µL/h for the polymer phase and 100 to 450 µL/h for the outer phase, with a maximum of 200 µL/h within the 25 µm × 50 µm channels and 450 µL/h within the 50 µm × 80 µm channels. Both channel geometries allowed the production of rod-shaped microgels with minimal diameters of 3 ± 0.8 µm in the swollen state in water after purification (Figure 5.2). The advantage of the 50 µm × 80 µm channel over the 25 µm × 50 µm channel was the handling of the

Tab. 5.2: Microfluidic parameters tested for the production of ultra-thin rod microgels.

Channel dimensions (width x height, µm)	Laser power (mW)	On-time (ms)	Flow rate polymer phase (µL/h)	Flow rate oil phase (µL/h)	Microgel dimensions (width x length, µm)
25x50	50	1	5	120	10 ± 1 x 190 ± 18
		0.5	4	150	4 ± 0.2 x 52 ± 5
		1	5	200	4 ± 0.6 x 180 ± 43
50x80		1	10	300	7 ± 0.5 x 70 ± 4
		0.5	10	300	7 ± 0.8 x 55 ± 2
		0.25	5	300	3 ± 0.8 x 28 ± 5

microfluidic device, making it less sensitive to pressure changes. The microfluidic channel dimensions, irradiation times, and oil and polymer flow rates are summarized with the obtained microgel sizes in Table 5.2.

5.2.2 Analysis of jets by computational fluid dynamic simulation and confocal microscopy

We used confocal microscopy to study the jet forming inside a 50 µm × 80 µm microfluidic channel and the distances between the polymer jet and the PDMS walls (the oxygen source). Reconstruction of the confocal images revealed a more elongated 3D jet at the crossing section, as well as further down the microfluidic channel (Figure 5.3a (i-iii)). The resulting vertical (x–z) profile showed that a central jet formed but also an elongated part above the jet in contact with the PDMS surface. The latter may be a real structure or a ghost formed by the strongly fluorescent material in the channel and its reflection from the PDMS–liquid interface above.[281] Analysis of these potential artifacts by laser scanning confocal microscopy was beyond the scope of our study, so we used CFD simulations to see if the profiles may depend on the wetting asymmetry of the oil and polymer phases on the glass and PDMS walls. Figure 5.3b-e shows a 3D simulation of jet formation in a 50 µm × 80 µm channel based on the physical properties of the polymer solution and oil phase described above and in Table 5.1. More details about the simulation model are provided in the Appendix. Different contact angles of the polymer phase and the walls were applied during the simulation, such as 180° at the top PDMS and bottom (glass), 90° and 90°, 0° and 180°, and 0° and 0°. The contact angles of the oil phase were then calculated as 180° minus the contact angle of the polymer phase. The first condition (180° at the top and bottom), where a focused cylindrical jet is formed (Figure 5.3b), was anticipated inside the microfluidic channel because we applied a hydrophobic coating.

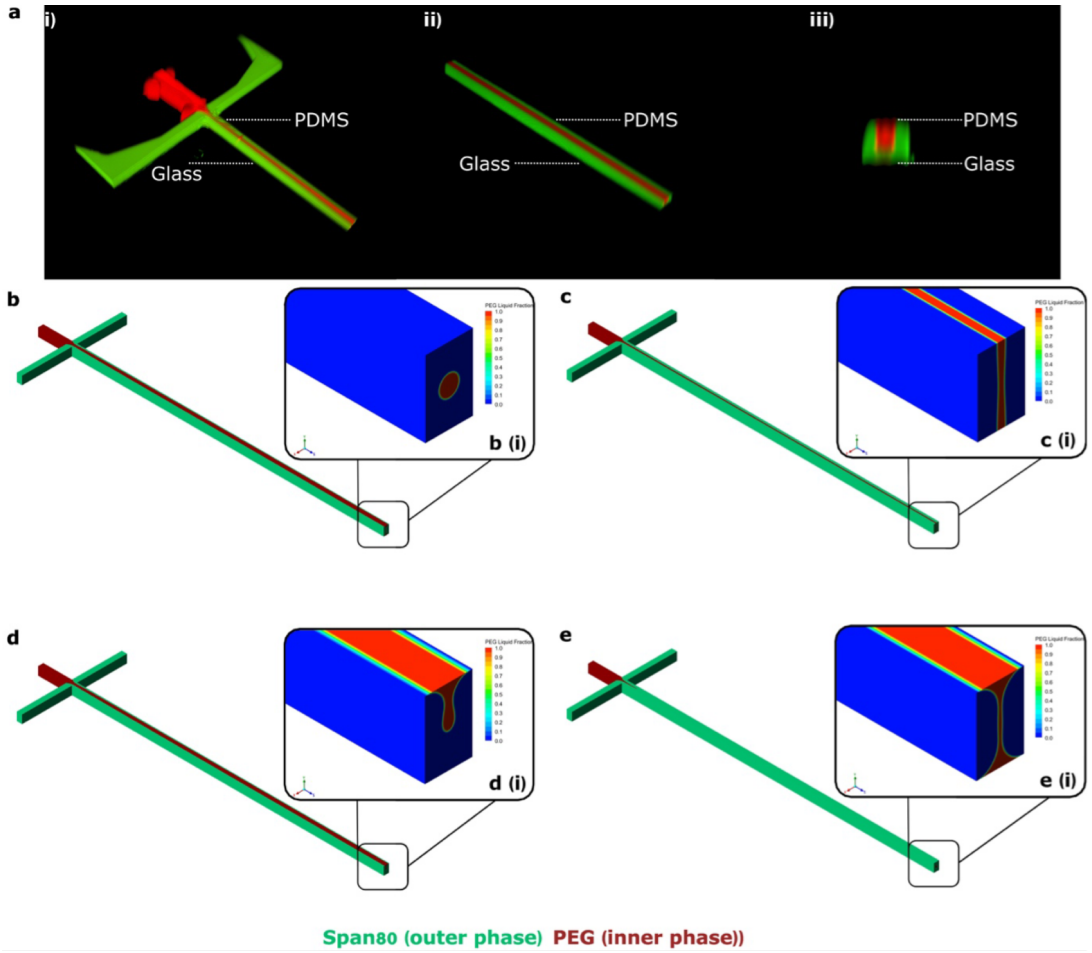

Fig. 5.3: Formation of a 3D jet in the 50 × 80 µm microchannel chip. (a) Confocal images showing the formation of a 3D jet, captured along different regions of the flow such as (i) near the T-junction where flow focusing occurs, (ii) and (iii) further down the jet where light irradiation takes place (inner phase = pre-polymer in red; outer phase = Span80 in green). (b-e) The results of a simulation model with different contact angles of the inner pre-polymer phase at the top (PDMS) and bottom (glass) walls of microchannel: (b) 180°–180°, (c) 90°–90°, (d) 0°–180° and (e) 0°– 0°.

However, confocal images suggested a different flow profile. This may be explained by the simulations indicating that two contact angles of 90° (Figure 5.3c) or contact angles of 0° and 180° (Figure 5.3d) lead to more elongated jets. The last condition (0° at the top and bottom; Figure 5.3e) is the least likely. Importantly, the produced microgels were cylindrical and much thinner than the cross-section of the polymer phase predicted by the simulation results in Figure 5.3c (22 µm in diameter). This finding, together with the fact that the smallest microfluidic channel (25 µm × 25 µm) could not produce rod microgels, again suggests that the jet may not be polymerized over its entire height when briefly exposed to light and in contact with oxygen. These observations indicate the existence of a "dead zone" due to the presence of oxygen

adjacent to the PDMS top wall inside the channel where free radical polymerization does not occur during CJP.

To confirm the effect of oxygen inhibition on free radical polymerization, we designed a chip with a nitrogen channel around the main reaction channel to scavenge unwanted oxygen. The design is based on a previous report and can be found in Figure 5.4.[152] We chose a 25 µm × 25 µm channel (does not form microgels in the presence of oxygen) and used 40 % (w/w) PEGDA (700 Da) in the pre-polymer solution. Microgels 12 ± 1 µm in width and 280 ± 18 µm in length (in the swollen state) could be produced using this setup. The highest possible flow rate to obtain stable microgels using this setup with the 25 x 25 µm channel and nitrogen flow was 65 µL/h. With a higher flow rate and the formation of a thinner jet, no microgels could be formed. This is likely because the higher flow rates reduced the time of the jet in the irradiation spot, resulting in insufficient crosslinking. Therefore, thinner microgels than 10 µm could not be achieved by adding the nitrogen channel along the smaller channels.

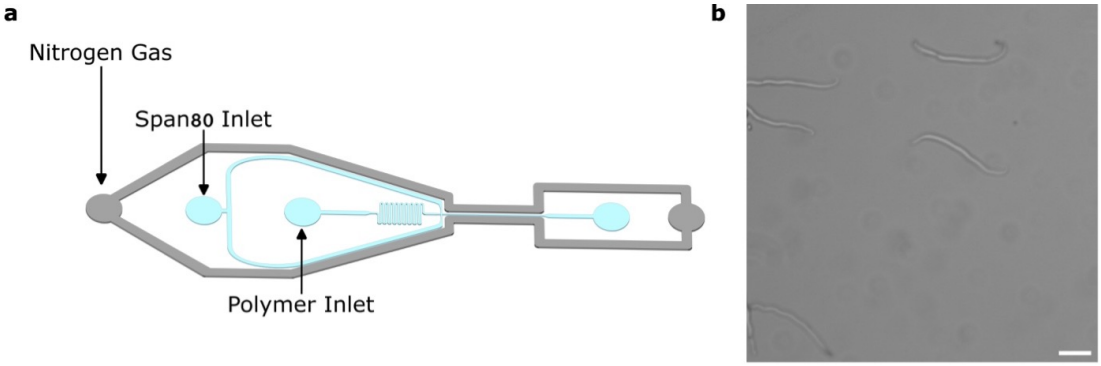

Fig. 5.4: Production of microgels inside 25 x 25 µm channel with additional nitrogen gas inlet. a) Channel design comprising nitrogen gas channel, based on.[152] b) Microgels produced inside 25 x 25 µm channel with nitrogen compartment using 40 % (w/w) PEGDA as pre-polymer solution and 75 % (v/v) Span80 with 25 % (v/v) n-Hexadecane as oil phase. The flow rates are 15 µL/h for the inner and 50 µL/h for the outer phase, with a laser modulation ON-time of 5 ms at 50 mW. The microgels are 12 µm in width and 280 µm in length. Scale bar is 100 µm.

5.2.3 Magnetic alignment of ultra-thin rod-shaped microgels inside 3D Anisogels

The 40 % (w/w) PEGDA ultra-thin rod microgels were magnetized with SPIONs, as previously reported for PRINT microgels.[35,67] For PRINT microgels, only 1.8 µg/mL of SPIONs (< 10 µM iron) was required to orient the microgels in 20 s due to their high aspect ratio. In multiple studies, the magnetization of rod microgels was achieved through the addition of the nanoparticles to the pre-cursor solution.[66,68,161,258] However, in CJP, this approach did not prove to be suitable due to insufficient and heterogeneous functionalization, which will be discussed in the following subsections.

In situ magnetic functionalization of rod microgels

Together with Susan Babu we tested several magnetic nanoparticles to render the CJP-produced microgels magneto-responsive (Table 5.3). Alignment in a weak magnetic field (70 mT) was analyzed in water and a 1.25 % (w/v) PEG-based hydrogel precursor solution that can be gelled enzymatically to fix the microgel alignment and form an Anisogel.[65,66] The PEG system currently used in the Anisogel as surrounding hydrogel to fixate the aligned microgels is called the PEGKQ hydrogel.[65,66] It contains PEG-VS (8-arm, 20 kDa) functionalized with two different peptides, Ac-FKGGGPQGIWGQERCG-NH_2 (K-peptide) or NQEQVSPLERCG-NH_2 (Q-peptide), via Michael-type addition with the free thiol on the cysteine (C). The Q-peptide is a substrate for FXIIIa, which is a transglutaminase that couples the amine of the lysine (K) to glutamine (Q).

Tab. 5.3: SPIONs tested for CJP-made microgels, with different physical and chemical properties.

SPIONs	EMG700	PBG300	PEGMA
Diameter	10 nm	10 nm	70 nm
Surface modification	anionic	non-ionic surfactant	PEGMA

The anionic-coated SPIONs (EMG700, 400 µg/mL) used for the PRINT microgels were not suitable to magnetize the CJP rod microgels because the nanoparticles aggregated and sedimented in the pre-polymer solution (Figure 5.5a). This is probably due to the lithium-based photo-initiator interacting with the anionic surfactant because of

charge interactions leading to agglomerations and an inhomogeneous distribution of the nanoparticles. Irgacure 2959 is used as a photo-initator in PRINT because ultra-fast gelation is not required in this method, where these interactions do not occur.[66] When testing PBG300 SPIONs with a non-ionic PEG-based surfactant, no SPIONs aggregation was observed (Figure 5.5b). However, a higher SPIONs concentration of 800–1600 µg/mL was required for the microgels to respond to the magnetic field, with a minimum alignment time of 7 s (Figure 5.5c).

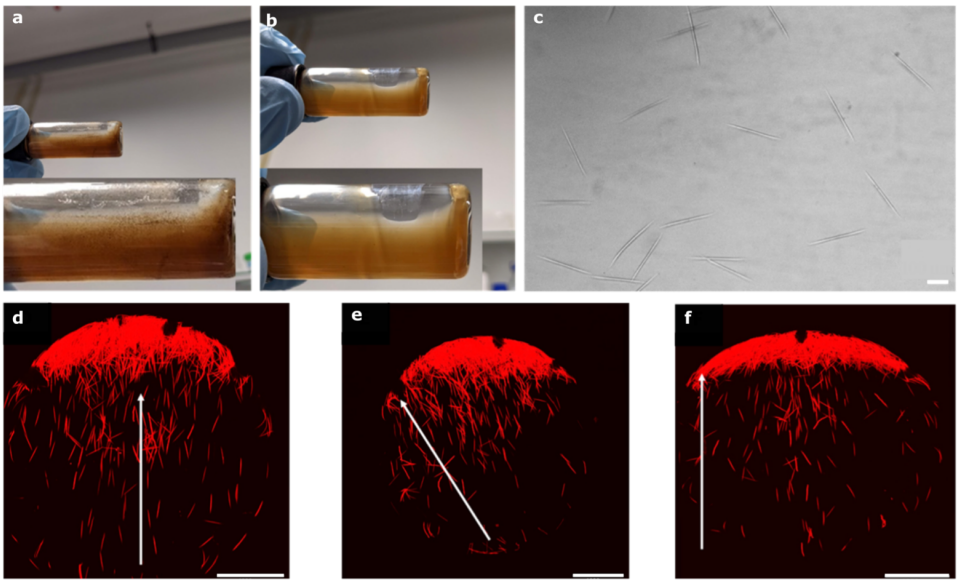

Fig. 5.5: In situ addition of EMG700 and PBG300 SPIONs. a) Settlement of EMG700 SPIONs in the polymer precursor solution containing LAP after 1 hour post ultrasonication. The polymer precursor solution consists of water-soluble LAP, 40 % (w/w) PEGDA (700 Da), and PEG filler (400 kDa) to ensure sufficient entrapment of nanoparticles inside the microgels, as this PEGDA concentration leads to a smaller mesh size compared to a 20 % (w/w) PEGDA solution.[122] b) No such settlement is observed for PBG300 SPIONs dispersed in the same precursor solution after 1 hour post ultrasonication. c) While the formed microgels do not respond to an external magnetic field at a SPIONs concentration of 400 µg/mL, We observe a response to the magnetic field when increasing the nanoparticle concentration to 800 µg/mL or 1600 µg/mL. With 800 µg/mL SPIONs, the microgels align within an average of 13 s in water, which is reduced to 7 s for a SPIONs concentration of 1600 µg/mL. Image shows microgels in water containing 1600 µg/mL of PBG300 SPIONs, made using the 50 µm wide channel. Scale bar = 100 µm. d-f) Maximum intensity projections of 100 µm thick z-stacks of Anisogels made using these magnetic microgels (red). Scale bar = 1000 µm. The white arrows indicate the direction of the applied magnetic field. Magneto-responsive microgels are mixed with a PEGKQ precursor solution. After pipetting the solution with the microgels inside a well, positioned within an external magnetic field, the microgels align but transversally move towards one side of the well within the first 5 min during the crosslinking of the PEGKQ hydrogel.

The alignment of these magnetic rod microgels was then tested inside a 3D PEG hydrogel precursor solution to form an Anisogel, but we observed unwanted transversal movement of the rod microgels towards one side of the well (Figure

5.5d-f).[65] This movement probably reflects the heterogeneous dispersion of SPIONs throughout the microgel network. The heterogeneous distribution of SPIONs would create pockets of higher than average magnetization, attracting such points towards the magnet and causing microgel accumulation along the wall of the well. We observed agglomerations of PBG300 SPIONs inside the purified rod microgels when performing a Prussian blue iron staining (Figure 5.6).

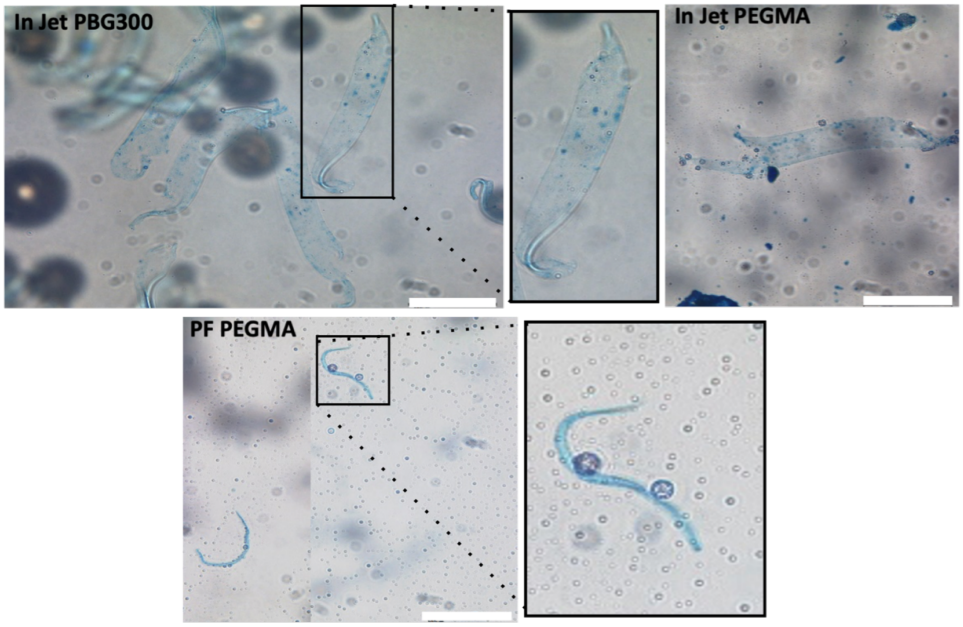

Fig. 5.6: Prussian blue iron staining of CJP microgels. SPIONs appear in blue inside the rod microgels: in situ functionalization with PBG300 SPIONs or PEGMA SPIONs (In Jet), post-functionalized with PEGMA SPIONs (PF). All in situ samples show SPIONs agglomerations (dark blue spots), whereas post-functionalized sample shows a homogeneous blue color. Scale bars=100 µm.

Magnetic post-functionalization of rod microgels

To achieve a more homogenous SPIONs distribution, we coupled the SPIONs to the microgel network after production instead of mixing them with the precursor solution before crosslinking. To achieve this, we used custom-made magnetic nanoparticles (70 nm diameter) with a non-ionic PEGMA surface coating, which can chemically couple to unreacted free acrylates of the microgel network via FRP. A previous study has demonstrated that surface-magnetized solid rods can orient in very weak magnetic fields (1–10 mT), with a mathematical model suggesting that surface-magnetized solid rods require a 69% weaker magnetic field than anisotropic elements with magnetic nanoparticles throughout their entire volume.[163] Such an approach could, therefore,

also allow for a decrease in nanoparticle concentration. To post-functionalize the microgels with SPIONs, a solution consisting of 1 % (w/w) LAP, PEGMA SPIONs and microgels was exposed to a self-constructed light emitting diode (LED) in the UV range (λ = 365 nm, spot diameter 4.7 mm, 135 mW/cm) for 10 min. Compared to in situ functionalization there are no agglomerations visible in the Prussian blue staining (Figure 5.6). To investigate the impact of the aspect ratio on the required amounts of nanoparticles to align the microgels, we compared microgels with a diameter of 10 µm and AR of 15, 19 or 30. After purification, the magnetic response of the microgel rods was tested in water using a weak magnetic field (70 mT). Different concentrations of magnetic nanoparticles (200–600 µg/mL with respect to the total volume of the microgels) were incubated with the microgels (Figure 5.8a). We found that a SPIONs concentration of 200 µg/mL was sufficient for higher AR (19, 30), whereas 600 µg/mL was required for lower AR (15), to magnetically align the microgels in 3 s. After sufficient time for complete alignment, the degree of alignment was quantified by determining the full width half maximum (FWHM) of the histogram depicting the angles of microgel orientation in relation to the magnetic field lines (Figure 5.8b). We assumed satisfactory alignment when the FWHM was < 90°.[66,67] Only the SPIONs concentration of 600 µg/mL achieved a sufficiently low FWHM for all aspect ratios, but microgels with an AR of 30 also oriented at lower SPIONs concentrations. We did not expect microgels with a lower AR (15) to require a higher SPIONs concentration for alignment because in the case of PRINT microgels, the shorter PRINT microgels rotate more rapidly (AR of 2.5 compared to 20 for a microgel width of 10 µm).[164] Even though longer aspect ratios result in a higher magnetic driving force, the viscous torque of higher aspect ratios normally increases more strongly than the magnetic torque, counteracting the rotation. This may not be the case for CJP microgels as these are now much softer than the PRINT microgels (2 kPa vs 35 kPa), suggesting a higher porosity and thus reduced viscous torque. The elastic modulus of microgels is indicative for the crosslinking density. Furthermore, SPIONs on the outside of the microgels likely increase the magnetic torque compared to interstitial SPIONs. We were unable to fully align rods with diameters of 3–4 µm and lengths of 25–50 µm in water (Figure 5.7). This might be due to their smaller aspect ratio or microgel clustering during centrifugation.

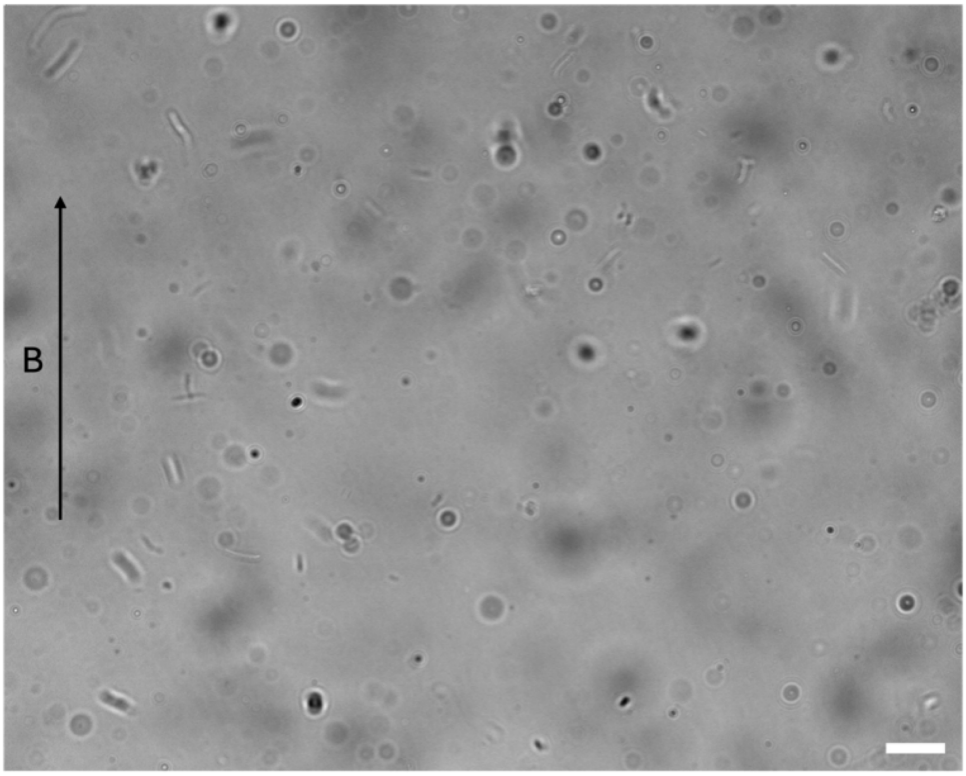

Fig. 5.7: Magnetic functionalization of ultra-thin rod microgels. PEGMA SPIONs post-functionalized 3 x 25 µm rod microgels inside a 70 mT magnetic field. The arrow indicates the direction of the magnetic field. Rod microgels show no alignment, maybe due to much lower aspect ratio (8). Scale bar is 50 µm.

The lowest possible AR to align microgels with a diameter of 10 µm was 13 with post-functionalization in 600 µg/mL of PEGMA-coated SPIONs. As we aim to reduce the amount of synthetic material, we selected these rods to investigate whether cellular alignment is possible with CJP-produced microgels inside the Anisogel. In addition, we observed in unpublished work alignment of cells using PRINT microgels with a width of 10 µm and length of 100 µm (AR of 10). The CJP microgels (AR: 13) were added to the PEGKQ precursor solution (1 % (v/v)) and 600 µM of the cell-adhesion peptide GRGDSPC together with mouse L929 fibroblasts (700 cells/µL). These microgels were much softer (Young's modulus 2 kPa, Figure 5.8c) than the PRINT microgels used in previous studies with a minimum Young's modulus of 35 kPa.[66] As the surrounding 1.25 % (w/v) PEGKQ hydrogel only has a storage modulus of 10 Pa, the PRINT microgels lead to large differences in stiffness between the microgels and the surrounding gel. Using the much softer CJP-produced microgels, we determined whether cells still experience sufficient mechanical anisotropy to grow in a unidirectional manner following the aligned microgels. The samples were incubated for seven days and the orientation of the cells was assessed by confocal

microscopy and quantitative image analysis. The fibroblasts showed more growth in the direction of the aligned microgels (Figure 5.8d) but only seemed to align when close to a microgel (Figure 5.8e). In comparison, the control with randomly oriented microgels showed no cellular alignment (Figure 5.8f). Quantification of the alignment by calculating FWHM (Figure 5.8g) revealed that the FWHM of the rod microgels was < 90° but the cells showed much less alignment (FWHM > 90°) compared to our previous studies using PRINT microgels. This suggests that the stiffness difference of the microgels and the surrounding hydrogel plays an important role in terms of cellular guidance. Less mechanical anisotropy may be sensed by the cells because the CJP-produced microgels were 20-fold softer than the PRINT microgels. To compensate for this effect, we may need to use longer or stiffer microgels or a higher microgel concentration. The ability to produce softer rod microgels and render them magnetic makes it now possible to study important biomechanical questions, such as the stiffness threshold of the rods with respect to the surrounding hydrogel matrix, to induce cellular alignment. This is especially important when mimicking different native tissues, as we can now provide the flexibility to study the needed mechanical guidance cues depending on the cell types. More information on the quantification of the FWHM can be found Materials and Methods section.

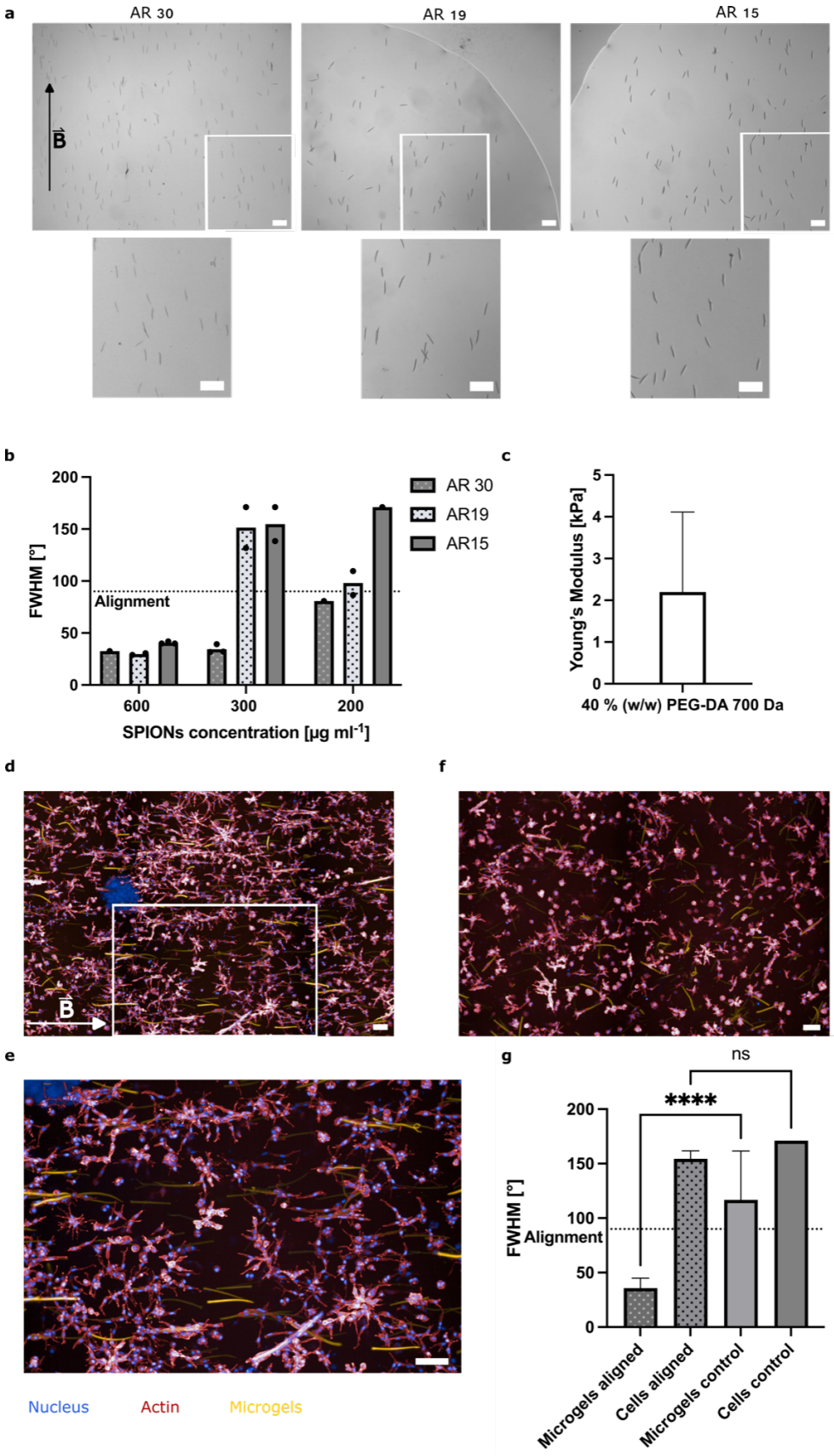

Fig. 5.8: CJP microgel and cell alignment. (continued on next page)

Figure 5.8 (continued): (a) Alignment of post-functionalized rod microgels with PEGMA SPIONs featuring different aspect ratios (AR = 30, 19, or 15) in water with the highest SPIONs concentration of 600 µg/mL. The arrow indicates the direction of the magnetic field (70 mT). White boxes indicate magnification of the images placed below. Scale bars = 200 µm. (b) Image analysis to quantify the FWHM of microgels containing different amounts of PEGMA SPIONs and featuring different aspect ratios. Alignment is satisfactory when FWHM < 90°. (c) Young's modulus of 40 % (w/w) PEGDA thin rod microgels measured by colloidal AFM. d) Anisogel preparation with L929 mouse fibroblasts (700 cells/µL) (red) and post-functionalized magneto-responsive rod-shaped microgels (10 μm × 130 μm) with 600 µM GRGDSPC inside a PEGKQ matrix, cultured for seven days. The white arrow indicates the magnetic field direction for all images. Scale bar = 100 µm. (e) Magnified image of fibroblasts growing inside the Anisogel. The magnified region is bounded by the white box in image (d). Scale bar = 100 µm. (f) Control L929 mouse fibroblasts (700 cells/µL) (red) cultured in randomly oriented post-functionalized magneto-responsive rod-shaped microgels. Scale bar = 100 µm. (g) Image analysis to quantify the FWHM of microgel and cell alignment inside hydrogels with aligned (Anisogel) and unaligned (control) microgels. Alignment is satisfactory when FWHM < 90°. Data are means ± standard errors. Statistical significance was determined by one-way ANOVA with Tukey's multiple comparison test (*p < 0.5; **p < 0.01; ***p < 0.001; ****p < 0.0001).

5.2.4 Production of ultra-porous and ultra-soft rod-shaped microgels

Conventional polymer networks, specifically those in synthetic hydrogels and microgels, typically possess nanometer-sized pores.[62,282] However, such pore sizes do not always support sufficient diffusion of macromolecules for tissue engineering. Several techniques have been developed to introduce microporosity and macroporosity into hydrogels and microgels.[283,284] For example, pH-degradable monodisperse supramolecular nanogels have been used as a sacrificial colloidal template to produce microgels containing pores of 300–360 nm.[284] Unlike methods that require sacrificial templates, CJP achieves high porosities mainly due to the short irradiation time and the low conversion of the polymer network, rendering the microgels intrinsically porous. The addition of unreactive filler molecules to stabilize the jet may also contribute to porosity by inducing phase separation during free-radical gelation, followed by the removal of the non-reacted phase during purification.[35,122,195] We exploited brief irradiation (milliseconds to seconds) to produce ultra-porous and ultra-soft microgels. Short irradiation times combined with oxygen inhibition generate polymer networks with low conversions.[122] This leads to softer CJP rod microgels that swell more than PRINT microgels based on the same polymer concentrations. Previously, pore sizes of 510 nm have been reported for CJP microgels prepared from 20 % (w/w) PEGDA (700 Da) compared to 110 nm for equivalent PRINT microgels.[122] Softer and more porous rod microgels are useful for tissue engineering due to their superior diffusion properties and similar mechanical

behavior to soft native tissues such as the brain. This is particularly important when rod-shaped microgels are interlinked to form 3D MAP scaffolds. When cells grow and fill the free space between microgels, the microgel network can support the cells with a better diffusion of oxygen and nutrients. This inhibits the formation of a necrotic core and supports the growth of larger tissues. MAP scaffolds have thus far been prepared using rod-shaped or spherical microgels with elastic moduli > 10 kPa and mesh sizes in the nanometer range.[28–30,170] To test the effect of the molecular structure of the reactive polymer on the microgel network and its stiffness, we compared the linear PEGDA precursor to multi-arm star sPEG-acrylates (sPEG-Ac) when cross-linked by free radical polymerization using 1 % (w/w) LAP. Four star polymers were tested: four-arm sPEG-Ac 10 and 20 kDa, and eight-arm sPEG-Ac 10 and 20 kDa (Table 5.4).

Tab. 5.4: Rheological compositions as well as compositions used in microfluidics.

Method	4 arm sPEG-Ac 10 kDa	4 arm sPEG-Ac 20 kDa	8 arm sPEG-Ac 10 kDa	8 arm sPEG-Ac 20 kDa	PEGDA 700 Da
Bulk Hydrogels	5 % w/w	5 % w/w	5 % w/w	5 % w/w	5 % w/w
Microgels	8 and 10 % w/w	8 and 10 % w/w	5 and 10 % w/w	3 and 10 % w/w	20 and 40 % w/w

Before the microfluidic experiments, we determined the gelation times and storage moduli of bulk hydrogels prepared from all reactive polymers at a concentration of 5 % (w/w) using rheology (Figure 5.9a-c). The softest gel was achieved using linear PEGDA (0.6 ± 0.1 kPa), in line with our previous observations.[121] This supports the hypothesis that sPEG-Ac generates denser and more stable networks than PEGDA. Although a shorter, linear molecule has more reactive groups for the same weight concentration than four- or eight-arm branched molecules with a higher molecular weight, larger molecules have a greater volume, helping the reactive groups to interact with each other. On the other hand, for both sPEG-Ac structures, the gelation time tends to increase with molecular weight, probably because there are fewer reactive groups available at a constant weight concentration (Figure 5.9c). Even so, the 20-kDa four-arm sPEG-Ac produced a hydrogel with a lower storage modulus (10.6 ± 0.8 kPa) than its 10-kDa equivalent (11.9 ± 0.04 kPa), whereas the 20-kDa eight-arm sPEG-Ac produced a hydrogel with a higher storage modulus (14.5 ± 0.8 kPa) than its 10-kDa equivalent (5.6 ± 0.08 kPa). The unexpected latter result may reflect the high coil density of the 10-kDa eight-arm sPEG-Ac, making the reactive groups less available.[121] Similarly, the storage moduli of hydrogels prepared from 10-kDa

eight-arm sPEG-Ac were much lower than those prepared from four-arm sPEG-Ac despite the extra arms providing additional reactive acrylate groups. Given that bulk hydrogels prepared from multi-arm polymers have higher storage moduli than those prepared from linear PEGDA, we tested the use of sPEG-Ac in CJP to determine whether this polymer architecture yields stable microgels at polymer concentrations below 20 % (w/w), aiming to reduce the amount of synthetic material. The four different sPEG-Ac variants and PEGDA were each mixed with PEG filler (400 kDa) and 1 % (w/w) LAP, and were used as the dispersed phase in an 80 × 100 µm microfluidic chip (Figure 5.9d). Pure Span80 was used as the continuous phase. Interestingly, under these conditions, a minimum jet width of 30 µm was required to obtain stable microgels. All rod microgels were produced at the same flow rates of 50 µL/h for both the dispersed and continuous phases, with laser on-times of 50 ms at a frequency of 10 Hz. The lowest polymer concentrations that produced stable microgels were 3 % (w/w) for 20-kDa eight-arm sPEG-Ac, 5 % (w/w) for 10-kDa eight-arm sPEG-Ac, 8 % (w/w) for four-arm sPEG-Ac (10 or 20 kDa), and 20 % (w/w) for PEGDA (700 Da). The lowest concentration of 3 % (w/w) matched the rheological data, where 20-kDa eight-arm sPEG-Ac showed the highest storage modulus at a given pre-polymer concentration. The low concentration of 5 % (w/w) for 10-kDa eight-arm sPEG-Ac was more surprising because this resulted in the lowest storage modulus of all bulk hydrogels prepared from sPEG-Ac. This may reflect the difference in exposure time between CJP and rheology, because a larger number of arms may be more important than chain mobility in the formation of stable microgel networks during short irradiation times. The Young's moduli of the microgels as determined by AFM are shown in Figure 5.9e. For the four-arm sPEG-Ac at 8 % (w/w), the reactive polymers produce microgels with Young's moduli of 1.1 ± 1.6 kPa and 0.30 ± 0.1 kPa for the 10 and 20 kDa variants, respectively, in agreement with the bulk hydrogel rheology data. Microgels prepared from 5 % (w/w) eight-arm sPEG-Ac (10 kDa) had a Young's modulus of 0.6 ± 0.5 kPa, whereas those produced from 3 % (w/w) eight-arm sPEG-Ac (20 kDa) had a Young's modulus of 1.2 ± 0.2 kPa. To our knowledge, this is the first report of such soft, rod-shaped microgels. In contrast, the microgels prepared from 20 % (w/w) linear PEGDA had a Young's modulus of 2.5 ± 1.2 kPa. The pore size of the soft microgels was investigated by confocal microscopy and image analysis (Figure 5.9f+g). The softest microgels, prepared from 8 % (w/w) four-arm sPEG-Ac (20 kDa), also featured the largest pores, ranging from 1 to 5 µm in diameter and accounting for 94% of the area occupied by pores. The equivalent microgels prepared from 8 % (w/w) four-arm sPEG-Ac (10 kDa) featured pores mostly ranging from 1 to 3 µm in diameter and accounting for 66% of the area occupied by pores. For microgels

prepared from the eight-arm sPEG-Ac variants at the lowest possible concentrations (5 % (w/w) for the 10-kDa variant and 3 % (w/w) for the 20-kDa variant), most pores were 1–3 µm in diameter and accounted for 96% or 84% of the area is occupied by pores, respectively. This is concordant with the mechanical properties, where 20-kDa eight-arm sPEG-Ac produced the stiffest microgels. All ultra-porous and ultra-soft rod microgels had diameters exceeding 50 µm due to the minimal required jet widths of 30 µm. Producing thinner ultra-porous and ultra-soft microgels is hindered by the high ratio of stabilizing non-reactive filler to reactive PEG.

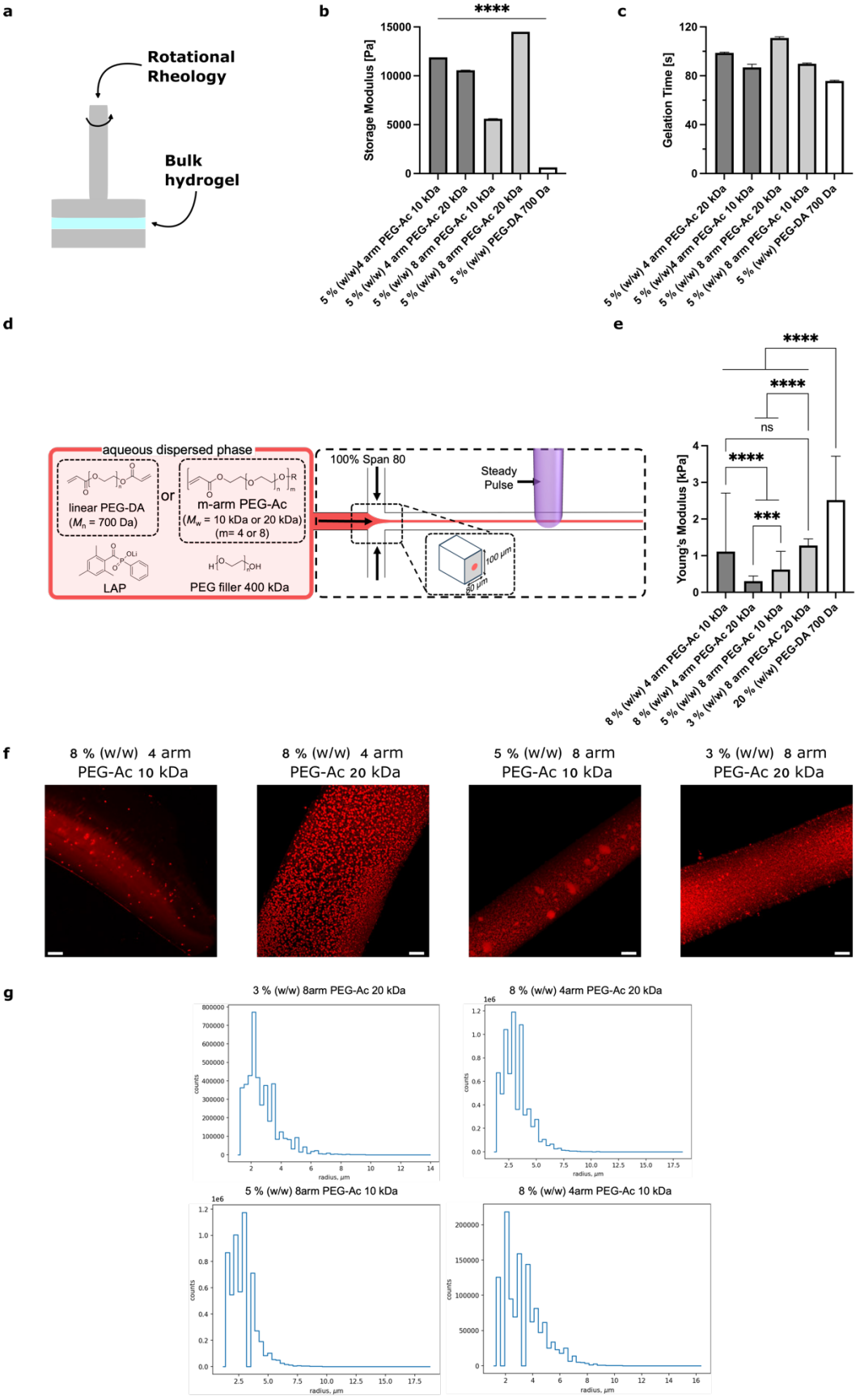

Fig. 5.9: Mechanical properties of ultra-soft microgels. (continued on next page)

Figure 5.9 (continued): Mechanical properties of ultra-soft microgels. (a) Rotational rheology set up of bulk hydrogels to measure (b) the storage modulus and (c) the gelation time. (d) Microfluidic set up with channel dimensions and pre-polymer used to produce ultra-soft microgels. (e) Young's modulus of rod shaped microgels with the lowest possible polymer concentration and different precursors in CJP. Data are means ± standard errors (n≥3). Statistical significance was determined by one-way ANOVA with Holm-Sidak's multiple comparisons test (b) and one-way ANOVA with Tukey's multiple comparisons test (e) (*p < 0.5; **p < 0.01; ***p < 0.001; ****p < 0.0001). (f) Porosity analysis of rod microgels (red). Scale bars = 15 µm. Displayed images were processed for better visibility (background removed) but porosity analysis was applied to raw images.

To investigate the influence of the precursor molecules on the mechanical and structural properties of the ultra-soft and ultra-porous rod-shaped microgels in more detail, we set the polymer concentration to 10 % (w/w) for all sPEG-Ac variants and to 20 % (w/w) for PEGDA to ensure stable microgel production, and analyzed the microgels by colloidal AFM, Brillouin microscopy, ODT, and SAXS. First, the Young's moduli of the microgels were determined by colloidal AFM (Figure 5.10a). For sPEG-Ac, the stiffest microgels were produced from 20-kDa eight-arm sPEG-Ac, resulting in a Young's modulus of 1.6 ± 1.3 kPa, whereas the 20-kDa four-arm sPEG-Ac was the least stiff (0.5 ± 0.2 kPa). ODT and Brillouin microscopy were used to characterize the mechanical properties of the microgels in more detail (Figure 5.10b-c). The refractive index (RI) is proportional to the mass density of the sample and suggested a lower density for four-arm samples compared to eight-arm samples. Microgels prepared from 20-kDa four-arm sPEG-Ac had the lowest RI, in agreement with the lowest measured Young's modulus, indicating that these samples contain the most water. However, the Brillouin frequency shift, which is related to the longitudinal modulus (the inverse of compressibility) of the microgels, showed a different trend.[285] Usually, a higher Brillouin frequency shift is expected for samples containing less water with higher Young's moduli or higher RI. The higher Brillouin frequency shift of four-arm compared to eight-arm sPEG-Ac microgels, regardless of the molecular weight, was therefore unexpected (Figure 5.10c). The higher storage moduli of nanocomposite hydrogels with lower Brillouin moduli have previously been attributed to their characterization at different length scales.[285] Whereas Brillouin microscopy focuses on a local area of the sample, the storage or Young's moduli describe stiffness at the macroscopic scale. Therefore, these observations suggest more heterogeneous mechanical properties at smaller length scales. In the case of nanocomposite hydrogels, this may reflect the addition of nanoparticles, whereas in our microgels the highly porous network might be the cause for this heterogeneity.

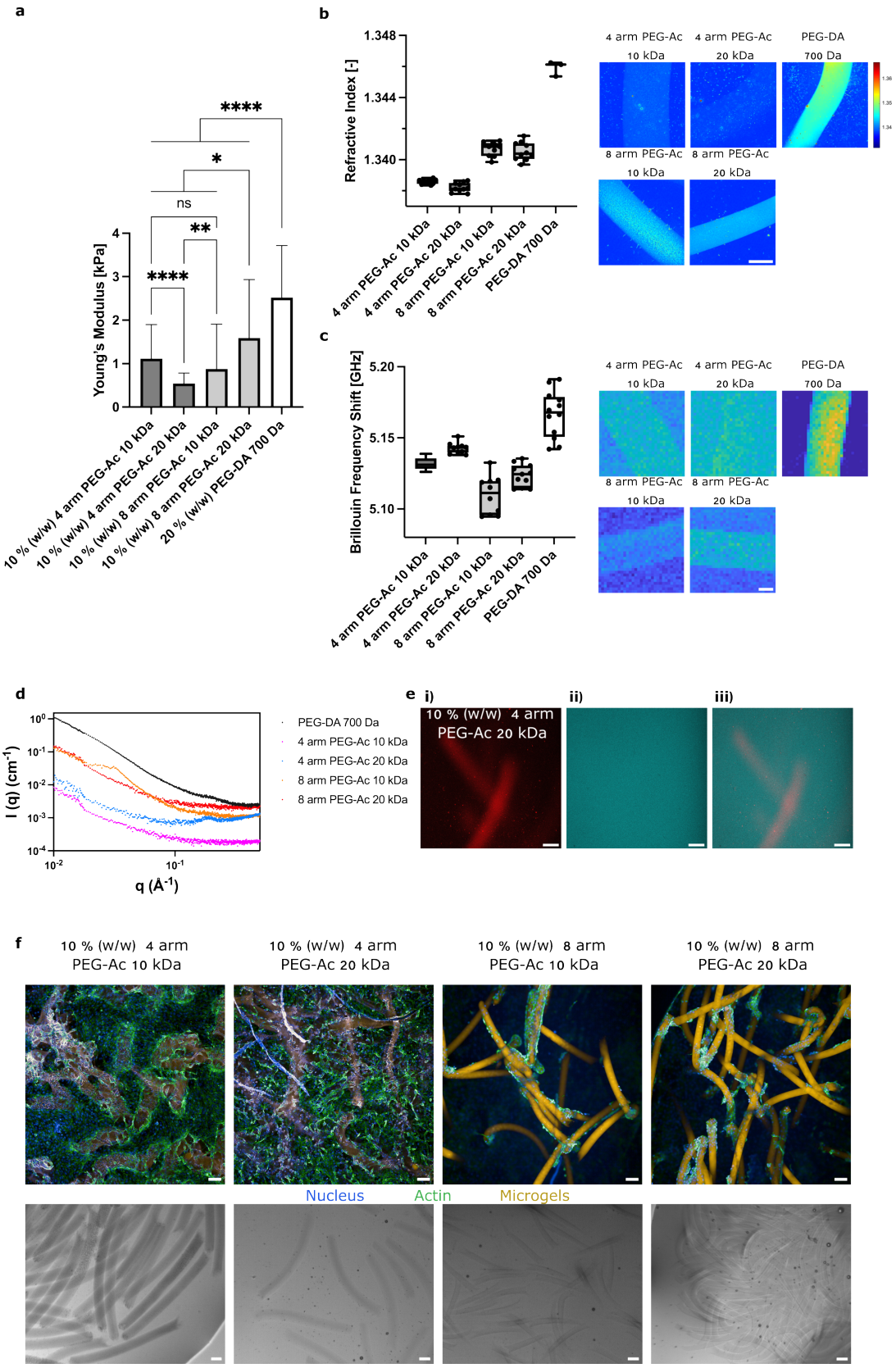

Fig. 5.10: Mechanical and structural properties of rod microgels prepared from multi-arm sPEG-Ac (10% (w/w)) and linear PEGDA (20% (w/w)) and cell-microgel interaction.(continued on next page)

Figure 5.10 (continued): (a) Young's modulus determined by AFM. (b) from different microgel compositions containing either 10 % (w/w) sPEG-Ac (4 arm and 8 arm, 10 kDa and 20 kDa respectively), or 20 %(w/w) PEGDA. Scale bar is 50 µm. (c) Brillouin frequency shift from same microgel samples. Scale bar is 20 µm. Data are means ± standard errors. Statistical significance was determined by one-way ANOVA with Tukey's multiple comparisons test (*p < 0.5, **p < 0.01, ***p < 0.001, and ****p < 0.0001). (d) SAXS profiles in Log Log Scale of 20 % (w/w) PEGDA rod microgels and 10 % (w/w) multi-arm sPEG-Ac. (e) Diffusion experiment using FITC-dextran 500 kDa and 10 % (w/w) 4 arm PEG-Ac 20 kDa microgels. Confocal images of the rhodamineB (red) labeled microgels (i) inside a water-based solution of 0.05 mM FITC-dextran (blue) showing the immediate diffusion of the fluorescently labeled dextran into the microgels (ii). Merged both channels (iii). Scale bars are 100 μm. (e) Cells interact differently with four- and eight-arm sPEG-Ac. Bright-field images of 10 % (w/w) rod microgels with different multi-arm sPEG-Ac (top) and interactions between L929 fibroblasts (200 μL^{-1}) on respective GRGDSPC-functionalized rod microgels (bottom). Scale bars = 100 µm.

The nanostructures of 10 % (w/w) sPEG-Ac and 20 % (w/w) PEGDA microgels were also analyzed by SAXS (Figure 5.10d). The SAXS profiles of all multi-arm sPEG-Ac microgel samples exhibit a typical uncharged polymer solution in the concentration regime. The scattering curves can be described by a Lorentzian function that characterizes the scattering from the polymer chain in the high q regime (q > 0.1 $Å^{-1}$) and the polymer chain clustering effect in the low q regime (q < 0.1 $Å^{-1}$).[286] The scattering patterns of the four samples differ significantly in the high q region due to variations in the conformation of polymer chains within each sample. Specifically, a correlation peak emerges near q = 0.2 $Å^{-1}$ for 4-arm sPEG-Ac 20 kDa, corresponding to characteristic distance of about 3.1 nm. We assume this peak is a result of the accumulation of arm chains in the sample, leading to a reduction in the backbone scattering intensity. The sample exhibits a tendency to form domains through the stacking of these smaller chains. Consequently, this effect could diminish the inter-chain interactions, which may explain the low Young's modulus of these microgels, and correlates well to the larger pore sizes and lower RI observed for 4 arm sPEG-Ac microgels. Microgels consisting of 8 arm sPEG-Ac 10 kDa and 20 kDa, as well as the linear PEGDA 700 Da, also seem to exhibit a correlation peak, although much less resolved compared to the 4 arm PEG-Ac 20 kDa samples. This could indicate that in these samples, the arm chains accumulate less. In the low q regime, all microgel samples made from star-PEG molecules similarly follow a power-law scattering behavior with an exponent α=-2. This indicates the presence of Gaussian-like coil clustering in the sample. The maximum value of α for 8-arm sPEG-Ac-10K Da is -1.8, while the minimum value of α for 4-arm sPEG-Ac-10K is -2.3. A lower n signifies a denser scatterer. In contrast, microgels prepared with linear PEGDA (700 Da) scatter more, as this sample comprises a higher initial polymer concentration during preparation (20 %(w/w) versus 10 % (w/w)). Previous reports

on the structure of PEG-based microgels show the presence of correlation peaks in the data, interpreted as the distance between cross-link-domains.[287] As such peaks are not visible in the data presented here, the density of cross-links per volume appears to be too low, which is likely due to the very short light exposure.

In a previous paper where nanoporous microgels were produced with plug-flow microfluidics, we demonstrated limitations in diffusion of fluorescently labeled dextrans depending on their size and the properties of the pre-polymer solution.[121] With the micrometer range pores of the ultraporous CJP microgels, we would have unhindered diffusions of larger growth factors and other proteins, like chondroitinase ABC (121 kDa), which is known to degrade scar tissue after spinal cord injury. To assess the potential of enhanced diffusion using sPEG-Ac CJP microgels, we incubated the softest microgels with 10 % (w/w) 4 arm sPEG-Ac 20 kDa with fluorescently labeled dextran (FITC-dextran, 500 kDa) (Figure 5.10e). This dextran exhibits a stokes radius of 14.7 nm, being larger than the previously probed sizes of 2.3 – 6 nm.[121] We recorded confocal images of the Rhodamin B labeled microgels prior (Figure 5.10e (i)) and right after mixing the microgels with the dextran solution (Figure 5.10e (ii)), showing the immediate diffusion into the microgels. Therefore, we believe that the ultraporous CJP microgels have a high potential as building blocks of MAP scaffolds. To study the ability of cells to adhere and spread onto the microgels, microgels prepared with 10 % (w/w) of the four sPEG-Ac variants were biofunctionalized with a cell-adhesion peptide (GRGDSPC) post-production (1 mM with 22 microgels per microliter) before seeding with mouse L929 fibroblasts (12 microgels and 200 cells per microliter). The rod microgels were 50–120 µm in width and 600–1000 µm in length. After cultivation for 7 days, the cells behaved very differently on microgels prepared from four-arm compared to eight-arm sPEG-Ac (Figure 5.10f). Cells on the four-arm sPEG-Ac microgels mostly interacted with each other and the well surface, forming a monolayer into which the rod microgels were incorporated. In contrast, cells attached to the eight-arm sPEG-Ac microgels, which remained separated with a few microgels stacked on top of each other. These results were expected because cells usually interact more with stiffer microgels, even though the 10-kDa four-arm and eight-arm sPEG-Ac resulted in similar Young's moduli.[288] This suggests a link between the RI and cell interaction. We then determined whether fibroblasts can assemble the microgels into a 3D MAP scaffold. Usually, spherical or rod-shaped microgels are chemically interlinked, resulting in 3D constructs with a fixed framework that limits cellular self-organization.[28,289] Therefore, we recently investigated how cells can build such scaffolds without chemical interlinking, based on the cell-induced

interlinking of biobased spherical microgels.[170] Different scaffold geometries were produced by these cells depending on the ratio of cells to microgels, the microgel stiffness, and the presence of cell-adhesion peptides on the microgels. Here, we selected the eight-arm sPEG-Ac microgels for assembly into 3D constructs based on the experiments where cells were seeded on top of the microgels (Figure 5.11a). As no significant difference was observed in interactions between cells and the 10-kDa and 20-kDa eight-arm sPEG-Ac microgels (Figure 5.11a), we selected the softer microgels for subsequent experiments because this reduces the amount of synthetic material required and maximizes diffusion. To produce MAP scaffolds, GRGDSPC-modified microgels (12 microgels/µL) were seeded with 1000–2500 cells ţL^{-1} (300,000–500,000 cells in total) on a PDMS-coated well plate, which prevents cells from attaching to the well surface and thus supports the formation of 3D constructs. The microgels and cells were co-incubated for 7 days and the resulting cellular constructs are shown in Figure 5.11b. Reliable quantitative analysis was ensured by staining the microgels and cells with two different immunofluorescent dyes. The total actin surface area and actin volume of the 3D cell/microgel assemblies were higher when we added more cells (Figure 5.11c-f), although the difference between 350,000 and 500,000 cells was not significant. Interestingly, the cell volume fraction (78 %) was similar for all cell numbers, even though the higher cell numbers led to overall larger constructs, and the variability of these volume fractions was high, especially at higher cell numbers. The cell volume fraction obtained with rod-shaped microgels was slightly higher than with spherical microgels (60-70 %).[170] This suggests that MAP scaffolds prepared from rod-shaped microgels increase macroporosity due to the high aspect ratio of the microgels.[28,29]

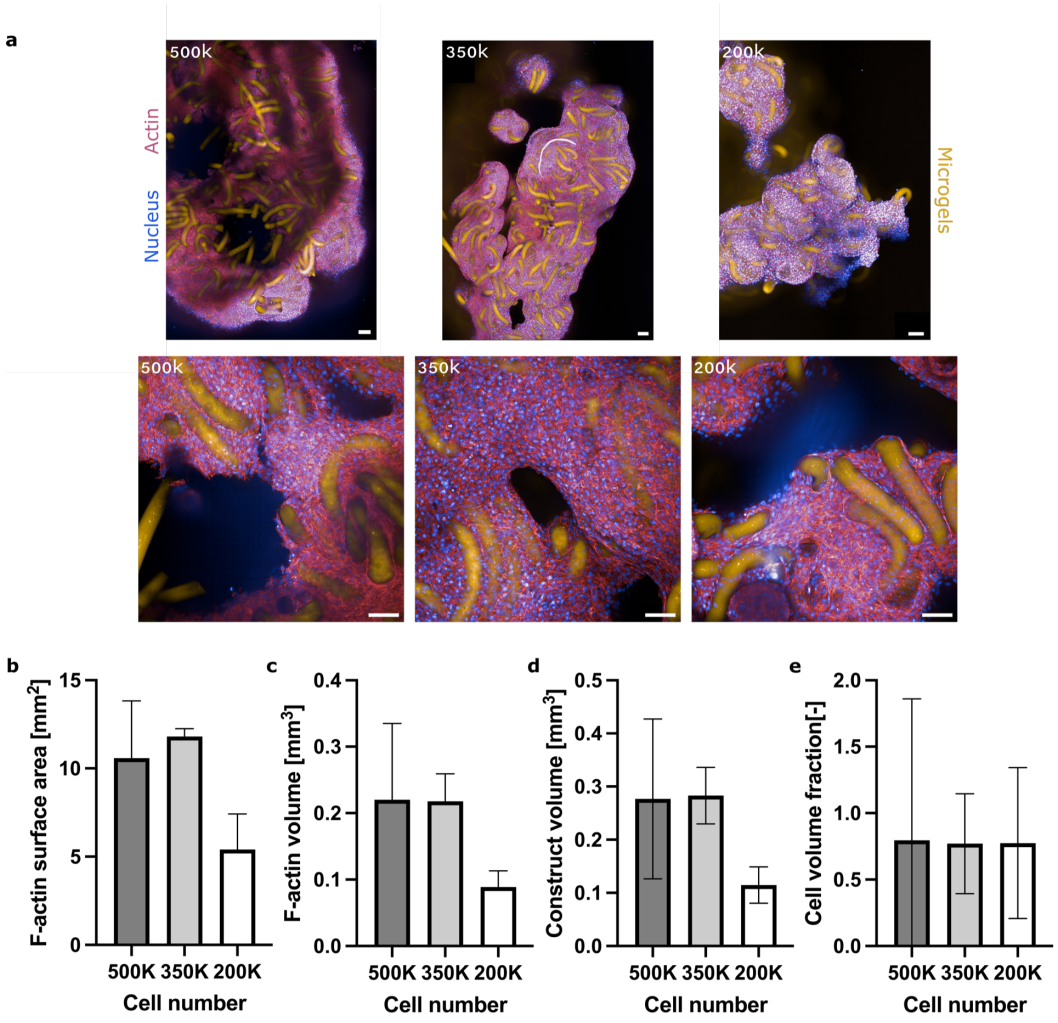

Fig. 5.11: Cell–microgel assembly. (a) Difference in microgel assembly: 3D cell-induced self-assembly of microgels with different numbers of L929 cells (500,000, 350,000 or 200,000) but a constant quantity of rod microgels. GRGDSPC-functionalized microgels were stained with rhodamine B (orange), F-actin (red), and DAPI (cell nuclei, blue). Scale bars = 100 µm. (b-e) Effect of cell number on microgel assembly: Quantitative image analysis (Imaris) of 3D constructs displaying (b) F-actin surface area, (c) F-actin volume, (d) construct volume, and (e) cell volume fraction versus cell number. Data are means ± standard errors.

5.3 Conclusion

We have, demonstrated for the first time, that CJP-based microfluidics is suitable for the continuous production of ultra-thin or ultra-soft and ultra-porous rod microgels. The microfluidic design was adjusted to ensure sufficient photo-polymerization enabling unique microgel properties. This expands the toolbox of material building blocks to produce more structured and denser 3D cellular constructs. Ultra-thin

PEGDA microgels produced by CJP are 20 times softer than the softest rod microgel prepared using PRINT. We established a protocol to post-functionalize the rod microgels with magnetic nanoparticles, resulting in magneto-responsive rods that align within 5 s even in a weak magnetic field. Their positions and orientation can be fixed by a surrounding 3D hydrogel to form an Anisogel. Preliminary results indicate that the lower difference in stiffness between the rod microgel and the surrounding hydrogel matrix reduces cellular alignment compared to equivalent PRINT rods. In addition to ultra-thin microgels, CJP was also used to produce ultra-soft rod microgels from sPEG-Ac, with large pores (2–5 µm). To enable cell-induced assembly of ultra-soft and ultra-porous microgels into MAP scaffolds, the microgels were post-modified with the cell-adhesion peptide GRGDSPC. Cell interactions with the microgels were dependent on the microgel's mechanical and structural properties. Only rod microgels prepared from eight-arm sPEG-Ac could be assembled by cells into large 3D MAP scaffolds. The fraction of cells found inside these 3D constructs was 78 %, which is higher than when spherical microgels were used in a previous study.[170] CJP can therefore produce ultra-thin or ultra-soft and ultra-porous microgels that are suitable and customizable for a wide variety of tissue engineering applications. They can, in the future, be introduced into automated pipetting systems to create *in vitro* tissue models and will provide insight into the degree of physical guidance cells need to grow and align in a specific direction.

5.4 Materials and Methods

5.4.1 Preparation of PDMS-based microfluidic devices

Microfluidic chips were produced by soft lithography[122] using the SYLGARD 184 Silicone Elastomer Kit (Dow Silicones, Corning, NY, USA). The PDMS and curing agent were mixed at a 10:1 ratio. Unwanted irradiation outside the laser spot was prevented by dissolving 60 mg Oil Red (ThermoFisher Scientific, Waltham, MA, USA) and 3 mg Quinoline Yellow (ThermoFisher) in 2 g of toluene, and adding 1 % (w/w) of the dye solution to the mixture, which was placed in a desiccator under vacuum (10^{-3} mbar) to remove air. The mixture was then cast in the mold and the air was evacuated again in the desiccator. The PDMS was cured in an oven for 10 min at 110 °C and left in a sealed Petri dish at room temperature overnight to complete the crosslinking process. The cured PDMS was cut out and the inlet and outlet holes were created using a biopsy puncher with an inner diameter (ID) of 0.75 mm. The PDMS form was washed three times with isopropanol and water and dried under nitrogen gas. A glass microscope slide (75 × 50 × 0.13 mm; Carl Roth, Karlsruhe, Germany) was rinsed three times with acetone and isopropanol. The PDMS replica and glass slide were then bonded in a 100E oxygen plasma oven (PVA TePla, Wettenberg, Germany) at an oxygen flow rate of 25-27 mL/min and a pressure of 0.2 mbar for 40 s at 100 W, followed by baking for 3 h at 60 °C to complete the adhesion. A hydrophobic surface coating was applied to the microfluidic channels by silanization with 97 % tridecafluoro-1,1,2,2-tetrahydrooctyl-trichlorosilane (Sigma-Aldrich, St Louis, MO, USA). The microfluidic device was placed in a desiccator with the silane and evacuated overnight, and excess silane on the surface was removed using paraffin oil (VWR-Chemicals, Radnor, PA, USA).

5.4.2 Preparation of pre-polymer solutions

The pre-polymer solutions were prepared in brown glass vials to prevent photo-initiation. Four- or eight-arm PEG-acrylate (molecular weight = 10 or 20 kDa) (JenKem Technology USA Inc., Plano, TX, USA) or PEGDA (700 Da) (Sigma-Aldrich) were dissolved at concentrations of 3-40 % (w/w) in an aqueous 3 % (w/w) solution of non-reactive PEG (400 kDa) (Sigma-Aldrich) filler to obtain an

end mass of 2000 mg. We added 1 % (w/w) LAP (Sigma-Aldrich) as a photo-initiator and 1 µL methacryloxyethyl thiocarbamoyl rhodamine B (Polysciences, Warrington, PA, USA) solution (10 mg in 100 µL DMSO (Sigma-Aldrich)) to label the microgels.

5.4.3 Microgel production

Microgels were produced as previously described.[122] The microfluidic station comprised two Pump 11 Elite syringe pumps (Harvard Apparatus, Holiston, MA, USA) and a DM IL LED inverted microscope (Leica Microsystems, Wetzlar, Germany) equipped with a Point Grey Fl3-U3-12Y3M-C camera (FLIR Systems, Wilsonville, OR, USA). The polymer solution and oil phase were injected using 1-mL or 5-mL gastight 1000 series syringes (Hamilton, Bonaduz, Switzerland) connected via polytetrafluorethylene (PTFE) tubing (BOLA S 1810-06, AD 0.9 mm x ID 0.400 mm; TECHLAB, Blacksburg, VA, USA). The syringe containing the pre-polymer solution was covered with aluminum foil and the microgels were collected in a protein LoBind tube (Eppendorf, Hamburg, Germany) filled with ethanol. An RLDE405M-100-5 laser module (Roithner Lasertechnik, Vienna, Austria) was mounted under the microscope stage to provide illumination at 405 nm and an angle of 45° to the sample surface, in a plane perpendicular or parallel to the microfluidic channel. Parallel positioning of the laser spot resulted in longer microgels due to the oval shape of the laser spot (∼115 x 60 µm). The power was set to 50 mW, and confirmed using a PM200 optical power and energy meter with a S302C sensor (Thorlabs, Newton, NJ, USA). The laser light polarization plane was adjusted to minimize reflection from the glass surface. Custom electronics based on Arduino DUE (Arduino, Milan, Italy) and custom software was used to generate laser pulses. The laser on-time was varied from 250 µs to 50 ms and the off-time was the on-time plus 50 ms to ensure separation of the rod microgels. Longer irradiation times generate longer rod microgels at a constant velocity. Both the exposure time and the velocity determine the width and length of the rod microgels.[122] The microgels were collected inside a LoBind Eppendorf tube filled with ethanol (99.8 %, VWR-Chemicals) and were purified by five rounds of centrifugation with ethanol and three with water (5000 rpm, 10 min using an Eppendorf 5810 R centrifuge). All bright-field images were recorded on an AE2000 inverted microscope (Motic, Barcelona, Spain) using a 10× objective equipped with a Point Grey Fl3-U3-12Y3M-C camera.

5.4.4 Numerical Simulation

Ansys Fluent 2023 R1 (Ansys, Canonsburg, PA, USA) was used for all numerical simulations of fluid flow inside the microfluidic channel. This software uses the finite volume method to solve the governing equations numerically. The fluids inside the microchannel were considered incompressible. Isothermal and laminar flow conditions were imposed, and a maximum root mean square (RMS) residual error of 10^{-5} was chosen for continuity and momentum equations and 10^{-4} for volume fraction equations. The volume of fluid (VoF) model was used for multiphase fluid flow. The physical properties of both phases (oil and polymer) were set based on experimental measurements. A grid study ensured the use of proper element sizes. Additional details of numerical modeling and simulation are provided below.

Details about the Simulation

Ansys Fluent 2023 R1 was used for all the numerical simulations of the fluid flow inside the microfluidic channel. The volume of fluid (vof) model is used for modeling multiphase fluid flow. In this method, a single set of momentum equations is solved throughout the fluid domain, and conservation of mass equation is utilized to track the volume fraction of each fluid. Thus, the general equations to be solved for such set of conditions and for q^{th} phase are:

$$\frac{1}{\rho_q}\left[\frac{\partial}{\partial t}\left(\alpha_q \rho_q\right) + \nabla .\left(\alpha_q \rho_q \vec{v}_q\right) = S_{\alpha_q} + \sum_{p=1}^{2}\left(\dot{m}_{pq} - \dot{m}_{qp}\right)\right] \tag{5.5}$$

$$\frac{\partial}{\partial t}\left(\rho\vec{v}\right) + \nabla .\left(\rho\vec{v}\vec{v}\right) = -\nabla\ \mathrm{p} + \nabla .\left[\mu\left(\nabla\vec{v} + \nabla\vec{v}^{T}\right)\right] + \rho\vec{g} + \vec{F} \tag{5.6}$$

where $\rho, \mu, p, g, \alpha, \vec{v}, Sand\vec{F}$ are fluid density, fluid viscosity, pressure, gravitational acceleration, phase volume fraction, velocity vector, source term and external force vector, respectively. $\dot{m}_{pq}$ the mass transfer from from phase q to phase p. Details of the solution method for a steady state simulation are listed in the Table 5.5. The mesh is automatically generated using Ansys mesh. No slip boundary condition was set at walls. A constant volumetric flow rate of 150 µL/h for oil phase and 50 µL/h for polymer phase is set at the respective inlets of the microfluidic device. The relative pressure is set to zero at the outlet. Different contact angles (0°, 90° and 180°) were considered for the polymer phase at the top (glass) and bottom (PDMS) walls of

Tab. 5.5: Details of the solution method for simulation of flow inside microchannel in Ansys Fluent.

		Spatial Discretization			
	Pressure Velocity Coupling	**Gradient**	**Pressure**	**Momentum**	**Volume Fraction**
Method	Coupled	Least Squares Cell Based	PRESTO!	Second Order Upwind	Compressive

microchannels. The iterative solution run until full convergence of all equations is reached. To ensure the use of proper element size, the grid study was performed on three cases of fine, medium and coarse meshes considering the velocity profile and polymer volume fraction on a diagonal line at the outlet of the microchannel (Figure 5.12) to guarantee mesh independency of the results.

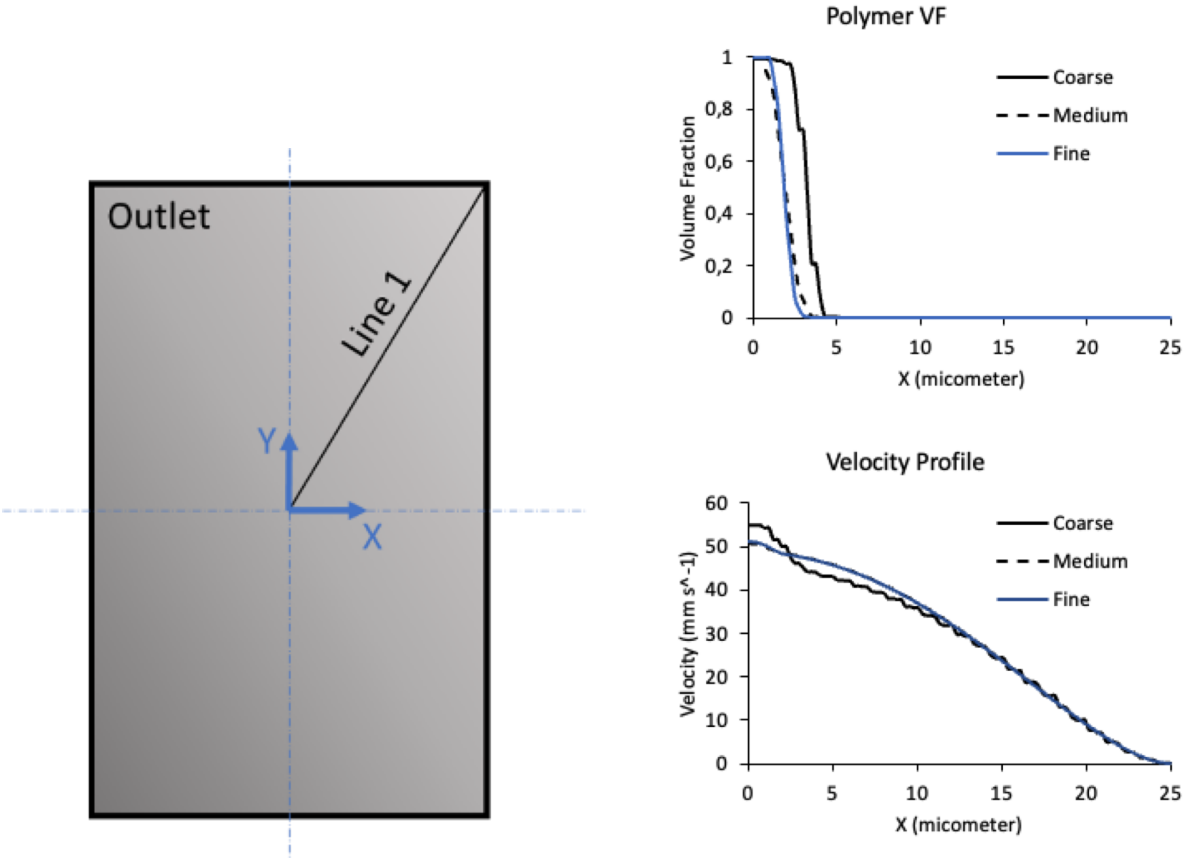

Fig. 5.12: Velocity profile and polymer volume fraction of different mesh sizes at the X positions on line 1. As it seen for medium and fine mesh, the velocity profile and polymer liquid fraction profile are very close indicating the decrease of the error by decreasing the mesh sizes. This guarantee the mesh independency of the final results.

5.4.5 Confocal microscopy of jet microfluidics

The pre-polymer solution was prepared as described above but without an initiator, and the oil phase was dyed with 99 % Cumarin 153 (Sigma-Aldrich). The samples were imaged using an SP8 tandem confocal microscope fitted with a 10×/0.3 NA air objective (Leica Microsystems). Z-stacks 200-250 µm thick were acquired for each sample. Images were captured at the appropriate excitation wavelengths and the emission signals were captured using hybrid detectors or photomultipliers, as appropriate. Images were processed and 3D reconstructions of the jet were prepared from confocal images using specific plugins provided by Fiji.[290] We first adjusted the brightness and contrast of each channel (red = polymer, green = oil) to optimize the visualization of the jet structure and then merged both channels in each z-stack position. We then used the "3D viewer" plugin to reconstruct the 3D images.

5.4.6 Prussian blue staining protocol

Microgels were incubated with 5 % (w/v) potassium hexacyanoferrate (II) (MORPHISTO, Offenbach am Main, Germany) for 5 min at 40 °C. To the mixture an equal volume of 5 % (v/v) HCl (MORPHISTO) was added to react at 40 °C for 30 min. The microgel suspension was purified by centrifugation with distilled water as described above, and images were captured by fluorescence microscopy using a DM RX instrument (Leica Microsystems).

5.4.7 Magnetic functionalization of rod microgels and verification of magnetic alignment

For the *in situ* functionalization either EMG700 (Ferrotec, Bedford, NH, USA) or PBG300 (Ferrotec) SPIONs were added in the desired concentration to the pre-polymer solution. To post-functionalize, the microgels were mixed with a solution containing 1 % (w/w) LAP and 200–600 µg/mL PEGMA SPIONs (micromod Partikeltechnologie, Rostock, Germany) and were then exposed to a custom LED in the UV range (λ = 365, spot diameter 4.7 mm, 135 mW/cm) for 10 min. The quantity of nanoparticles was calculated relative to the microgel volume in the microgel dispersion to keep the microgel volume constant. The microgels were then purified by centrifugation with

ultrapure water three times (5000 rpm, 10 min, Eppendorf 5810 R centrifuge). The magnetic response was tested by pipetting a small droplet onto a glass slide exposed to a magnetic field of 70 mT.

5.4.8 Sterilization of rod microgels

Before cell experiments, the (magneto-responsive) rod microgels were sterilized by immersing them in ethanol and exposing them to UV light for 1 h. Afterwards, they were purified by centrifugation with ultrapure water as above, and stored in ultrapure water at 4 °C.

5.4.9 Matrix hydrogel preparation

The PEG hydrogel was prepared as previously described.[65,252] Briefly, two separate batches of eight-arm star PEG-VS (20 kDa; CreativePEGworks) were conjugated with peptide solutions in triethanolamine, pH 8 (Sigma-Aldrich). The peptide sequences were H-NQEQVSPLERCG-NH_2 (Q-peptide; 1358.6 Da, GenScript, NL) and Ac-FKGGGPQGIWGQERCG-NH_2 (K-peptide; 1717.6 Da, GenScript). Conjugation to cysteine residues involved Michael-type addition by incubating the solutions for 2 h at 37 °C. The solutions were then dialyzed for 4 days against water at 4 °C to remove any unreacted peptides. The solutions were lyophilized, dissolved in water, UV sterilized, and stored at -20 °C until further use. For gel preparation, equimolar amounts of the two PEG conjugates were mixed at a total concentration of 1.25 %(w/v) in cell culture medium, along with a 10× calcium buffer (0.1 M $CaCl_2$, 0.5 M Tris, 1.1 M NaCl (Sigma-Aldrich)), 1 %(v/v) of the rod microgels, and 600 µM of the cell adhesion peptide GRGDSPC (CPC Scientific, Milpitas, CA, USA), as well as L929 mouse fibroblasts (passage 8-12, (Deutsche Sammlung von Mikroorganismen und Zellenkulturen GmbH, DSMZ ACC-2) (700 cells/µL). Gelation was initiated by adding 1250 U FXIIIa (CSL Behring, King of Prussia, PA, USA), which was activated by diluting 200 U/mL thrombin (Sigma–Aldrich) to 20 U/mL in a buffer (25 mM $CaCl_2$, 10 mM Tris, 150 mM NaCl) and incubating with the FXIII pro-enzyme for 30 min at 37 °C, shaking gently every 5 min. The FXIIIa was then aliquoted and stored at -80°C until further use. The hydrogel mix was pipetted in 15-µL droplets into 15-well ibidi plates and flipped to ensure the distribution of the microgels in three

dimensions. A self-made magnetic holder was placed around the plate, with opposing magnets creating a field of $\sim$ 70 mT across the hydrogel droplets. The hydrogels were flipped back after 5 min and incubated at 37°C in a 5 % CO_2 atmosphere to complete the gelation. The magnets were removed and 45 µL of DMEM (Gibco, Thermo Fisher Scientific) supplemented with 10 % FBS (Gibco or Biowest, Nuaillé, France) and 1 % antibiotics/mycotics (AMB; Gibco), and incubated for seven days at 37°C in a 5 % CO_2 atmosphere.

5.4.10 Immunostaining of hydrogel samples and cells

After seven days in culture, the samples were washed twice with phosphate-buffered saline (PBS, pH = 7.4, c = 1x, Thermo Fisher Scientific) and the cells were fixed with 4 % PFA (Sigma-Aldrich) for 30 min at room temperature (3D: 1 h), followed by washing with PBS for 10 min (3D: 30 min), 0.1 % (v/v) Triton X-100 (Sigma-Aldrich) for 10 min (3D: 20 min) and PBS for 10 min (3D: 30 min). F-actin filaments were stained using phalloidin-633 diluted 1:1000 (Abcam, Cambridge, UK) in 4 % BSA in PBS for 1 h (3D: 4h), followed by washing with PBS. Cell nuclei were stained using 4',6-diamidino-2-phenylindole (DAPI) (Thermo Fisher Scientific) diluted 1:100 in PBS for 20 min, followed by washing twice with PBS. The samples were washed three times with PBS for 10 min and stored at 4 °C. The stained cells were imaged using an Opera Phenix Plus High-Content Screening System (PerkinElmer, Shelton, CT, USA) with 10x/0.3 NA or 20x/1.0 NA air objectives. Z-stacks with a z-gap of 7.4 (10x objective) or 3.6 µm (20x objective) were recorded for each sample. For quantification of the 3D MAP constructs, the z-stacks were converted to Imaris file format using Imaris File Converter v9.91 and stitched together with Imaris Stitcher. The images are analyzed with Imaris v10.0 software (Oxford Instruments, Oxford, UK) by creating 3D volume renderings of the F-actin stained structures, as well as Rhodamine B stained microgels, using the surface rendering module with individually selected thresholds. To exclude unwanted structures in the cell volume, structures with a voxel number < 100 were omitted. To investigate the influence of cell/microgel ratios, we quantified the construct volume, F-actin area and F-actin volume, and microgel volume. The cell volume fraction was quantified as a fraction of the sum of microgels and F-actin (cell) volume resulting in the total construct volume.

5.4.11 Analysis of microgel and cellular alignment

Microgel and cell images obtained by laser scanning confocal fluorescence microscopy were analyzed using a python program[291] as described in more below.First a background image is created blurring the original images with a Gaussian kernel (for example: 241 pixels window width with 40 pixels standard deviation), and subtracted from the original. The resulted negative pixels are set to 0. In a second run a smoothing filter is applied the (e.g. width of window 11 pixels, standard deviation of 1 pixel). Orientation is determined using an elliptical Mexican hat filter (the second derivative of a Gaussian, with a window width of 41 pixels, standard deviations 10 and 0.5 pixels in the long and short directions respectively). The filter kernel is rotated between 0 and 180 degrees at 20 angle values. The maxima along these 20 angles are determined for each pixel and the corresponding angle values recorded. Optionally a blob removal gets performed using removing pixels which has a coherence parameter larger than 0.5 calculated via the structure tensor method.[292] On this maxima image, a threshold was defined using the method of Otsu to separate object pixels from the background. On the remaining object pixels, the corresponding angles were converted to a histogram, which can also be rotated such that its maximum points towards 0.

5.4.12 Rheology measurements

Rheological characterization was carried out using a Discovery HR-3 hybrid rheometer (TA Instruments, New Castle, DE, USA) with 20-mm parallel plate geometry. We transferred 381 µL of the pre-polymer solution to the rheometer at 25°C followed by the time-dependent measurement of polymerization under 10 mW/cm^2 UV light with a frequency of 1 Hz and an oscillation strain of 1 %. We also took frequency-dependent measurements at a set oscillation strain of 1 % and strain-dependent measurements at a set frequency of 1 Hz. Each material was measured as triplicate samples.

5.4.13 Stiffness of microgels determined by AFM

AFM point force spectroscopy was carried out using a Dimension Icon AFM (Bruker, Billerica, MA, USA) and a CP-PNPL-PS-D-5 colloidal probe (NanoAndMore, Wetzlar, Germany) with a nominal diameter of ∼2 µm. The force probe was mounted on a

liquid probe holder glass prism. Samples were measured in the lid of a 3 cm diameter Petri dish containing water to a height of ∼1 mm. Force curves were measured with an approach and retraction speed set to 1 µm/s, and a waiting time of 100 ms at contact. The maximum relative force was set to 4 nN. All curves were exported as ASCII files. The approach part of the curves was analyzed using the custom script AFMIndentation[293] in Python[294] based on the Hertz model (equation below). The Poisson ratio was assumed to be that of an incompressible material (ν = 0.5). The last 20 % of the data points were fitted to a line and subtracted as background.

$$F(\delta) = \frac{4}{3}\frac{E}{1-\nu^2}\sqrt{R}(\delta - \delta_0)^{\frac{3}{2}}) \tag{5.7}$$

The model was fit up to a force of 5 nN, practically the whole force range of the curve using a nonlinear fit (leastsq() from Scipy[295] finding both the Young's modulus and the contact point. At least three microgels (N > 3) were indented per condition and an average of all the indentation results per microgel was calculated as its Young's modulus.

5.4.14 Porosity analysis

A TCS SP8 3X confocal microscope (Leica Microsystems) with an 86x/1.2 NA water immersion objective (Leica HC PL APO CS2-STED White) was used to examine microgels labeled with Rhodamine B (Polysciences, Warrington, PA, USA) embedded inside a hydrogel. The excitation wavelength was set to 541 nm and the detection band was restricted to 560-700 nm with a multiband spectrophotometer in front of a HyD hybrid detector (Leica Microsystems). All images were captured at a room temperature (22.5 °C) in a 1024 x 1024 pixel format with 20 nm pixel size. Images were processed using a custom python script[294] based on ImageP.[296] Images were sharpened by removing off-plane light with background correction. Background was calculated by convolving images with a somewhat flattened Gaussian kernel using a standard deviation of 10 pixels, but truncated to a window size of 41 pixels (normalized to its sum). Then this background was subtracted, and negative intensity values were set to zero. The resulting image was smoothened by convolving it with another Gaussian kernel (standard deviation of 1 pixel, window size 7 pixels) then converted to a binary image cut with a threshold determined using Otsu's method.[297] The identified pores were skeletonized based on a distance transform, where local maxima were identified with a minimum step size of 1 (intensity difference between

neighbors). Because the distance transform sets the pixels to the square of their Euclidian distance from the nearest edge pixel, the double of the square root of the maximum pixels provides a local size measure of the pores. These values were collected and used to build histograms of the distances within the image.

5.4.15 Brillouin microscopy

Brillouin frequency shift maps were acquired using a confocal configuration for acoustic phonon excitation and signal detection, and a Brillouin spectrometer consisting of a two-stage virtually imaged phase array (VIPA) etalon, as previously described.[298] Briefly, the sample was illuminated with a frequency-modulated diode laser beam (λ = 780.24 nm, DLC TA PRO 780; Toptica, Munich, Germany). The laser light was coupled into a single-mode fiber and directed into the side port of an Axio Observer 7 inverted microscope stand (Carl Zeiss, Jena, Germany), where an objective lens (20x/0.5 NA, EC Plan-Neofluar; Carl Zeiss) illuminated the focused laser beam on the sample mounted on a motorized microscope stage. The backscattered light from the sample was collected by the same objective lens and coupled into the second single-mode fiber to achieve confocality before delivery to the Brillouin spectrometer. In the Brillouin spectrometer, two VIPA etalons (OP-6721-6743-4; Light Machinery, Ottawa, Canada) with the free spectral range of 15.2 GHz converted the frequency shift of the light into the angular dispersion in the Brillouin spectrum, which was acquired by a sCMOS camera (Prime BSI; Teledyne, Thousand Oaks, CA, USA) with an exposure time of 0.5 s per measurement point. The two-dimensional Brillouin frequency map of the sample was created by scanning the x-y motorized microscope stage with a translational step size of 0.5 µm. The Brillouin microscope was controlled with custom acquisition software written in C++[299] and the Brillouin frequency shift was evaluated using custom software.[300]

5.4.16 Optical diffraction tomography

The RI distribution of microgel rods was assessed by ODT, which uses Mach-Zehnder interferometry to capture multiple complex optical fields from diverse incident angles.[301] A solid-state laser beam (λ = 532 nm, 50 mW; CNI Optoelectronics Technology, Changchun, China) was split into two paths, one serving as a reference

beam and the other illuminating the sample on the stage of an Axio Observer 7 inverted microscope via a tube lens (f = 175 mm) and a water-dipping objective lens (40x/1.0 NA; Carl Zeiss). The diffracted beam from the sample was collected by a water immersion objective lens (63x/1.3 NA; Carl Zeiss). We reconstructed 3D RI tomograms by illuminating the sample from 150 incident angles and scanning with a dual-axis GVS212/M galvanomirror (Thorlabs) aligned with the conjugate plane of the sample. The diffracted beam interfered with the reference beam at an image plane, generating a spatially modulated hologram that was recorded using a CMOS camera (MQ042MG-CM-TG; XIMEA, Münster, Germany) with a field-of-view covering 173.6 x 173.6 µm. Complex optical fields were extracted from the recorded holograms using a Fourier transform-based field retrieval algorithm. The 3D RI distribution of the samples was then reconstructed using Fourier diffraction theorem with first-order Rytov approximation[302,303] as described in detail elsewhere.[304] We used a MATLAB script for ODT reconstruction.[305]

5.4.17 Small-angle X-ray scattering

SAXS experiments were carried out using beamline KWS-X (XENOCS XUESS 3.0 XL) at JCNS MLZ.[306] The X-ray source is a D2+ MetalJet (Excillum, Kista, Sweden) with a liquid metal anode operating at 70 kV and 3.57 mA with Ga-Kα radiation (wavelength λ = 1.314 Å). Samples were analyzed in a glass capillary (2 mm ID) at room temperature (25 °C). The sample-to-detector distances were 0.5 m and 1.7 m, which covered a scattering vector q range of 0.002–1.1 $Å^{-1}$. Q is the scattering vector, where $Q = \frac{4\pi}{\lambda} \sin\theta$, and 2θ is the scattering angle. The SAXS patterns were normalized to an absolute scale and azimuthally averaged to obtain intensity profiles, from which the solvent background was subtracted.

5.4.18 Cell culture

L929 mouse fibroblasts were cultured in DMEM supplemented with 10 % FBS and 1 % antibiotics and mycotics at 37 °C in a humidified 5 % CO_2 atmosphere, as described above. For cell culture experiments, glass-bottom plates were coated with sterile PDMS using the SYLGARD184 Silicone Elastomer Kit as described above, and crosslinked at 60 °C for 90 min. A droplet of microgel suspension (20 µL) was transferred to the

PDMS and sedimented for 1 h. The well plates were filled up with media then seeded with L929 fibroblasts at a concentration of 200 cells/µL. The cells were cultivated for seven days as described above.

5.4.19 Diffusion experiment

A water-based solution consisting of FITC- dextran (0.05 mM, 500 kDa, Sigma-Aldrich) was prepared and mixed with the Rhodamin B labeled microgels. Confocal images were recorded using a SP8 tandem confocal microscope fitted with a 10x/0.3 NA air objective (Leica Microsystems). Z-stacks of 200-250 µm thick were acquired for each sample. Images were captured at the appropriate excitation wavelengths (561 nm Rhodamin B and 488 nm FITC-dextran) and the emission signals were captured using hybrid detectors or photomultipliers, as appropriate.

5.4.20 Statistical analysis

All data points are means with error bars indicating standard deviations with a sample size of at least 3, or as otherwise stated in the text. Statistical significance was determined by one-way or two-way analysis of variance (ANOVA) with Tukey's or Holm-Sidak's multiple comparisons test. Statistical tests were carried out using GraphPad Prism v10 (GraphPad Software, Boston, MA, USA) and significance was indicated as follows: *$p < 0.05$, **$p < 0.01$, ***$p < 0.001$, and ****$p < 0.0001$.

6 Development of an injectable dynamic covalent chemistry based hydrogel

6.1 Introduction

Recreating the ECM is a central challenge in tissue engineering. It is a dynamic microenvironment that regulates cell behavior through its hierarchical organization, viscoelastic properties, and biochemical signals.[2] Hydrogels have been extensively researched as candidates for ECM-mimetic scaffolds because their water-swollen can be adapted in many aspects regarding their (bio)chemical and mechanical properties.[307] However, hydrogels crosslinked with static covalent bonds or weak physical interactions do often not provide the adaptibility needed to resemble the ECM constant remodeling and responsiveness.[255]

Dynamic covalent crosslinking chemistries have emerged as a promising strategy, exhibiting reversible bonds that can provide structural stability of covalent networks while enabling bond exchange under physiological conditions.[172] Thus, dynamic covalent hydrogels are able to remodel as a reaction to cell-generated forces, can recover from shear or adapt their mechanical properties over time, and can degrade in a controlled manner.[202,308,309] These advantages make them interesting candidates in tissue engineering and regenerative medicine.

DCC-based hydrogels have been widely studied and applied in various 3D tissue engineering applications.[171] A key feature of dynamic covalent bonds is that they provide tissue-like stress relaxation, which is essential for regulating cell spreading, migration, and differentiation.[171,173,174] Furthermore, these reversible chemistries

enable recovery after deformation, making them suitable candidates for bioprinting and delivery by injection.[175–178] Several types of DCC have been developed, each presenting distinct properties needed to replicate characteristics of different native tissues. Hydrazone bonds, formed between hydrazine and aldehyde or ketone groups provide reversible behavior with adjustable gelation kinetics, dynamic remodeling capabilities, and good biocompatibility. Such features make them suitable for 3D cell culture and organoid systems.[171,179] Schiff base (imine) bonds, obtained through amines and aldehydes or ketones, are also reversible under mild conditions and present self-healing properties, as well as adjustable stiffness.[171,180] Other examples (a table including more examples can be found in Chapter 1), including boronate ester bonds, or disulfide exchange have been used in tissue engineering applications being responsive to pH or redox conditions.[176,181] These systems respond to environmental cues such as pH or redox conditions, enabling adaptive behavior needed for tissue-specific applications. Importantly, the relaxation time related to different chemistries can span distinct length scale, making it possible to mimic different native tissues. Boronic acid derivatives, for example, can tune stress relaxation over orders of magnitude.[184] Schiff base linkages, such as imine, hydrazone, and oxime bonds, can comprise relaxation times from seconds to months, which corresponds well to the mechanical properties found in the the brain or cartilage.[173,185,186,186] These bonds have been extensively studied using natural polymers such as HA,[191] but also PEG-based polymers.[191,310] The advantage of using Schiff Base PEG-based hydrogels is their strong self-healing capacity, making them ideal for injectable hydrogels or 3D bioprinting, as well as their mechanical properties that can be superior to other dynamic hydrogels.[187] Their hydrogel degradability can be slow and controlled making them good candidates for long-term scaffolds to support tissue regeneration.[188] Other DCC exhibit faster degradation rates, due to high pH sensitivity or higher glucose levels.[189]

Despite significant progress, the applicability of synthetic dynamic covalent hydrogels remains limited by the polymer architecture, reaction kinetics at physiological pH, and injectability. To date, most oxime and hydrazone-based systems have relied on HA with little advancement using PEG.[180,311] When looking for alternatives to our current PEGKQ hydrogel, Schiff base hydrogels emerged as strong candidates owing to their mechanical stability and tunability. In this chapter, we focused on developing a PEG-based Schiff base system that combined hydrazone and oxime chemistry to identify a new hydrogel matrix suitable for replacing the anisogel. This work was inspired by previous research of Boehnke *et al.*,[180] who employed 8-arm sPEG with

hydrazide, aldehyde, and aminooxy functional groups. By combining both types of cross-linking, they demonstrated enhanced control over the degradation behavior, as hydrazone linkages are more labile than oxime linkages. The biocompatibility was confirmed by incorporating a cell-adhesive peptide and successfully encapsulating MSCs. However, only one PEG architecture was tested and material characterization was limited to the storage modulus and self-healing experiments.

Building on this work, in this chapter 4-arm sPEG as an alternative backbone architecture is introduced. We hypothesize that reducing the number of arms would reduce the steric hindrance, thus altering the mechanical properties and injectability. In addition, strategies are introduced to accelerate the reaction kinetics at physiological pH. To improve gelation kinetics we employed a biocompatible catalyst that has previously been shown to enhance HA-based hydrazone formation.[191] We also considered a new catalyst and analyzed its potential. In this chapter, we determine the mechanical properties and the potential of the hydrogel to replace our current PEGKQ hydrogel matrix.

6.2 Results and Discussion

6.2.1 Synthesis of PEG-based precursors

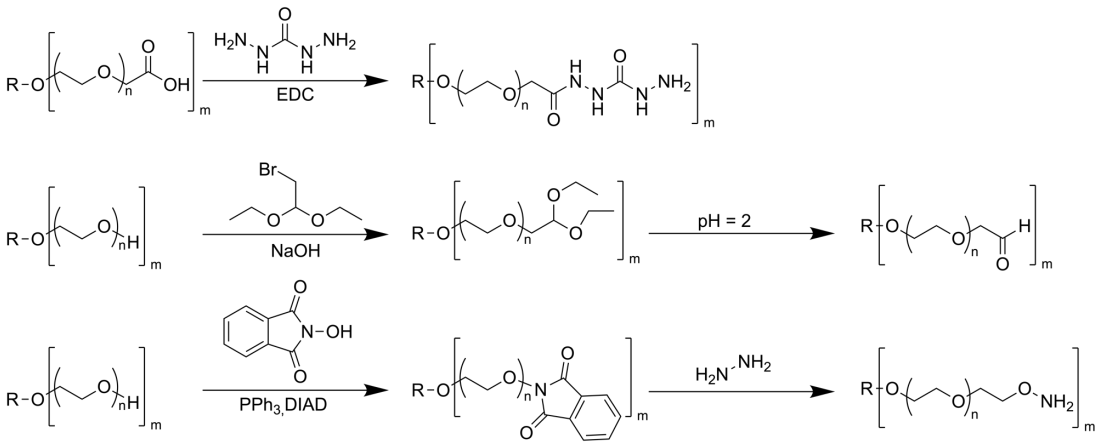

Fig. 6.1: Synthesis steps to form hydrogel precursor polymers to generate hydrazone/ oxime PEG based on a previous publication.[180]

The three components to form hydrazone and oxime hydrogels (aldehyde, aminooxy, and hydrazide) were prepared from 8-arm PEG (MW 20 kDa) based on a previous publication,[180] as well as 4-arm PEG (MW 10 kDa) (Figure 6.1). Choosing this architecture and molecular weight kept the chain length constant. Therefore, we could study the effect of the number of arms on the hydrogel formation and mechanical properties. Furthermore, there are no comparative studies regarding the alteration of the polymer architecture. Previously, two different hydrazide polymers were used, which exhibited different degradation rates. PEG-carbodihydrazide (PEG-CDH) presented a greater bond stability, with hydrogels stable over multiple days (>2) than PEG-adipohydrazide (PEG-ADH). Hydrogels made of PEG-ADH degraded within two days when incubated in cell media. This was attributed to the increased resonance stability when the carbon chain is shorter between the hydrazide groups.[312] For that reason, we focused on carbohydrazide functionalized PEG, as we were aiming for cell culture studies > seven days. The hydrazide polymers were obtained through 1-ethyl-3-(3-dimethylaminopropyl)carbodiimide (EDC)-coupling using PEG-COOH with 8 or 4 arms.[313] We achieved an end group functionalization of 90 % for both PEG-CDH, 8-arm 20 kDa and 4-arm 20 kDa, respectively. PEG-aldehyde (PEGCHO) was prepared using Williamson ether synthesis with PEG-OH (8-arm 20 kDa, 4 arm 10 kDa) and 2-bromo-1,1-diethoxyethane where we obtained an end group conversion of 88 % and 74 % for PEG-CHO, 8-arm 20 kDa and 4-arm 10 kDa. The acetal was cleaved in both cases as previously reported using a phosphate buffer at pH 2 with increased temperature (60 °C).[314] First synthesizing the acetal enabled longer storage of the polymer until further use. The aminooxy-functionalized sPEG (PEG-AO) was synthesized performing a Mitsunobu reaction using N-hydroxyphthalimide with a subsequent reduction employing hydrazine to yield PEG-AO comprising 89 % and 97 % end group functionality for 8 arm and 4 arm, respectively.

6.2.2 Mechanical characaterization at pH 5.5

The hydrogels were formed by mixing equal amounts of each hydrazide and/or aminooxy-functionalized PEG with the aldehyde varying the number of arms in a phosphate buffer (100 mM) at pH 5.5. In case of a three component hydrogel, the aminooxy and hydrazide functionalized polymers were mixed at a 1:1 ratio. A pH of 5.5 was reported to yield a gelation time < 5 min, while a pH of 7.0 was known to significantly slow oxime formation.[315,316] Therefore, we first focused on a pH 5.5 to

evaluate gelation time and mechanical properties, varying polymer architecture and aminooxy vs. hydrazide contribution. Previously, polymer concentrations of 3.5 and 5.0 % (w/v) of total PEG were analyzed resulting in a gelation time of 60 s at pH 5.5, comprising storage moduli in a range of 1500 to 3500 Pa.[180] We first determined the lowest possible polymer concentration using a two component system consisting of PEG-CDH or PEG-AO and PEG-CHO (Figure 6.2).

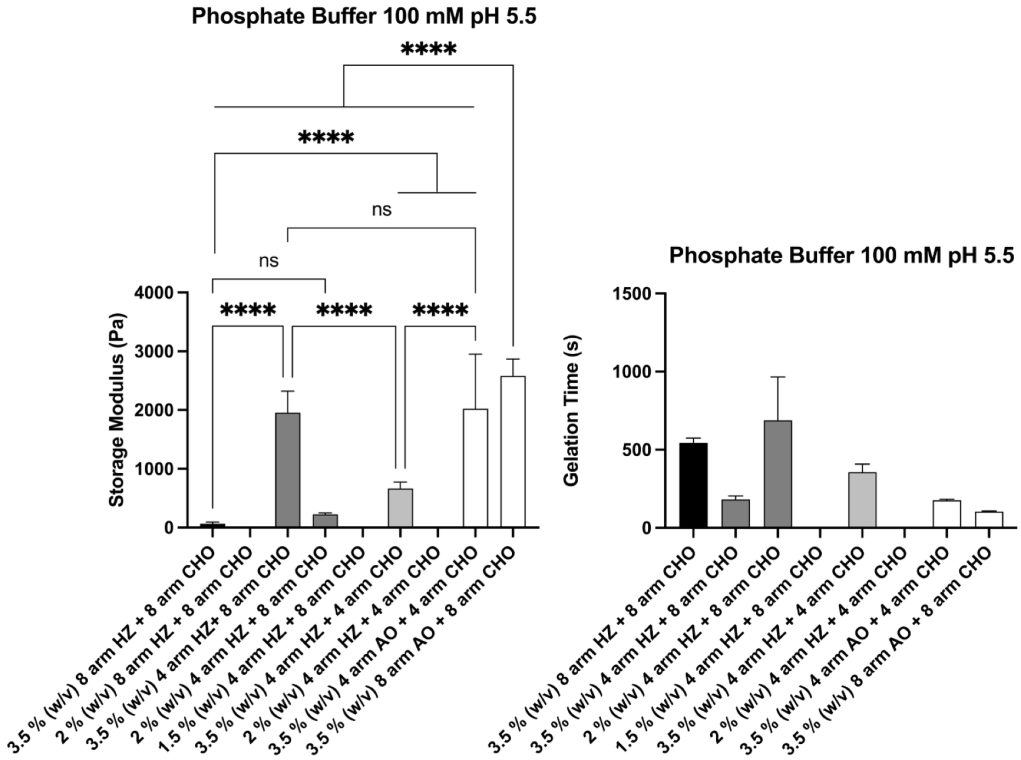

Fig. 6.2: Rheological characterization of bulk hydrogels made of PEG-CHO and PEG-CDH or -AO with different total PEG concentrations at pH 5.5 altering the number of arms. Data are means ± standard errors. Statistical significance was determined by one-way ANOVA with Tukey's multiple comparison test (*p < 0.5; **p < 0.01; ***p < 0.001; ****p < 0.0001).

We observed, using rotational rheology, that the lowest possible concentration of 2 % (w/v) was achieved combining 4-arm PEG-CDH (MW 10 kDa) with 8-arm PEG-CHO (MW 20 kDa) presenting a storage modulus (G') of 226.10 ± 20.60 Pa and a gelation time of 688.00 ± 277.40 s. Surprisingly, using 8-arm PEG-CDH and 8-arm PEG-CHO (MW 20 kDa) was limited to 3.5 %(w/v) exhibiting a G' of 64.20 ± 32.20 Pa and a gelation time of 544.30 ± 30.64 s. Although 2 % (w/v) using 8-arm PEG-CDH (MW 20 kDa) with 8-arm PEG-CHO (MW 20 kDa) a storage modulus of 6.82 ± 2.15 Pa was detected, no gelation time could be determined, indicating that with this composition the hydrogel was not sufficiently cross-linked. The lower storage

modulus using only 8 arm components versus a combination of 4-arm PEG-CDH with 8-arm PEG-CHO might be due to the enhanced diffusion when using less branched polymers. Interestingly, hydrogels with a concentration of 3.5 %(w/v) but 4-arm PEG-CDH and 4-arm PEG-CHO (MW 10 kDa, each) showed a lower storage modulus of 664.60 $\pm$ 109.40 Pa but a shorter gelation time of 356.67 $\pm$ 51.07 s, than their 8-arm counterpart. The better diffusivity when using less branched polymers could reduce the gelation time, though the functional groups might be more difficult to reach when the polymer chains are shorter. When replacing the hydrazide with the aminooxy polymer we observed an increase in storage modulus and a decrease in gelation time (Figure 6.2). However, using oxime vs hydrazide showed greater network formation when using 8 vs 4 arm PEG, which was the opposite when using hydrazide functionalized PEG. This might be due to different reaction kinetics when forming oxime versus hydrazone bonds, as the data indicates faster gelation kinetics for oxime formation, which is supported by literature.[222] Faster reaction kinetics might have a greater impact than diffusion, though to confirm these observations more experiments have to be performed.

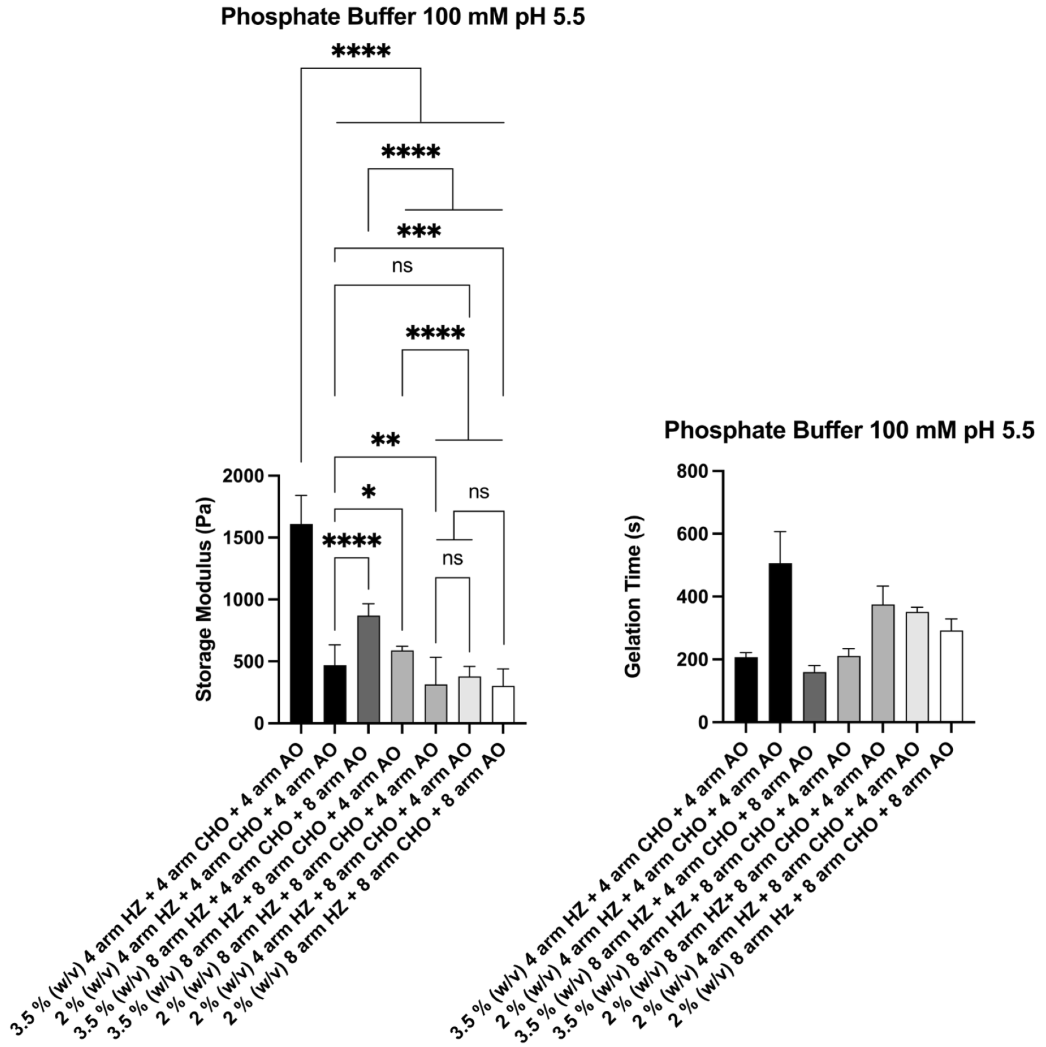

Fig. 6.3: Rheological characterization of bulk hydrogels made of PEG-CHO and PEG-CDH or -AO with different total PEG concentrations at pH 5.5 altering the number of arms. Data are means ± standard errors. Statistical significance was determined by one-way ANOVA with Tukey's multiple comparison test (*p < 0.5; **p < 0.01; ***p < 0.001; ****p < 0.0001).

Looking at the three component system with equal amounts of CDH to AO a lowest polymer concentration of 2 % (w/v) of total PEG was achieved for multiple conditions, which is likely due to the introduction of the AO group, as observed above. Probing only 4-arm PEG components vs only 8-arm PEG components showed an increase in G' when using only 4-arm from 303.30 ± 136.70 Pa to 469.4 ± 164.4 Pa, but also an increase in gelation time from 292.40 ± 36.90 s to 506.30 ± 100.80 s (Figure 6.3). These results are in opposite to our findings above, where using less branched polymer decreases the gelation time. Here, more experiments are needed to fully understand how the diffusion and reaction rate impact the network formation. The stiffest hydrogel composition was obtained using 3.5 % (w/v) of only 4-arm

polymer components reaching a G' of 1609.00 ± 231.10 Pa. All hydrogel compositions exhibited shear recovery behavior, showing thixotropy (Figure 6.4), where the two component system recovered faster than the three component system. Hydrazone bonds are known to provide self-healing attributes owing to their kinetic exchange dynamics.[308,317,318]

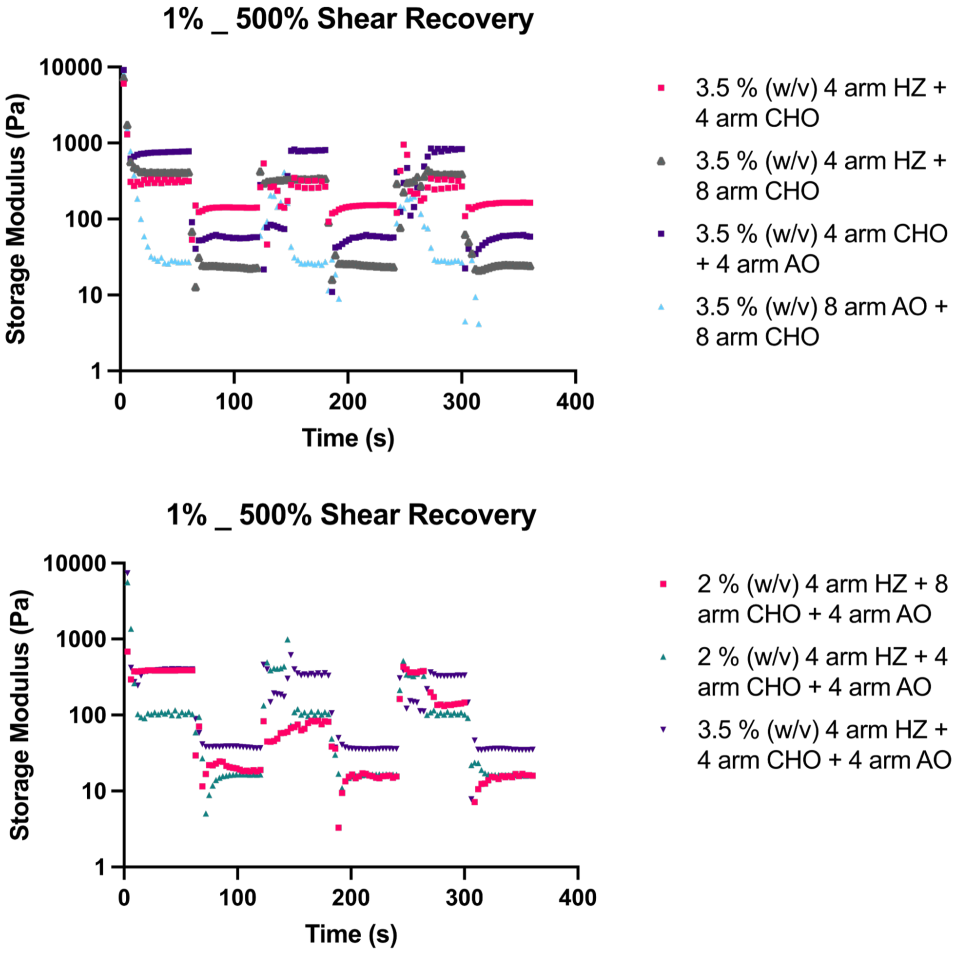

Fig. 6.4: Shear stress experiments at 1 and 500 % probing different hydrogel compositions at pH 5.5.

With the aim of replacing our current hydrogel system, we conducted an initial experiment preparing a hydrogel as an Anisogel. We prepared the polymer components (8-arm PEG-CHO and 4-arm PEG-CDH) at pH 5.5, and added 1 vol % rod microgels prepared via PRINT. The microgels were 10x10x50 μm^3 in dimensions and were composed of 20 % (w/v) PEGDA with 400 µg/ml SPIONs (EMG700). The total PEG concentration was set to 2 % (w/v), as this was the lowest possible concentration with this combination. The components were mixed and alignment was obtained through an external magnetic field (50 mT). We observed a distribution

of the rod microgels in 3D, as well as alignment of the rod microgels parallel to the magnetic field lines (Figure 6.5).

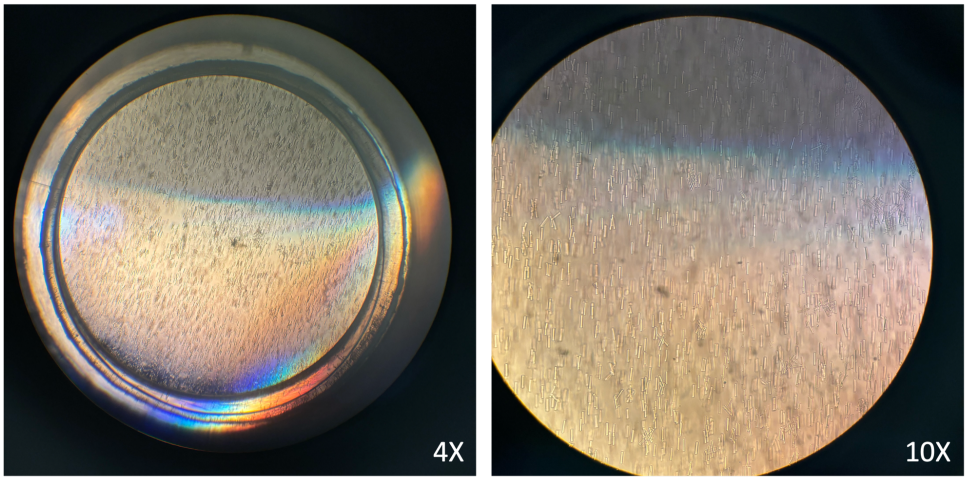

Fig. 6.5: Anisogel experiment using a DCC hydrogel. The hydrogel was made of 2 % (w/v) total PEG concentration using 8 arm PEG-CHO and 4 arm PEG-CDH with 1 vol % PRINT rod microgels with dimensions of 10x10x50 μm^3 using an external magnetic field (50 mT).

6.2.3 Enhancing the reaction kinetics at pH 7.4 through the addition of a catalyst

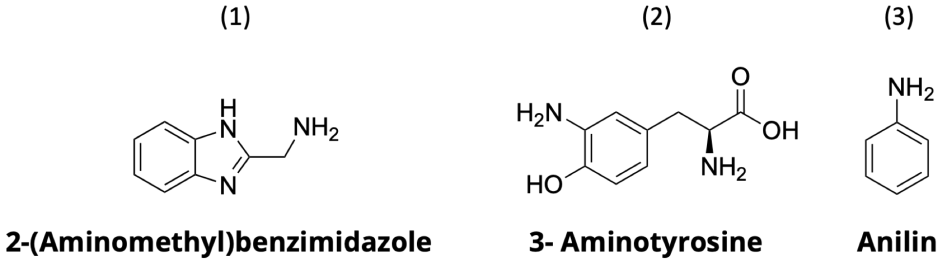

Fig. 6.6: Different catalysts used in this work to accelerate the reaction kinetics. Catalyst (1) and (3) are based on previous research.[191,192]

As the gelation time of oxime and hydrazone bonds drastically increase as physiological pH 7.4 from minutes to multiple hours, we were looking for alternative approaches to prepare the hydrogels.[315,319] Hydrazone formation is typically going through a tetrahedral intermediate, that is rate limiting at neutral pH.[320,321] Considering using this hydrogel with the Anisogel system, such long gelation times are not feasible, as for example *in vitro*, all rod microgels present in

the matrix would sediment to the bottom of the hydrogel. To solve this issue, there are several measures that can be considered. One would be to adapt the functional groups, such as analyzing the difference of aliphatic or aromatic derivatives with respect to the reaction rate.[190] However, as this would mean to synthesize new compounds, we decided to look for ways to catalyze the reaction. Based on literature, a biocompatible benzimidazole-based catalyst has been proven to catalyze HA-based hydrazone chemistries, and to increase the reaction rate by 30-fold (Figure 6.6 (1)).[191] Additionally, using a catalyst can offer the possibility to temporally tune the dynamic exchange of the bonds, which in return affects the mechanical properties of the hydrogel.[191] Furthermore, we looked for amino acids that resemble the structure of aniline, a well known catalyst for this type of reaction, though aniline cannot be used in this context due to its cytotoxicity.[192,315,319] We opted for 3-aminotyrosine (Figure 6.6 (2)), an unnatural amino acid, that could comprise biocompatibility. To assess the effect on the reactivity using the different catalysts proposed above, we conducted a small screening using model molecules (carbodihydrazide and benzaldehyde at a 1:2 ratio). We added the different catalysts at a concentration of 100 mM to two buffers comprising a pH of 5.5 and 7.4, and used the analytical HPLC to follow the reaction. As a standard, we used aniline in the same concentration to compare the reaction rate (Figure 6.6 (3)). The results are depicted in Figure 6.7 .

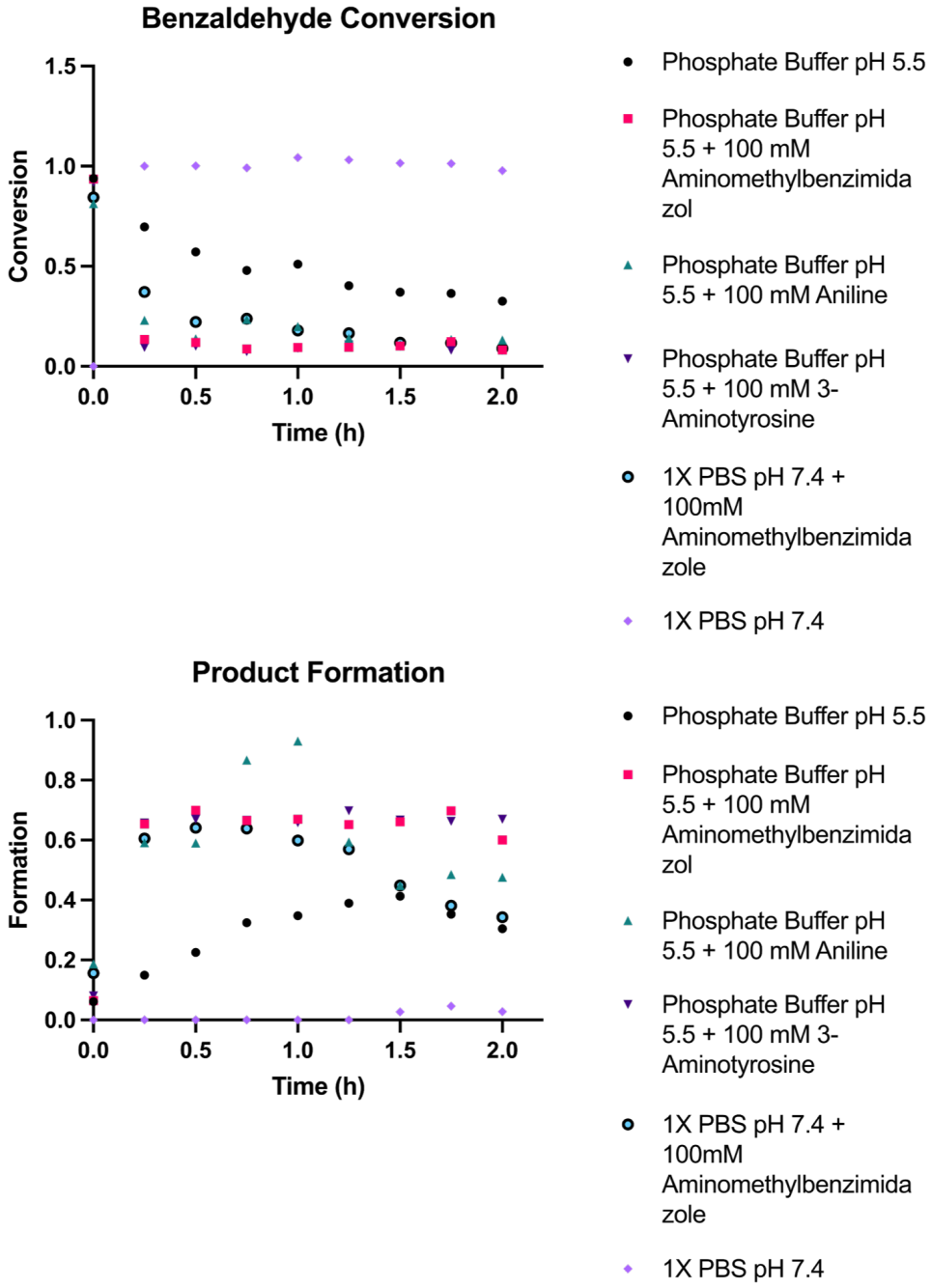

Fig. 6.7: Small molecular screening analyzing the reaction rate using different catalysts at different pH. To model the reaction benzaldehyde and carbohydrazide were used at a reaction concentration of 1 mM. Three different catalysts were used at a concentration of 100 mM supplemented to either a phosphate buffer (100 mM) at pH 5.5 or 1x PBS at pH 7.4. The reaction was followed via analytical HPLC monitoring at λ = 220 and 254 nm while time points were recorded every 0.25 h.

A significant increase in reaction rate was observed using both proposed catalysts at physiological pH. Interestingly, the addition of a catalyst at pH 5.5 increases the

reaction rate even when compared to the solution of purely buffer at pH 5.5. At pH 7.4 no product was formed in the measured time frame when only using 1x PBS. Afterwards, the catalyst (Figure 6.6 (1)) was used to make hydrogels at different polymer concentrations while varying the functional groups (Figure 6.8). At pH 7.4 we were able to form hydrogel using PEG-CDH and PEG-CHO at a total PEG concentration of 3.5 % (w/v). The gelation time was decreased from hours (data not shown) to below 15 min. The shortest gelation time was achieved when using both 4-arm PEG components with about 400 s. Mixing all three components enabled the formation of hydrogels at the given pH with a polymer concentration of 2 % (w/v), giving G' < 100 Pa. At 3.5 % (w/v) the gelation time was decreased to below 50 s with storage moduli between 500 and 800 Pa.

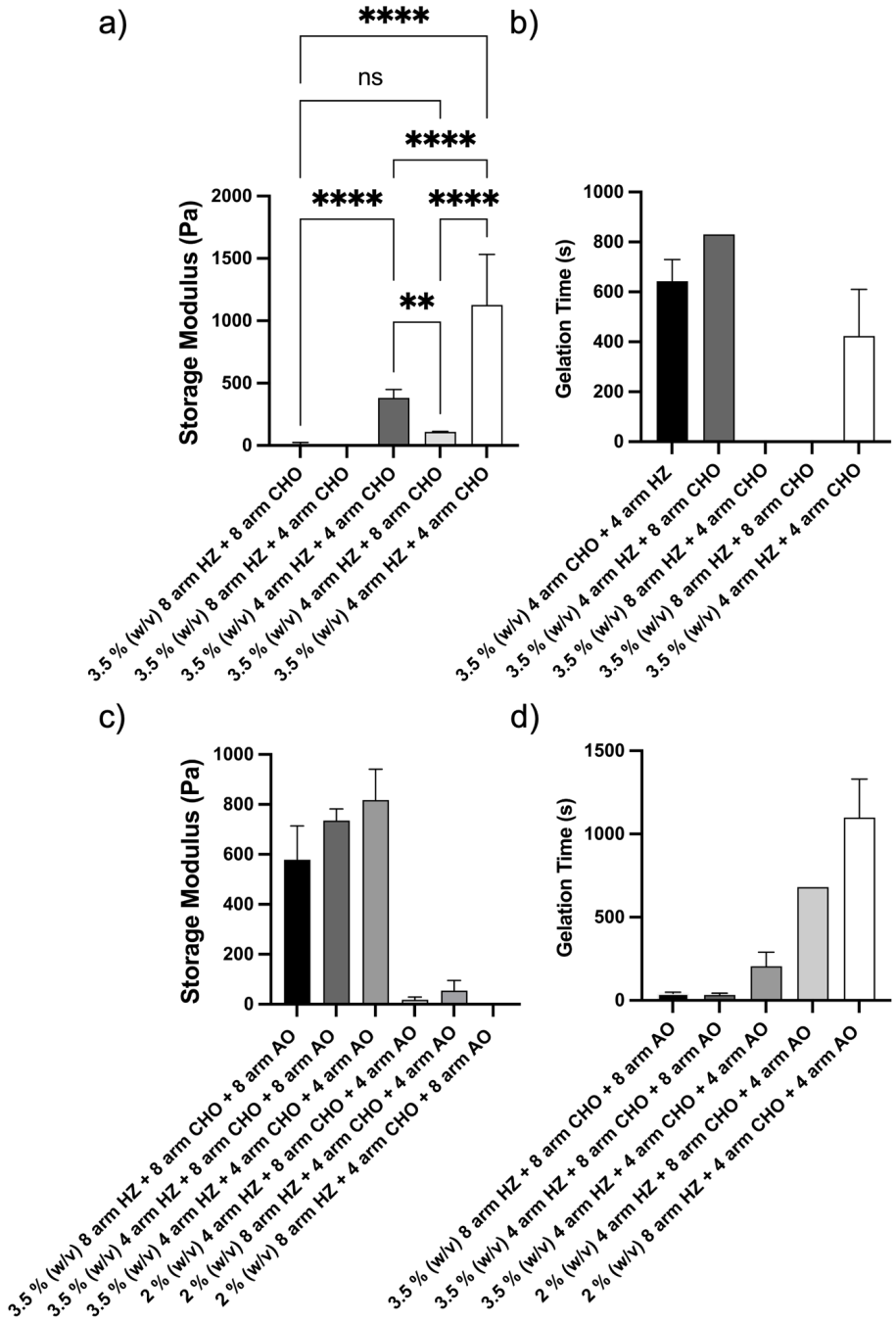

Fig. 6.8: Rheological characterization of catalyzed hydrogel formation at pH 7.4. Benzimidazole was added (100 mM) to 1x PBS to form the hydrogels at different concentrations and polymer combinations. a) Storage modulus of the two component system and the corresponding b) gelation time. c) Storage modulus of the three component system and the corresponding d) gelation time. The hydrogel made of 8 arm hydrazide, 4 arm aldehyde and 8 arm aminooxy with 2 % (w/v) was too soft to yield a gelation time. Data are means ± standard errors. Statistical significance was determined by one-way ANOVA with Tukey's multiple comparison test (*p < 0.5; **p < 0.01; ***p < 0.001; ****p < 0.0001).

6.2.4 Evaluating the injectability of different hydrogel compositions

With the idea to find an alternative to our current surrounding Anisogel matrix, this chapter focused on the injectability of the dynamic covalent hydrogel. In previous work using a 4-arm PEG-based hydrogel cross-linked via dynamic covalent thia-conjugate additions, rheological analysis presented shear thickening behavior at low shear rates before showing flow instability at higher shear rates.[322] Nonetheless, they reported extrudable hydrogels at clinically relevant settings with injections forces below 50 N.[323] To assess the different behavior when exposed to shear we conducted rotational rheology measuring the viscosity while varying the shear rate from 0.01 to 10 1/s (Figure 6.9). We chose different hydrogel compositions and compared hydrogels prepared at pH 5.5 and pH 7.4 with supplemented catalyst. In all probed conditions we could observe first an increase in viscosity at low shear rates (0.01-0.1), depicting shear thickening behavior, followed by flow instability at higher shear rates (0.1-10) (Figure 6.9).

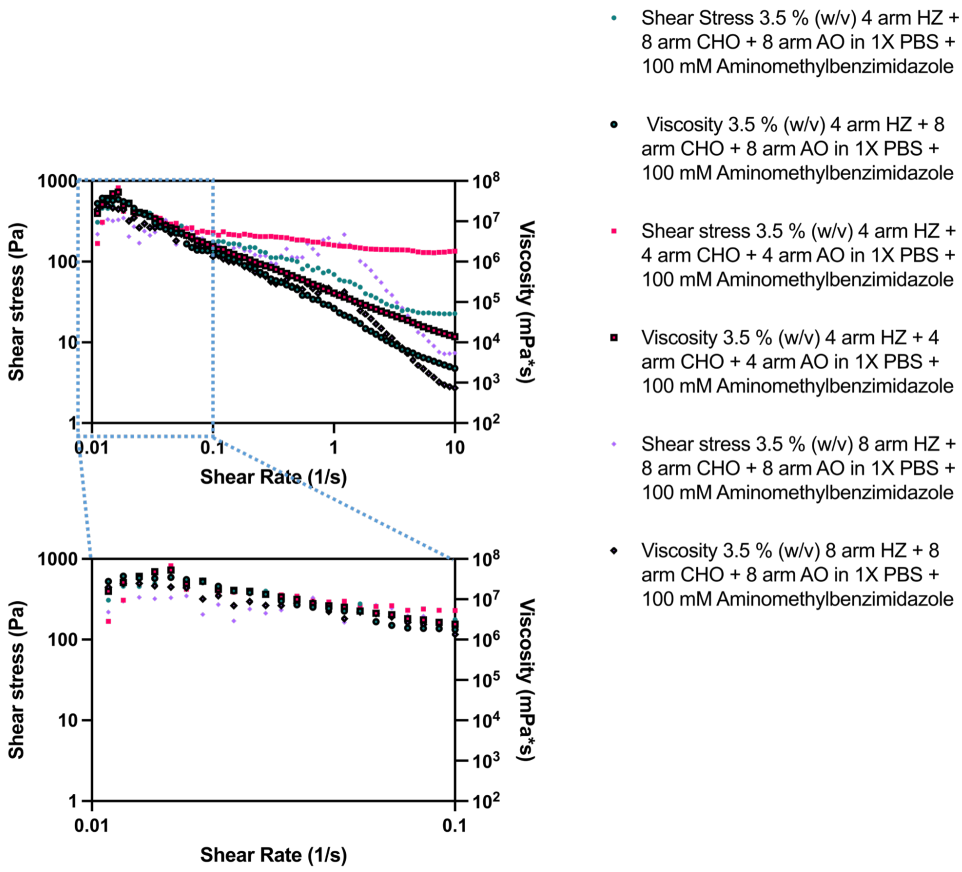

Fig. 6.9: Rheological analysis of viscosity behavior sweeping different shear rates of hydrogels with and without catalyst in 1x PBS at pH 7.4.

Injection force experiments showed injection through breaking of the hydrogel rather than flowing (data not shown), which supports the rheological findings.

6.3 Conclusion

In this chapter, an alternative to our current static Anisogel was proposed and characterized comprising PEG-based dynamic covalent cross-links. Different hydrogels were prepared at pH 5.5 using 4 or 8 arm sPEG architectures while keeping the chain length constant. Furthermore, an approach to accelerate the gelation time at physiological pH using two different biocompatible catalysts has been introduced. The results show a gelation time < 50 s using a catalyst compared to hours without a catalyst at physiological pH. This significantly increases the possibility of using this hydrogel in tissue engineering applications. In the future, the catalyst concentration needs to be further adjusted to find the limitation, with the aim to use as little catalyst as possible.

6.4 Materials and Methods

Unless specifically mentioned, all solvents were purchased as ACS grade solvents and used without any further purification. Anhydrous solvents used were either freshly distilled or passed through activated alumina columns. Reagents were purchased at the highest commercial quality from Sigma-Aldrich, Fisher Scientific, Oakwood Chemical, or Combi-Blocks and were used without further purification, unless otherwise stated. Yields refer to isolated material, unless otherwise stated. Analytical HPLC was carried out on a Agilent 1260 Infinity II HPLC system equipped with an autosampler and a UV detector using a Poroshell 120 2.7 µm C18 120 Å column (Analytical: 2.7 µm, 4.6 × 100 mm) with monitoring at λ = 220 and 254 nm and with a flow rate of 0.8 mL/min. NMR spectra were recorded on Bruker AV400 instrument and are calibrated using residual undeuterated solvent. The following abbreviations were used to explain multiplicities: s = singlet, d = doublet, t = triplet, q = quartet, m = multiplet. Flash column chromatography was performed on a Biotage Isolera One 3.0 autocolumn instrument. All silica chromotagraphy unless specifically was carried out on the Biotage using KP-Sil high-performance columns repacked using the Silicycle silica (P60, particle size 40–63 µm, column sizes described in each experimental procedure).

6.4.1 Synthesis

The protocols are based on a previous publication[180] and are further optimised and adapted also to 4 arm PEG. The equivalents were kept the same for 8 and 4 arm polymer functionalization.

PEG-hydroxyphthalimide

This synthesis followed a Mitsunobu reaction. The used glassware was dried in the oven overnight prior to use. When attaching the glassware, argon was already added during cooling. 8-arm PEG (500 mg, 0.025 mmol) was dissolved in anhydrous dichloromethane (5-10 mL) in a two-neck round bottom flask under argon. N-hydroxyphthalimide (65.25 mg, 0.40 mmol) and triphenylphosphine (104.92 mg, 0.40 mmol) were added to the solution. The reaction was cooled to 0 °C before adding

diisopropyl azodicarboxylate (DIAD) (70.88 uL, 0.36 mmol) dropwise. The reaction was warmed to 23 °C and stirred for 18 hours under argon. Afterwards DCM was evaporated. The resulting PEG-hydroxyphthalimide was purified by precipitating in ice-cold ether (40x vol DCM) and stirred for 30 min prior to filtering and drying at HV. This yielded a the desired product as a white-yellow solid (85 % yield, 89 % conversion). 1H NMR (400 MHz,CDCl3) δ 7.82-7.80 (m, 2H, aromatic Hs, CCHCH), 7.74 (m, 2H, aromatic Hs, CCHCH), 4.37- 4.34 (t, 2H, OCH2CH2ON) 3.86-3.34 (m, 227H, PEG protons) ppm.

PEG-carbohydrazide

8-arm PEG-COOH (200 mg, 0.01 mmol) was dissolved in a minimal amount of pH 5.5 phosphate buffer (100mM) (3 mL) in a one-neck round bottom flask. Carbohydrazide (270 mg, 3 mmol) was separately dissolved in a minimal amount (10 mL) of pH 5.5 phosphate buffer before it was added to the PEG-COOH solution. While stirring, EDC (310 mg, 2 mmol) was added to the reaction before adjusting the pH to 4-5 using aqueous HCl. The reaction was stirred overnight before neutralizing with aqueous NaOH (1M) and dialyzing against MeOH/water for three days. Started with 50:50, then after 24 h 80:20, then again after 24 h 0:100. Lyophilization yielded the final, pure PEG-hydrazide product as a white powder (95% yield, 90% conversion). 1H NMR (400 MHz, CDCl3) δ 4.16-4.11 (s, 2H, OCH2CO), 3.80-3.77 (m,227H, PEG protons) ppm.

PEG-Acetal

8-arm PEG (2000 mg, 0.1 mmol) was dissolved in toluene (50 mL) together with powdered NaOH (2693 mg, 48 mmol, 480 eq.) in a two-neck round bottom flask (100 mL) equipped with a Dean Stark trap. The mixture was refluxed for 5h to remove water. Afterwards, the reaction was cooled to 24 °C and 2-bromo-1,1- diethoxyethane (1805 µL, 12 mmol) was added under argon. The reaction was refluxed under argon at 125 °C for 48 hours (balloom). Toluene was removed through evaporation before adding DCM to dissolve the product. NaOH was filtered off before adding water and neutralizing with conc. HCl. The product was extracted 5x with DCM and dried over $MgSO_4$. The solvent was removed and the product precipitated in ice-cold diethyl ether and stirred for 30 min. The white powder was filtered and dried on HV to yield PEG-acetal as a white solid (50% yield, 81% conversion). 1HNMR (400 MHz, CDCl3)

δ 4.14-4.12 (t, 1H, CH2CHO2), 3.83-3.76 (q, 4H, OCH2CH3), 3.75-3.43 (m, 227H, PEG protons), 1.39-1.18 (t, 6H, CH2CH3) ppm.

PEG-Aldehye

Previously synthesized PEG-acetal (308 mg, 0.015 mmol) was dissolved in pH 2 phosphate buffer (10 mL, 100mM) in a one-neck round bottom flask and stirred at 50 °C for 18 h. The polymer was extracted 5x with methylene chloride after neutralizing with aq. NaOH. The extraction was dried over $MgSO_4$ and filtered off before evaporating the solvent. Precipitation into ether yielded the desired PEG-aldehyde as a white solid (67% yield, 88% conversion). 1H NMR (400 MHz, CDCl3) δ 9.76-9.72 (s, 1H, CHO), 3.75-3.61 (m, 227H, PEG protons) ppm.

PEG-aminooxy

PEG-hydroxyphthalimide (300 mg, 0.015 mmol) was dissolved in anhydrous dichloromethane (1 mL) to which hydrazine hydrate (27 uL, 0.45 mmol) was added. The reaction was allowed to stir at 23°C for three hours under argon. The reaction was filtered through silica to remove the white precipitate that formed. The organic solvent was removed under vacuum to yield the desired product as a white solid (265 mg, 93% yield, complete deprotection). 1H NMR (400 MHz, CDCl3) δ 3.90-3.43 (m, 227H, PEG protons) ppm.

6.4.2 Hydrogel formation

PEG-CDH, -AO, and -CHO were first solubilized in MilliQ to prepare stock solutions of 20 % (w/v). The individual components were then mixed in phosphate buffer at equal molar parts to obtain the desired total PEG concentration. AO and CDH were kept at a 1:1 ratio throughout this study. Catalyst 1 was dissolved in PBS (1X, pH 7.4) and phosphate buffer (100 mM, pH 5.5) to obtain a catalyst concentration of 100 mM.

6.4.3 Rheological measurements

For rheological measurements an Anton Paar Modular Compact Rheometer MCR 302 equipped with Parallel Plate 8 mm diameter (serial no: 59230) and a solvent trap was used. The hydrogels were formed *in situ* and measured at 37 °C with 40 µL per sample. A time sweep was recorded at 1% constant strain and 1 Hz. A frequency sweep was measured from 0.01-100 Hz at 1 % constant strain. For the viscosity measurements, the viscosity was determined increasing the shear rate from 0.01 to 10 1/s.

6.4.4 analytical HPLC

To perform the small molecule screening stock solutions of carbohydrazide and 4-hydroxybenzaldehyde were prepared at a concentration of 2 mM, respectively. 1 mL of reaction solution was prepared in tested medium to yield a reaction concentration of 1 mM. At given timepoints 50 µL were taken out of reaction solution and diluted 1:5 with 50:50 ACN:H20 to inject 50 µL. The reaction was followed over time using phosphate buffer pH 5.5, 1X PBS pH 7.4 or each supplemented with 100 mM of the tested catalyst.

6.4.5 Statistical analysis

All data points are means with error bars indicating standard deviations with a sample size of at least 3, or as otherwise stated in the text. Statistical significance was determined by one-way or two-way analysis of variance (ANOVA) with Tukey's or Holm-Sidak's multiple comparisons test. Statistical tests were carried out using GraphPad Prism v10 (GraphPad Software, Boston, MA, USA) and significance was indicated as follows: *p < 0.05, **p < 0.01, ***p < 0.001, and ****p < 0.0001.

7 Conclusion and outlook

Hydrogels are widely used in the field of tissue engineering and regenerative medicine owed to their injectability, water-swollen nature, biocompatibility, and structural similarity to the ECM. Despite these features, most hydrogels are isotropic and cannot provide the hierarchical architecture and directional cues found in the native tissue. This thesis addressed these limitations by developing synthetic PEG-based multiphasic anisotropic hydrogels using rod microgels, thus introducing spatial organization and functionality across multiple length scales. Different unique rod microgels were designed and produced using microfluidics, with subsequent application in various tissue engineering contexts. In **Chapter 3** microgels obtained through plug flow microfluidics served as a degradable sacrificial template to form hollow kidney tubules within synthetic PEG-based hydrogels as a surrounding matrix. This model successfully mimicked key features of renal tissue, including the formation of epithelial tubule-like structures and enabled the modeling of fibrotic injury with enhanced cellular response compared to conventional 2D systems. In the future this model can be further developed by modeling different types of kidney injury, such as hypoxia for AKI or IL1β for inflammatory kidney injury. Furthermore, smaller microgels could be employed that would better mimic the human kidney with 25-40 µm in diameter. Additionally, this model does not yet present immune cell populations or fluid flow, which would be needed to fully capture the complexity of *in vivo* kidney disease. Within the scope of translating tissue models into automated pipetting and robotic systems, **Chapter 4** tackled the challenge of scalability of rod microgels. For the first time, the production of degradable rod microgels was significantly increased through an innovative microfluidic approach, increasing throughput and reducing fabrication time. A combinative approach using SE and parallelization of FF channels was developed. Two different polymerization mechanisms were tested while assessing the feasibility and limitations of on-chip gelation, and characterizing the material properties. To further improve the upscaling of radical-free crosslinking chemistries, a 3D

microfluidic chip design could be envisioned, where the initiating phase is introduced from the top. Furthermore, the rod microgels can be functionalized with cell adhesive peptides or magnetic nanoparticles to be employed in various tissue engineering applications. Going smaller in rod dimensions, **Chapter 5**, introduced a refined microfluidic chip design to obtain ultra-thin and -soft rod microgels using CJP. The microfluidic system was analyzed using CFD simulations as well as experimentally. A novel protocol was introduced rendering the rod microgels magneto-responsive through post-functionalization. Initial experiments were conducted to use these magneto-responsive soft microgels in Anisogel experiments. CJP was not only explored in terms of microgel dimensions but also to broaden the library of microgels as tissue engineering blocks, making use of the short irradiation time to produce ultra-soft and ultra-porous rod microgels with unique porosity properties. Here, multiple characterization methods elucidate the unique character of these rod microgels. The ultra-soft and -porous rod microgels were rendered with a cell adhesive peptide and applied to form 3D constructs via cellular assembly. The current throughput of our single-channel system is still lower than the microgel production using PRINT. Nonetheless, we are actively working on scaling strategies based on parallelized technologies. Here, the biggest challenge lies within the laser set up, as it requires an array of powerful laser beams comprising an even distribution of intensity. Furthermore, these unique rod microgels serve as building blocks to study the effect of microgel stiffnesses and porosities on cellular behavior. Having established various components on the micrometer scale, **Chapter 6** focused on developing an alternative bulk hydrogel comprising dynamic covalent cross-links in contrast to conventional covalent cross-links used in our group. The polymer precursors were synthesized comprising different polymeric architectures, which were then employed to form different hydrogels. This chapter tackled the challenge of preparing the hydrogels at physiological pH by introducing different catalysts, followed by characterization of the bulk properties comparing networks with and without presence of a catalyst. This hydrogel system can be further analyzed regarding cell encapsulation and growth in 3D. The mechanical properties, such as storage modulus or relaxation time can then be altered observing the cellular response. Regarding the catalyst, the minimum required concentration to catalyze the reaction needs to be determined as well as the impact on the relaxation time altering the concentration of the catalyst. Furthermore, the catalyst can be added at different time points, which means that the exchange properties will be affected. In doing so, one could analyze the impact of exchange dynamics at different time points and the effect on cellular mechanisms.

Bibliography

[1] J. D. Humphrey, E. R. Dufresne, M. A. Schwartz, *Nature reviews Molecular cell biology* **2014**, *15*, 802–812.

[2] C. Frantz, K. M. Stewart, V. M. Weaver, *Journal of cell science* **2010**, *123*, 4195.

[3] H. Järveläinen, A. Sainio, M. Koulu, T. N. Wight, R. Penttinen, *Pharmacological reviews* **2009**, *61*, 198–223.

[4] N. Möhl, L. D. Laporte, *Multiphasic Anisotropic Systems*, chapter Chapter 7, pp. 231–278.

[5] M. B. Chan-Park, J. Y. Shen, Y. Cao, Y. Xiong, Y. Liu, S. Rayatpisheh, G. C.-W. Kang, H. P. Greisler, *Journal of Biomedical Materials Research Part A: An Official Journal of The Society for Biomaterials, The Japanese Society for Biomaterials, and The Australian Society for Biomaterials and the Korean Society for Biomaterials* **2009**, *88*, 1104–1121.

[6] D. A. Morrow, T. L. Haut Donahue, G. M. Odegard, K. R. Kaufman, *Tensile material properties of skeletal muscle tissue in longitudinal and transverse directions*, *Vol. 43215*, American Society of Mechanical Engineers, **2008**.

[7] M. Böl, R. Kruse, A. E. Ehret, K. Leichsenring, T. Siebert, *Journal of biomechanics* **2012**, *45*, 2673–2679.

[8] D. A. Morrow, T. L. H. Donahue, G. M. Odegard, K. R. Kaufman, *Journal of the mechanical behavior of biomedical materials* **2010**, *3*, 124–129.

[9] M. Takaza, K. M. Moerman, C. K. Simms, *Journal of the mechanical behavior of biomedical materials* **2013**, *27*, 214–225.

[10] R. Pietsch, B. B. Wheatley, T. L. Haut Donahue, R. Gilbrech, R. Prabhu, J. Liao, L. N. Williams, *Journal of Biomechanical Engineering* **2014**, *136*, 111003.

[11] J. Wong, E. Kuhl, *Computer methods in biomechanics and biomedical engineering* **2014**, *17*, 1217–1226.

[12] T. J. Klein, J. Malda, R. L. Sah, D. W. Hutmacher, *Tissue Engineering Part B: Reviews* **2009**, *15*, 143–157.

[13] R. C. Thomson, A. G. Mikos, E. Beahm, J. C. Lemon, W. C. Satterfield, T. B. Aufdemorte, M. J. Miller, *Biomaterials* **1999**, *20*, 2007–2018.

[14] L. D. Harris, B.-S. Kim, D. J. Mooney, *Journal of Biomedical Materials Research: An Official Journal of The Society for Biomaterials, The Japanese Society for Biomaterials, and the Australian Society for Biomaterials* **1998**, *42*, 396–402.

[15] E. S. Place, J. H. George, C. K. Williams, M. M. Stevens, *Chemical society reviews* **2009**, *38*, 1139–1151.

[16] R. Langer, J. P. Vacanti, C. A. Vacanti, A. Atala, L. E. Freed, G. Vunjak-Novakovic, *Tissue engineering* **1995**, *1*, 151–161.

[17] K. Y. Lee, D. J. Mooney, *Chemical reviews* **2001**, *101*, 1869–1880.

[18] M. S. Jhon, J. D. Andrade, *Journal of biomedical materials research* **1973**, *7*, 509–522.

[19] P. J. Kondiah, Y. E. Choonara, P. P. Kondiah, T. Marimuthu, P. Kumar, L. C. Du Toit, V. Pillay, *Molecules* **2016**, *21*, 1580.

[20] R. Lanza, R. Langer, J. P. Vacanti, A. Atala, *Principles of tissue engineering*, Academic press, **2020**.

[21] M. Whitaker, R. Quirk, S. Howdle, K. Shakesheff, *Journal of Pharmacy and Pharmacology* **2001**, *53*, 1427–1437.

[22] S.-M. Lien, L.-Y. Ko, T.-J. Huang, *Acta biomaterialia* **2009**, *5*, 670–679.

[23] D. J. Griffon, M. R. Sedighi, D. V. Schaeffer, J. A. Eurell, A. L. Johnson, *Acta biomaterialia* **2006**, *2*, 313–320.

[24] Y. Yang, L. D. Laporte, M. L. Zelivyanskaya, K. J. Whittlesey, A. J. Anderson, B. J. Cummings, L. D. Shea, *Tissue Engineering Part A* **2009**, *15*, 3283–3295.

[25] X. He, E. Jabbari, *Biomacromolecules* **2007**, *8*, 780–792.

[26] N. Huebsch, E. Lippens, K. Lee, M. Mehta, S. T. Koshy, M. C. Darnell, R. M. Desai, C. M. Madl, M. Xu, X. Zhao, et al., *Nature materials* **2015**, *14*, 1269–1277.

[27] O. Y. Dudaryeva, L. Cousin, L. Krajnovic, G. Gröbli, V. Sapkota, L. Ritter, D. Deshmukh, Y. Cui, R. W. Style, R. Levato, C. Labouesse, M. W. Tibbitt, *Advanced Materials* **2025**, *37*, 2410452.

[28] D. Rommel, M. Mork, S. Vedaraman, C. Bastard, L. P. Guerzoni, Y. Kittel, R. Vinokur, N. Born, T. Haraszti, L. De Laporte, *Advanced Science* **2022**, *9*, 2270060.

[29] A. C. Suturin, A. J. Krüger, K. Neidig, N. Klos, N. Dolfen, M. Bund, T. Gronemann, R. Sebers, A. Manukanc, G. Yazdani, et al., *Advanced Healthcare Materials* **2022**, *11*, 2200989.

[30] D. R. Griffin, W. M. Weaver, P. O. Scumpia, D. Di Carlo, T. Segura, *Nature materials* **2015**, *14*, 737–744.

[31] D. Macaya, M. Spector, *Biomedical materials* **2012**, *7*, 012001.

[32] R. Rizzo, A. Bonato, P. Chansoria, M. Zenobi-Wong, *ACS Biomaterials Science & Engineering* **2022**, *8*, 3871–3882.

[33] S. Zhang, M. A. Greenfield, A. Mata, L. C. Palmer, R. Bitton, J. R. Mantei, C. Aparicio, M. O. De La Cruz, S. I. Stupp, *Nature materials* **2010**, *9*, 594–601.

[34] C. M. Tringides, D. J. Mooney, *Macromolecular bioscience* **2024**, *24*, 2300044.

[35] J. C. Rose, M. Cámara-Torres, K. Rahimi, J. Köhler, M. Möller, L. De Laporte, *Nano letters* **2017**, *17*, 3782–3791.

[36] H. Liu, P. Chansoria, P. Delrot, E. Angelidakis, R. Rizzo, D. Rütsche, L. A. Applegate, D. Loterie, M. Zenobi-Wong, *Advanced Materials* **2022**, *34*, 2204301.

[37] D. Petta, V. Basoli, D. Pellicciotta, R. Tognato, J. Barcik, C. Arrigoni, E. Della Bella, A. R. Armiento, C. Candrian, R. G. Richards, et al., *Biofabrication* **2020**, *13*, 015004.

[38] R. Penner, E. Neher, *Journal of Experimental Biology* **1988**, *139*, 329–345.

[39] R. T. Kendall, C. A. Feghali-Bostwick, *Frontiers in pharmacology* **2014**, *5*, 123.

[40] H. Urabe, R. Akimoto, S. Kamiya, K. Hosoki, H. Ichikawa, T. Nishiyama, *Molecular and Cellular Biochemistry* **2021**, *476*, 361–368.

[41] H. Liu, M. Wu, Y. Jia, L. Niu, G. Huang, F. Xu, *NPG Asia Materials* **2020**, *12*, 45.

[42] R. B. Borgens, J. W. Vanable Jr, L. F. Jaffe, *Proceedings of the National Academy of Sciences* **1977**, *74*, 4528–4532.

[43] H. Joodaki, M. B. Panzer, *Proceedings of the Institution of Mechanical Engineers, Part H: Journal of Engineering in Medicine* **2018**, *232*, 323–343.

[44] K. Namsheer, C. S. Rout, *RSC advances* **2021**, *11*, 5659–5697.

[45] P. Srisuk, F. V. Berti, L. P. da Silva, A. P. Marques, R. L. Reis, V. M. Correlo, *ACS Biomaterials Science & Engineering* **2018**, *4*, 1779–1787.

[46] Z. Zhang, W. Chen, D. M. Tiemessen, E. Oosterwijk, P. H. Kouwer, *Advanced Healthcare Materials* **2022**, *11*, 2102389.

[47] R. K. Das, V. Gocheva, R. Hammink, O. F. Zouani, A. E. Rowan, *Nature materials* **2016**, *15*, 318–325.

[48] S. Ye, J. W. Boeter, M. Mihajlovic, F. G. van Steenbeek, M. E. van Wolferen, L. A. Oosterhoff, A. Marsee, M. Caiazzo, L. J. van der Laan, L. C. Penning, et al., *Advanced functional materials* **2020**, *30*, 2000893.

[49] Y. Zhang, C. Tang, P. N. Span, A. E. Rowan, T. W. Aalders, J. A. Schalken, G. J. Adema, P. H. Kouwer, M. M. Zegers, M. Ansems, *Advanced Science* **2020**, *7*, 2001797.

[50] J. K. Mouw, G. Ou, V. M. Weaver, *Nature reviews Molecular cell biology* **2014**, *15*, 771–785.

[51] E. Prince, E. Kumacheva, *Nature Reviews Materials* **2019**, *4*, 99–115.

[52] U. Streppel, D. Michaelis, R. Kowarschik, A. Bräuer, *Physical review letters* **2005**, *95*, 073901.

[53] D. Kip, M. Soljacic, M. Segev, E. Eugenieva, D. N. Christodoulides, *Science* **2000**, *290*, 495–498.

[54] S. Biria, P. P. Malley, T. F. Kahan, I. D. Hosein, *The Journal of Physical Chemistry C* **2016**, *120*, 4517–4528.

[55] M. Anyfantakis, B. Loppinet, G. Fytas, S. Pispas, *Optics letters* **2008**, *33*, 2839–2841.

[56] J. P. Armstrong, E. Pchelintseva, S. Treumuth, C. Campanella, C. Meinert, T. J. Klein, D. W. Hutmacher, B. W. Drinkwater, M. M. Stevens, *Advanced healthcare materials* **2022**, *11*, 2200481.

[57] D. Ceballos, X. Navarro, N. Dubey, G. Wendelschafer-Crabb, W. R. Kennedy, R. T. Tranquillo, *Experimental neurology* **1999**, *158*, 290–300.

[58] N. Dubey, P. Letourneau, R. Tranquillo, *Biomaterials* **2001**, *22*, 1065–1075.

[59] M. Antman-Passig, O. Shefi, *Nano letters* **2016**, *16*, 2567–2573.

[60] Q. Feng, Y. Liu, J. Huang, K. Chen, J. Huang, K. Xiao, *Scientific reports* **2018**, *8*, 2082.

[61] N. Singh, G. J. Jenkins, R. Asadi, S. H. Doak, *Nano reviews* **2010**, *1*, 5358.

[62] Y. Kittel, A. J. Kuehne, L. De Laporte, *Advanced Healthcare Materials* **2022**, *11*, 2101989.

[63] S. Babu, F. Albertino, A. Omidinia Anarkoli, L. De Laporte, *Advanced healthcare materials* **2021**, *10*, 2002221.

[64] A. C. Daly, L. Riley, T. Segura, J. A. Burdick, *Nature Reviews Materials* **2020**, *5*, 20–43.

[65] C. Licht, J. C. Rose, A. O. Anarkoli, D. Blondel, M. Roccio, T. Haraszti, D. B. Gehlen, J. A. Hubbell, M. P. Lutolf, L. De Laporte, *Biomacromolecules* **2019**, *20*, 4075–4087.

[66] S. Babu, I. Chen, S. Vedaraman, J. Gerardo-Nava, C. Licht, Y. Kittel, T. Haraszti, J. Di Russo, L. De Laporte, *Advanced Functional Materials* **2022**, *32*, 2202468.

[67] J. C. Rose, D. B. Gehlen, A. Omidinia-Anarkoli, M. Fölster, T. Haraszti, E. E. Jaekel, L. De Laporte, *Advanced healthcare materials* **2020**, *9*, 2000886.

[68] D. L. Braunmiller, S. Babu, D. B. Gehlen, M. Seuß, T. Haraszti, A. Falkenstein, J. Eigen, L. De Laporte, J. J. Crassous, *Advanced Functional Materials* **2022**, *32*, 2202430.

[69] T. H. Qazi, J. Wu, V. G. Muir, S. Weintraub, S. E. Gullbrand, D. Lee, D. Issadore, J. A. Burdick, *Advanced Materials* **2022**, *34*, 2109194.

[70] K. N. Bitar, S. Raghavan, *Neurogastroenterology & Motility* **2012**, *24*, 7–19.

[71] D. G. Seifu, A. Purnama, K. Mequanint, D. Mantovani, *Nature Reviews Cardiology* **2013**, *10*, 410–421.

[72] J. X. Law, L. L. Liau, B. S. Aminuddin, B. H. I. Ruszymah, *International journal of pediatric otorhinolaryngology* **2016**, *91*, 55–63.

[73] J. O. Aceves, S. Heja, K. Kobayashi, S. S. Robinson, T. Miyoshi, T. Matsumoto, O. J. Schäffers, R. Morizane, J. A. Lewis, *Scientific Reports* **2022**, *12*, 14997.

[74] M. M. Nielsen, D. Witherden, W. Havran, *Nature Reviews Immunology* **2017**, *17*, 733–745.

[75] N. Torras, M. García-Díaz, V. Fernández-Majada, E. Martínez, *Frontiers in Bioengineering and Biotechnology* **2018**, *6*.

[76] K. Parikh, A. Antanaviciute, D. Fawkner-Corbett, M. Jagielowicz, A. Aulicino, C. Lagerholm, S. Davis, J. Kinchen, H. H. Chen, N. K. Alham, N. Ashley,

E. Johnson, P. Hublitz, L. Bao, J. Lukomska, R. Andev, E. Björklund, B. Kessler, R. Fischer, R. Goldin, H. Koohy, A. Simmons, *Nature* **2019**, *567*, 49 – 55.

[77] R. Thuenauer, E. Rodriguez-Boulan, W. Römer, *The Analyst* **2014**, *139 13*, 3206–18.

[78] E. Trimm, K. Red-Horse, *Nature Reviews. Cardiology* **2022**, *20*, 197 – 210.

[79] J. K. Hennigs, C. Matuszcak, M. Trepel, J. Körbelin, *Cells* **2021**, *10*.

[80] S. Xu, I. Ilyas, P. Little, H. Li, D. Kamato, X. Zheng, S. Luo, Z. Li, P. Liu, J. Han, I. C. Harding, E. Ebong, S. Cameron, A. Stewart, J. Weng, *Pharmacological Reviews* **2021**, *73*, 924 – 967.

[81] A. Krüger-Genge, A. Blocki, R. Franke, F. Jung, *International Journal of Molecular Sciences* **2019**, *20*.

[82] B. Yuan, Y. Jin, Y. Sun, D. Wang, J. Sun, Z. Wang, W. Zhang, X. Jiang, *Advanced Materials (Deerfield Beach, Fla.)* **2012**, *24*, 890–896.

[83] S. Cheng, Y. Jin, N. Wang, F. Cao, W. Zhang, W. Bai, W. Zheng, X. Jiang, *Advanced Materials* **2017**, *29*, 1700171.

[84] Q. Zhao, J. Wang, H. Cui, H. Chen, Y. Wang, X. Du, *Advanced Functional Materials* **2018**, *28*, 1801027.

[85] L. E. Niklason, R. S. Langer, *Transplant immunology* **1997**, *5*, 303–306.

[86] W. Godbey, B. S. Hindy, M. E. Sherman, A. Atala, *Biomaterials* **2004**, *25*, 2799–2805.

[87] A. Nieponice, L. Soletti, J. Guan, B. M. Deasy, J. Huard, W. R. Wagner, D. A. Vorp, *Biomaterials* **2008**, *29*, 825–833.

[88] M. Lovett, K. Lee, A. Edwards, D. L. Kaplan, *Tissue Engineering Part B: Reviews* **2009**, *15*, 353–370.

[89] B. Artegiani, H. Clevers, *Human molecular genetics* **2018**, *27*, R99–R107.

[90] Y. Xu, C. Kuppe, J. Perales-Patón, S. Hayat, J. Kranz, A. T. Abdallah, J. Nagai, Z. Li, F. Peisker, T. Saritas, et al., *Nature genetics* **2022**, *54*, 1690–1701.

[91] C. M. Sakolish, G. J. Mahler, *RSC advances* **2017**, *7*, 4216–4225.

[92] M. H. Little, A. N. Combes, *Genes & Development* **2019**, *33*, 1319–1345.

[93] H. Wu, K. Uchimura, E. L. Donnelly, Y. Kirita, S. A. Morris, B. D. Humphreys, *Cell stem cell* **2018**, *23*, 869–881.

[94] L. Yin, G. Du, B. Zhang, H. Zhang, R. Yin, W. Zhang, S.-M. Yang, *Scientific Reports* **2020**, *10*, 6568.

[95] S. Musah, R. Bhattacharya, J. Himmelfarb, *Annual review of biomedical engineering* **2024**, *26*.

[96] G. Addario, D. Eussen, S. Djudjaj, P. Boor, L. Moroni, C. Mota, *Macromolecular Bioscience* **2024**, *24*, 2300440.

[97] D. Bouwens, N. Kabgani, C. Bergerbit, H. Kim, S. Ziegler, S. Ijaz, A. Abdallah, T. Haraszti, S. Maryam, A. Omidinia-Anarkoli, et al., *Biomaterials* **2025**, *316*, 123009.

[98] K. A. Homan, D. B. Kolesky, M. A. Skylar-Scott, J. Herrmann, H. Obuobi, A. Moisan, J. A. Lewis, *Scientific reports* **2016**, *6*, 34845.

[99] K. T. Kroll, K. A. Homan, S. G. Uzel, M. M. Mata, K. J. Wolf, J. E. Rubins, J. A. Lewis, *Biofabrication* **2024**, *16*, 045003.

[100] A. J. Boys, S. L. Barron, D. Tilev, R. Owens, *Frontiers in Bioengineering and Biotechnology* **2020**, *8*.

[101] P. Zhao, H. Gu, H. Mi, C. Rao, J. Fu, L. Turng, *Frontiers of Mechanical Engineering* **2018**, *13*, 107–119.

[102] A. Eltom, G. Zhong, A. Muhammad, *Advances in Materials Science and Engineering* **2019**.

[103] A. Abdal-hay, M. Bartnikowski, S. Hamlet, S. Ivanovski, *Materials science & engineering. C, Materials for biological applications* **2018**, *82*, 10–18.

[104] J. G. Torres-Rendon, M. Köpf, D. Gehlen, A. Blaeser, H. Fischer, L. D. Laporte, A. Walther, *Biomacromolecules* **2016**, *17*, 905–913.

[105] A. J. Seymour, S. Shin, S. Heilshorn, *Advanced Healthcare Materials* **2021**, *10*.

[106] N. C. Negrini, M. Bonnetier, G. Giatsidis, D. Orgill, S. Faré, B. Marelli, *Acta biomaterialia* **2019**, *87*, 61–75.

[107] A. M. Compaan, K. Song, W. Chai, Y. Huang, *ACS applied materials & interfaces* **2020**.

[108] Z. Wang, Q. Ye, S. Yu, B. Akhavan, *Advanced Healthcare Materials* **2023**, *12*, 2370102.

[109] J. Zhu, *Biomaterials* **2010**, *31*, 4639–4656.

[110] C.-C. Lin, K. S. Anseth, *Pharmaceutical research* **2009**, *26*, 631–643.

[111] M. Zacchigna, F. Cateni, S. Drioli, G. M. Bonora, *Polymers* **2011**, *3*, 1076–1090.

[112] E. Bakaic, N. M. Smeets, T. Hoare, *RSC advances* **2015**, *5*, 35469–35486.

[113] S. P. Zustiak, J. B. Leach, *Biomacromolecules* **2010**, *11*, 1348–1357.

[114] S. C. Rizzi, M. Ehrbar, S. Halstenberg, G. P. Raeber, H. G. Schmoekel, H. Hagenmüller, R. Müller, F. E. Weber, J. A. Hubbell, *Biomacromolecules* **2006**, *7*, 3019–3029.

[115] G. M. Whitesides, *nature* **2006**, *442*, 368–373.

[116] L. P. Guerzoni, J. C. Rose, D. B. Gehlen, A. Jans, T. Haraszti, M. Wessling, A. J. Kuehne, L. De Laporte, *Small* **2019**, *15*, 1900692.

[117] J. Ehlert, J. Kronemann, N. Zumbrägel, M. Preller, *Molecules* **2019**, *24*, 4272.

[118] X.-m. Meng, D. J. Nikolic-Paterson, H. Y. Lan, *Nature Reviews Nephrology* **2016**, *12*, 325–338.

[119] N. Yamashita, R. Kramann, *Trends in Endocrinology & Metabolism* **2024**, *35*, 31–48.

[120] C. Kuppe, M. M. Ibrahim, J. Kranz, X. Zhang, S. Ziegler, J. Perales-Patón, J. Jansen, K. C. Reimer, J. R. Smith, R. Dobie, et al., *Nature* **2021**, *589*, 281–286.

[121] Y. Kittel, L. P. Guerzoni, C. Itzin, D. Rommel, M. Mork, C. Bastard, B. Häßel, A. Omidinia-Anarkoli, S. P. Centeno, T. Haraszti, et al., *Angewandte Chemie International Edition* **2023**, *62*, e202309779.

[122] A. J. Krüger, O. Bakirman, L. P. Guerzoni, A. Jans, D. B. Gehlen, D. Rommel, T. Haraszti, A. J. Kuehne, L. De Laporte, *Advanced Materials* **2019**, *31*, 1903668.

[123] T. Nisisako, T. Torii, *Lab on a Chip* **2008**, *8*, 287–293.

[124] W. Li, J. Greener, D. Voicu, E. Kumacheva, *Lab on a Chip* **2009**, *9*, 2715–2721.

[125] D. Conchouso, D. Castro, S. Khan, I. G. Foulds, *Lab on a Chip* **2014**, *14*, 3011–3020.

[126] H.-H. Jeong, V. R. Yelleswarapu, S. Yadavali, D. Issadore, D. Lee, *Lab on a Chip* **2015**, *15*, 4387–4392.

[127] S. Yadavali, H.-H. Jeong, D. Lee, D. Issadore, *Nature communications* **2018**, *9*, 1222.

[128] E. Amstad, M. Chemama, M. Eggersdorfer, L. R. Arriaga, M. P. Brenner, D. A. Weitz, *Lab on a Chip* **2016**, *16*, 4163–4172.

[129] E. Stolovicki, R. Ziblat, D. A. Weitz, *Lab on a Chip* **2018**, *18*, 132–138.

[130] A. Ofner, I. Mattich, M. Hagander, A. Dutto, H. Seybold, P. A. Rühs, A. R. Studart, *Advanced Functional Materials* **2019**, *29*, 1806821.

[131] J. M. de Rutte, J. Koh, D. Di Carlo, *Advanced Functional Materials* **2019**, *29*, 1900071.

[132] S. P. Danielsen, H. K. Beech, S. Wang, B. M. El-Zaatari, X. Wang, L. Sapir, T. Ouchi, Z. Wang, P. N. Johnson, Y. Hu, et al., *Chemical reviews* **2021**, *121*, 5042–5092.

[133] M. Chen, G. Bolognesi, G. Vladisavljević, *Molecules* **2021**, *26*.

[134] M. Y. Hwang, S. G. Kim, H. Lee, S. Muller, *Soft matter* **2017**, *13 34*, 5785–5794.

[135] N. E. Friend, I. W. Zhang, M. M. Hu, A. J. McCoy, R. N. Kent III, S. J. DePalma, B. M. Baker, S. C. Lesher-Pérez, J. P. Stegemann, A. J. Putnam, *Journal of Biomedical Materials Research Part A* **2025**, *113*, e37900.

[136] M. Gregoritza, K. Abstiens, M. Graf, A. M. Goepferich, *European Journal of Pharmaceutics and Biopharmaceutics* **2018**, *127*, 194–203.

[137] R. P. Tello, S. Wang, F. Fontana, A. Correia, G. Molinaro, S. L. Cérda, S. Hietala, J. Hirvonen, G. Barreto, H. Santos, *Biomaterials science* **2023**.

[138] C. Hoyle, C. Bowman, *Angewandte Chemie* **2010**, *49 9*, 1540–73.

[139] N. T. Brummelhuis, H. Schlaad **2012**, 2017–2056.

[140] A. Lowe, *Polymer Chemistry* **2010**, *1*, 17–36.

[141] J. M. G. Cowie, V. Arrighi, *Polymers: chemistry and physics of modern materials*, CRC press, **2007**.

[142] A. Ravve in *Principles of polymer chemistry*, Springer, **2012**, pp. 17–67.

[143] A. L. Colebatch, A. S. Weller, *Chemistry–A European Journal* **2019**, *25*, 1379–1390.

[144] S. Zavada, N. Mchardy, T. F. Scott, *Journal of materials chemistry. B* **2014**, *2 17*, 2598–2605.

[145] C. E. Hoyle, T. Y. Lee, T. Roper, *Journal of Polymer Science Part A: Polymer Chemistry* **2004**, *42*, 5301–5338.

[146] N. B. Cramer, S. K. Reddy, A. K. O'Brien, C. N. Bowman, *Macromolecules* **2003**, *36*, 7964–7969.

[147] Z. Jiang, R. Shaha, R. McBride, K. Jiang, M. Tang, B. Xu, A. Goroncy, C. Frick, J. Oakey, *Biofabrication* **2020**, *12*.

[148] K. D. Dwyer, K. L. Coulombe, *Bioactive Materials* **2021**, *6*, 2198–2220.

[149] K. T. Tran, T. D. Nguyen, *Journal of Science: Advanced Materials and Devices* **2017**, *2*, 1–14.

[150] A. S. Utada, A. Fernandez-Nieves, H. A. Stone, D. A. Weitz, *Phys. Rev. Lett.* **2007**, *99*, 094502.

[151] D. Dendukuri, P. Panda, R. Haghgooie, J. M. Kim, T. A. Hatton, P. S. Doyle, *Macromolecules* **2008**, *41*, 8547–8556.

[152] K. Krutkramelis, B. Xia, J. Oakey, *Lab on a Chip* **2016**, *16*, 1457–1465.

[153] A. K. O'Brien, C. N. Bowman, *Macromolecular Theory and Simulations* **2006**, *15*, 176–182.

[154] C. Decker, *Die Makromolekulare Chemie: Macromolecular Chemistry and Physics* **1979**, *180*, 2027–2030.

[155] C. Decker, J. Faure, L. RYCHIA **1979**.

[156] C. W. Miller, C. E. Hoyle, S. Jönsson, C. Nason, T. Lee, W. Kuang, K. Viswanathan, ACS Publications, **2003**.

[157] V. V. Krongauz, C. P. Chawla, J. Dupre, **2003**.

[158] R. Simič, J. Mandal, K. Zhang, N. Spencer, *Soft Matter* **2021**, *17*, 6394 – 6403.

[159] K. Lim, B. Schon, N. Mekhileri, G. C. J. Brown, C. M. Chia, S. Prabakar, G. Hooper, T. Woodfield, *ACS biomaterials science & engineering* **2016**, *2 10*, 1752–1762.

[160] J. R. Tumbleston, D. Shirvanyants, N. Ermoshkin, R. Janusziewicz, A. R. Johnson, D. Kelly, K. Chen, R. Pinschmidt, J. P. Rolland, A. Ermoshkin, et al., *Science* **2015**, *347*, 1349–1352.

[161] L. Steinbeck, D. L. Braunmiller, H. J. Wolff, V. Huettche, J. Wang, M. Wessling, J. J. Crassous, J. Linkhorst, *Advanced Materials Technologies* **2023**, *8*, 2300044.

[162] D. Dendukuri, S. S. Gu, D. C. Pregibon, T. A. Hatton, P. S. Doyle, *Lab on a Chip* **2007**, *7*, 818–828.

[163] R. M. Erb, R. Libanori, N. Rothfuchs, A. R. Studart, *Science* **2012**, *335*, 199–204.

[164] J. C. Rose, M. Fölster, L. Kivilip, J. L. Gerardo-Nava, E. E. Jaekel, D. B. Gehlen, W. Rohlfs, L. De Laporte, *Polymer Chemistry* **2020**, *11*, 496–507.

[165] P. de Gennes, *Macromolecules* **1980**, *13*, 1069–1075.

[166] S. Alexander, *Journal De Physique* **1977**, *38*, 983–987.

[167] M. Daoud, J. Cotton, *Journal de Physique* **1982**, *43*, 531–538.

[168] D. Dukes, Y. Li, S. Lewis, B. Benicewicz, L. Schadler, S. K. Kumar, *Macromolecules* **2010**, *43*, 1564–1570.

[169] A. Jusufi, C. N. Likos, *Reviews of Modern Physics* **2009**, *81*, 1753–1772.

[170] S. Bulut, D. Günther, M. Bund, C. Haats, T. Bissing, C. Bastard, M. Wessling, L. De Laporte, A. Pich, *Advanced Healthcare Materials* **2024**, *13*, 2302957.

[171] M. Rizwan, A. E. G. Baker, M. S. Shoichet, *Advanced Healthcare Materials* **2021**, *10*, 2100234.

[172] Y. Han, Y. Cao, H. Lei, *Gels* **2022**, *8*.

[173] T. B. Kohlan, Y. Wen, C. M. Mini, A. Finne-Wistrand, *Carbohydrate polymers* **2024**, *338*, 122173.

[174] B. Yang, K. Wei, C. Loebel, K. Zhang, Q. Feng, R. Li, S. H. D. Wong, X. Xu, C. Lau, X. Chen, P. Zhao, C. Yin, J. Burdick, Y. Wang, L. Bian, *Nature Communications* **2021**, *12*.

[175] Y. Chen, D. Diaz-Dussan, D. Wu, W. Wang, Y.-Y. Peng, A. B. Asha, D. Hall, K. Ishihara, R. Narain, *ACS macro letters* **2018**, *7 8*, 904–908.

[176] M. E. Smithmyer, C. C. Deng, S. E. Cassel, P. J. LeValley, B. Sumerlin, A. M. Kloxin, *ACS macro letters* **2018**, *7 9*, 1105–1110.

[177] X. Yang, G. Liu, L. Peng, J. Guo, L. Tao, J. Yuan, C. Chang, Y. Wei, L. Zhang, *Advanced Functional Materials* **2017**, *27*.

[178] L. L. Wang, C. Highley, Y. Yeh, J. H. Galarraga, S. Uman, J. Burdick, *Journal of biomedical materials research. Part A* **2018**, *106 4*, 865–875.

[179] Y. Han, Y. Cao, H. Lei, *Gels* **2022**, *8*, 577.

[180] N. Boehnke, C. Cam, E. Bat, T. Segura, H. Maynard, *Biomacromolecules* **2015**, *16 7*, 2101–8.

[181] I. Marić, L. Yang, X. Li, G. M. Santiago, C. G. Pappas, X. Qiu, J. Dijksman, K. Mikhailov, P. van Rijn, S. Otto, *Angewandte Chemie* **2023**.

[182] L. J. Smith, S. Taimoory, R. Tam, A. E. G. Baker, N. B. Mohammad, J. Trant, M. Shoichet, *Biomacromolecules* **2018**, *19 3*, 926–935.

[183] H.-Y. Liu, M. Korc, C.-C. Lin, *Biomaterials* **2018**, *160*, 24–36.

[184] V. Yesilyurt, A. M. Ayoob, E. A. Appel, J. Borenstein, R. Langer, D. G. Anderson, *Advanced Materials* **2017**, *29*.

[185] B. M. Richardson, D. G. Wilcox, M. A. Randolph, K. S. Anseth, *Acta biomaterialia* **2019**, *83*, 71–82.

[186] Y.-H. Lin, J. Lou, O. Chaudhuri, *bioRxiv* **2024**.

[187] J. Xu, Y. Liu, S. Hsu, *Molecules* **2019**, *24*.

[188] T. Hozumi, T. Kageyama, S. Ohta, J. Fukuda, T. Ito, *Biomacromolecules* **2017**, *19 2*, 288–297.

[189] B. Begum, T. S. Koduru, S. N. Madni, N. F. Anjum, S. Seetharaman, B. Veeranna, V. K. Gupta, *Gels* **2024**, *10*.

[190] C. Pete, et al. **2013**.

[191] J. Lou, F. Liu, C. D. Lindsay, O. Chaudhuri, S. C. Heilshorn, Y. Xia, *Advanced Materials* **2018**, *30*, 1705215.

[192] F. Trausel, B. Fan, S. A. van Rossum, J. H. van Esch, R. Eelkema, *Advanced Synthesis & Catalysis* **2018**, *360*, 2571–2576.

[193] J. K. Oh, R. Drumright, D. J. Siegwart, K. Matyjaszewski, *Progress in polymer science* **2008**, *33*, 448–477.

[194] H. Zhang, J. Nunes, S. Gratton, K. Herlihy, P. Pohlhaus, J. DeSimone, *New Journal of Physics* **2009**, *11*, 075018.

[195] A. J. Krüger, J. Köhler, S. Cichosz, J. C. Rose, D. B. Gehlen, T. Haraszti, M. Möller, L. De Laporte, *Chemical Communications* **2018**, *54*, 6943–6946.

[196] D. Liu, H. Zhang, F. Fontana, J. T. Hirvonen, H. A. Santos, *Advanced drug delivery reviews* **2018**, *128*, 54–83.

[197] J. Wu, S. Yadavali, D. A. Issadore, D. Lee, *Advanced Materials Technologies* **2022**, *7*, 2101160.

[198] L. P. Guerzoni, J. Bohl, A. Jans, J. C. Rose, J. Koehler, A. J. Kuehne, L. De Laporte, *Biomaterials science* **2017**, *5*, 1549–1557.

[199] A. Pardo, S. M. Bakht, M. Gómez-Florit, R. Rial, R. Monteiro, S. Teixeira, P. Taboada, R. L. Reis, R. M. Domingues, M. Gomes, *Advanced Functional Materials* **2022**, *32*.

[200] A. Joshi, M. Kamaraj, N. Moghimi, H. Heidari, A. Aghamaleky-Sarvestany, C. S. A. Rahim, D. N. Rodriguez-Sanchez, C. Hu, S. Aravindan, D. R. Nair, N. F. Huang, B. B. Thomas, D. Sareen, E. Yoshihara, V. Jucaud, A. Khademhosseini, J. V. John, *Small* **2025**, e2500261.

[201] H. Kim, J. Jang, J. Park, K.-P. Lee, S. Lee, D.-M. Lee, K. H. Kim, H. K. Kim, D.-W. Cho, *Biofabrication* **2019**, *11*, 035017.

[202] S. J. Rowan, S. J. Cantrill, G. R. Cousins, J. K. Sanders, J. F. Stoddart, *Angewandte Chemie International Edition* **2002**, *41*, 898–952.

[203] J. Gačanin, J. Hedrich, S. Sieste, G. Glaßer, I. Lieberwirth, C. Schilling, S. Fischer, H. Barth, B. Knöll, C. V. Synatschke, et al., *Advanced Materials* **2019**, *31*, 1805044.

[204] C. Tong, J. Wondergem, M. van den Brink, M. C. Kwakernaak, Y. Chen, M. Hendrix, I. Voets, E. Danen, S. E. L. Dévédec, D. Heinrich, R. E. Kieltyka, *ACS Applied Materials & Interfaces* **2022**, *14*, 17042 – 17054.

[205] K. Hayashi, M. Matsuda, M. Nakahata, Y. Takashima, M. Tanaka, *Polymers* **2022**, *14*.

[206] P. Dankers, T. M. Hermans, T. W. Baughman, Y. Kamikawa, R. E. Kieltyka, M. Bastings, H. M. Janssen, N. Sommerdijk, A. Larsen, M. Van Luyn, et al., *Advanced materials (Deerfield Beach, Fla.)* **2012**, *24*, 2703–2709.

[207] M. M. Bastings, T. M. Hermans, A. Spiering, E. W. Kemps, L. Albertazzi, E. E. Kurisinkal, P. Y. Dankers, *Macromolecular bioscience* **2019**, *19*, 1800296.

[208] M. M. Bastings, S. Koudstaal, R. E. Kieltyka, Y. Nakano, A. Pape, D. A. Feyen, F. J. van Slochteren, P. A. Doevendans, J. P. Sluijter, E. Meijer, et al., *Advanced Healthcare Materials* **2014**, *3*, 69–69.

[209] M. H. Bakker, E. van Rooij, P. Y. Dankers, *Chemistry–An Asian Journal* **2018**, *13*, 3501–3508.

[210] X. Ma, A. Agas, Z. Siddiqui, K. Kim, P. Iglesias-Montoro, J. Kalluru, V. Kumar, J. Haorah, *Bioactive Materials* **2020**, *5*, 124–132.

[211] D. Kumar, V. L. Workman, M. O'Brien, J. McLaren, L. White, K. Ragunath, F. Rose, A. Saiani, J. E. Gough, *Advanced Functional Materials* **2017**, *27*, 1702424.

[212] S. Wan, S. Borland, S. M. Richardson, C. L. Merry, A. Saiani, J. E. Gough, *Acta Biomaterialia* **2016**, *46*, 29–40.

[213] Y. Qi, H. Min, A. Mujeeb, Y. Zhang, X. Han, X. Zhao, G. J. Anderson, Y. Zhao, G. Nie, *ACS applied materials & interfaces* **2018**, *10*, 6972–6981.

[214] Y. Kobayashi, J. Nouet, E. Baljinnyam, Z. Siddiqui, D. H. Fine, D. Fraidenraich, V. A. Kumar, E. Shimizu, *Bioactive Materials* **2022**, *14*, 290–301.

[215] I. Krupa, N. J. Treacy, S. Clerkin, J. L. Davis, A. F. Miller, A. Saiani, J. K. Wychowaniec, E. G. Reynaud, D. F. Brougham, J. Crean, *Current Protocols* **2024**, *4*, e1096.

[216] Z. Li, L. Liu, Y. Chen, *Acta biomaterialia* **2020**.

[217] O. Chaudhuri, J. Cooper-White, P. A. Janmey, D. J. Mooney, V. B. Shenoy, *Nature* **2020**, *584*, 535–546.

[218] D. Wu, H. Lei, X. Xie, L. Zhou, P. Zheng, Y. Cao, Y. Zhang, *Nano Research* **2022**, *15*, 4294–4301.

[219] S. Nam, K. H. Hu, M. J. Butte, O. Chaudhuri, *Proceedings of the National Academy of Sciences* **2016**, *113*, 5492–5497.

[220] S. Münster, L. M. Jawerth, B. A. Leslie, J. I. Weitz, B. Fabry, D. A. Weitz, *Proceedings of the National Academy of Sciences* **2013**, *110*, 12197–12202.

[221] J. Lou, S. Friedowitz, K. Will, J. Qin, Y. Xia, *Advanced Materials* **2021**, *33*.

[222] M. Rizwan, A. E. G. Baker, M. Shoichet, *Advanced Healthcare Materials* **2021**, *10*.

[223] B. Marco-Dufort, J. Willi, F. Vielba-Gomez, F. Gatti, M. W. Tibbitt, *Biomacromolecules* **2020**, *22*, 146–157.

[224] J. Dahlmann, A. Krause, L. Möller, G. Kensah, M. Möwes, A. Diekmann, U. Martin, A. Kirschning, I. Gruh, G. Dräger, *Biomaterials* **2013**, *34*, 940–951.

[225] D. Zhu, H. Wang, P. Trinh, S. C. Heilshorn, F. Yang, *Biomaterials* **2017**, *127*, 132–140.

[226] C. Loebel, R. L. Mauck, J. A. Burdick, *Nature materials* **2019**, *18*, 883–891.

[227] M. Rizwan, G. S. Peh, H.-P. Ang, N. C. Lwin, K. Adnan, J. S. Mehta, W. S. Tan, E. K. Yim, *Biomaterials* **2017**, *120*, 139–154.

[228] S. A. Fisher, P. N. Anandakumaran, S. C. Owen, M. S. Shoichet, *Advanced Functional Materials* **2015**, *25*, 7163–7172.

[229] M. P. Lutolf, J. L. Lauer-Fields, H. G. Schmoekel, A. T. Metters, F. E. Weber, G. B. Fields, J. A. Hubbell, *Proceedings of the National Academy of Sciences* **2003**, *100*, 5413–5418.

[230] A. Liu, K. Wu, S. Chen, C. Wu, D. Gao, L. Chen, D. Wei, H. Luo, J. Sun, H. Fan, *Biomacromolecules* **2020**, *21*, 3745–3755.

[231] V. A. Polyakov, M. I. Nelen, N. Nazarpack-Kandlousy, A. D. Ryabov, A. V. Eliseev, *Journal of physical organic chemistry* **1999**, *12*, 357–363.

[232] S. Mukherjee, M. R. Hill, B. S. Sumerlin, *Soft matter* **2015**, *11*, 6152–6161.

[233] J. Collins, M. Nadgorny, Z. Xiao, L. A. Connal, *Macromolecular rapid communications* **2017**, *38*, 1600760.

[234] P. Casuso, I. Odriozola, A. Pérez-San Vicente, I. Loinaz, G. Cabañero, H.-J. Grande, D. Dupin, *Biomacromolecules* **2015**, *16*, 3552–3561.

[235] H. Østergaard, C. Tachibana, J. R. Winther, *The Journal of cell biology* **2004**, *166*, 337.

[236] L. B. Poole, *Free Radical Biology and Medicine* **2015**, *80*, 148–157.

[237] L. Wang, L. Li, X. Wang, D. Huang, F. Yang, H. Shen, Z. Li, D. Wu, *Polymer Chemistry* **2016**, *7*, 1429–1438.

[238] B. D. Fairbanks, S. P. Singh, C. N. Bowman, K. S. Anseth, *Macromolecules* **2011**, *44*, 2444–2450.

[239] C. Bonnans, J. Chou, Z. Werb, *Nature reviews Molecular cell biology* **2014**, *15*, 786–801.

[240] J. Li, N. Li, B. Liu, S. Li, H. Zhang, *International Journal of Bioprinting* **2024**, *10*, 1951.

[241] J. Jansen, K. C. Reimer, J. S. Nagai, F. S. Varghese, G. J. Overheul, M. de Beer, R. Roverts, D. Daviran, L. A. Fermin, B. Willemsen, et al., *Cell stem cell* **2022**, *29*, 217–231.

[242] R. Morizane, A. Q. Lam, B. S. Freedman, S. Kishi, M. T. Valerius, J. V. Bonventre, *Nature biotechnology* **2015**, *33*, 1193–1200.

[243] M. Takasato, P. X. Er, H. S. Chiu, B. Maier, G. J. Baillie, C. Ferguson, R. G. Parton, E. J. Wolvetang, M. S. Roost, S. M. Chuva de Sousa Lopes, et al., *Nature* **2015**, *526*, 564–568.

[244] N. Annabi, A. Tamayol, J. A. Uquillas, M. Akbari, L. E. Bertassoni, C. Cha, G. Camci-Unal, M. R. Dokmeci, N. A. Peppas, A. Khademhosseini, *Advanced materials* **2014**, *26*, 85–124.

[245] F. A. Ruiter, F. L. Morgan, N. Roumans, A. Schumacher, G. G. Slaats, L. Moroni, V. L. LaPointe, M. B. Baker, *Advanced Science* **2022**, *9*, 2200543.

[246] C. Annunziata, H. Fattahpour, D. Fong, M. Hadjiargyrou, P. Sanaei, *Bulletin of Mathematical Biology* **2023**, *85*, 25.

[247] E. Fuchs, E. Sahai, A. T. Weeraratna, B. Deneen, C. C.-L. Wong, A. Simon, *Developmental Cell* **2023**, *58*, 2819–2821.

[248] A. B. Bloom, M. H. Zaman, *Physiological genomics* **2014**, *46*, 309–314.

[249] B. A. Nerger, S. Sinha, N. N. Lee, M. Cheriyan, P. Bertsch, C. P. Johnson, L. Mahadevan, J. V. Bonventre, D. J. Mooney, *Advanced Materials* **2024**, *36*, 2308325.

[250] C. Bastard, D. Günther, J. Gerardo-Nava, M. Dewerchin, P. Sprycha, C. Licht, A. Lüken, M. Wessling, L. De Laporte, *Advanced Therapeutics* **2024**, *7*, 2300091.

[251] V. X. Truong, K. M. Tsang, J. S. Forsythe, *Biomacromolecules* **2017**, *18*, 757–766.

[252] M. Ehrbar, S. C. Rizzi, R. G. Schoenmakers, B. San Miguel, J. A. Hubbell, F. E. Weber, M. P. Lutolf, *Biomacromolecules* **2007**, *8*, 3000–3007.

[253] P. Bankhead, M. B. Loughrey, J. A. Fernández, Y. Dombrowski, D. G. McArt, P. D. Dunne, S. McQuaid, R. T. Gray, L. J. Murray, H. G. Coleman, et al., *Scientific reports* **2017**, *7*, 1–7.

[254] D. Seliktar, *Science* **2012**, *336*, 1124–1128.

[255] S. R. Caliari, J. A. Burdick, *Nature methods* **2016**, *13*, 405–414.

[256] L. Riley, L. Schirmer, T. Segura, *Current opinion in biotechnology* **2019**, *60*, 1–8.

[257] D. E. Stornello, J. Kim, Z. Chen, K. Heaton, T. H. Qazi, *ACS Biomaterials Science & Engineering* **2025**, *11*, 1242–1252.

[258] A. Omidinia-Anarkoli, S. Boesveld, U. Tuvshindorj, J. C. Rose, T. Haraszti, L. De Laporte, *small* **2017**, *13*, 1702207.

[259] J. C. Rose, D. B. Gehlen, T. Haraszti, J. Köhler, C. J. Licht, L. De Laporte, *Biomaterials* **2018**, *163*, 128–141.

[260] N. Khuu, S. Kheiri, E. Kumacheva, *Trends in Chemistry* **2021**, *3*, 1002–1026.

[261] S. Xu, Z. Nie, M. Seo, P. Lewis, E. Kumacheva, H. A. Stone, P. Garstecki, D. B. Weibel, I. Gitlin, G. M. Whitesides, *Angewandte Chemie* **2005**, *117*, 734–738.

[262] S. Ma, N. Mukherjee, E. Mikhailova, H. Bayley, *Advanced Biosystems* **2017**, *1*, 1700075.

[263] A. K. Fraser, C. S. Ki, C.-C. Lin, *Macromolecular Chemistry and Physics* **2014**, *215*, 507–515.

[264] Y. Jang, C. Cha, J. Jung, J. Oh, *Macromolecular Research* **2018**, *26*, 1143–1149.

[265] L. Zhang, K. Chen, H. Zhang, B. Pang, C.-H. Choi, A. S. Mao, H. Liao, S. Utech, D. J. Mooney, H. Wang, et al., *Small* **2018**, *14*, 1702955.

[266] N. Hauck, T. A. Neuendorf, M. J. Männel, L. Vogel, P. Liu, E. Stündel, Y. Zhang, J. Thiele, *Soft Matter* **2021**, *17*, 10312–10321.

[267] S. Lee, J. de Rutte, R. Dimatteo, D. Koo, D. Di Carlo, *ACS nano* **2021**, *16*, 38–49.

[268] S. Xin, O. M. Wyman, D. L. Alge, *Advanced healthcare materials* **2018**, *7*, 1800160.

[269] C.-C. Lin, C. S. Ki, H. Shih, *Journal of applied polymer science* **2015**, *132*.

[270] D. Günther, C. Bergerbit, A. Marsee, S. Vedaraman, A. P. Moliner, C. Bastard, G. Eelen, J. L. G. Nava, M. Dewerchin, P. Carmeliet, et al., *Biofabrication* **2025**, *17*, 025015.

[271] D. M. Headen, J. R. García, A. J. García, *Microsystems & Nanoengineering* **2018**, *4*, 1–9.

[272] J. Lölsberg, J. Linkhorst, A. Cinar, A. Jans, A. J. Kuehne, M. Wessling, *Lab on a Chip* **2018**, *18*, 1341–1348.

[273] S. Boesveld, A. Jans, D. Rommel, M. Bartneck, M. Möller, L. Elling, C. Trautwein, P. Strnad, A. J. Kuehne, *ACS applied materials & interfaces* **2019**, *11*, 25017–25023.

[274] K. M. Meek, C. Knupp, *Progress in retinal and eye research* **2015**, *49*, 1–16.

[275] J. P. Rolland, B. W. Maynor, L. E. Euliss, A. E. Exner, G. M. Denison, J. M. DeSimone, *Journal of the American Chemical Society* **2005**, *127*, 10096–10100.

[276] P. Panda, S. Ali, E. Lo, B. G. Chung, T. A. Hatton, A. Khademhosseini, P. S. Doyle, *Lab on a Chip* **2008**, *8*, 1056–1061.

[277] C. M. Hwang, W. Y. Sim, S. H. Lee, A. M. Foudeh, H. Bae, S.-H. Lee, A. Khademhosseini, *Biofabrication* **2010**, *2*, 045001.

[278] L. R. Kuck, A. W. Taylor, *BioTechniques* **2008**, *45*, 179–186.

[279] R. M. Olabisi, Z. W. Lazard, C. L. Franco, M. A. Hall, S. K. Kwon, E. M. Sevick-Muraca, J. A. Hipp, A. R. Davis, E. A. Olmsted-Davis, J. L. West, *Tissue Engineering Part A* **2010**, *16*, 3727–3736.

[280] J. R. Nair, A. Chiappone, M. Destro, L. Jabbour, G. Meligrana, C. Gerbaldi, *Membranes* **2012**, *2*, 687–704.

[281] J.-A. Conchello, J. W. Lichtman, *Nature methods* **2005**, *2*, 920–931.

[282] B. V. Slaughter, S. S. Khurshid, O. Z. Fisher, A. Khademhosseini, N. A. Peppas, *Advanced materials* **2009**, *21*, 3307–3329.

[283] N. Annabi, J. W. Nichol, X. Zhong, C. Ji, S. Koshy, A. Khademhosseini, F. Dehghani, *Tissue Engineering Part B: Reviews* **2010**, *16*, 371–383.

[284] S. Bulut, S.-H. Jung, T. Bissing, F. Schmitt, M. Bund, S. Braun, A. Pich, *Small* **2023**, *19*, 2303783.

[285] Z. Meng, T. Thakur, C. Chitrakar, M. K. Jaiswal, A. K. Gaharwar, V. V. Yakovlev, *Acs Nano* **2017**, *11*, 7690–7696.

[286] B. Hammouda, D. L. Ho, S. Kline, *Macromolecules* **2004**, *37*, 6932–6937.

[287] D. J. Waters, K. Engberg, R. Parke-Houben, L. Hartmann, C. N. Ta, M. F. Toney, C. W. Frank, *Macromolecules* **2010**, *43*, 6861–6870.

[288] R. Sunyer, A. J. Jin, R. Nossal, D. L. Sackett **2012**.

[289] N. F. Truong, E. Kurt, N. Tahmizyan, S. C. Lesher-Pérez, M. Chen, N. J. Darling, W. Xi, T. Segura, *Acta biomaterialia* **2019**, *94*, 160–172.

[290] J. Schindelin, I. Arganda-Carreras, E. Frise, V. Kaynig, M. Longair, T. Pietzsch, S. Preibisch, C. Rueden, S. Saalfeld, B. Schmid, et al., *Nature methods* **2012**, *9*, 676–682.

[291] T. Haraszti, *Orientation analysis based on an oriented Gauss: Mexican hat filter*, https://github.com/tomio13/ImageP/blob/main/Example/Gauss-edge.py, **2016 (accessed August 17, 2025)**.

[292] B. Jähne in *Digital Image Processing*, Springer, **2002**, pp. 145–175.

[293] *AFM Indentation Script*, https://github.com/tomio13/AFMforce/, **2024 (accessed August 17, 2025)**.

[294] *Python*, https://www.python.org/, **(accessed August 17, 2025)**.

[295] *Spicy*, [Online; accessed 15-September-2025].

[296] *ImageP*, https://github.com/tomio13/ImageP, **(accessed August 17, 2025)**.

[297] N. Otsu, *IEEE Transactions on Systems, Man, and Cybernetics* **1979**, *9*, 62–66.

[298] R. Schlüßler, S. Möllmert, S. Abuhattum, G. Cojoc, P. Müller, K. Kim, C. Möckel, C. Zimmermann, J. Czarske, J. Guck, *Biophysical journal* **2018**, *115*, 911–923.

[299] *Brillouin Acquisition*, https://github.com/BrillouinMicroscopy/BrillouinAcquisition, **2024 (accessed August 17, 2025)**.

[300] *BMicro*, https://github.com/BrillouinMicroscopy/BMicro, **2024 (accessed August 17, 2025)**.

[301] K. Kim, J. Guck, *Biophysical journal* **2020**, *119*, 1946–1957.

[302] E. Wolf, *Optics communications* **1969**, *1*, 153–156.

[303] Y. Sung, W. Choi, C. Fang-Yen, K. Badizadegan, R. R. Dasari, M. S. Feld, *Optics express* **2009**, *17*, 266–277.

[304] K. Kim, H. Yoon, M. Diez-Silva, M. Dao, R. R. Dasari, Y. Park, *Journal of biomedical optics* **2014**, *19*, 011005–011005.

[305] *ODT Reconstruction*, https://github.com/OpticalDiffractionTomography/ODT_Reconstruction, **2024 (accessed August 17, 2025)**.

[306] *SAXS*, https://mlz-garching.de/saxs-lab, **2024 (accessed August 17, 2025)**.

[307] A. S. Hoffman, *Advanced drug delivery reviews* **2012**, *64*, 18–23.

[308] G. Deng, F. Li, H. Yu, F. Liu, C. Liu, W. Sun, H. Jiang, Y. Chen, *ACS Macro Letters* **2012**, *1*, 275–279.

[309] E. A. Appel, M. W. Tibbitt, M. J. Webber, B. A. Mattix, O. Veiseh, R. Langer, *Nature communications* **2015**, *6*, 6295.

[310] P. K. Sharma, S. Taneja, Y. Singh, *ACS Applied Materials & Interfaces* **2018**, *10*, 30936–30945, PMID: 30148349.

[311] S. Wang, G. N. Nawale, O. P. Oommen, J. Hilborn, O. P. Varghese, *Polymer Chemistry* **2019**, *10*, 4322–4327.

[312] O. P. Oommen, S. Wang, M. Kisiel, M. Sloff, J. Hilborn, O. P. Varghese, *Advanced Functional Materials* **2013**, *23*, 1273–1280.

[313] M. Patenaude, T. Hoare, *ACS Macro Letters* **2012**, *1*, 409–413.

[314] Y.-J. Zhao, Y.-Q. Zhai, G.-H. Ma, Z.-G. Su, *Journal of Applied Polymer Science* **2009**, *111*, 1638–1643.

[315] A. Dirksen, T. M. Hackeng, P. E. Dawson, *Angewandte Chemie* **2006**, *118*, 7743–7746.

[316] G. N. Grover, J. Lam, T. H. Nguyen, T. Segura, H. D. Maynard, *Biomacromolecules* **2012**, *13*, 3013–3017.

[317] D. E. Apostolides, T. Sakai, C. S. Patrickios, *Macromolecules* **2017**, *50*, 2155–2164.

[318] P. K. Sharma, S. Taneja, Y. Singh, *ACS applied materials & interfaces* **2018**, *10*, 30936–30945.

[319] A. Dirksen, T. M. Hackeng, P. E. Dawson, *Angewandte Chemie* **2006**, *118*, 7743–7746.

[320] W. P. Jencks, *Journal of the American Chemical Society* **1959**, *81*, 475–481.

[321] W. P. Jencks, *Progress in Physical Organic Chemistry* **1964**, 63–128.

[322] A. D. Crowell, T. M. FitzSimons, E. V. Anslyn, K. M. Schultz, A. M. Rosales, *Macromolecules* **2023**, *56*, 7795–7807.

[323] T. E. Robinson, E. A. Hughes, A. Bose, E. A. Cornish, J. Y. Teo, N. M. Eisenstein, L. M. Grover, S. C. Cox, *Advanced Healthcare Materials* **2020**, *9*, 1901521.

[324] B.-S. Kim, D. J. Mooney, *Trends in biotechnology* **1998**, *16*, 224–230.

[325] A. Eltom, G. Zhong, A. Muhammad, *Advances in Materials Science and Engineering* **2019**.

[326] I. D. Hosein, *Chemistry of Materials* **2020**, *32*, 2673–2687.

[327] K. Griesbaum, *Angewandte Chemie* **1970**, *82*, 276–290.

[328] R. Plummer, D. J. Hill, A. K. Whittaker, *Macromolecules* **2006**, *39*, 8379–8388.

[329] R. Schlüßler, K. Kim, M. Nötzel, A. Taubenberger, S. Abuhattum, T. Beck, P. Müller, S. Maharana, G. Cojoc, S. Girardo, et al., *elife* **2022**, *11*, e68490.

[330] *Scipy*, https://www.scipy.org/, **(accessed August 17, 2025)**.

[331] E. A. Mol, Z. Lei, M. T. Roefs, M. H. Bakker, M.-J. Goumans, P. A. Doevendans, P. Y. Dankers, P. Vader, J. P. Sluijter **2019**.

Acronyms

2D	two-dimensional
2PP	two-photon polymerization
3D	three-dimensional
AFM	atomic force microscopy
AKI	acute kidney injury
AMB	amphotericin B
AR	aspect ratio
BSA	bovine serum albumin
Ca	Capillary
CFD	computational fluid dynamics
CJP	compartmentalized jet polymerization
CNF	cellulose nanofibrils
CPs	conductive polymers
CSLM	confocal scanning laser microscopy
DCC	dynamic covalent chemistries
DCM	dichloromethane
DMEM	(Dulbeccos Modified Eagle Medium
DMSO	dimethly sulfoxide
ECM	extracellular matrix
EDC	1-ethyl-3-(3-dimethylaminopropyl)carbodiimide
ES	electrical stimulation
FBS	fetal bovine serum
FDA	Food and Drug Administration
FF	flow-focused

FLight	filamented light
FRP	free radical polymerization
FWHM	full width half maximum
FXIIIa	activated Factor XIII
GelMA	Gelatin methacryoyl
HA	hyaluronic acid
hiPSCs	human induced pluripotent stem cells
hMSCs	human mesenchymal stem cells
HPLC	High Performance Liquid Chromatography
iEDDA	inverse electron demand Diels-Alder
iPSCs	induced pluripotent stem cells
LAP	Lithium-Phenyl-2,4,6-trimethylbenzoyl phosphinate
LED	light emitting diode
MAP	microporous annealed particle
MAPs	microporous annealed particles
MMP	matrix metalloproteinases
MSCs	mesenchymal stem cells
NHDFs	normal human dermal fibroblasts
NMR	nuclear magnetic resonance
ODT	optical diffraction tomography
OMI	optical modulation instability
PA	peptide amphiphiles
PASA	poly (aniline-co-*N*-(4-sulfophenyl) aniline
PBS	phosphate buffered saline
PDMS	polydimethylsiloxane
PEG	poly (ethylene) glycol
PEGDA	poly (ethylene glycol) diacrylate
PEGMA	poly (ethylene glycol) methacrylate
PEG-VS	poly (ethylene glycol) vinylsulfone
PFA	paraformaldehyde
PFPE	perfluoropolyether

PGA	poly (glycolic acid)
PGMEA	propylene glycol methyl ether acetate
PICs	polyisocyanides
PKD	polycystic kidney disease
PLA	poly (lactic acid)
PLGA	poly (lactic-co-glycolic) acid
PRINT	particle replication in non-wetting templates
PT	proximal tubule
PTFE	polytetrafluoroethylene
RI	refractive index
SAPHs	self-assembling peptide hydrogels
SAXS	small angle x-ray scattering
SE	step-emulsification
SEM	scanning electron microscopy
SFL	stop-flow lithography
SIM	sound-induced morphogenesis
SPAAC	strain promoted azide-alkyne cycloaddition
sPEG	star poly (ethylene glycol)
SPIONs	superparamagnetic iron oxide nanoparticles
TEMED	*N,N,N′,N′*-Tetramethylethane-*1,2*-diamine
UCLA	University of California, Los Angeles
UPy	ureido-pyrimidinone
UV	ultra violett
We	Weber